Università degli Studi di Genova
Aix-Marseille Université

SCUOLA DI SCIENZE MATEMATICHE, FISICHE E NATURALI
ED 352 – PHYSIQUE ET SCIENCES DE LA MATIÈRE

SINGLE-ELECTRON DYNAMICS IN TOPOLOGICALLY PROTECTED SYSTEMS

Thesis presented to obtain the degree of

DOTTORE DI RICERCA and DOCTEUR

by

MATTEO ACCIAI

Defense on 20/12/2019 in front of the jury:

Riccardo FERRANDO	Università di Genova	Chairman
Maura SASSETTI	Università di Genova	Supervisor
Thierry MARTIN	Aix-Marseille Université	Co-supervisor
Laurent RAYMOND	Aix-Marseille Université	Examinator
Ulf GENNSER	Université Paris-Saclay	Examinator
Roberto RAIMONDI	Università Roma Tre	Referee

ABSTRACT

Electron quantum optics is a fast growing research field which aims at preparing, controlling and coherently manipulating single- to few-electrons states in mesoscopic condensed matter systems, in the same way as single photons can be manipulated in conventional quantum optics. Recently developed coherent single-electron sources are used to generate few-electron excitations in ballistic conductors, where their propagation is not affected by backscattering and phase coherence is preserved.

Among several interesting problems related to electron quantum optics, an important question is whether and how interaction effects can influence the evolution of single-electron excitations generated by coherent sources. This will be the main topic of this thesis, where we investigate the properties of excitations created by applying a voltage pulse to a quantum conductor. The thesis can be conceptually divided into two main blocks, depending on which kind of interactions are taken into account.

At first we consider a couple of conduction channels coupled by repulsive electron-electron interactions, focusing on two scenarios. Initially, co-propagating edge channels in the integer quantum Hall effect are considered, followed by counterpropagating channels emerging at the edge of a quantum spin Hall insulators. In both systems, electronic interactions induce a fractionalization process causing the initially generated excitations to split into smaller ones, carrying only a fraction of the injected charge. These fractionalized excitations are carefully analyzed both in the time domain as well as in energy and momentum space, which allows to access their particle-hole content. The analysis is based on an analytic approach relying on Luttinger liquid theory and bosonization techniques and applies to any voltage drive. Moreover, specializing to the relevant case of excitations created by quantized Lorentzian voltage pulses, known as Levitons, we show that the noise generated when they are partitioned at a scatterer is minimal, regardless of interactions.

Further on, a completely different kind of interaction is addressed, namely superconducting correlations. In particular, we investigate the transport properties of a superconducting tunnel junction under the effect of an arbitrary periodic drive, showing that Levitons do minimize the low frequency noise in this kind of device too.

RÉSUMÉ

L'optique quantique électronique est un domaine de recherche en pleine croissance qui vise à préparer, contrôler et manipuler de manière cohérente des états à électrons uniques dans des systèmes mésoscopiques en matière condensée, de la même manière que les photons peuvent être manipulés dans le domaine de l'optique quantique conventionnelle. Des sources d'électrons uniques, récemment développées, peuvent être utilisées afin de générer des excitations à quelques électrons dans des conducteurs balistiques, où la propagation n'est pas affectée par la rétrodiffusion et la cohérence de phase est préservée.

Parmi les nombreux problèmes liés à l'optique quantique électronique, une question particulièrement importante est celle de comprendre les effets des intéractions électroniques sur l'évolution des excitations produites par les sources d'électrons. Cela sera le sujet principal de cette thèse, dans laquelle on étudie les propriétés des excitations créées dans un conducteur quantique grâce à des impulsions de tension.

Tout d'abord on considère une couple de canaux conducteurs en présence d'intéractions répulsives, en distinguant deux scénarios. Le premier est rélatif au cas de canaux co-propageants, tels que l'on les trouve dans les états de bord de l'effet Hall quantique entier. Le deuxième concerne une couple de canaux contre-propageants qui émergent dans l'effet Hall quantique de spin. Dans les deux cas, les intéractions sont telles que les excitations initiellement introduites dans le système à cause de l'impulsion de tension se séparent en des composants ayant une fraction de la charge originaire. Ces excitations "fractionnées" sont étudiées soit dans le domaine temporel soit dans la représentation énérgie, ce qui permet d'obtenir des informations rélatives au contenu de couples particule-trou. On utilise une approche analytique, valable pour des impulsions de tension quelconques, basée sur la théorie du liquide de Luttinger et la technique de la bosonisation. En plus, en considérant des excitations générées par des impulsions de forme lorentzienne, connues comme Lévitons, on démontre que le bruit dû à la présence d'un centre de diffusion est minimisé, indépendemment des intéractions.

Ensuite, on adresse des systèmes où les corrélations électroniques sont tout à fait differentes, c'est-à-dire des supraconducteurs. En particulier, on étudie les propriétés de transport d'une jonction tunnel supraconductrice amenée hors de l'équilibre par des impulsions de tension périodiques de forme arbitraire et on démontre que les Lévitons minimisent le bruit à basse fréquence dans ce système aussi.

CONTENTS

LIST OF PUBLICATIONS

This thesis is based on the following publications co-authored by myself:

[1] M. Acciai, M. Carrega, J. Rech, T. Jonckheere, T. Martin, and M. Sassetti, "Probing interactions via nonequilibrium momentum distribution and noise in integer quantum Hall systems at $\nu = 2$," Phys. Rev. B **98**, 035426 (2018).

[2] M. Acciai, M. Carrega, J. Rech, T. Jonckheere, D. Ferraro, T. Martin, and M. Sassetti, "Single-electron excitations and interactions in integer quantum Hall systems at $\nu = 2$," Journal of Physics: Conference Series **1182**, 012003 (2019).

[3] M. Acciai, F. Ronetti, D. Ferraro, J. Rech, T. Jonckheere, M. Sassetti, and T. Martin, "Levitons in superconducting point contacts," Phys. Rev. B **100**, 085418 (2019).

[4] M. Acciai, A. Calzona, M. Carrega, T. Martin, and M. Sassetti, "Spectral properties of interacting helical channels driven by lorentzian pulses," New Journal of Physics **21**, 103031 (2019).

Other publications, not included in this thesis, are:

[5] A. Calzona, M. Acciai, M. Carrega, F. Cavaliere, and M. Sassetti, "Time-resolved energy dynamics after single electron injection into an interacting helical liquid," Phys. Rev. B **94**, 035404 (2016).

[6] M. Acciai, A. Calzona, G. Dolcetto, T. L. Schmidt, and M. Sassetti, "Charge and energy fractionalization mechanism in one-dimensional channels," Phys. Rev. B **96**, 075144 (2017).

[7] D. Ferraro, F. Ronetti, L. Vannucci, M. Acciai, J. Rech, T. Jonckheere, T. Martin, and M. Sassetti, "Hong-Ou-Mandel characterization of multiply charged Levitons," The European Physical Journal Special Topics **227**, 1345–1359 (2018).

[8] F. Ronetti, M. Acciai, D. Ferraro, J. Rech, T. Jonckheere, T. Martin, and M. Sassetti, "Symmetry Properties of Mixed and Heat Photo-Assisted Noise in the Quantum Hall Regime," Entropy **21**, 730 (2019).

LIST OF FIGURES

ACRONYMS

EQO   Electron Quantum Optics

QPC   Quantum Point Contact

HOM   Hong-Ou-Mandel

HBT   Hanbury Brown-Twiss

2DEG   Two-Dimensional Electron Gas

1D   One-Dimensional

2D   Two-Dimensional

2DTI   Two-Dimensional Topological Insulators

IQHE   Integer Quantum Hall Effect

FQHE   Fractional Quantum Hall Effect

QSHE   Quantum Spin Hall Effect

QD   Quantum Dot

LL   Luttinger Liquid

HLL   Helical Luttinger Liquid

SQPC   Superconducting Quantum Point Contact

OPTIQUE QUANTIQUE ÉLECTRONIQUE

Le développement technologique dans les dispositifs à semiconducteurs a permis d'observer des effets quantiques cohérents et a amené au contrôle de plus en plus précis des propriétés quantiques à l'échelle des électrons uniques. Ceci a ouvert des scénarios très intéressants, l'un desquels est sans doute représenté par l'optique quantique électronique. Ce domaine de recherche assez récent vise à préparer, contrôler et manipuler de manière cohérente des états à électrons uniques dans des systèmes mésoscopiques en matière condensée, de la même manière que les photons peuvent être manipulés dans le domaine de l'optique quantique "conventionnelle". Une telle possibilité est sans doute très intéressante en elle-même, mais elle est aussi importante du point de vue applicatif. Deux exemples sont représentés par la métrologie, où le contrôle des courants au niveau d'électrons uniques peut être utilisé pour une définition précise de l'ampère, et par le calcul quantique, dans la mesure où l'information pourrait être codifiée et manipulée à travers des états à électrons uniques.

Afin que le programme de l'optique quantique électronique puisse être réalisé, trois ingrédients au minimum doivent être disponibles : des sources capables d'émettre des électrons uniques, des canaux balistiques où ils peuvent se propager en préservant leur cohérence de phase (de façon que les effets quantiques ne soient pas perdus) et, enfin, l'équivalent des séparateurs de faisceau pour faire de l'interférométrie. Tous ces composants sont disponibles du point de vue expérimental, ce qui a permis dans les dernières années de réaliser plusieurs expériences. Avant de présenter comment ces trois composants sont réalisés dans les systèmes en matière condensée, il vaut la peine de souligner que l'optique quantique électronique n'est pas une simple reproduction de celle conventionnelle avec les photons, étant donné que, au-delà des similarités entre elles, des différences évidentes sont aussi présentes. Il y a tout d'abord une différence dans la statistique entre électrons et photons, ce qui amène à des résultats différents si on fait de l'interférométrie. En plus, l'état fondamental d'un système d'électrons dans un matériel n'est pas le vide, mais la mer de Fermi, et donc l'émission d'un électron dans un tel état n'est pas la même chose que la création d'un photon dans le vide. Enfin, au contraire des photons, les électrons interagissent entre eux, ce qui peut être important pour l'interprétation des résultats expérimentaux. L'étude des interactions dans le domaine de l'optique quantique électronique
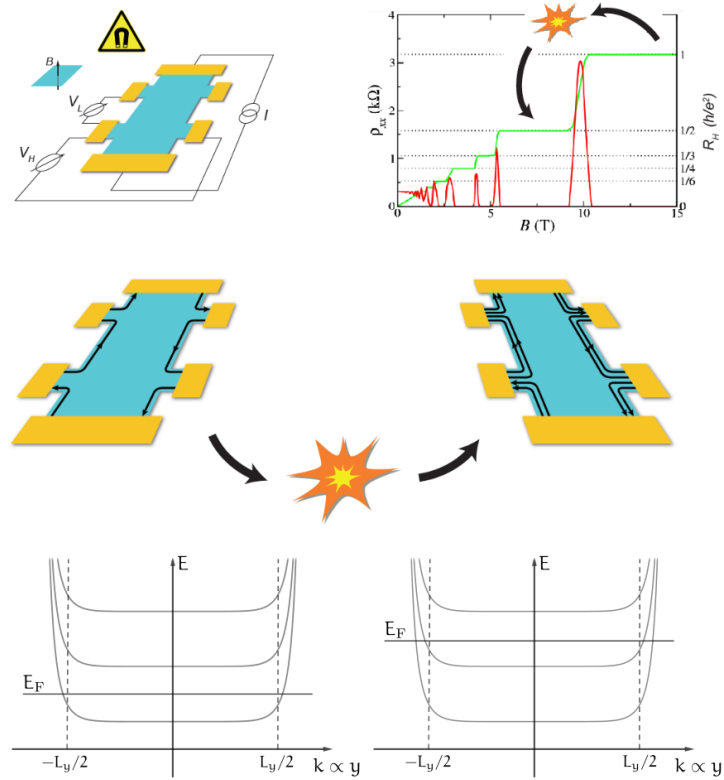
FIGURE R.1 : Résumé de la phénoménologie de l'effet Hall quantique entier. Un champ magnetique est appliqué perpendiculièrement à un gaz bidimensionnel d'électrons. Une mesure de la résistence de Hall R_H montre des plateaux dont les valeurs sont quantifiées : $R_H = h/(\nu e^2)$, où $\nu \in \mathbb{N}$ est connu comme facteur de remplissage. Ce phénoméme est accompagné de la présence d'états métalliques localisés au bords du système, pour ça appelés états de bord. Leur présence est expliquée en considérant un potentiel de confinement (dû à la finitude de l'échantillon) qui modifie les niveaux de Landau près des bords, où ils sont par conséquent croisés par le niveau de Fermi E_F.

est précisément le sujet principal de cette thèse et sera développé dans les trois derniers Chapitres.

Canaux balistiques : l'effet Hall quantique entier

Des canaux balistiques unidimensionnels peuvent être obtenus à partir d'un système bidimensionnel dans le régime de l'effet Hall quantique entier. Cet effet se manifeste alors qu'un gaz bidimensionnel d'électrons est soumis à un champ magnétique très intense, appliqué perpendiculairement au plan de l'échantillon. Comme découvert par von Klitzing en 1980, si on impose un courant le long d'une direction et on mesure la résistence dans la direction perpendiculaire à celle du courant, appelée résistence de Hall (R_H), on obtient le ré-

sultat montré en Fig. R.1. Après un comportement linéaire à faibles champs magnétiques, R_H développe des plateaux dont les valeurs ne dépendent que de deux constantes fondamentales et un nombre entier : $R_H = h/(ne^2)$. Ici, h est la constante de Planck, $-e$ la charge de l'électron et $\nu \in \mathbb{N}$ est appelé facteur de remplissage et représente le nombre de niveaux de Landau qui sont remplis[1]. Les niveaux de Landau (étudiés pour la première fois par L. Landau, d'où leur nom) émergent de la description quantique-mécanique d'un système d'électrons indépendants sous l'effet d'un champ magnétique. La solution de l'équation de Schrödinger montre que le spectre du système est composé de niveaux équidistants, séparés par un écart qui augmente linéairement avec le champ magnétique. Pourtant, une conséquence de cette description est que le système devrait être isolant, ce qui est évidemment incompatible avec les mesures expérimentales.

Cette contradiction a été expliquée et résolue par l'introduction de l'idée de canaux de bord, c'est-à-dire des états métalliques émergeants aux bords du système. Donc, la conduction de courant n'est possible que le long des bords de l'échantillon, tandis que l'intérieur reste effectivement isolant. Il y a plusieurs façons de comprendre comment les états de bord émergent ; ici on n'adresse qu'une. L'ingrédient fondamental est la présence d'un potentiel de confinement pour les électrons, que l'on doit nécessairement considérer parce que un système réel n'est pas infini. Ce potentiel de confinement est pratiquement absent à l'intérieur du système mais il croît très rapidement près des ses bords. Par conséquent, les niveaux de Landau sont "pliés" vers le haut et donc le niveau de Fermi les croise près des bords, comme montré en Fig. R.1. En observant cette figure il est aussi évident que le nombre de canaux pour chaque bord est lié à la position du niveau de Fermi et, donc, au nombre des niveaux de Landau remplis, qui est determiné à son tour du facteur de remplissage.

La propriété la plus importante des états de bord est leur protection topologique. Le terme "topologique" est emprunté aux mathématiques, où il est utilisé pour indiquer des propriétés globales des objets géométriques, celles qui ne dépendent pas des détails locaux. De la même façon, en matière condensée une phase topologique est un état de la matière dont les propriétés sont à attribuer à quelque caractéristique "globale" tout à fait indépendante des détails particuliers du système où cet état est réalisé, comme par exemple le type d'échantillon ou la présence de désordre. Cela est exactement ce qui se passe dans l'effet Hall quantique entier, le premier exemple de phase topologique de la matière du point de vue historique. La découverte des propriétés topologiques de l'effet Hall quantique (entier initialement et fractionnaire quelques années après) a été extrêmement importante, car elle nous a fait comprendre que les transitions de phase ne peuvent

---

[1] En géneral, ν n'est pas un nombre entier, mais la phénoménologie que l'on décrit ici se vérifie dans cette condition.

pas toujours être attribuées au cassement d'une symétrie. L'effet Hall a donc amené la topologie dans la physique de la matière condensée et aujourd'hui la recherche de nouveux matériaux topologiques est très active dans la communauté scientifique.

L'origine topologique de l'effet Hall quantique est la raison pour laquelle la quantification de la résistance R_H est extrêmement précise (jusqu'à une partie par milliard). Il est aussi possible de démontrer que cela implique que la propagation des électrons le long des canaux de bord doit être balistique et la rétrodiffusion absente. Du point de vue pratique, des libres parcours moyens de plusieurs micromètres ont été mesurés dans les systèmes Hall. Cette brève discussion montre que les canaux de bord représentent un outil idéal pouvant jouer le rôle de guide d'onde en optique quantique électronique.

Sources d'électrons uniques

Les sources cohérentes d'électrons uniques représentent le développement expérimental fondamental qui a marqué la naissance de l'optique quantique électronique. En particulier, deux approches principales ont été employées : le condensateur mésoscopique (2007) et une source qui exploite des impulsions de tensions (2013). Dans ce résumé on ne décrit que la deuxième approche, qui est la seule considérée dans la partie originale de la thèse.

L'idée à la base de cette source est assez simple. Si on applique une impulsion de tension $V(t)$ dépendant du temps à un conducteur balistique unidimensionnel, une excitation est générée dans le canal. En particulier, pour un canal non-interagissant, la réponse en courant est $I(t) = e^2 h^{-1} V(t)$. Par conséquent, la charge (divisée par $-e$) transportée par l'excitation créée dans le système est

$$q = -\frac{e}{h} \int_{-\infty}^{+\infty} dt\, V(t)\,.$$

Toutefois, même si q est un nombre entier, on ne peut pas dire de n'avoir excité que q électrons. En fait, il est en général très probable que des paires électron/trou accompagnent l'excitation générée par l'impulsion $V(t)$. Il est néanmoins possible de modeler la forme du signal de façon que exactement q électrons soient excités au dessus de la mer de Fermi et aucune paire électron/trou ne soit présente. Cette prédiction, due à Levitov et collaborateurs, établit que la forme du signal $V(t)$ doit être lorentzienne :

$$V(t) = -\frac{nh}{2\pi e} \frac{2w}{w^2 + t^2}\,, \qquad n \in \mathbb{N}\,,$$

où *w* est une échelle temporelle determinant la largeur de l'impulsion. La charge associée à ce signal est évidemment $q = n$ et les excitations qu'il génère ont été appelées Lévitons. Un Léviton est donc une excitation minimale.

(a)

(b)
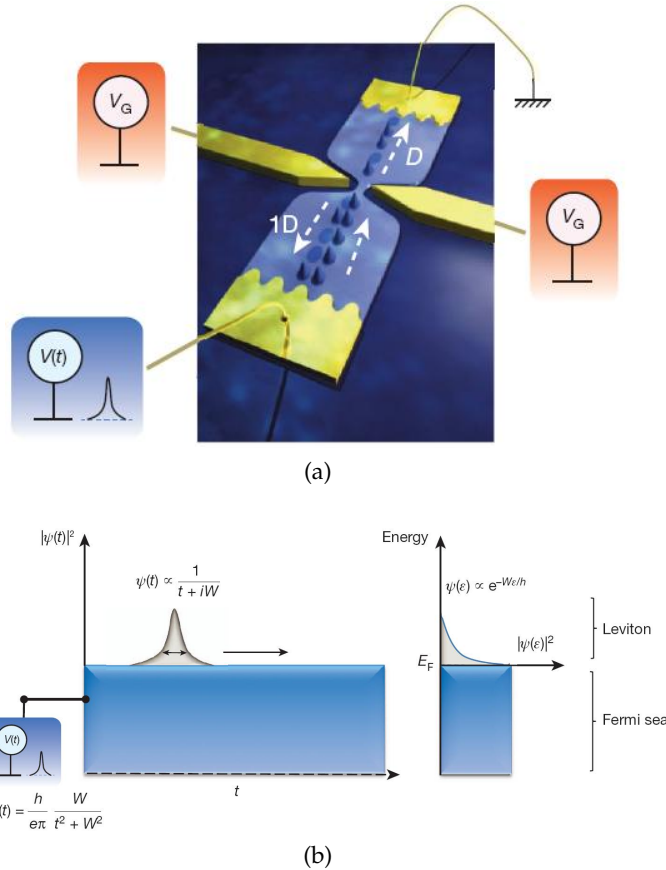
FIGURE R.2 : En haut (a) : schéma de la configuration employée pour la détection des Lévitons. En bas (b) : représentation de la fonction d'onde d'un Léviton et de sa distribution en énergie.

La prédiction de Levitov a été confirmée en 2013 par le groupe expérimental de D. C. Glattli qui a exploité le fait que le nombre en excès de paires électron/trou générées par un signal $V(t)$ peut être obtenu en mesurant le bruit de courant qui se crée quand les excitations dues à $V(t)$ sont envoyées vers une barrière qui les transmet avec un probabilité que l'on peut contrôler. Le système utilisé pour la mesure est un contact ponctuel quantique dans le régime balistique, representé en Fig. R.2 (en haut). Ici, le contact ponctuel quantique joue un double rôle : il crée le canal unidimensionnel et il agit aussi comme séparateur de rayon, en transmettant les excitations, qui arrivent du términal où $V(t)$ est appliqué, avec un probabilité D. En mesurant le bruit de courant dans le terminal qui se trouve après le contact ponctuel quantique, les expérimentateurs ont démontré que le nombre de paires électron/trou dues au signal lorentzien proposé per Levitov dévient zéro, différemment des autres signaux. Cela signifie que le Léviton est véritablement une excitation minimale décrivant un électron au dessus de la mer de Fermi, comme on voit en Fig. R.2 (en bas).
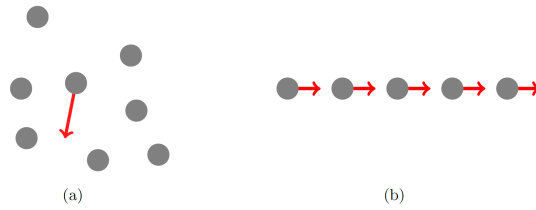
FIGURE R.3 : Comparaison schématique entre les systèmes unidimensionnels et ceux à dimensionnalité plus haute. Dans le dernier cas (gauche), des excitations de quasi-particule sont possibles. Au contraire, dans les systèmes unidimensionnels (droite) on n'a que des excitations collectives, parce que le mouvement d'un électron influence nécessairement celui des autres particules, à cause des interactions.

INTÉRACTIONS DANS LES SYSTÈMES UNIDIMENSIONNELS

Quand on considère les effets des interactions électroniques, les systèmes unidimensionnels ont un comportement très different et tout à fait particulier par rapport à ce qui se passe en dimensionnalités plus hautes. En fait, au lieu de la théorie du liquide de Fermi (développée par le physicien russe L. Landau), les systèmes unidimensionnels sont décrits par la théorie du liquide de Luttinger qui prévoit des effets très particuliers, dont la "fractionalisation" de charge et la séparation de charge et spin sont les plus éclatants. La fractionalisation de charge sera illustrée en détail dans les prochaines Sections de ce résumé. Pour l'instant, on veut simplement donner une idée intuitive de la raison pour laquelle les systèmes unidimensionnels sont spéciaux. Un résumé schématique de ça est présenté en Fig. R.3.

La théorie du liquide de Fermi, valable pour décrire les interactions électroniques en dimensions $d > 1$, est basée sur l'idée de quasi-particule. En bref, une quasi-particule est une excitation individuelle qui peut être regardée comme un électron (avec des paramètres renormalisés) habillé par une nuage de fluctuations de densité de charge. Ces quasi-particules interagissent très faiblement entre elles, ce qui implique qu'un gaz d'électrons interagissant en $d > 1$ préserve plus ou moin les mêmes propriétés qualitatives que l'on observe dans un gaz de Fermi non-interagissant.

Les péculiarités des systèmes unidimensionnels interagissant résident dans le fait qu'il n'est pas possible d'avoir des excitations individuelles, ce qui rend l'idée de quasi-particule inapplicable. Au contraire, les excitations sont uniquement collectives et ont un caractère bosonique. En fait, il est possible de démontrer que l'opérateur férmionique peut s'exprimer à travers d'un partenaire bosonique. Cette procédure, connue comme bosonisation, est à la base du traitement exact des interactions électroniques dans théorie du liquide de Luttinger.
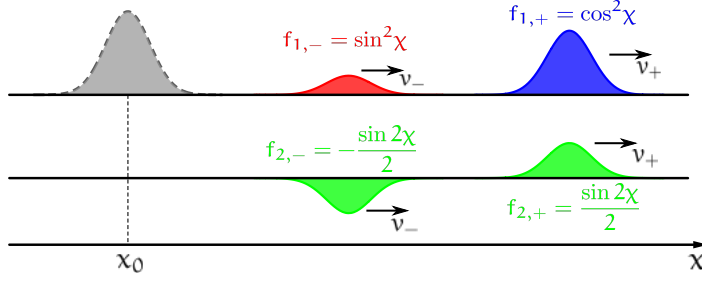
FIGURE R.4 : Fractionalisation de charge dans un couple de canaux co-propageants. Une excitation introduite dans le système en position x_0 se divise en quatre parties, chacune desquelles emporte avec soi un fraction de la charge originaire. Ces fractions dépendent des interactions à travers du paramètre χ.

CANAUX CO-PROPAGEANTS EN PRÉSENCE D'INTERACTIONS

Dans le Chapitre 3 on étudie l'effet des interactions dans un couple de canaux co-propageants, tels que l'on les trouve dans l'effet Hall quantique à facteur de remplissage $\nu = 2$. On considère un modèle proposé par Levkivskyi and Sukhorukhov, qui s'inspire de la théorie de Luttinger et prends en compte des interactions locales densité-densité. La solution du modèle montre que les deux canaux originaires se mélangent entre eux à cause des interactions et les excitations du système sont des fluctuations de charge se propageant à deux vitesses, v_+ et v_-. Ceci est la raison à la base de la fractionalisation de charge, montrée dans la Fig. R.4. Par conséquent, si on introduit une excitation sur le canal externe, elle évolue se séparant en quatre parties qui emportent chacune une fraction de la charge originaire. Ces fractions sont

$$f_{1,-} = \sin^2\chi, \qquad f_{1,+} = \cos^2\chi,$$
$$f_{2,-} = -\frac{\sin 2\chi}{2}, \qquad f_{2,+} = \frac{\sin 2\chi}{2}.$$

Ici, le paramètre χ est appelé angle de mélange et peut varier entre $\chi = 0$ (pas d'interactions) et $\chi = \pi/4$ (couplage maximal entre les deux canaux du système). Il vaut la peine de noter que la charge totale sur le canal interne est toujours zéro, les charges de ses deux excitations étant égales et opposées. Ça est dû au fait que l'interaction entre les deux canaux est capacitive et donc il n'est pas possible de transférer de la charge du canal externe à celui interne.

On a étudié les propriétés des excitations en utilisant la fonction de Wigner, qui permet de voir au même temps le procès de fractionalisation et le contenu énergetique des excitations. Il est donc possible à travers de cet outil de s'apercevoir si elles sont minimales ou pas. Comme on peut s'attendre, on a des excitations minimales au moment où leur charge est un multiple entier de la charge électronique élé-

mentaire ; par ailleurs, des paires électron/trou sont excitées dans le système dans le cas de charge non entière.

Du point de vue expérimental, on ne peut pas contrôler la charge des excitations "fractionalisées", mais uniquement celle de l'excitation initiellement introduite dans le système, c'est-a-dire q. Pourtant, en exploitant le lien $q_{2,\pm} = \pm q \sin\chi \cos\chi$ entre q et les charges $q_{2,\pm}$ des excitations se propageant dans le canal interne, on peut montrer qu'il est possible d'obtenir des informations sur l'interaction à partir de mesures de bruit. Spécifiquement, on a considéré d'ajouter un contact ponctuel quantique, polarisé de telle manière que le canal externe est complètement transmis, tandis que celui interne est partiellement refléchi. Le bruit du courant rétrodiffusé en cette configuration permet d'obtenir des informations intéressantes. Tout d'abord, il peut être lié au nombre d'électrons et trous excités par le signal $V(t)$. Ensuite, on démontre qu'il peut être utilisé pour définir une quantité $\mathcal{X}$ ayant des maxima en correspondence des valeurs entières et démi-entières de $q_{2,+}$. Ce comportement, se vérifiant dans le cas où $V(t)$ est une onde rectangulière, permet d'extraire la valeur de χ : en fait, en mesurant les valeurs $q = \bar{q}$ pour lesquelles $\mathcal{X}$ a des maxima, on obtient χ du lien $q_{2,+} = \bar{q} \sin\chi \cos\chi$, en sachant que $q_{2,+}$ sont des nombres entiers ou démi-entiers.

CANAUX CONTRE-PROPAGEANTS DANS L'EFFET HALL QUANTIQUE DE SPIN

Grâce aux récents développements expérimentaux, d'autres systèmes différant des états de l'effet Hall quantique pourraient être intéressants afin d'étendre le domaine de l'optique quantique électronique. L'un d'entre eux est représenté par les états de bord de l'effet Hall quantique de spin. Cette phase de la matière a aussi des propriétés topologiques, mais elle diffère de l'effet Hall quantique dans la mesure où ses états de bord sont contre-propageants (au lieu de co-propageants) et la projection du spin des électrons est liée à la direction de propagation le long du canal. Cette propriété, connue sous l'expression anglaise de *spin-momentum locking*, est topologiquement protégée par la présence de la symétrie d'inversion temporelle, qui est un ingrédient fondamental pour que cette phase de la matière puisse être achevée. Une représentation de l'effet Hall de spin est donnée en Fig. R.5.

Dans le Chapitre 4 on étudie comment les interactions entre les deux canaux contre-propageants influencent une excitation générée par une impulsion de tension. De façon similaire à ce que l'on a décrit dans la Section précédente, les interactions prises en compte dans le modèle de Luttinger mélangent les canaux originaires : le système est décrit par des fluctuations de charge qui se propagent en directions opposées, avec une vitesse renormalisée. Par conséquent, le procès de fractionalisation de l'excitation créée par le signal $V(t)$ est diffèrent
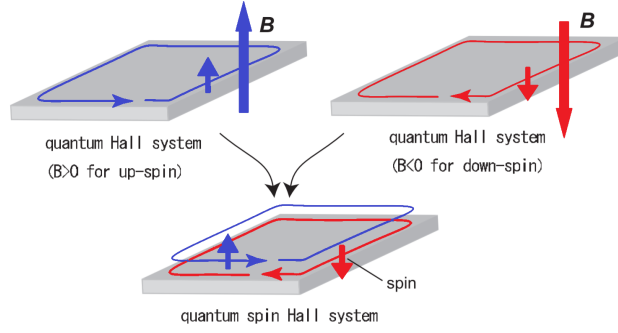
FIGURE R.5 : L'effet Hall quantique de spin vu comme combinaison de deux états de l'effet Hall quantique à $\nu = 1$ ayant des chiralités opposées.
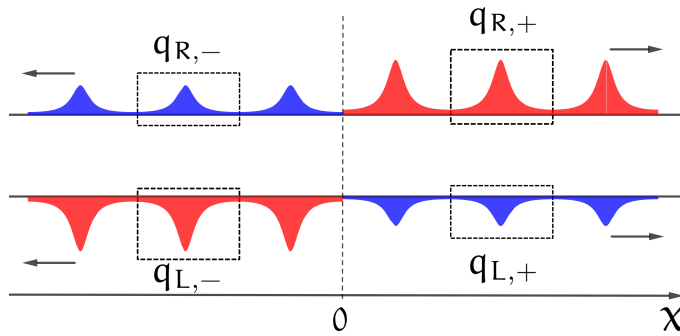
FIGURE R.6 : Procès de fractionalisation d'une succession d'excitations générées au point $x = 0$ par un signal périodique $V(t)$.

par rapport à ce que l'on a vu pour les canaux co-propageants et il est représenté en Fig. R.6. La figure a été réalisée dans le cas d'un signal $V(t)$ périodique, comme considéré dans le Chapitre 4. Les deux canaux originaires, qui se propageraient vers droite (R) et gauche (L) en absence d'interactions, sont dessinés comme s'ils étaient spatialement séparés, tandis qu'en réalité ils ne sont distingués que par la projection du spin des électrons, grâce au *spin-momentum locking*.

De toute façon, quatre excitations émergent dans le système, deux se propageant vers la droite [$(R, +)$ et $(L, +)$] et deux vers la gauche [$(R, -)$ et $(L, -)$]. Leurs charges sont

$$q_{R,+} = q\,\frac{1+K}{2} = -q_{L,-}\,,$$

$$q_{R,-} = q\,\frac{1-K}{2} = -q_{L,+}\,,$$

où q est la charge pour période associée au signal $V(t)$. La quantité K est le paramètre fondamental de ce modèle : elle est appelée constante de couplage de Luttinger et décrit l'intensité des interactions dans ce modèle. Un système non-interagissant correspond à $K = 1$, tandis que $K < 1$ décrit le cas d'interactions répulsives. Il est à noter que si

$K = 1$, seulement les excitations $(R, +)$ et $(L, -)$ sont présentes et ont une charge q et $-q$, respectivement.

Comme déjà noté précédemment, l'évolution en espace réel des excitations fractionalisées ne permet d'avoir aucune information sur leur contenu en termes de paires électron/trou. Afin d'avoir une telle description, on a étudié la fonction spectrale en excès des excitations, c'est-à-dire la fonction spectrale obtenue après la subtraction de la contribution d'équilibre, qui évidemment ne peut pas dépendre du signal $V(t)$. Des excitations minimales ont une fonction spectrale en excès qui a partout le même signe que celui de leur charge. Les résultats que l'on a obtenus montrent que des excitations de forme lorentzienne avec une charge entière ne sont minimales que pour les canaux $(R, +)$ et $(L, -)$.

Pourtant, le bruit en excès associé au partitionnement d'une excitation lorentzienne ayant une charge entière est toujours zéro, tant pour le canal $(R, +)$ que pour $(L, +)$. Cette propriété n'est donc due qu'à la particulière forme du signal lorentzien et ne dépend pas des interactions. Ceci démontre que, dans les systèmes interagissant, on doit faire attention à associer les zéros du bruit en excès à des excitations minimales. Il est néanmoins possible d'exploiter les Lévitons pour extraire la constante de Luttinger décrivant l'intensité des interactions, d'une façon similaire à celle presentée dans la Section précédente. En fait, étant donné que le bruit en excès dû au partitionnement des excitations sur le canal $(R, +)$ est annulé quand $q_{R,+} = n \in \mathbb{N}$, ça signifie que les zéros se trouvent en correspondence des valeurs de charge

$$q = \frac{2n}{1 + K} \, .$$

Par conséquant, en mesurant la valeur de q correspondant au n-ème zéro, on peut trouver celle de K en résolvant l'équation précédente.

EFFETS LIÉS À LA SUPRACONDUCTIVITÉ

Ayant étudié les effets des interactions électroniques répulsives en deux systèmes differents, dans cette dernière partie on considère des correlations tout à fait differentes, c'est-à-dire celles que l'on trouve en présence des supraconducteurs. En particulier, on veut voir si les Lévitons préservent les propriétés que l'on a précédemment décrites, notamment pour ce qui concerne le bruit en présence d'un contact ponctuel quantique.

Pour cette raison, on considère le système représenté en Fig. R.7, où deux électrodes supraconducteurs sont rapprochés en formant une jonction tunnel, c'est-à-dire que les deux parties du système sont très faiblement couplées entre elles. Des impulsions de tension périodiques sont appliquées à l'électrode de gauche et amènent le système hors de l'équilibre.
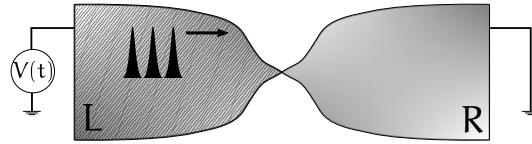
FIGURE R.7 : Un contact ponctuel supraconducteur. Le système est amené hors de l'équilibre par l'application d'un signal périodique $V(t)$ qui crée des excitations qui sont ensuite transmises avec une certaine probabilité de la partie gauche à vers la droite, où on mesure le courant et le bruit.

Le calcul du courant I et du bruit S conduit au résultat suivant :

$$I = I_0 + \zeta_{2q}(I_1 + I_J),$$
$$S = S_0 + \zeta_{2q}S_1,$$

où $\zeta_z = 1$ si $z \in \mathbb{Z}$ et $\zeta_z = 0$ autrefois. Les termes I_0 et S_0 sont associés au transfert de quasi-particules de Bogoloibov à travers de la jonction. Ils sont des fonctions continues de la charge q. Les autres contributions au courant et au bruit ne sont présentes que pour des valeurs démi-entier de q. En particulier I_J est un courant non dissipatif se réduisant au courant de Josephson quand $V(t) = 0$ et il est associé à un transfert cohérent de paires de Cooper. Comme on peut noter, il n'a pas un partenaire dans le bruit. Les termes I_1 et S_1 ont une interpretation plus compliquée aillant au-delà du but de ce résumé. Ici en fait on ne veut que souligner deux résultats.

Le premier est que l'on obtient une expression pour I_J qui généralise le courant de Josephson pour un signal $V(t)$ périodique arbitraire. Cette expression devient très simple dans le cas où le *gap* énergétique du supraconducteur est l'échelle énergétique la plus importante. On obtient dans ce cas une séquence de courants de Josephson aux valeurs entières et démi-entières de la charge q et la hauteur rélative des valeurs atteintes par I_J à des différents q n'est déterminée que par des coefficients dépendant du signal $V(t)$. Il est intéressant de mentionner qu'il est toujours possible de dériver une si simple expression pour les Lévitons, sans qu'aucune hypothèse sur la valeur du *gap* soit nécessaire.

Le deuxième est que le bruit en excès, $\Delta S = S - 2eI$, devient zéro pour les Lévitons, indépendemment des valeurs du *gap* et de la fréquence du signal $V(t)$. Ayant observé cette propriété dans tous le systèmes considérés dans cette thèse, on peut conclure qu'elle n'est due qu'à la particulière forme du signal lorentzien et les interactions ne jouent aucun rôle afin que le bruit en excès devienne zéro.

PERSPECTIVES

Dans cette thèse, on a étudié l'effet des interactions électroniques sur des excitations générées dans un conducteur quantique balistique par des impulsions de tension, avec une attention particulière au cas d'un signal lorentzien qui crée des excitations connues comme Lévitons. Les differents systèmes considérés sont les canaux de bord de l'effet Hall quantique à facteur de remplissage $\nu = 2$, les canaux contre-propageants de l'effet Hall quantique de spin et un jonction entre deux supraconducteurs. Le premier d'entre eux a déjà été employé pour des expériences d'optique quantique électronique et des effets liés aux interactions ont été observés. Les canaux contre-propageants représentent un possible système pour étendre le domaine de l'optique quantique électronique : des développements très recents ayant réalisé un contact ponctuel quantique dans un isolant topologique bidimensionnel sont très importants pour atteindre cet objectif. Enfin les résultats du dernier Chapitre représentent une première généralisation de l'optique quantique électronique à systèmes supraconducteurs et peuvent être utilisés comme point de départ pour considérer des supraconducteurs topologiques, où la présence des fermions de Majorana pourrait se traduire en des nouveux et intéressants effets physiques.

INTRODUCTION

The technological progress in semiconductor devices has lead to the observation of coherent quantum effects in mesoscopic systems and, interestingly, also to the more and more precise control of quantum properties, down to the single-electron level. This has opened exciting scenarios, one of which is certainly represented by electron quantum optics [1–3]. This is a fast growing research field which aims at preparing, controlling and coherently manipulating single- to few-electrons states in mesoscopic condensed matter systems, in the same way as single photons can be manipulated in conventional quantum optics. In order for such a program to succeed, the minimal necessary ingredients are: sources able to reliably generate single-electron excitations, waveguides where electrons can propagate retaining their phase coherence and beamsplitters allowing the implementation of interferometric setups. Quite amazingly, all these components are currently available from an experimental point of view.

Single-electron sources are actually the experimental breakthrough that gave rise to electron quantum optics. In particular, two main approaches have been developed. The first one has been implemented by Fève *et al.* [4] in 2007 and relies on a driven quantum dot that alternatively emits single electrons and holes. A pictorial representation of this source is provided in the left panel of Fig. I.1. Integrating such sources in systems hosting one-dimensional conducting channels playing the role of waveguides, has made it possible to implement interferometric setups for single electrons, as sketched in the right panel of Fig. I.1.

More recently, in 2013, Dubois *et al.* [5] have experimentally confirmed a previous theoretical prediction by Levitov and coworkers [6–8] that single-electron excitations can be generated by properly engineering the shape of an external drive applied to a one-dimensional quantum conductor. In particular, they showed that Lorentzian pulses carrying a charge which is an integer multiple of the electronic one, generate minimal purely electronic excitations, free of spurious electron-hole pairs. After the experimental confirmation of Levitov's prediction, these "clean" excitations have been called Levitons.

Concerning waveguides, their condensed matter analogue is represented by the so-called edge states. They are metallic one-dimensional states which, as their name suggests, emerge at the edge of peculiar two-dimensional systems. First discovered in the context of the integer quantum Hall effect [9–13], it is nowadays understood that edge states are a signature of topological systems [14], which currently are of great interest in the condensed matter community [15, 16] and whose
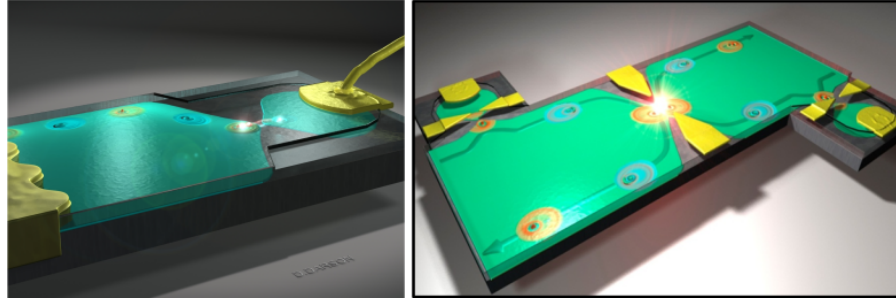
Figure I.1: Left: artistic view of a single-electron source, injecting electrons in a quantum conductor. Right: two single-electron sources are used together in order to perform an interference experiment, where electrons are emitted into chiral edge channels and collide at a quantum point contact. This picture summarizes the main ingredients of electron quantum optics: single-electron sources create excitations, edge channels are waveguides for their propagation and quantum point contacts play the role of beamsplitters. Credits: B. Plaçais's Mesoscopic Physics group at LPA-ENS (http://www.phys.ens.fr/~placais).

importance is nicely witnessed by the 2016 Nobel prize for Physics. The word topological is borrowed from mathematics and is used to indicate that systems in this peculiar phase of matter can be described by properties that are insensitive to local details. As a result, topological systems are extremely robust with respect to local perturbations. For instance, in quantum Hall edge states, backscattering is forbidden, a fact which makes them ideal waveguides for electron quantum optics. They have indeed been exploited in several experiments, as reviewed in Ref. [3].

However, quantum Hall edge states do not represent the only instance of topologically protected channels: another notable example is provided by helical edge states emerging in two-dimensional topological insulators. Proposed in 2006 [17] and soon after experimentally confirmed [18], these systems have non-trivial topological bulk properties which reflect in the presence of edge states featuring the so-called spin-momentum locking. This means that the direction of propagation of electrons along the edge is inherently related to their spin projection. Moreover, they are topologically protected as long as time reversal symmetry is preserved. These features make helical edge states a very appealing platform for extending electron quantum optics beyond quantum Hall systems and the recent implementations of quantum point contacts in two-dimensional topological insulators [19, 20] are a promising step forward in this direction.

Among several interesting problems related to electron quantum optics, an important question is whether and how interaction effects can influence the evolution of single-electron excitations generated by coherent sources. This is the main subject of this thesis, where

we investigate the interplay between single-electron excitations and interactions in different systems which are of relevance to electron quantum optics, either for current experimental setups (quantum Hall channels) or for potential future applications (helical edge states, superconducting systems).

The study of interaction effects is particularly important in one-dimensional systems, which have a completely different behavior with respect to higher-dimensional ones. The latter are well described by Landau's theory of Fermi liquid [21], whose fundamental ingredient is the concept of quasiparticle, which can be regarded as an almost free electron with renormalized parameters. On the contrary, the low energy excitations in one-dimensional interacting systems are collective and have a bosonic character. This results in a different paradigm, the Luttinger liquid theory [22], within which exotic phenomena emerge, such as charge fractionalization [23, 24] and spin-charge separation [25]. In view of what will be discussed in this thesis, it is important to mention that interaction effects are relevant not only from a theoretical point of view, but have also experimental evidence, both in integer quantum Hall edge channels [23, 26] (where electron quantum optics experiments have already been performed) and in helical systems, as recently demonstrated [27, 28].

In this thesis, the analysis of single-electron excitations in the presence of interactions will be focused on excitations generated by voltage pulses, with particular attention to the Lorentzian drive generating Levitons. Indeed, the common topic to the Chapters representing the original part of this work is the investigation of how Levitons are affected by the presence of interactions in different cases. Specifically, we consider as interacting systems: integer quantum Hall edge channels, counterpropagating helical modes and superconductors. While the former are relevant to current experiments, the other two examples represent interesting possibilities to broaden the domain of electron quantum optics. In particular, our study of Levitons in the presence of superconductivity can be taken as a starting point to address the case of topological superconductors, where the emergence of Majorana zero modes can lead to new physical effects.

The thesis is composed of five Chapters, the last three of which contain the original part of this work and are based on the publications listed on page vii.

In CHAPTER 1 we introduce the main ideas behind electron quantum optics in non-interacting systems, discussing both theoretical aspects and some experimental results. In particular, we illustrate the fermionic analogues of waveguides, beamsplitters and photon sources. As far as the latter are concerned, we focus on single-electron excitations generated by voltage pulses and the properties of Levitons in non-interacting systems are presented in detail. This Chapter also contains a brief discussion of the quantum Hall effect, which is an

ideal playground for implementing electron quantum optics setups as it provides natural waveguides for electrons, namely topologically protected chiral edge states.

In CHAPTER 2 we review the theoretical description of interactions in one-dimensional fermionic systems, which are well explained by Luttinger liquid theory instead of Landau's Fermi liquid theory which applies in higher-dimensions. In view of the subsequent Chapters, the Luttinger model for co- and counterpropagating one-dimensional channels is introduced and charge fractionalization in both cases is discussed.

In CHAPTER 3 a pair of copropagating chiral quantum Hall channels at filling factor $\nu = 2$ is considered and interactions between them are taken into account. We investigate the generation of excitations by voltage pulses and we study in detail the properties of the different wave packets which emerge due to charge fractionalization. In particular, we address their particle-hole content and discuss the conditions under which minimal excitations are introduced in the system. Finally, we show that by measuring the charge current noise due to the additional presence of a quantum point contact, it is possible to extract information about interactions between the two edge channels. This Chapter is based on our original results published in Refs. [29, 30].

In CHAPTER 4 we consider a pair of interacting counterpropagating helical channels and we investigate the interplay between interactions and non-equilibrium effects due to an external voltage drive. Charge fractionalization also occurs in this context due to interactions and we analyze the spectral functions of the different excitations emerging in the system. Through this analysis, we show that, unlike what happens in non-interacting systems, the minimization of the noise resulting from the partitioning of Lorentzian-shaped excitations is not necessarily related to a minimal excitation. Nevertheless, a minimal noise is in any case achieved when the fractionalized excitations are Lorentzian-shaped and carry an integer charge, a fact that can be exploited to extract information about the interaction strength in the system. This Chapter is based on our publication [31].

In CHAPTER 5 we investigate the effect of superconducting correlations on Levitons. To this end we study the effect of an external periodic drive on a so-called superconducting point contact, namely a constriction between two superconductors, much shorter than the superconducting coherence length. We derive general results for arbitrary shapes of the drive and then apply them to the case of Levitons. In particular, we show that a train of Lorentzian pulses with quantized area minimizes the noise also in the presence of a superconducting background, further strengthening the result that this peculiar property of Levitons is uniquely due to the particular shape of the drive and is robust with respect to interactions. These findings have been published in Ref. [32].

ELECTRON QUANTUM OPTICS IN NON-INTERACTING SYSTEMS

In this Chapter we provide a general overview of Electron Quantum Optics (EQO) [1–3], together with a theoretical description of its basic aspects. This relatively new field of research in condensed matter physics aims at preparing, manipulating and measuring quantum states at the single-electron level, thus having potential relevant implications for quantum information processing [33–35]. The introductory theoretical description presented in this Chapter is the simplest possible and is limited to non-interacting free fermions. Effects of electron-electron interactions will be extensively investigated in the following Chapters and constitute the main focus of this thesis.

The Chapter is organized as follows. In Sec. 1.1 we introduce EQO and the electronic version of a beamsplitter. In Sec. 1.2, we describe the Integer Quantum Hall Effect (IQHE), emphasizing that its origin is of topological nature and explaining why this fact is interesting and useful in EQO. Sec. 1.3 is dedicated to an overview of different single-electron sources. Sec. 1.4 then specializes to a voltage source emitting single-electron excitations called Levitons. Finally, the theoretical machinery for describing EQO in non-interacting systems is presented in Sec. 1.5, while Sec. 1.6 describes how Levitons were experimentally observed.

1.1 INTRODUCTION

As suggested by the name, EQO is inspired to a great deal by "conventional" quantum optics with photons. Indeed, the main idea which has initially driven the birth and development of EQO was to reproduce in solid-state systems optics-like experiments where single photons can be coherently emitted and manipulated. Such a possibility is very interesting in itself and potentially relevant from the point of view of quantum information. Indeed, in the same way as the coherent manipulation of photons allows to study entanglement, non locality and quantum cryptography [36, 37], the possibility of coherently operating on single-electron states can be in principle exploited to build quantum logic gates [38]. A comprehensive review of the current progress in coherent single-electron control, together with relevant applications, can be found in the recent paper [39].

The essential tools to build a quantum optic setup are coherent sources to generate single-photon states, waveguides to control their propagation and beamsplitters that can be used to partition incoming

waves and recombine them to perform interferometric experiments. Quite amazingly, all these ingredients have a condensed matter counterpart and this makes it possible to implement quantum optics-like experiments with electrons. In particular:

- beamsplitters are replaced by Quantum Point Contact (QPC)s;

- waveguides can be implemented by relying on topological edge channels;

- coherent photon sources are replaced by on-demand single electron sources, which have been a major experimental breakthrough of the late 2000's.

All of these will be introduced in this Chapter. Before doing so, however, an important point to emphasize is that EQO also allows to go beyond the standard paradigm of "conventional" quantum optics. Indeed, together with strong and appealing analogies, some differences and peculiarities are also noteworthy. First of all, electrons are fermions while photons are bosons and this difference in the particles statistics can produce relevant effects. Moreover, whereas photons are emitted in vacuum, we always have to remember the presence of the underlying Fermi sea when we think of electrons propagating in solid-state devices. Last but not least, electrons do interact with each other and this can be a source of new and interesting effects and produce a richer phenomenology. We will come back to this point in the following Chapters.

The electronic analog of a beamsplitter is the so-called QPC, which has been developed in the 80's as a way to create one-dimensional electronic systems starting from two-dimensional ones [40–45]. In particular, a QPC can be implemented by depositing metallic gates on the surface of a Two-Dimensional Electron Gas (2DEG) which can be formed at the interface of a semiconductor heterostructure (GaAs/AlGaAs being the prototypical one). As the name suggests, in a 2DEG the motion of electrons is confined in a plane, due to the formation of a potential barrier at the interface between the materials composing the heterostructure. By acting on the gates and imposing a negative voltage polarization, a depletion in the underlying electron fluid occurs, in such a way that the system exhibits the behavior of a One-Dimensional (1D) quantum conductor. Indeed, depending on the polarization of the QPC, a certain number of quantum channels forms in the constriction, as it is shown in Fig. 1.1. Here, the 2DEG lies in the plane of the Figure and the QPC is represented by the two metallic side gates (grey regions). Due to the confinement in the vertical direction, 1D conduction channels form across the region of the QPC. It is important to emphasize that QPCs are very versatile tools, since by tuning the voltage polarization applied to the gates, the transmission of the constriction can be varied continuously, closing or opening conduction
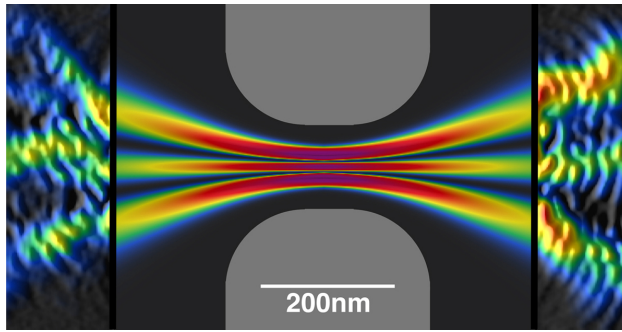
Figure 1.1: Quantum conduction channels formed in a 2DEG due to the presence of a QPC (grey metallic gates). The central region displays simulated data, while the side bands are obtained from actual measurements. This shows the close agreement between the measure and its description in terms of quantum channels. Credits: National Science Foundation; image taken from https: //www.nsf.gov/news/mmg/mmg_disp.jsp?med_id=51672&from=.

channels. Suppose for instance to set the QPC in such a way that a single conduction channel is present in the system. Then, by further acting on the gate polarization, the transmission of this channel can be modified at will. As a result, if an excitation is created in the channel and sent towards the constriction, the QPC will act as a beamsplitter as that excitation will be transmitted or reflected with a certain probability. We will see an implementation of such a setup when describing an important experimental result [5] about EQO in Sec. 1.6. Of course, in this case, the reflected excitation goes back to the direction from where it came. However, there are systems where electron can propagate along veritable "waveguides" whose shape can be controlled. Such waveguides are naturally provided by topologically protected edge channels in the IQHE, which we introduce in the following Section. Thus by integrating a QPC in these systems, it is possible to implement an electronic beamsplitter in which the reflected excitations do not come back to the emission point [2].

1.2 TOPOLOGICAL EDGE CHANNELS IN THE INTEGER QUANTUM HALL EFFECT

We now want to discuss how it is possible to engineer in solid-state devices actual waveguides for electrons. The first obvious requirement for this purpose is that electrons must not lose their phase coherence during their motion, otherwise any coherent quantum effect would be washed out. In this respect 2DEGs in GaAs/AlGaAs heterostructures are the natural playground, since they have very high mobilities [46, 47] (up to 35×10^6 cm^{2}V^{-1}s^{-1} at a temperature $\theta \approx 300$ mK [48]) and very long mean free path and phase coherence length (up to

10-20 μm at $\theta \approx 20$mK [49]). By means of electrostatic gates placed on top of the heterostructure it is possible to design in these systems "rails" allowing to shape electron trajectories. However, a much more convenient platform can be exploited and will be discussed in detail in this Section. Here we anticipate the result: when a 2DEG is exposed to a high magnetic field at low temperature, it enters the IQHE regime and conducting edge channels arise at the boundary of the 2DEG. These channels have the notable property of being topologically protected in such a way that backscattering is forbidden and the propagation along them is therefore chiral. The word *topological* is borrowed from mathematics, where it denotes "global" properties which are insensitive to local details. It is used in this context to emphasize that the edge states protection is very robust and independent of the sample's details (disorder, impurities and so on).

The discovery of the IQHE has been a real revolution in condensed matter physics: it was indeed the first example of a topological state and changed our understanding of the phases of matter, paving the way to the search for topological materials. We are now going to review the main aspects of the IQHE, whose edge states play a major role in EQO. The discussion is aimed at emphasizing the topological properties behind the quantization of the Hall conductance.

In 1980 von Klitzing, Dorda and Pepper [9] discovered a totally unexpected behavior when a 2DEG at low temperature is placed under a very high perpendicular magnetic field. They measured the Hall resistance R_H as a function of the applied magnetic field intensity B and observed a very strange phenomenon. While at low B the Hall resistance increases linearly with the magnetic field, as expected from the classical Hall effect prediction, by increasing B to higher intensities it becomes quantized, displaying plateaus at the values

$$R_H = \rho_{xy} = \frac{h}{e^2}\frac{1}{m}, \quad m \in \mathbb{N}, \tag{1.1}$$

where h is the Planck's constant and $-e$ the electron charge. This behavior is shown in Fig. 1.2 (top right). The transition between different plateaus is quite sharp and the quantization of the Hall resistance according to (1.1) is astonishingly precise: up to a part in a billion, independently of the particular sample. For this reason, the IQHE has also had applications in metrology [50, 51]. In correspondance of each plateau, the longitudinal resistance ρ_{xx} vanishes, while it is finite at the transition between consecutive plateaus. The conductivity tensor $\sigma = \rho^{-1}$ features a quantized Hall conductance

The Hall conductance is quantized and depends only on universal constants.

$$\sigma_H = \sigma_{xy} = m\frac{e^2}{h} \tag{1.2}$$

and a vanishing longitudinal conductance $\sigma_{xx} = 0$. The integer m is called filling factor and counts the number of the filled Landau levels.
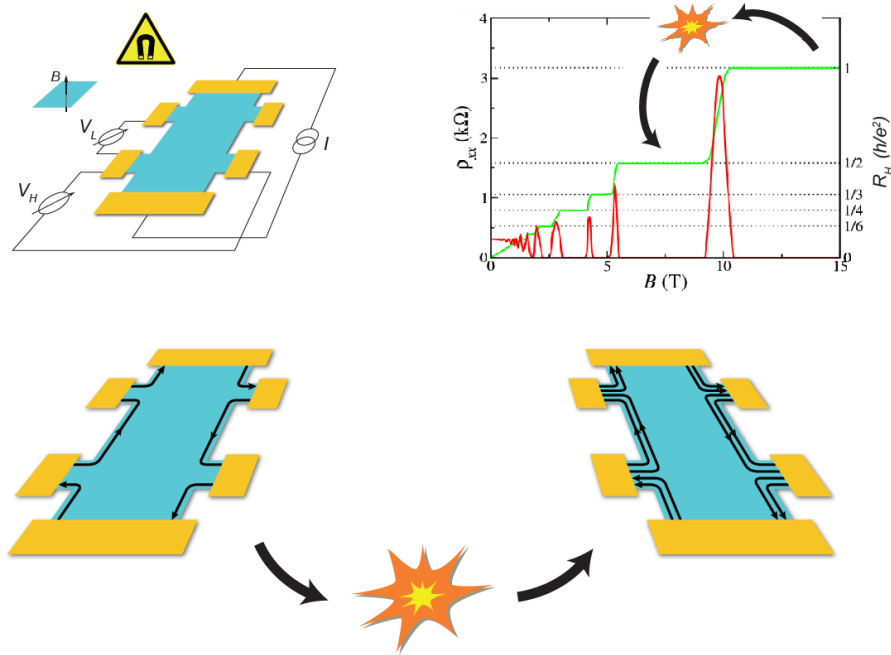
Figure 1.2: The IQHE. Top left: sketch of a quantum Hall bar: a 2DEG (light-blue region) is exposed to a strong perpendicular magnetic field. By driving a current I through the sample, the Hall and longitudinal resistances are measured. Top right: behavior of the Hall resistance R_H and the longitudinal resistance ρ_{xx} as a function of the magnetic field intensity B. R_H displays quantized plateaus in correspondence of which ρ_{xx} vanishes. Bottom: the 2DEG is insulating in the bulk, but metallic gapless edge states emerge at the boundaries of the system. This point will be addressed in Sec. 1.2.2. The transition between two consecutive plateaus is a quantum phase transition and comes together with the removal or addition of an edge state. Image adapted from [52].

The fact that σ_H only depends on universal constants and its quantization is extremely precise cannot be a coincidence and must be related to some deep property of the system. This is where topology comes into play. We now briefly review how the Hall conductivity is directly related to a topological invariant known as the Chern number. This important result was established in a seminal paper by Thouless, Kohmoto, Nightingale and den Nijs [53]; due to this work, the Chern number in the context of IQHE is also referred to as the TKNN invariant.

1.2.1 *Hall conductivity and topology*

Before making contact with the TKNN paper, we need to introduce the notion of Berry phase, discussed by Berry in 1984 [54] and anticipated in an earlier work by the Indian physicist Pancharatnam [55]. Suppose that the Hamiltonian H describing the system we are interested in depends on a set of parameters $\vec{\zeta} = (\zeta_1, \ldots, \zeta_N)$. These are simply labels and not dynamical variables. Then, for every set of parameters, we can find a set of eigenstates $|\phi_n(\vec{\zeta})\rangle$ satisfying

$$H(\vec{\zeta})\,|\phi_n(\vec{\zeta})\rangle = E_n(\vec{\zeta})\,|\phi_n(\vec{\zeta})\rangle\,. \tag{1.3}$$

Suppose now that the quantum state $|\psi(0)\rangle$ of the system at $t = 0$ is the n-th eigenstate: $|\psi(0)\rangle = |\phi_n[\vec{\zeta}(0)]\rangle$ and assume that it is non-degenerate. What happens now if we perform an adiabatic evolution $\vec{\zeta}(t)$ in the parameter space? The adiabatic theorem [56] ensures[1] that the evolved state $|\psi(t)\rangle$ follows the time evolution of the eigenstate $|\phi_n\rangle$, at most picking a phase factor:

$$|\psi(t)\rangle = e^{i\theta^{(n)}(t)}\,|\phi_n[\vec{\zeta}(t)]\rangle\,. \tag{1.4}$$

The phase can be calculated by plugging this expression for $|\psi(t)\rangle$ into the Schrödinger equation:

$$\begin{aligned} i\hbar\frac{d}{dt}\left[e^{i\theta^{(n)}(t)}\,|\phi_n[\vec{\zeta}(t)]\rangle\right] &= H[\vec{\zeta}(t)]\,|\phi_n[\vec{\zeta}(t)]\rangle \\ &= E_n[\vec{\zeta}(t)]e^{i\theta^{(n)}(t)}\,|\phi_n[\vec{\zeta}(t)]\rangle\,. \end{aligned} \tag{1.5}$$

By now taking the inner product with $\langle\phi_n[\vec{\zeta}(t)]|$ and performing a time integration we find

$$\theta^{(n)}(t) = -\frac{1}{\hbar}\int_0^t E_n[\vec{\zeta}(\tau)]d\tau + i\int_0^t \left\langle \phi_n[\vec{\zeta}(\tau)]\,\middle|\,\frac{d}{d\tau}\phi_n[\vec{\zeta}(\tau)]\right\rangle d\tau\,. \tag{1.6}$$

The first term is the well known dynamical phase; the second is a geometric one, known as the Berry phase, and can be written as a

---

[1] The statement is true if there is a gap between the eigenstate under investigation and the rest of the spectrum. In other words, one has to be sure that during the adiabatic evolution level crossing is avoided.

line integral along the path $\mathcal{P}$ described by the evolution $\vec{\zeta}(t)$ in the parameter space:

$$\gamma^{(n)} = \int_{\mathcal{P}} \vec{A}^{(n)}(\vec{\zeta}) \cdot d\vec{\zeta}, \quad \vec{A}^{(n)}(\vec{\zeta}) = i \left\langle \phi_n(\vec{\zeta}) \middle| \nabla_{\vec{\zeta}} \middle| \phi_n(\vec{\zeta}) \right\rangle . \quad (1.7)$$

Being a line integral, $\gamma^{(n)}$ does not depend on how the path in the parameter space is covered (provided of course that the evolution is such that the adiabatic theorem holds), but just on the path itself. The quantity $\vec{A}^{(n)}(\vec{\zeta})$ is called the Berry connection and it is always real[2]. There is a close analogy between the Berry connection and the electromagnetic vector potential (hence the choice of notation for indicating it). Indeed, under a gauge transformation of the eigenstates

Berry phase and Berry connection.

$$|\phi_n(\vec{\zeta})\rangle \to e^{if(\vec{\zeta})} |\phi_n(\vec{\zeta})\rangle , \quad (1.8)$$

with f a smooth function of the parameters, the Berry connection transforms as

$$\vec{A}^{(n)}(\vec{\zeta}) \to \vec{A}^{(n)}(\vec{\zeta}) - \nabla_{\vec{\zeta}} f(\vec{\zeta}) . \quad (1.9)$$

Let us now consider a *closed* loop $\mathcal{P}$ in the parameter space. Then $|\phi_n[\vec{\zeta}(0)]\rangle = |\phi_n[\vec{\zeta}(t_0)]\rangle$, t_0 being the time at which the system returns to the initial parameter configuration[3]. Such a property has to be maintained by every gauge transformation:

$$e^{if[\vec{\zeta}(0)]} |\phi_n[\vec{\zeta}(0)]\rangle = e^{if[\vec{\zeta}(t_0)]} |\phi_n[\vec{\zeta}(t_0)]\rangle . \quad (1.10)$$

This is equivalent to say that

$$f[\vec{\zeta}(0)] - f[\vec{\zeta}(t_0)] = 2\pi p , \quad p \in \mathbb{Z} . \quad (1.11)$$

On the other hand, if we look at Eq. (1.7) we realize that the last equation is nothing but the variation of the Berry phase under the gauge transformation. We then conclude that, for a closed loop $\mathcal{P}$, the Berry phase is gauge-invariant modulo 2π. This means that the Berry phase cannot be gauged away and must have physical relevance. Further exploiting the electromagnetic analogy, it is possible to define a Berry curvature which is a gauge-invariant quantity

The Berry phase is gauge-invariant modulo 2π.

$$\Omega_{\alpha\beta}^{(n)} = \partial_\alpha A_\beta^{(n)} - \partial_\beta A_\alpha^{(n)} , \quad (1.12)$$

---

2 Indeed, from the condition $\left\langle \phi_n(\vec{\zeta}) \middle| \phi_n(\vec{\zeta}) \right\rangle = 1$ (eigenstate normalization) it follows

$$0 = \nabla_{\vec{\zeta}} \left\langle \phi_n(\vec{\zeta}) \middle| \phi_n(\vec{\zeta}) \right\rangle = \left\langle \nabla_{\vec{\zeta}}\phi_n(\vec{\zeta}) \middle| \phi_n(\vec{\zeta}) \right\rangle + \left\langle \phi_n(\vec{\zeta}) \middle| \nabla_{\vec{\zeta}}\phi_n(\vec{\zeta}) \right\rangle \propto \mathrm{Im}\vec{A}^{(n)}(\vec{\zeta}) .$$

3 This is because eigenstates are assumed to be single-valued functions in the parameter space, so that, if $\vec{\zeta}(0) = \vec{\zeta}(t_0)$, the associated eigenstates must also be equal. It is not always possible to choose $|\phi_n(\vec{\zeta})\rangle$ as globally single-valued over the whole parameter space. In this case, one has to resort to local overlapping patches where a single-valued parametrization can be found [14, 57].

where ∂_α is a shorthand notation for $\partial/\partial_{\zeta_\alpha}$. Now, if we assume that the Berry connection is smooth over the parameter space, we can write

$$\gamma^{(n)} = \oint_{\mathcal{P}=\partial S} \vec{A}^{(n)}(\vec{\zeta}) \cdot d\vec{\zeta} = \iint_S \Omega^{(n)}_{\alpha\beta} d\zeta^\alpha \wedge d\zeta^\beta \,, \tag{1.13}$$

where S is a simply connected surface whose boundary is $\mathcal{P} = \partial S$ (for a three-dimensional parameter space, the above equation is just the usual Stokes theorem and the Berry curvature is simply the curl of the Berry connection).

What happens when S is a surface with *no boundaries*? One would be tempted to conclude that the integral in the r.h.s. of (1.13) vanishes because $\partial S = \emptyset$. However, this is wrong and a theorem in differential geometry ensures that

$$\iint_S \Omega^{(n)}_{\alpha\beta} d\zeta^\alpha \wedge d\zeta^\beta = 2\pi C_n \,, \tag{1.14}$$

The integral of the Berry curvature over a closed surface is quantized and gives the Chern number.

where C_n is a topological invariant known as the first Chern number and is an integer (for a proof see for instance [14, 57]). The reason why the integral (1.14) can be non-zero is that the application of the Stokes theorem in (1.13) requires that the Berry connection be a smooth function everywhere on S and this is not the case when the topology of the system is non-trivial [14, 57–59]. This is why a nonvanishing Chern number can be seen as a "topological obstruction" preventing the application of the Stokes theorem. The reason for introducing the Berry curvature is that it allows to make contact with the TKNN invariant which is proportional to the Hall conductivity σ_H and is exactly the integral of the Berry curvature over a close surface, namely the Brillouin zone appearing in band theory.

In the work by TKNN [53], Bloch electrons in a rectangular 2D lattice in the presence of a perpendicular magnetic field were considered. This is also known as the Hofstadter problem. The presence of the lattice periodic potential is essential in order to exploit Bloch's theorem [60, 61], which guarantees that the eigenstates have the form

$$|\phi_n\rangle = e^{i\vec{k}\cdot\vec{r}} \left|u^{(n)}_{\vec{k}}\right\rangle \,, \tag{1.15}$$

where $\vec{r} = (x,y)$, $\vec{k} = (k_x, k_y)$ and $|u^{(n)}_{\vec{k}}\rangle$ are Bloch states, n denoting the band index. In order to have a well-defined quasi-momentum $\vec{k}$, it is necessary to choose $\varphi = abBe/\hbar = p/q$, with $p, q \in \mathbb{Z}$. Here, a and b are the sizes of the unit cell in the two directions, B is the magnetic field and φ is the dimensionless magnetic flux per unit cell. This choice of φ, which is required in order for the translation operators to commute with each other and the Hamiltonian, comes together with a modified Brillouin zone, defined by $k_x \in (-\pi/qa, \pi/qa]$ and $k_y \in (-\pi/b, \pi/b]$, and is called magnetic Brillouin zone [53, 59, 62, 63]. The spectrum of this problem is highly non trivial as a function of

φ and is known as the Hofstadter's butterfly [64, 65], which displays fractal properties when φ is irrational. By using the Kubo formula [66] in linear response theory, TKNN showed that the Hall conductance can be expressed as

$$\sigma_H = \frac{e^2}{\hbar} \sum_n \iint_{\mathbb{T}^2} d^2k \left[i \left\langle \frac{\partial u_{\vec{k}}^{(n)}}{\partial k_x} \middle| \frac{\partial u_{\vec{k}}^{(n)}}{\partial k_y} \right\rangle - i \left\langle \frac{\partial u_{\vec{k}}^{(n)}}{\partial k_y} \middle| \frac{\partial u_{\vec{k}}^{(n)}}{\partial k_x} \right\rangle \right].$$

$$(1.16)$$

Here, the integral is computed over the magnetic Brillouin zone, which is a 2D torus $\mathbb{T}^2$, and the sum runs over all the occupied bands. Importantly, in this problem there is a band gap, i.e. the system is a band insulator. The term in square brackets is nothing but the Berry curvature: to see this it is sufficient to use the definitions (1.12) and (1.7) and notice that in our case the parameter space is two-dimensional, $\vec{\zeta}$ being replaced by $\vec{k}$ and the generic eigenstates $|\phi_n(\vec{\zeta})\rangle$ by Bloch states. Now, from (1.14), we know that the integrals in (1.16) are quantized and then the Hall conductivity is given by the sum of the Chern numbers of occupied bands:

$$\sigma_H = \frac{e^2}{h} \sum_n C_n \equiv C \frac{e^2}{h}.$$

$$(1.17)$$

The computation of the Chern number C_n of a given band is very complicated and the reader is referred to the literature for details about this point [14, 62]. Here we simply notice that, by comparing (1.2) and (1.17), we have the identification between the total Chern number and the filling factor: $m = C$ [15].

We thus have come to the conclusion that there is a deep connection between a physical observable, the Hall conductivity, and a topological invariant, the Chern number. This explains the extremely precise quantization of σ_H and also its independence of the sample's details: these are indeed local features; on the contrary, topological properties are global and unaffected by local deformations. In particular, the Chern number can change only in integer steps and, in order for that to happen, a "global" action on the system is needed. Such a transition involves a gap closure: indeed, topologically equivalent Bloch Hamiltonians $H(\vec{k})$ are those which can be adiabatically deformed into one another without closing the gap in the spectrum. Therefore, a transition between topologically distinct phases has to go through a gap closure. This is exactly what happens between two consecutive plateaus in the IQHE.

As a further remark, we mention that there is a close analogy between the Berry curvature defined in (1.12) and the Gaussian curvature of a 2D surface. In the same way as the Chern number is a topological invariant, the Gauss-Bonnet theorem [58] states that the integral of the Gaussian curvature over a closed compact 2D surface gives the Euler

characteristics, which is an integer number: $\chi = 2(1-g)$ (g is called the genus of the surface and classifies topologically distinct classes of surfaces, basically counting the holes). Differently from the Euler characteristic, the Chern number is not a property of the surface over which the Berry curvature is integrated (the Brillouin zone), but is rather associated with the manifold of the eigenstates $|u_{\vec{k}}^{(n)}\rangle$ defined over it.

Before continuing the description of the IQHE state, it is important to mention that this is not the only system featuring a quantized Hall conductance. Actually it is not even necessary to have a magnetic field for this to happen. All that matters is the breaking of time-reversal symmetry. Systems with a band gap still exhibiting a finite Hall response (and thus having a non vanishing Chern number) are known as Chern insulators and their behavior is called Quantum Anomalous Hall Effect [67, 68].

1.2.2   Edge states

It is now time to address an important question: what happens at the edges of the sample? This question is relevant both from the experimental and the theoretical point of view. In the first case, because in an actual setup there is a finite sample, to which metallic contacts are connected in order to perform the measurement. On the theoretical side, this question is deeply connected with another important point yet unexplored, which is the following. In the Hofstadter problem considered by TKNN (and also in other models having a non zero Hall response) the system is gapped and, as such, insulating. The same is true in its continuum limit (i.e. no lattice potential), where there is a gap between consecutive Landau Levels. How is then possible to have a finite conductance? The answer lies precisely in the presence of the edges, where metallic states appear as a consequence of the non-trivial topology of the system. A simple but very general argument, based on the discussion in the previous Section, can help us understand why such states have to be there. Consider bringing two systems in topologically distinct phases close to each other. By going across the interface between them, the topological invariant (the Chern number, say) changes its value. But we know that in order for this to happen, the system must undergo a gap closure, otherwise the topological invariant cannot change. Therefore, we come to the general conclusion that, at the interface between two topologically distinct phases, gapless edge states have to be present. This is precisely what happens in the IQHE: the system is in contact with the vacuum (or a trivial insulator), which has Chern number $C = 0$. Then, depending on what the Chern number of the IQHE state is, a corresponding number of edge channels emerge at the boundary of the system, as shown in Fig. 1.2.

Metallic edge states emerge at the interface between topologically distinct phases.

This rather abstract argument can be made more rigorous and there are different ways of quantitatively discussing the edge channels. In the following we just sketch one of them and refer the reader to the literature for further details [10–13, 63]. We work in the continuum limit, neglecting the lattice potential. So we consider free electrons in the xy plane (L_x and L_y being the sizes of the sample in the two directions), under a perpendicular magnetic field $\vec{B} = B\hat{z}$. The Hamiltonian is $H = (\vec{p} + e\vec{A})^2/(2m_e)$, with $\vec{p} = -i\hbar(\partial_x, \partial_y, 0)$, $\vec{A}$ the magnetic vector potential and m_e the electron mass. The spectrum of the system is given by the Landau levels [69]

$$E_m = \hbar\omega_c \left(m + \frac{1}{2} \right), \tag{1.18}$$

where $0 \leqslant m \in \mathbb{N}$ and $\omega_c = eB/m_e$ is the cyclotron frequency. These levels are highly degenerate and can accomodate $N_{deg} = \varphi/\varphi_0$ electrons, with $\varphi = BL_xL_y$ the magnetic flux through the sample and $\varphi_0 = h/e$ the flux quantum. In order to prove this, we have to compute the wavefunctions of the problem. Unlike the energy spectrum (1.18), they do depend on the particular gauge choice for the vector potential $\vec{A}$, which has therefore to be specified. In the Landau gauge $\vec{A} = -By\hat{y}$, the wavefunctions must have the form

$$\phi_{m,k}(x,y) = e^{ikx}Y_{m,k}(y) \tag{1.19}$$

because the Hamiltonian does not depend on x. By assuming periodic boundary conditions in the x direction, the momentum k is quantized in the usual way

$$k = \frac{2\pi r}{L_x}, \quad r \in \mathbb{Z}. \tag{1.20}$$

By using the expression (1.19), the Hamiltonian becomes

$$H = \frac{p_y^2}{2m_e} + \frac{1}{2}\omega_c \left(y - k\ell_B^2 \right), \tag{1.21}$$

where $\ell_B = \sqrt{\hbar/eB}$ is called the magnetic length. The above result describes a harmonic oscillator, whose potential is centered at the position $y = k\ell_B^2$. Therefore, the wavefunctions $Y_{m,k}(y)$ in (1.19) are given by [69]

$$Y_{m,k}(x,y) = \mathcal{N} \exp\left[-\frac{(y - k\ell_B^2)^2}{2\ell_B^2} \right] \mathcal{H}_m(y - k\ell_B^2), \tag{1.22}$$

where $\mathcal{N}$ is a normalization factor and $\mathcal{H}_m$ are the Hermite polynomials [70]. The important thing to notice about this expression is that the spatial localization of the states depends on k: each wavefunction is localized at $y_0 = k\ell_B^2$. Thus, by imposing that $|y_0| < L_y/2$ (meaning that the center each harmonic oscillator has to be inside the sample)
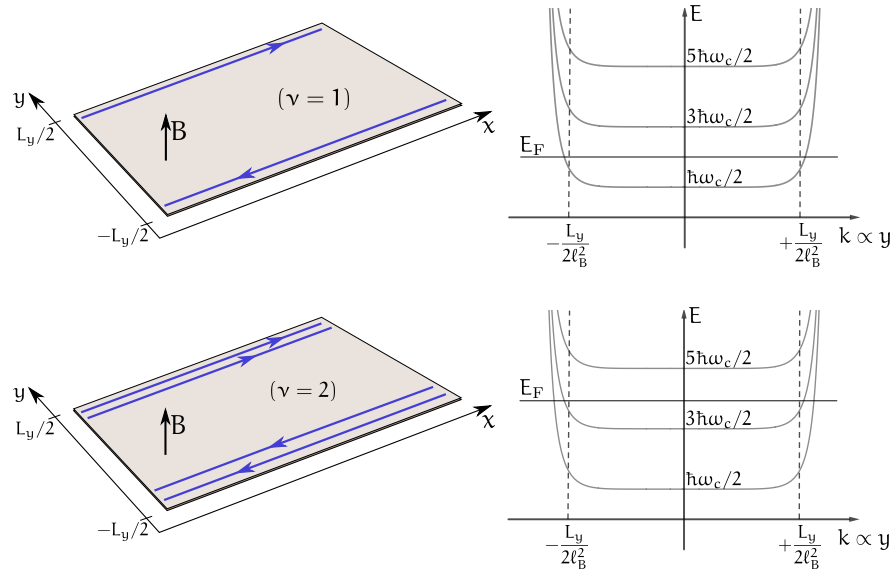
Figure 1.3: Bending of the Landau levels (1.18) at the edge of the sample due to the confining potential $U_c(y)$. When m Landau levels are filled (i.e. the filling factor is $\nu = m$), the Fermi energy intersects the spectrum in m couples of points and m chiral channels emerge at each edge of the Hall bar (the cases $m = 1$ and $m = 2$ are shown here).

and using (1.20), one finds $|r| < L_x L_y/(4\pi\ell_B^2)$. Thus, the number of states in each Landau level is given by $N_{deg} = \varphi/\varphi_0$, as stated before. An important quantity in the quantum Hall effect is the filling factor[4] ν, defined as the fraction of filled Landau levels. If we denote by N the total number of electron in the system, the filling factor is clearly given by

$$\nu = \frac{N}{N_{deg}} = \frac{hn_e}{eB}, \tag{1.23}$$

n_e being the electron density in the system.

The last ingredient we need in order to explain edge states is a confining potential in the y direction to describe the finiteness of the sample. Thus we add to the Hamiltonian a term $U_c(y)$, with the properties of being zero inside the sample and increasing at its edges (i.e. at $y = \pm L_y/2$) to keep the electrons confined. If we further assume that $U_c(y)$ is slowly varying on the scale of the magnetic length, the energy of each eigenstate (1.22) will be raised by the quantity $U_c(y_0)$. As a consequence, Landau levels corresponding to states close to the edges are bent, so that the spectrum as a function of k assumes the structure sketched in Fig. 1.3.

---

4 Here we use the letter ν for the filling factor, differently from the letter m used in (1.1). The reason for this is that the filling factor ν in (1.23) can also assume fractional values, while m is an integer number.

From this picture we can finally understand the conductance quantization from an "edge perspective": when the Fermi energy lies in the gap between the first and second Landau levels, it intersect the bent spectrum in two points, roughly at $k = \pm L_y/(2\ell_B^2)$. As a consequence, we have two states with a non vanishing and opposite group velocities: a right-moving state, with positive group velocity and a left-moving one, with negative group velocity. Moreover, given the proportionality between k and y, we know that those states are located at the edges of the sample (near $y = \pm L_y/2$) and, therefore, *spatially separated*. The situation at filling factor $\nu = 1$ we have just described is represented in Fig. 1.3 (top left), where it can be seen that a conduction channel appears at the edges of the Hall bar, while the bulk is insulating. The right-moving channel is located on the upper edge of the sample, because the state with positive group velocity in the bent spectrum is at $k = +L_y/(2\ell_B^2)$. Conversely, for the same reason, the left-moving channel is located on the lower edge of the sample. The bottom part of Fig. 1.3 pictures the case of filling factor $\nu = 2$. Here, the Fermi level intersects the spectrum four times and consequently four edge states are formed, two right-moving and two left-moving. Therefore, two copropagating channels emerge at each edge of the sample.

The spatial separation of edge edge states with different chiralities has the important consequence that backscattering between them is exponentially suppressed with the transverse size of the sample L_y and in practice is forbidden; therefore, electrons move chirally along the edges in perfectly transmitting channels. From the Landauer picture of quantum transport [71, 72], we know that each of such channels bears a conductance quantum[5] $G_Q = e^2/h$. Moreover, from Fig. 1.3, it is obvious that when an integer number of Landau levels is filled, i. e. $\nu = m \in \mathbb{N}$, the Fermi energy intersects the spectrum m times and therefore m channels emerge at each edge. On the whole, the conductance of the system is then nothing but the Hall conductance (1.2). Remarkably, disorder effects unavoidably present in realistic samples, actually help (if they are not too strong) stabilizing the edge channels [11] and obtaining better defined plateaus.

In conclusion, we have seen that the IQHE naturally provides chiral edge channels which are real one-way waveguides for electrons and, as such, a perfect playground for EQO purposes. Moreover, they have been known almost since the discovery of the IQHE and the systems where they emerge are experimetally well mastered. For this reason, the majority of EQO experiments have indeed been performed in IQHE edge channels.

However, these are not the only possibility and other kinds of edge states have later been discovered in new topological materials. One notable example is the Fractional Quantum Hall Effect (FQHE), discov-

Edge states in the IQHE are chiral and backscattering is forbidden.

---

5 Here there is no factor 2 since electrons are spin-polarized as a consequence of the high magnetic field.

ered in 1982 [73]: this peculiar state exhibits a fractionally quantized Hall conductance $\sigma_H = \nu e^2/h$, with $\nu \in \mathbb{Q}$. Just as in the integer case, it is a topological phase, but a very peculiar one, as it requires strong electronic correlations. The simplest FQHE states are described by the so-called Laughlin sequence ($\nu = 1/(1 + 2p)$, with p integer) [74], where a single chiral channel emerges at the edge of the system, while the edge states for other filling factors are more complicated [75, 76] and, in some cases, still debated [77–79]. Extensions of EQO towards fractional filling factors in the Laughlin sequence have been considered in the literature [80–88], but will not be discussed in this thesis. A further interesting possibility is represented by helical edge states emerging at the boundaries of Two-Dimensional Topological Insulators (2DTI)s [17]. This subject will be addressed in Chapter 4.

1.3   SINGLE-ELECTRON SOURCES: OVERVIEW

As we have seen, the condensed matter counterparts of beamsplitters (QPCs) and waveguides have been known since a long time (at least as far as edge channels in the IQHE are concerned). It was not until recently, though, that coherent on-demand single-electron sources became available and well established. There are nowadays a few ways of generating and controlling single-electron wave packets in quantum conductors and they are nicely reviewed in Ref. [39]. In summary, the state of the art concerning single-electron sources is the following.

- Mesoscopic capacitor. This source is based on a driven Quantum Dot (QD), coupled to a 2DEG in the IQHE regime and is able to inject single electrons with well defined energy above the Fermi sea. It was the first single-electron source to be implemented.

- Leviton source. It is based on the application of a properly engineered voltage pulse to a 1D quantum conductor. It has the advantage that it can inject multiple electrons at the same time and its implementation does not require nanolithography techniques.

- Dynamical quantum dots. This source exploits a QD whose confining potential can be modulated in order to trap and release electrons in a cyclic way. It is typically implemented by relying on two parallel electrostatic gates deposited on top of a 2DEG, with a small opening between them that defines the QD region. This source generates electrons far above the Fermi sea (the typical energy of electrons ejected from the QD is 100 meV, while the Fermi energy is about 10 meV) [89–91].

- Surface acoustic waves. Like in the previous case, electrons are first trapped in a QD and then emitted by the application of a sur-

face acoustic wave, generated via the piezo-electric effect, which kicks electrons out of the QD [92, 93]. This source is difficult to implement, but was shown to be very accurate and allows for single shot detection of electrons.

Here, I will briefly introduce the mesoscopic capacitor [4] and present in more detail the Leviton source [5], the latter being the most relevant one for the purpose of the present thesis. We refer to the review [39] for further information about the last two entries of the previous list.

1.3.1 *Mesoscopic capacitor*
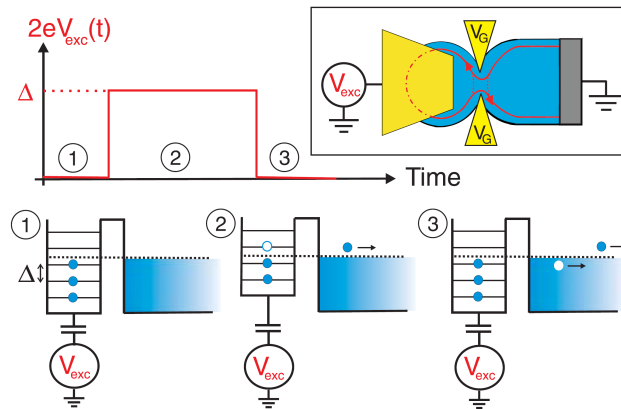
Figure 1.4: Setup and operating mechanism of the mesoscopic capacitor source. Image taken from [4].

In 2007, G. Fève *et al.* at Laboratoire Pierre Aigrain accomplished the implementation of the first on-demand single-electron source. This emitter is based on a non-adiabatically driven mesoscopic capacitor [4, 94]. The system is sketched in Fig. 1.4 and is realized in a GaAs/Al-GaAs 2DEG in the IQHE regime. By means of metallic gates a part of the 2DEG is confined and a QD is created, whose transmission is controlled by the gate polarization voltage V_G. A coupling between the QD and the edge states of the 2DEG is therefore present. In particular, the gate potential V_G is set in such a way that inner edge states[6] are fully reflected so that only one edge mode couples to the QD. Finally, an additional top gate (yellow region above the QD in Fig. 1.4) can be used to shift the chemical potential of the QD with respect to the Fermi level of the 2DEG.

Due to confinement, the spectrum of the QD is made of discrete energy levels, spaced by a characteristic scale Δ. Typical experimental values are $\Delta \approx 2$-4 K [4]. By acting on the top gate with a step voltage $eV_{exc}(t)$ of amplitude $\Delta/2$, these energy levels are shifted in

---

6 The experiment was performed at filling factor $\nu = 2$, thus two edge channels are present in the Hall bar.
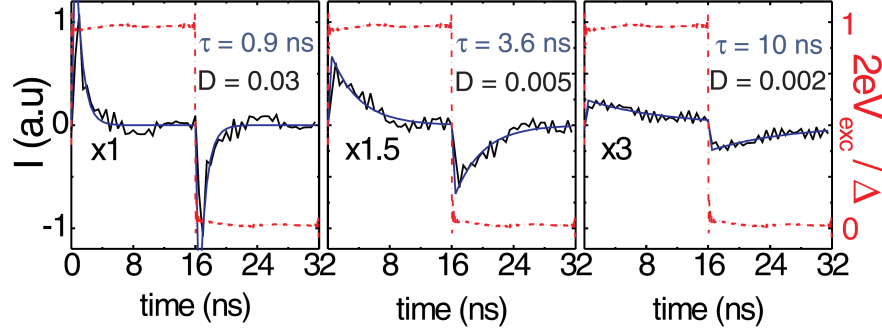
Figure 1.5: Real-time average current describing the emission of single electrons and holes from the mesoscopic capacitor into the edge channel of the 2DEG. Image taken from [4].

such a way that the uppermost occupied level of the QD is abruptly brought above the Fermi level (step 1); thus the electron tunnels into the edge state of the 2DEG (step 2), with a typical time scale τ, which is controlled by the transmission D between the dot and the edge mode. Finally, the QD levels are brought back to their original position and an electron tunnels from the edge mode into the dot, i.e. a hole is emitted in the 2DEG (step 3). By cyclically repeating this precedure, the periodic emission of single electrons and holes into the edge channel is achieved.

Real-time measurements in Fig. 1.5 show an exponentially decreasing average current [4]

$$\langle I(t) \rangle = \pm \frac{e}{\tau} \frac{e^{-t/\tau}}{1 + e^{-T/2\tau}} , \tag{1.24}$$

where T is the period of the cycle and the plus (minus) sign in front of the previous expression applies in the first (second) half of the cycle. Provided that $\tau \ll T$, the integral per half-period of the previous relation gives precisely an elementary charge, thus suggesting that a veritable emission of single electrons and holes is achieved. In order to be completely sure of this statement, one has to go beyond average current measurements, so as to rule out the possibility that the above mentioned quantization is just an average effect (for instance an electron is emitted in the first half period, no electrons in the third, two electrons in the fifth, thus compensating for the missing emission in the third). This can be done by considering current correlations [95, 96]. In particular, it has been shown that the accuracy of the mesoscopic capacitor as a single-electron source strongly depends on its operating regime [97]. The two extreme conditions are represented in Fig. 1.6. The left panel is the so-called optimal regime, where the energy of the uppermost occupied level of the QD is at $\Delta/2$ below the Fermi level of the 2DEG. In this regime the mesoscopic capacitor operates as a real single-electron emitter. This is not the case when the situation is
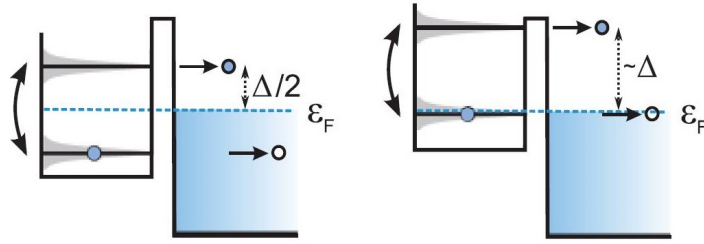
Figure 1.6: Two different operating conditions of the mesoscopic capacitor. Left: optimal regime. Right: resonant regime. Image taken from [95].

as represented in the right panel, i. e. the so-called resonant regime. Here, there is always a QD level at resonance with the Fermi energy and the device can be shown to produce unwanted electron-hole pair excitations, visible in the noise spectrum [95].

As a final remark, we emphasize that the mesoscopic capacitor is an emitter providing single electrons with a well defined energy, which is clearly related to the level spacing Δ in the QD. In particular, in the optimal emission regime, the energy of the injected electron is centered at $\epsilon_0 = \Delta/2$ and distributed as a Lorentzian. On the contrary, from Fig. 1.5 it is transparent that the emission is not localized in time. We will see in Sec. 1.3.2 that a complementary source exists, providing a localized emission in time and, consequently, an energy which is not well defined.

After the full understanding of the different properties and operating regimes of the mesoscopic capacitor had been achieved, several EQO experiments exploiting this single-electron source have been implemented [2, 3, 23, 26, 98, 99]. In particular, the electronic version of the Hanbury Brown-Twiss (HBT) experiment [100], where a stream of single electrons is excited along the edge and subsequently partitioned at a QPC was reported [2]. Further on, also the electronic Hong-Ou-Mandel (HOM) interferometer [101] was implemented [98]. In this case, the geometry is more complicated and requires two operating single electron sources with a tunable delay between them, as depicted in Fig. 1.7. This kind of setup can be used to probe the indistinguishability of incoming states and the output is very different for photons and electrons. In the first case there is a so-called *bunching effect*: when two identical photons arrive at the same time at the beamsplitter, they stick together and exit the interferometer on the same arm. Therefore the coincidence counts rate in the output arms vanishes. Conversely, identical electrons impinging on the beamsplitter at the same time are forced to exit on different arms, due to the Pauli principle. As a consequence the coincidence counts rate is doubled with respect to the one observed at a time delay larger than the wave packets temporal extension. This effect is referred to as *anti-bunching*. Its ex-

(a) Experimental image of an electronic HOM interferometer. Image taken from [26].

(b) Expected coincidence counts, in the two cases of photons and electrons. Taken from [39].
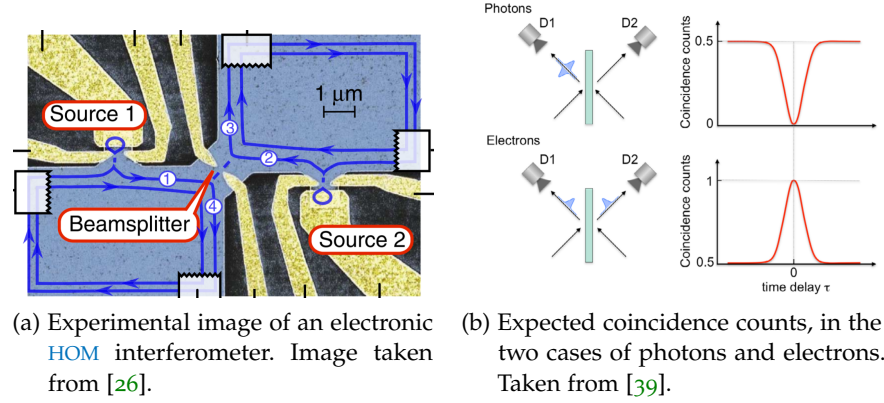
Figure 1.7: Electronic HOM interferometer.

perimental observation has been one of the major achievements in EQO. This was done through noise measurements: instead of looking at the coincidence rate, one looks at its fluctuations. In the case of electrons, fluctuations should be completely suppressed, as the two identical particles would always exit the interferometer on different arms and detected in coincidence. The partial noise suppression experimentally observed in Ref. [98] was later attributed to the effect of interactions along the quantum Hall edge states [102], thus indicating that electronic correlations can play an important role.

1.3.2 *Voltage pulse source*

A perhaps conceptually simpler way of generating excitations in a 1D quantum conductor exploits the application of a very short voltage pulse to the system. As the conductance of a ballistic quantum channel is (neglecting spin) the conductance quantum $G_Q = e^2/h$, it follows that charge carried by the excitation generated by $V(t)$ is simply

$$\mathcal{C} = \frac{e^2}{h} \int_{-\infty}^{+\infty} V(t)dt \,. \tag{1.25}$$

Equivalently, the number q of electrons associated with the excitation is

$$q = \frac{\mathcal{C}}{-e} = -\frac{e}{h} \int_{-\infty}^{+\infty} V(t)dt \,. \tag{1.26}$$

However, this does not mean that any voltage drive such that the previous integral gives $q = n \in \mathbb{N}$ actually injects n electrons. This is because, while on average it is certainly true that n electrons are injected, the integral (1.26) tells us nothing about the possible creation of neutral particle-hole pair excitations.

The goal is then to find a shape of $V(t)$ ensuring that no such neutral excitations are created. This seemingly very complicated task has a

quite simple solution, first found by L. Levitov and coworkers [6, 7] well before the birth of EQO. The answer is that the voltage pulse has to be a superposition of Lorentzian functions with quantized area and the same sign:

$$V(t) = \mp \frac{\hbar}{e} \sum_{p=1}^{n} \frac{2w_p}{w_p^2 + (t - t_p)^2} \, . \tag{1.27}$$

Here, w_p is a parameter describing the temporal extension of each Lorentzian pulse and t_p is the emission time. When the negative (positive) sign in (1.27) is chosen, this drive generates n electrons (holes), without any particle-hole pair excitations. After Levitov, such excitations have been dubbed Levitons [5].

We will prove this result in Sec. 1.4, which is dedicated to a quite detailed analysis of Levitons in a non-interacting system. At this stage, we just show in Fig. 1.8 the sketch of the experimental implementation [5] which confirmed the theoretical prediction, together with a schematic representation of the main properties of a single-Leviton wavefunction. The experiments employed a periodic train of quantized Lorentzian pulses, applied to a contact connected to a 2DEG. The 1D conductor is created by means of a QPC, with tunable transmission D, as depicted in Fig. 1.8a. The current fluctuations due to the presence of the QPC are measured in the right contact and allow to probe the "cleanness" of the produced excitations [7, 8]. From Fig. 1.8b we observe that the temporal profile of the current is a Lorentzian, while the energy distribution of the excitation is a decreasing exponential which leaves the Fermi sea untouched. Thus a Leviton is a single-electron excitation on top of the Fermi sea.

1.4 LEVITONS AS MINIMAL EXCITATIONS

In this Section we begin to set the theoretical tools for describing electron quantum optics setups. In particular, we prove that Lorentizan pulses with quantized area do indeed generate minimal excitations. From now on, we choose units in which $\hbar = 1$.

As stated at the beginning of the Chapter, here the analysis will be limited to non-interacting electrons. For this reason, we consider the simplest possible 1D conductor, i.e. a single quantum Hall chiral edge channel. By setting the chemical potential to zero, the Hamiltonian of this system is

$$H_0 = \int_{-\infty}^{+\infty} dx \, \Psi^\dagger(x)(-iv_F \partial_x)\Psi(x) \, , \tag{1.28}$$

where $\psi(x)$ is the fermionic annihilation field operator, destroying an electron at position x, and v_F is the Fermi velocity along the edge. Note that this Hamiltonian has a linear spectrum

$$\omega(k) = v_F k \, . \tag{1.29}$$
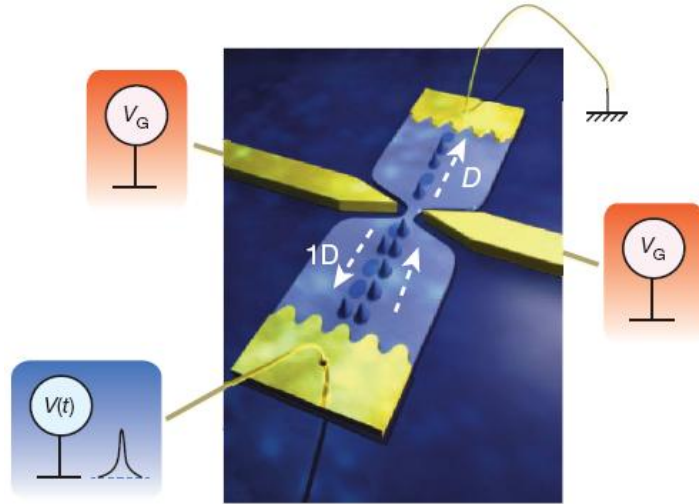
(a) Sketch of the experimental setup: a periodic train of Lorentzian pulses is applied to the left contact. A stream of single electrons is generated in a 1D channel, created in a 2DEG by means of a QPC with tunable transmission D.
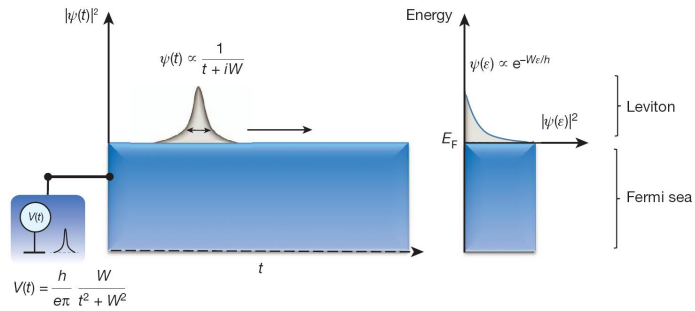
(b) Sketch of the temporal profile of a Leviton wavefunction and its energy distribution. As we can observe, the Fermi sea is untouched.

Figure 1.8: Sketch of the experimental setup for used for detecting Levitons and main properties of a single-Leviton wavefunction. Both images are taken from [5].

Even if the dispersion relation along the edge could deviate from this behavior, it is always possible to assume the linear relation (1.29) if we are interested in the low-energy physics of the system.

In order to find the voltage drive generating minimal excitations, we have first to understand how a generic $V(t)$ influences the time evolution $\Psi(x, t)$ of the electron field operator. We consider the situation depicted in Fig. 1.9, where a the time-dependent potential $V(t)$ is applied to the edge channel in the region $x \in (-\infty, 0)$. We describe this
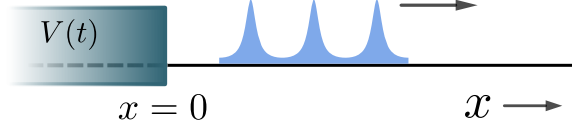
Figure 1.9: Voltage pulse source applied to a chiral edge channel. The potential $V(t)$ is applied uniformly in the region $(-\infty, 0)$ and generates excitations propagating to the right, due to the chirality of the edge mode.

with the function $U(x, t) = \Theta(-x)V(t)$, where $\Theta(x)$ is the Heaviside step function. The voltage couples to the charge density on the edge via the Hamiltonian

$$H_g = -e \int_{-\infty}^{+\infty} dx \, U(x, t)\Psi^\dagger(x)\Psi(x) \,. \tag{1.30}$$

Before finding the time evolution $\Psi(x, t)$, we want to better specify the setting of the problem with some general remarks. We assume that at $t = -\infty$ the system is in thermal equilibrium, with no applied drive, and thus is characterized by the time-independent equilibrium density matrix $\hat{\rho}_0$, stemming uniquely from the Hamiltonian H_0. Then, at $t = -\infty + \varepsilon$ (with ε an infinitesimal time), the drive $V(t)$ is switched on. In the remainder of this Section, we adopt the Heisenberg picture, so that the time evolution is entirely attributed to operators. As a result, the quantum average of any operator $O(x, t)$ will be performed as

$$\langle O(x, t) \rangle_0 = \mathrm{Tr}[\hat{\rho}_0 O(x, t)] \,, \tag{1.31}$$

where the time evolution $O(x, t)$ has to be determined with the full Hamiltonian $H = H_0 + H_g$.

Let us now return to the time evolution of the fermionic field. It is easy to derive the following Heisenberg equation of motion from the Hamiltonian $H = H_0 + H_g$:

$$i(\partial_t + v_F \partial_x)\Psi(x, t) = -eU(x, t)\Psi(x, t) \,. \tag{1.32}$$

Consider first the simple case of equilibrium, where $U(x, t) = 0$. In this situation, the solution to the above equation is simply

$$\Psi(x, t) = \psi(x - v_F t, 0) = \psi\left(0, t - \frac{x}{v_F}\right). \tag{1.33}$$

Thanks to the chirality in the time evolution of the equilibrium solution, we can use interchangeably ω and k as conjugate variables. In particular, the usual Fourier representation of the fermionic field as an integral over momenta can also be written as

$$\psi(x - v_F t, 0) = \frac{1}{\sqrt{2\pi v_F}} \int_{-\infty}^{+\infty} d\omega \, e^{-i\left(t - \frac{\omega x}{v_F}\right)} c(\omega), \tag{1.34}$$

where $c(\omega)$ is the operator annihilating an electron at energy ω. These operators satisfy the equilibrium average

$$\left\langle c^\dagger(\omega) c(\omega') \right\rangle_0 = \mathrm{Tr}[\hat{\rho}_0 c^\dagger(\omega) c(\omega')] = \delta(\omega - \omega') n_F(\omega), \tag{1.35}$$

where $n_F(\omega) = 1/(1 + e^{\omega/k_B \theta})$ is the Fermi function at temperature θ and k_B the Boltzmann constant.

We now come to the general solution of Eq. (1.32) in the presence of the driving term $U(x, t)$. It can be shown that the time evolution $\Psi(x, t)$ in this case is given by (see Appendix A.1 for details)

$$\Psi(x, t) = \psi(x - v_F t, 0) e^{ie \int_{-\infty}^{t} dt' \, U[x - v_F(t - t'), t']}. \tag{1.36}$$

By taking into account the spatial dependence of $U(x, t)$, the previous result can be further written, for $x > 0$, as

$$\Psi(x, t) = \psi(x - v_F t, 0) e^{i\alpha\left(t - \frac{x}{v_F}\right)}, \qquad \alpha(\tau) = e \int_{-\infty}^{\tau} dt' \, V(t'). \tag{1.37}$$

Notice that, even in the presence of the drive $V(t)$ the time evolution of the fermionic operator is chiral. This is indeed an inherent property of quantum Hall edge states. As a consequence, we can write

$$\Psi(x, t) = \frac{1}{\sqrt{2\pi v_F}} \int_{-\infty}^{+\infty} d\omega \, e^{-i\omega\left(t - \frac{x}{v_F}\right)} C(\omega), \tag{1.38}$$

where $C(\omega)$ is a fermionic operator. Its explicit expression can be obtained in this way. We define the Fourier transform

$$p(\omega) = \int_{-\infty}^{+\infty} d\tau \, e^{i\alpha(\tau)} e^{i\omega \tau} \tag{1.39}$$

and make use of the representation (1.34) in (1.37), arriving at

$$C(\omega) = \frac{1}{2\pi} \int_{-\infty}^{+\infty} d\omega' \, p(\omega') c(\omega - \omega'). \tag{1.40}$$

Thus, we see that $C(\omega)$ is built as a superposition of operators $c(\omega)$, shifted at all possible energies ω' and weigthed by the (complex)

coefficient $p(\omega')$ which depends on the voltage drive. Notice that when $V(t) = 0$ we have from (1.39) $p(\omega) = 2\pi\delta(\omega)$ and therefore $C(\omega) = c(\omega)$, as it should be.

This discussion shows that the effects of the drive can be included in the new operators $C(\omega)$, which define a modified occupation number distribution

$$f(\omega) = \left\langle C^\dagger(\omega)C(\omega) \right\rangle_0 = \text{Tr}[\hat{\rho}_0 C^\dagger(\omega)C(\omega)]. \tag{1.41}$$

By using (1.40) and the equilibrium average (1.35), we readily find

$$f(\omega) = \int_{-\infty}^{+\infty} \frac{d\omega'}{(2\pi)^2} \left|p(\omega')\right|^2 n_F(\omega - \omega'), \tag{1.42}$$

This result tells us that the new occupation number distribution is obtained as superposition of equilibrium Fermi functions, shifted at all possible energies ω' and weigthed by the probability density that the drive creates an excitation at energy ω'. This interpretation of the Fourier transform $|p(\omega)|^2/(2\pi)^2$ as a probability density is supported by the normalization condition

$$\int_{-\infty}^{+\infty} \frac{d\omega}{(2\pi)^2} |p(\omega)|^2 = 1, \tag{1.43}$$

which can be readily obtained from the definition (1.39).

We now have all we need to formalize the request that no holes are generated by the drive $V(t)$. Since a finite temperature can generate particle-hole pairs, let us consider the zero temperature limit, where any potential hole can be generated only by the drive (no holes are present at equilibrium). We can understand how to achieve our goal in two different ways. The first one is to notice that, if $p(\omega') = 0$ for $\omega' < 0$, then from (1.42) we observe that only upward shifts of the Fermi function n_F are allowed and, since at $\theta = 0$ we have $n_F(\omega - \omega') = \Theta(\omega' - \omega)$, it is impossible to modify the occupation number at negative energies $\omega < 0$. As a consequence, the Fermi sea remains untouched and no holes are generated. We can arrive at the same conclusion by calculating the number of holes N_h in the system, given by

$$N_h = \int_{-\infty}^{0} d\omega \left\langle C(\omega)C^\dagger(\omega) \right\rangle_0 . \tag{1.44}$$

A straightforward calculation yields

$$N_h = \frac{1}{(2\pi)^2} \int_{-\infty}^{0} d\omega \int_{-\infty}^{\omega} d\omega' \left|p(\omega')\right|^2 \tag{1.45}$$

and shows that $N_h = 0 \iff p(\omega) = 0$ for $\omega < 0$, as claimed before.

By looking back at the definition (1.39), is it clear that this is a constraint on the function $e^{i\alpha(t)}$. In particular, this function must be

analytic in the lower complex plane (when t is regarded as a complex variable) and must have at least one pole in the upper part of it to prevent $p(\omega)$ from vanishing everywhere. Finally, being a phase, $|e^{i\alpha(t)}| = 1$. Thus we choose

$$e^{i\alpha(t)} = \frac{t - t_0 + iw}{t - t_0 - iw}, \qquad t_0 \in \mathbb{R}, \, w > 0. \tag{1.46}$$

From this we arrive at the final result

$$V(t) = -\frac{i}{e}\frac{d}{dt}\ln e^{i\alpha(t)} = -\frac{1}{e}\frac{2w}{w^2 + (t - t_0)^2}, \tag{1.47}$$

which is precisely (1.27), for $n = 1$ (recall that here $\hbar = 1$). The generalization to more electrons is straightforward. We simply have to add more poles in the upper complex plane when constructing the function $e^{i\alpha(t)}$, together with corresponding zeros in the lower plane in order to have a unitary modulus:

$$e^{i\alpha(t)} = \prod_{p=1}^{n} \frac{t - t_p + iw_p}{t - t_p - iw_p}, \qquad t_p \in \mathbb{R}, \, w_p > 0. \tag{1.48}$$

This leads to the complete Eq. (1.27), with the minus sign. Finally, by following the same steps, it is now easy to show that a single-hole excitation is obtained by requiring that $e^{i\alpha(t)}$ has a pole in the lower complex plane, which amounts to reverse the sign of each w_p, thus obtaining the second option in (1.27).

1.5 FIRST-ORDER COHERENCE FUNCTION

In this Section we introduce some key quantities in EQO theory, i. e. coherence functions. After presenting the general definitions, we will specify to the case of a Lorentzian drive, further investigating the properties of Levitons. The idea of electronic coherence functions was proposed by Grenier *et al.* [1] and aims at transposing in the context of mesoscopic physics the formalism of optical coherences developed by Glauber [103–105]. In this Section we will consider the simplest case of first-order coherence functions. While it is possible, by direct analogy with Glauber's theory, to define also higher-order coherences [106–109], we will not consider them in this thesis. The electric field amplitude used in optics is replaced in EQO by the electronic annihilation and creation field operators.

1.5.1 *Definition and representations*

1.5.1.1 *Time representation*

First-order coherence functions are defined as follows [1, 110]:

$$\mathcal{G}^<(x_1, x_2; t_1, t_2) = \left\langle \Psi^\dagger(x_2, t_2)\Psi(x_1, t_1) \right\rangle_{\hat{\rho}} \tag{1.49}$$

is the first-order electron coherence, while

$$\mathcal{G}^>(x_1, x_2; t_1, t_2) = \left\langle \Psi(x_1, t_1)\Psi^\dagger(x_2, t_2) \right\rangle_{\hat{\rho}} \tag{1.50}$$

is the first-order hole coherence. Our notation is chosen to emphasize that these quantities are directly proportional to the lesser and greater Green functions. The above definitions are general and, in particular, the quantum averages are performed with respect to a generic density matrix $\hat{\rho}$, possibly describing a non-equilibrium state. From the above definitions, the following symmetry properties are easily shown:

$$\mathcal{G}^{\gtrless}(x_1, x_2; t_1, t_2) = \mathcal{G}^{\gtrless}(x_2, x_1; t_2, t_1)^*. \tag{1.51}$$

Moreover, electron and hole coherences are related by

$$\mathcal{G}^<(x_1, x_2; t, t) + \mathcal{G}^>(x_2, x_1; t, t) = \delta(x_1 - x_2), \tag{1.52}$$

as a direct consequence of the canonical anticommutation relations of fermion fields. For a single-channel chiral conductor as the one we are considering in this Chapter, field operators do not depend on space and time separately, but only via the chiral combination $x - v_F t$. We already encountered an explicit example of such behavior in (1.37). This is a great simplification. For instance, (1.54) can be also extended at different times and becomes

$$\mathcal{G}^<(x_1, x_2; t_1, t_2) + \mathcal{G}^>(x_2, x_1; t_2, t_1) = \delta((x_1 - v_F t_1) - (x_2 - v_F t_2)). \tag{1.53}$$

Actually, given the relation between position and time, we can directly eliminate the spatial dependence from (1.49) and (1.50) and care only about time variables. This is done by considering a particular position $x_1 = x_2 = x$ along the chiral channel and is a particularly appropriate choice when considering local measurements, which probe the system at a given space position.

In most cases in EQO we are interested in the effects of an external perturbation (e. g. a voltage pulse or an electron injected by the mesoscopic capacitor) on the equilibrium many-body system. This is why it is useful to define *excess* coherences

$$\Delta\mathcal{G}^{\gtrless}(t_1, t_2) = \mathcal{G}^{\gtrless}(t_1, t_2) - \mathcal{G}_0^{\gtrless}(t_1, t_2), \tag{1.54}$$

in order to discard the contribution of the Fermi sea, characterizing the equilibrium system:

$$\mathcal{G}_0^<(t_1, t_2) = \left\langle \Psi^\dagger(t_2)\Psi(t_1) \right\rangle_0, \tag{1.55a}$$

$$\mathcal{G}_0^>(t_1, t_2) = \left\langle \Psi(t_1)\Psi^\dagger(t_2) \right\rangle_0. \tag{1.55b}$$

Here, equilibrium averages are performed with respect to the density matrix $\hat{\rho}_0$, characterizing the equilibrium state. A first quantity which

is directly accessible from coherence functions in the time representation is the excess charge density[7] at time t, that is

$$\Delta\rho(t) = -e\,\Delta\mathcal{G}^{<}(t,t)\,, \tag{1.56}$$

Moreover, given the chirality of the system, this quantity is directly proportional to the excess charge current $\Delta J(t) = v_F\,\Delta\rho(t)$.

1.5.1.2   *Energy representation*

A different way to look at electron coherences is the energy representation. It is defined by taking the following double Fourier transform

$$\tilde{\mathcal{G}}^{\gtrless}(\omega_1,\omega_2) = \int_{-\infty}^{+\infty} dt_1 \int_{-\infty}^{+\infty} dt_2\,\mathcal{G}^{\gtrless}(t_1,t_2)e^{i(\omega_1 t_1 - \omega_2 t_2)}\,. \tag{1.57}$$

By using the representation

$$\Psi(t) = \frac{1}{\sqrt{2\pi v_F}} \int_{-\infty}^{+\infty} d\omega\,e^{-i\omega t}C(\omega) \tag{1.58}$$

it is immediate to find

$$\tilde{\mathcal{G}}^{<}(\omega_1,\omega_2) = \frac{2\pi}{v_F}\left\langle C^{\dagger}(\omega_1)C(\omega_2)\right\rangle_{\hat{\rho}}\,, \tag{1.59}$$

which shows that the energy representation is more suitable for accessing the occupation number distribution (obtained for $\omega_1 = \omega_2$). The equilibrium coherence function in energy representation is purely diagonal and reduces to

$$\tilde{\mathcal{G}}_0^{<}(\omega_1,\omega_2) = \frac{2\pi}{v_F}n_F(\omega_1)\delta(\omega_1 - \omega_2)\,. \tag{1.60}$$

Once again, we can define the excess coherence function as

$$\Delta\tilde{\mathcal{G}}^{<}(\omega_1,\omega_2) = \tilde{\mathcal{G}}^{<}(\omega_1,\omega_2) - \tilde{\mathcal{G}}_0^{<}(\omega_1,\omega_2)\,. \tag{1.61}$$

1.5.1.3   *Wigner representation*

Finally, there is a third and very useful way of describing of electron coherences. It is called the Wigner function representation and retains information about both the time dependence of excitations and their energy content. It was originally introduced by E. Wigner in 1932 [111] and allows a phase space representation of quantum mechanical particles in terms of a quasi-probability distribution function [112]. More details about this point are given in Appendix B.1. Here it is enough to say that (possible) negative values in the Wigner function are a hallmark of non-classical states. We will come back to this point when discussing a specific example.

---

7 The excess charge density $\Delta\rho$ has not to be confused with the density matrix $\hat{\rho}$!

In the framework of EQO electron and hole Wigner functions are defined as [113]

$$W^{\gtrless}(t, \omega) = \frac{1}{2\pi} \int_{-\infty}^{+\infty} d\tau \, \mathcal{G}^{\gtrless}\left(t + \frac{\tau}{2}, t - \frac{\tau}{2}\right) e^{i\omega\tau} \qquad (1.62)$$

and are real quantities owing to the property (1.51) [8]. In a chiral conductor they are not independent as they are related by

$$v_F \left[W^<(t, \omega) + W^>(t, -\omega) \right] = 1, \qquad (1.63)$$

which is a consequence of (1.53). From the definition (1.62) it is immediate to observe that the charge current can be obtained by integrating the electron Wigner function over the energy variable:

$$J(t) = -ev_F \int_{-\infty}^{+\infty} d\omega \, W^<(t, \omega). \qquad (1.64)$$

Conversely, by using (1.58) it is also possible to show that the integration with respect to time yields the occupation number distribution:

$$f(\omega) = v_F \int_{-\infty}^{+\infty} dt \, W^<(t, \omega). \qquad (1.65)$$

Therefore, $J(t)$ and $f(\omega)$ can be seen as marginal distributions obtained from the Wigner function. Finally, $W^<(t, \omega)$ is normalized to the average number of electrons in the system. Thus, if we define the excess Wigner function in the usual way,

$$\Delta W^{\gtrless}(t, \omega) = W^{\gtrless}(t, \omega) - W_0^{\gtrless}(t, \omega), \qquad (1.66)$$

the number of extra electrons present in the system due to the effect of a source is expressed as

$$\Delta N = v_F \int_{-\infty}^{+\infty} dt \int_{-\infty}^{+\infty} d\omega \, \Delta W^<(t, \omega). \qquad (1.67)$$

Despite this normalization, it is not possible to regard the Wigner function as a probability distribution because it can also assume negative values, as we will see in an explicit example.

---

8 Indeed, by using (1.51) we find

$$2\pi \, \mathrm{Im} W^{\gtrless}(t, \omega) = \int_{-\infty}^{+\infty} d\tau \left[\mathcal{G}^{\gtrless}\left(t + \frac{\tau}{2}, t - \frac{\tau}{2}\right) e^{i\omega\tau} - \mathcal{G}^{\gtrless}\left(t + \frac{\tau}{2}, t - \frac{\tau}{2}\right)^* e^{-i\omega\tau} \right]$$

$$= \int_{-\infty}^{+\infty} d\tau \left[\mathcal{G}^{\gtrless}\left(t + \frac{\tau}{2}, t - \frac{\tau}{2}\right) e^{i\omega\tau} - \mathcal{G}^{\gtrless}\left(t - \frac{\tau}{2}, t + \frac{\tau}{2}\right) e^{-i\omega\tau} \right] = 0$$

1.5.2 *Application to the study of Levitons*

We now apply the above introduced general tools to the specific case of a voltage pulse source discussed in Sec. 1.4, focusing in particular on Levitons. Let us start with the coherence function in time representation. We will consider the zero-temperature limit $\theta = 0$. Recall that the Heisenberg-picture time evolution of the fermionic field $\Psi(t)$ in the presence of a drive $V(t)$ reads [cf. Eq. (1.37)]

$$\Psi(t) = e^{i\alpha(t)}\psi(t), \tag{1.68}$$

where $\psi(t)$ is the evolution when no drive is applied. Then, the excess coherence function (1.54) in this particular case becomes[9]

$$\Delta\mathcal{G}^<(t_1, t_2) = \left(e^{-i\alpha(t_2)}e^{i\alpha(t_1)} - 1\right)\mathcal{G}_0^<(t_1, t_2). \tag{1.69}$$

The equilibrium contribution at zero temperature is

$$\mathcal{G}_0^<(t_1, t_2) = \left\langle \psi^\dagger(t_2)\psi(t_1)\right\rangle_0 = \frac{1}{2\pi i v_F}\frac{1}{t_2 - t_1 + i0^+}, \tag{1.70}$$

so that the excess coherence reads

$$\Delta\mathcal{G}^<(t_1, t_2) = \left(e^{ie\int_{t_2}^{t_1} dt' V(t')} - 1\right)\frac{1}{2\pi i v_F}\frac{1}{t_2 - t_1 + i0^+}. \tag{1.71}$$

By using

$$\frac{1}{t + i0^+} = \mathcal{P}\left(\frac{1}{t}\right) - i\pi\delta(t) \tag{1.72}$$

and noticing that the δ function does not contribute because the term in parentheses in (1.71) vanishes for $t_1 = t_2$, we can write

$$\Delta\mathcal{G}^<(t_1, t_2) = \left(e^{ie\int_{t_2}^{t_1} dt' V(t')} - 1\right)\frac{1}{2\pi i v_F}\mathcal{P}\left(\frac{1}{t_2 - t_1}\right). \tag{1.73}$$

According to (1.56), the diagonal limit $t_1 = t_2 = t$ gives the excess charge density or, equivalently, the current:

$$\Delta J(t) = -e v_F \,\Delta\mathcal{G}^<(t, t) = \frac{e^2}{2\pi}V(t). \tag{1.74}$$

This is the expected result, as a single chiral channel has a conductance of $e^2/(2\pi)$. Notice that this result holds for any drive $V(t)$ and not only for Levitons. If we specify to the case of a Lorentzian drive injecting a single electron, the phase $\exp[i\alpha(t)]$ in (1.69) is given by (1.46) and the excess electron coherence becomes

$$\begin{aligned}\Delta\mathcal{G}^<(t_1, t_2) &= \left(\frac{t_1 + iw}{t_1 - iw}\frac{t_2 - iw}{t_2 + iw} - 1\right)\frac{1}{2\pi i v_F}\mathcal{P}\left(\frac{1}{t_2 - t_1}\right)\\ &= \frac{w}{\pi v_F}\frac{1}{t_1 - iw}\frac{1}{t_2 + iw} = \frac{1}{v_F}\phi_1(t_1)\phi_1^*(t_2),\end{aligned} \tag{1.75}$$

---

9 Recall the discussion on page 21 about how averages are computed in the presence of the drive $V(t)$

where we defined[10]

$$\phi_1(t) = \sqrt{\frac{w}{\pi}} \frac{1}{t - iw} \,. \tag{1.76}$$

Since the dependence on t_1 and t_2 is factorized, the excess occupation number distribution has a very simple form. By plugging the above result into (1.57) we obtain

$$\Delta f(\omega) = \frac{v_F}{2\pi} \Delta \tilde{\mathcal{G}}^<(\omega, \omega) = \frac{1}{2\pi} \left| \tilde{\phi}_1(\omega) \right|^2 \,, \tag{1.77}$$

where we defined the Fourier-transformed wavefunction

$$\tilde{\phi}_1(\omega) = \int_{-\infty}^{+\infty} dt \sqrt{\frac{w}{\pi}} \frac{1}{t - iw} e^{i\omega t} = 2i\sqrt{\pi w}\, \Theta(\omega) e^{-\omega w} \,, \tag{1.78}$$

with $\Theta(\omega)$ the Heaviside step function. The possibility of expressing $\Delta f(\omega)$ as a square modulus is a direct consequence of the factorization of the excess electron coherence (1.75) in the time representation and is not common to any drive. We note that $\tilde{\phi}_1(\omega)$ is non zero only at positive energies, consistently with the fact that a Leviton is a single electron-excitation which leaves the Fermi sea unaffected. Indeed, $\tilde{\phi}_1(\omega)$ can be interpreted as the energy-space wavefunction associated with the single-Leviton state. The occupation number distribution $\Delta f(\omega)$ in energy space is exponentially decreasing, signaling that a Leviton is emitted close to the Fermi energy. In Fig. 1.10 we plot the particle current profile $j_e(t) = J(t)/(-e)$ for different values of the pulse width w and the corresponding $\Delta f(\omega)$. The more localized in time the pulse, the broader its distribution in energy.
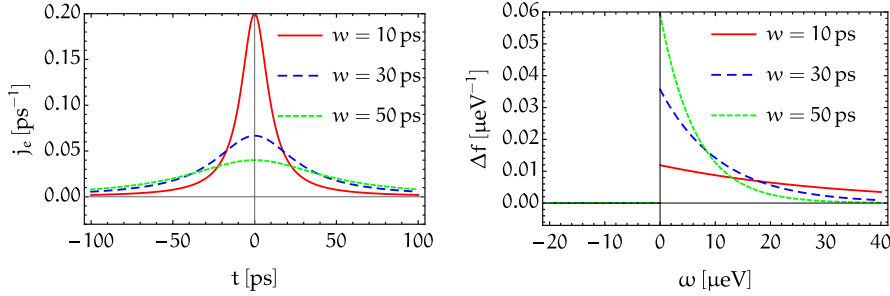
Figure 1.10: Left: particle current profile $j_e(t) = J(t)/(-e)$ as a function of time for different values of the width w. Right: probability density in energy space Δf as a function of ω for the same values of w as in the left panel.

If a single hole is injected, by following the lines of what was done above, it is easy to show that the single electron coherence becomes

$$\Delta \mathcal{G}^<(t_1, t_2) = -\phi_1^*(t_1)\phi_1(t_2) \tag{1.79}$$

---

10 The reason for the subscript in ϕ_1 will become evident later.

and, consequently,

$$\Delta f(\omega) = -\frac{1}{2\pi} \left| \tilde{\phi}_1(-\omega) \right|^2 . \tag{1.80}$$

This shows that the excess occupation number distribution is always negative and is nonvanishing only for $\omega < 0$. This behavior is exactly what we expect for the injection of a single hole.

How do these results generalize to a multi-particle state with n electrons or holes? From what we have discussed in Sec. 1.4, such a state can be simply built by applying to the quantum conductor a superposition of Lorentzian pulses with the same sign, as in (1.27). When considering the simultaneous injection of n identical electrons or holes, (1.27) becomes[11]

$$V(t) = \mp \frac{n}{e} \frac{2w}{w^2 + t^2} \quad (n > 0), \tag{1.81}$$

where we recall that the minus (plus) sign applies to electron (hole) states. Since this drive is just n times a single Lorentzian pulse, from (1.74) it follows that the current signal is not very different from the single-Leviton state. It is actually the same, apart from an overall factor of n. We may still ask how the n electrons or holes are distributed in energy space. Here things turn out to be much more interesting. We will investigate this problem by considering the Wigner function introduced in Sec. 1.5.1.3.

First of all we have to generalize the result (1.75). By using (1.48) in the case of a purely electronic state (with the same emission time and width for each Lorentzian), it is immediate to obtain

$$\Delta \mathcal{G}^<(t_1, t_2) = \left[\left(\frac{t_1 + iw}{t_1 - iw} \right)^n \left(\frac{t_2 - iw}{t_2 + iw} \right)^n - 1 \right] \frac{1}{2\pi i v_F} \mathcal{P} \left(\frac{1}{t_2 - t_1} \right) . \tag{1.82}$$

Now, starting from (1.75), it is possible to prove by induction that the previous equation can be written as [114–116]

$$\Delta \mathcal{G}^<(t_1, t_2) = \frac{1}{v_F} \sum_{j=1}^{n} \phi_j(t_1) \phi_j^*(t_2), \tag{1.83}$$

where the wavefunctions

$$\phi_j(t) = \sqrt{\frac{w}{\pi}} \frac{(t + iw)^{j-1}}{(t - iw)^j} \tag{1.84}$$

form a complete and orthonormal set, in the sense that

$$\int_{-\infty}^{+\infty} dt\, \phi_j^*(t) \phi_k(t) = \delta_{j,k} . \tag{1.85}$$

---

11 Referring to Eq. (1.27), we take the parameters $t_p = 0$ and $w_p = w$, for all p.

Notice that the wavefunction with $j = 1$ in (1.84) is precisely the single-Leviton wavefunction introduced in (1.76). This explains the notation we have used there. By taking the Fourier transform of (1.84) we obtain

$$\tilde{\phi}_j(\omega) = 2i\sqrt{\pi w}\,\Theta(\omega)L_{j-1}(2\omega w)e^{-\omega w}\,, \tag{1.86}$$

which is the generalization of (1.78). Here, L_j denotes the j-th Laguerre polynomial [70]. These functions enter the energy representation of the coherence function, which is, in a sense, the "dual" of (1.83):

$$\Delta\tilde{\mathcal{G}}^<(\omega_1,\omega_2) = \frac{1}{\nu_F}\sum_{j=1}^{n}\tilde{\phi}_j(\omega_1)\tilde{\phi}_j^*(\omega_2)\,. \tag{1.87}$$

Let us now come to the discussion of the Wigner function for these multi-particle states. Starting from the expression (1.83) it is possible to analytically evaluate it. This is done in Appendix B.2 and here we simply quote the answer and discuss the result. For the n-electron state the excess Wigner function is [113]

$$\Delta W^<(t,\omega) = \Theta(\omega)\frac{1}{\nu_F\sqrt{\pi}}\,e^{-2\omega w}$$
$$\times \sum_{j=0}^{n-1}\sum_{p=0}^{j}\frac{1}{p!}\left[\frac{2\omega w}{\sqrt{\omega t}}\right]^{2p+1}L_{j-p}^{(2p)}(4\omega w)J_{p+\frac{1}{2}}(2\omega t)\,, \tag{1.88}$$

where $L_j^{(k)}$ are generalized Laguerre polynomials and J_p is the Bessel function of order p [70]. The first thing to note is that $W^<(t,\omega) \propto \Theta(\omega)$, as expected for a purely electronic state. Moreover, there is an overall exponential decrease as a function of ω, whose rapidity is determined by the temporal extension w of the pulse. Apart from this, the analytic expression is quite involved. In order to have a better feeling of what is going on, we show in Fig. 1.11 the plots of (1.88) for n ranging from 1 to 4. It is evident that the Wigner function captures the familiar time dependence of the Lorentzian pulse (cfr. the real-time current profile in Fig. 1.10, left panel), the signal being stronger near the emission time $t = 0$ and progressively vanishing when $|t| \to \infty$.

It is interesting to see what happens when n is increased. The top left panel shows the case of a single-electron state: as we can see the signal is concentrated around the emission time $t = 0$ and at an energy close to the Fermi level (dark spot). If now we look at the case $n = 2$, we see that another spot appears, which is localized around $t = 0$, but at higher energy. This scheme repeats in the bottom panels. Each new electron is added at a higher energy with respect to the previous one. This is of course due to the Pauli principle, as it is impossible to put two electrons at the same energy at the same time. With the help of the Wigner function we can see how states at different energies are filled by increasing the number of injected electrons; in particular, low
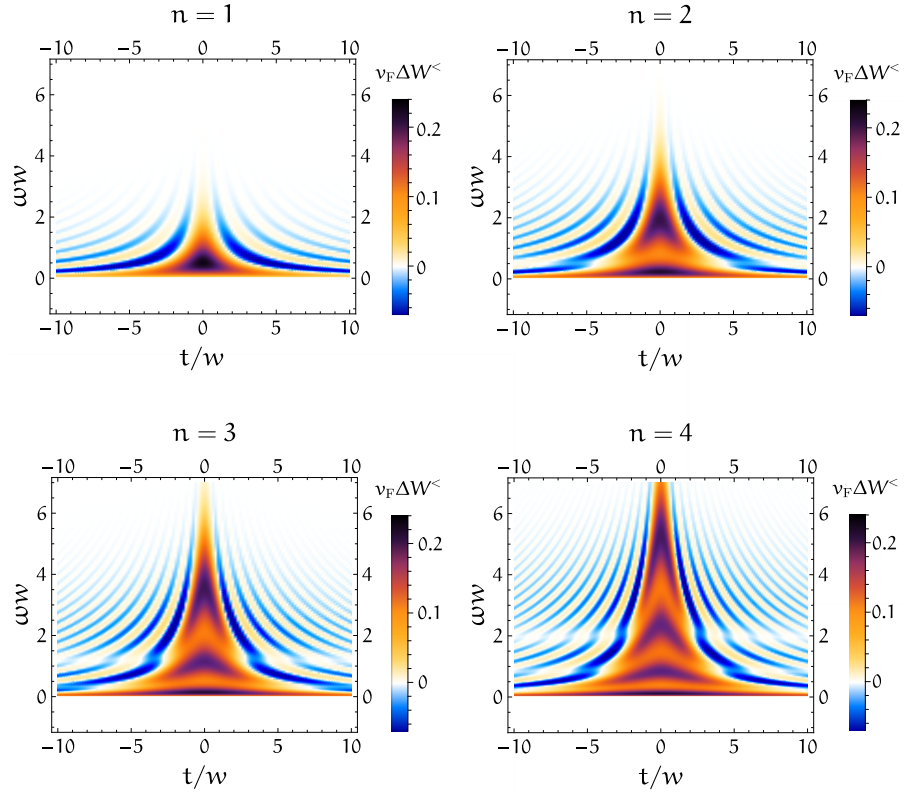
Figure 1.11: Electronic Wigner function $W^<(t, \omega)$ in (1.88) for multi-Leviton states, with n ranging from 1 to 4, as explicited above each panel. This representation allows to access both the energy content and the time profile of the excitations. Negative values (blue regions in the plots) are a signature of non-classical states.
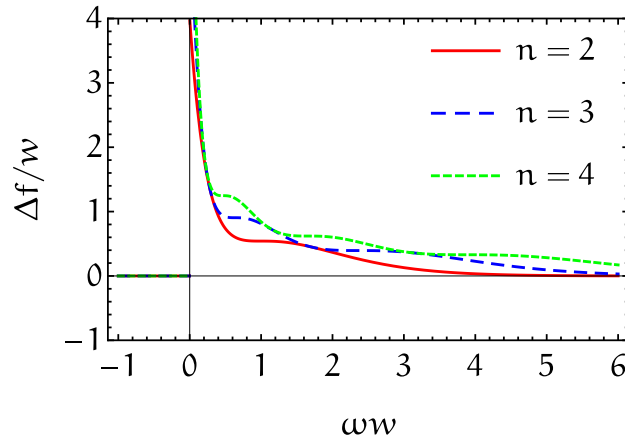
Figure 1.12: Plots of the distribution $\Delta f(\omega)$ in (1.90) for different values of the electron number n, as specified in the label. The energy profile is an exponential modulated by polynomial functions, which are responsible for the additional bumps that appear when increasing n.

energy states are filled first. It is transparent from the plots that the behavior as a function of energy is completely different from what happens as a function of time, where the current profile for n electrons is just n times the signal for a single one (cfr. Eqs. (1.74) and (1.81)). A final remark about Fig. 1.11 is that the Wigner function is negative in some regions (blue parts of the plot). This is a signature of the quantum character of the state and prevents from interpreting the Wigner function as a probability density [113].

Before concluding this Section, let us have a look at the behavior of the occupation number distribution $\Delta f(\omega)$. As we have discussed, it can be obtained by integrating Eq. (1.88) over time. Despite the appearances, the result is quite simple and is a direct generalization of the expression (1.77) found for a single-Leviton state:

$$\Delta f(\omega) = \frac{1}{2\pi} \sum_{j=1}^{n} \left| \tilde{\phi}_j(\omega) \right|^2 . \tag{1.89}$$

Notice that this simple result can be more easily obtained from the energy representation (1.87). After expliciting the wave functions $\tilde{\phi}_j(\omega)$ through Eq. (1.86) we obtain this final form:

$$\Delta f(\omega) = 2w \, \Theta(\omega) \sum_{j=0}^{n-1} L_j^2(2\omega w) e^{-2\omega w} . \tag{1.90}$$

This function features an exponentially decreasing envelope, modulated by the square of Laguerre polynomials. Some plots are shown in Fig. 1.12 and, apart from the $\Theta(\omega)$ already discussed, we can see that additional bumps at higher energies appear when n increases, just as happens in the Wigner function. We can also check that $\Delta f(\omega)$ is normalized to the total number of electrons injected by the drive, namely

$$\int_{-\infty}^{+\infty} d\omega \, \Delta f(\omega) = n . \tag{1.91}$$

This follows from the orhogonality of Laguerre polynomials with respect to the weight function $\exp(-x)$:

$$\int_{0}^{+\infty} dx \, L_j(x) L_k(x) e^{-x} = \delta_{j,k} . \tag{1.92}$$

By applying this relation with $j = k$ we see that the integral of each term in the sum (1.90) is equal to 1 and thus (1.91) is fulfilled.

1.6 EXPERIMENTAL EVIDENCE FOR LEVITONS

After having discussed the properties of Levitons in detail, we conclude this Chapter by mentioning very briefly how the existence of
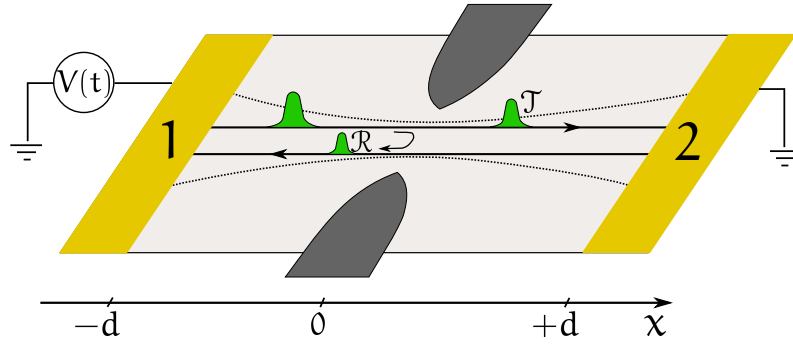
Figure 1.13: HBT setup in a 2DEG for detecting Levitons. A QPC (grey gates) is set in such a way that a conduction channel is created across the 2DEG. Within this channel, the propagation is not chiral and both right- and left-moving fermions are present. The gate voltage of the QPC can be used to tune the probabilities for an excitation incoming from the reservoir 1 to be transmitted across the QPC ($\mathcal{T}$) or reflected ($\mathcal{R} = 1 - \mathcal{T}$).

these peculiar excitations was experimentally confirmed [5]. This was done in the group of D. C. Glattli through noise measurements in the so-called HBT setup, which is sketched in Fig. 1.13. The experiment was not performed in the IQHE regime, but relies on the possibility of creating conduction channels in a 2DEG by means of a QPC, as discussed in Sec. 1.1. As depicted in Fig. 1.13, the QPC is set in such a way that a single conduction channel is created in the system. Contrary to IQHE edge states, here the propagation is not chiral and, thus, both right- and left-moving fermions are present in the conduction channel. The system is connected to two terminals (yellow regions). A drive $V(t)$ is applied to terminal 1 and generates excitations propagating to the right, while terminal 2 is grounded. Moreover, here the QPC also acts as a beamsplitter because it can be tuned in order for excitations incoming from terminal 1 to be transmitted across the constriction, with probability $\mathcal{T}$, or reflected, with probability $\mathcal{R} = 1 - \mathcal{T}$, as sketched in the Figure.

For experimental reasons, a *periodic* drive $V(t) = V(t + T)$ is used, because the measurement requires several cyclic repetitions to increase the signal-to-noise ratio. Thus, rather than the single-pulse excitations depicted in Fig. 1.13, a stream of such excitations is actually sent towards the QPC. Given this difference with respect to what we have discussed until now, instead of the total charge excited by the drive, the meaningful parameter is the charge per period. In particular, the number of charges (charge in units of $-e$) is

$$q = -\frac{e}{2\pi} \int_{-T/2}^{T/2} dt \, V(t) \,. \tag{1.93}$$

A QPC is used as a beamsplitter, with tunable transmission $\mathcal{T}$, and excitations incoming from the right are partly transmitted and partly

reflected. With this setup it is possible to measure the autocorrelation noise of the current $J_2(t)$ entering terminal 2, i.e. in the right part of Fig. 1.13, after the QPC. This quantity is defined as

$$S_{22} = \int_{-T/2}^{T/2} \frac{dt}{T} \int_{-\infty}^{+\infty} dt' \left\langle \delta J_2(t) \delta J_2(t') \right\rangle, \tag{1.94}$$

where $\delta J_2(t) = J_2(t) - \langle J_2(t) \rangle$ denotes fluctuations of the current with respect to its average value and T is the period of the drive. The zero-temperature result for the above autocorrelation noise in the HBT configuration is proven in Appendix C.1 and reads

$$S_{\text{HBT}} = e^2 v_F^2 \mathcal{T}(1 - \mathcal{T}) \int_{-T/2}^{+T/2} \frac{dt}{T} \int_{-\infty}^{+\infty} dt' \left[\mathcal{G}_R^<(t', t) \mathcal{G}_{0,L}^>(t, t') + \right. \\ \left. + \mathcal{G}_{0,L}^<(t', t) \mathcal{G}_R^>(t, t') \right], \tag{1.95}$$

where, as usual, the subscript 0 indicates equilibrium correlators, while the index R (L) refers to the right- (left-) moving fermions in the conduction channel. In order to evaluate these quantities, we simply notice that the time evolution of right-movers is [cf. Eq. (1.68)]

$$\Psi_R(t) = \psi_R(t) e^{i\alpha(t)}, \quad \alpha(t) = e \int_{-\infty}^{t} d\tau \, V(\tau), \tag{1.96}$$

while the operator for left-movers satisfies the free evolution $\Psi_L(t) = \psi_L(t)$, since no drive is applied to terminal 2. Therefore

$$\mathcal{G}_R^{\gtrless}(t, t') = e^{ie \int_{t'}^{t} d\tau \, V(\tau)} \mathcal{G}_{0,R}^{\gtrless}(t, t') \tag{1.97}$$

and the equilibrium coherence functions are

$$\mathcal{G}_{0,R/L}^<(t, t') = \left\langle \psi_{R/L}^\dagger(t') \psi_{R/L}(t) \right\rangle_0 = \int_{-\infty}^{+\infty} \frac{d\omega}{2\pi v_F} e^{i\omega(t'-t)} n_F(\omega), \tag{1.98a}$$

$$\mathcal{G}_{0,R/L}^>(t, t') = \left\langle \psi_{R/L}(t) \psi_{R/L}^\dagger(t') \right\rangle_0 = \int_{-\infty}^{+\infty} \frac{d\omega}{2\pi v_F} e^{i\omega(t-t')} n_F(\omega). \tag{1.98b}$$

We can proceed further by decomposing the voltage drive $V(t)$ into dc and ac contributions as follows

$$V(t) = V_{\text{dc}} + V_{\text{ac}}(t), \quad \int_{-T/2}^{T/2} dt \, V_{\text{ac}}(t) = 0, \tag{1.99}$$

where V_{dc} is a constant dc bias related to the charge per period q defined in (1.93) by $q\Omega = -eV_{\text{dc}}$, $\Omega = 2\pi T^{-1}$ being the angular frequency of the drive. Moreover, by exploiting the periodicity of $V(t)$ it is possible to write the following Fourier decomposition [114, 117]

$$e^{ie \int_0^t d\tau \, V(\tau)} = e^{-iq\Omega t} \sum_{\ell \in \mathbb{Z}} p_\ell \, e^{-i\ell\Omega t}, \tag{1.100}$$

where the coefficients p_ℓ are called photo-assisted amplitudes and are defined as

$$p_\ell = \int_{-T/2}^{T/2} \frac{dt}{T} \, e^{i\ell\Omega t} e^{ie \int_0^t d\tau \, V_{ac}(\tau)} \,. \tag{1.101}$$

For $\ell < 0$ ($\ell > 0$), they represent the probability amplitude for an electron to emit (absorb) $|\ell|$ quanta of energy Ω [114]. Notice that they can also be seen as a discrete version of Eq. (1.39), which we used for a generic non-periodic drive. By using the decomposition (1.100) into (1.97), after a lengthy but straightforward calculation one shows that the HBT noise in Eq. (1.95) assumes the simple form [cf. App. C.1]

$$S_{HBT} = \frac{e^2 \mathcal{T}(1-\mathcal{T})}{T} \sum_{\ell \in \mathbb{Z}} |p_\ell|^2 |\ell + q| \,. \tag{1.102}$$

Likewise, the noise S_{dc} obtained for a purely time-independent dc bias, $V(t) = V_{dc}$, is given by

$$S_{dc} = \frac{e^2 \mathcal{T}(1-\mathcal{T})}{T} |q| \equiv S_0 |q| \,, \tag{1.103}$$

This result can be directly obtained from (1.102) by setting $p_\ell = \delta_{\ell,0}$, which readily follows from (1.101) when $V_{ac} = 0$. We can finally define the *excess noise*

$$\Delta S = S_{HBT} - S_{dc} = S_0 \sum_{\ell < -q} |p_\ell|^2 |\ell + q| \,, \tag{1.104}$$

where $q > 0$ was assumed, for the sake of simplicity.

This quantity can be experimentally probed and actually is connected to the number of unwanted particle-hole pairs generated by the drive. The key result is the following: in a *non-interacting* system, the number of extra electron-hole pairs is directly proportional to the excess noise ΔS [7, 8]. Therefore, the excess noise ΔS has to vanish for Lorentzian pulses with integer q. From a mathematical point of view, this happens because the Lorentzian drive is the only one for which $p_\ell = 0$ for $\ell < -q$.

A vanishing excess noise is precisely what was measured in the experiment, whose result is shown in Fig. 1.14. The plots show the excess noise as a function of q, for three kind of signals: a sine, a square wave and a Lorentzian drive. Since the experiment is done at finite temperature, particle-hole pairs can also be thermally excited and this effect must be taken into account, as here we want to investigate whether such pairs are created as a consequence of the applied drive and not by thermal effect. It is possible to have an estimate of the thermally-excited pairs by generalizing Eq. (1.104) to finite temperatures, see Eq. (C.15) in App. C.1. The dashed lines in the plots show the expected thermal contribution obtained in such a way. As we can see, the Lorentzian drive is the only one whose excess noise
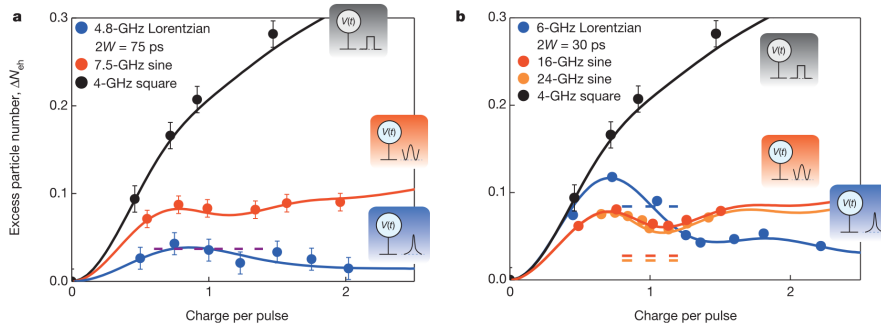
Figure 1.14: Experimental evidence for Levitons. Both panels show excess noise measurements for different kind of drives, as a function of the number of charges per period q. Dashed lines indicate the finite-temperature contribution to the excess noise and show that for a Lorentzian drive this is actually the only contribution, thus confirming the expected behavior of Levitons. Image taken from [5].

at integer q is entirely due to thermal contributions, thus implying that no particle-hole pair is generated as an effect of the drive and confirming the minimal character of Levitons. The experiment also shows a clear hierarchy between the three different drives, with the square wave being the noisiest one.

INTERACTING 1D FERMIONIC SYSTEMS

In the previous Chapter, we introduced EQO in non-interacting 1D fermion systems. Despite that context already enables the investigation of interesting physical effects, this thesis aims at giving a contribution to extend EQO studies to systems where interaction effects are important. This Chapter is therefore dedicated to a presentation of interacting 1D fermionic systems, together with the theoretical tools needed to describe them.

2.1 INTRODUCTION

When it comes to interaction effects, 1D systems behave very differently with respect to what happens in higher dimensions. There, interacting electrons are well described by the Fermi liquid theory [118], introduced by L. Landau in 1956 [21]. According to this theory, the interacting electron liquid basically retains the qualitative properties of a free system and can be described in terms of quasi-particles with renormalized parameters, which constitute the stable low-energy excitations of the system. These quasi-particles are essentially electrons dressed by density fluctuations around them and they interact very weakly with each other, even when the electron-electron Coulomb interaction is intense. This explains the success of Fermi liquid theory in describing several different materials.

However, as far as 1D systems are concerned, Landau's theory fails. A pictorial intuition of why this is the case is provided in Fig. 2.1, showing in an effective way the deep difference between 1D and higher dimensional systems. In the latter case, dressed quasi-particles
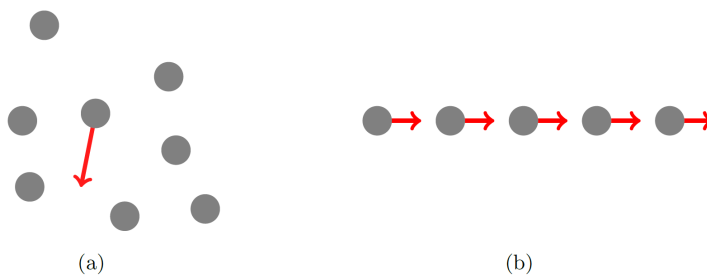
Figure 2.1: Comparison between interacting electrons in 1D and higher dimensions. Panel (a): in high dimensions, individual quasi-particle excitations are possible. Panel (b): in 1D, the motion of an individual electron has an effect on all the others, thus resulting in a collective excitation. Image adapted from [119].

are weakly interacting and can move without affecting each other too much. On the contrary, in 1D systems any individual motion influences all other particles, dragging or pushing them due to interactions. As a result, individual excitations are not well defined and the physics has therefore to be very different. From a more formal point of view, it can be shown that, for a quasi-particle of energy $\xi \ll E_F$ (measured from the Fermi level E_F), the decay rate is $\Gamma \propto \xi$ in 1D, while $\Gamma \propto \xi^2/E_F$ in higher dimensions [118, 120]. Then, in the latter case $\Gamma \ll \xi$ and the energy of the quasi-particle is well defined, making it a stable excitation, while in the former one the same reasoning does not apply and no stable quasi-particles exist.

A new theoretical paradigm replacing the Fermi liquid must then be introduced in order to describe 1D interacting system: it is the Luttinger Liquid (LL) concept. The model from which this theory originated was first studied by Tomonaga [121] and Luttinger [122]. This model of interacting fermions in 1D has the notable property of being exactly solvable by bosonization techniques [123], as we will show in the next Section. An important further development was made by Haldane [22], who suggested that the model would actually describe *any* 1D system at sufficiently low energy and proposed the term Luttinger Liquid to describe this universal low-energy theory. Its validity has been verified in several instances, by observing exotic phenomena such as anomalous tunneling effects [124], spin-charge separation [25, 125] and charge fractionalization [24, 126–128], all accounted for by LL theory. This success in describing several 1D interacting systems can be further understood insofar as the LL has been shown to be the fixed point of the renormalization group flow for interacting fermions in 1D, in the same way as Landau's theory is in higher dimensions [129]. Moreover, since excitations in 1D have essentially a bosonic character, LL theory also applies to the description of interacting bosons [119].

In what follows we illustrate the Luttinger model and its solution, by focusing on the two cases of interest for the present thesis, namely counter-propagating channels and co-propagating chiral ones, and referring to the wide literature for further details and generalizations [22, 119, 123, 130, 131]. Throughout the Chapter we set $\hbar = 1$.

2.2   SPINLESS LUTTINGER LIQUID

Let us consider N spinless fermions in a system of length L, subject to periodic boundary conditions. The Hamiltonian

$$H = H_0 + H_{int} \, , \tag{2.1}$$

is composed of a free part

$$H_0 = \int_{-L/2}^{L/2} dx \, \Psi^\dagger(x)\epsilon(-i\partial_x)\Psi(x) \, , \tag{2.2}$$
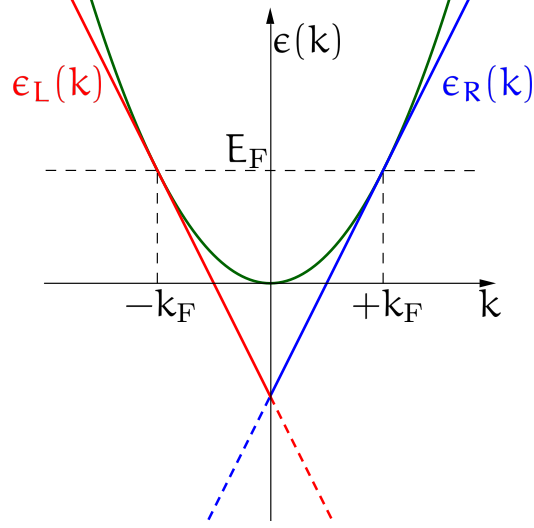
Figure 2.2: Linearization of the spectrum around the Fermi points $k = \pm k_F$. Starting from a generic dispersion (green curve), right (blue curve) and left (red curve) energy branches are obtained. Dashed lines indicate the addition of unphysical states, which are needed in order to apply the bosonization technique.

associated with the single particle spectrum $\epsilon(k)$, and an interaction term

$$H_{int} = \int_{-L/2}^{L/2} dx \int_{-L/2}^{L/2} dy\, \Psi^\dagger(x)\Psi^\dagger(y)U(x-y)\Psi(y)\Psi(x)\,, \qquad (2.3)$$

$U(x-y)$ being the two-body interaction potential. In both previous formulas, $\Psi(x)$ is a fermionic field operator annihilating an electron at position x.

2.2.1 *Linearization of the spectrum*

The explicit form of the dispersion relation $\epsilon(k)$ is not very important, because the first key approximation of the Luttinger model is to linearize the spectrum around the Fermi energy E_F, which is perfectly consistent in order to describe the low-energy physics of the system. The linearization procedure is sketched in Fig. 2.2 and defines the following two energy branches:

$$\epsilon_r(k) = E_F + v_F(\vartheta_r k - k_F)\,, \quad v_F = \left.\frac{d\epsilon}{dk}\right|_{k=k_F}\,, \qquad (2.4)$$

with $r = R/L$, $\vartheta_{R/L} = \pm 1$ and k_F the Fermi momentum. In this way, two distinct fermionic species are introduced: right-moving electrons, with positive group velocity, and left-moving ones, with opposite group velocity. At this stage the momentum k for the right (left)

branch is restricted to positive (negative) values. However, in order for the bosonization technique by which the model is solved to be applicable, the spectrum has to be unbounded [123]. Therefore, the second approximation of the model consists in extending the range of the momentum to $k \in (-\infty, +\infty)$ for both branches $\epsilon_r(k)$. This operation introduces an infinite number of unphysical states, which are represented by the dashed lines in the spectrum of Fig. 2.2.

After the described procedure, the linearized free Hamiltonian becomes

$$H_0 = v_F \sum_{r=R,L} \int_{-L/2}^{L/2} dx \, \Psi_r^\dagger(x)(-i\vartheta_r\partial_x)\Psi_r(x), \tag{2.5}$$

where we have introduced the fields $\Psi_r(x)$ annihilating an electron at position x on the branch r. These fields satisfy the canonical anticommutation relations

$$\begin{aligned} \left\{\Psi_r(x), \Psi_{r'}(x')\right\} &= \left\{\Psi_r^\dagger(x), \Psi_{r'}^\dagger(x')\right\} = 0 \\ \left\{\Psi_r(x), \Psi_{r'}^\dagger(x')\right\} &= \delta_{r,r'}\delta(x-x') \end{aligned} \tag{2.6}$$

and have the following plane-wave decomposition

$$\Psi_r(x) = \frac{1}{\sqrt{L}} \sum_{k=-\infty}^{+\infty} e^{i\vartheta_r kx} c_{k,r}, \tag{2.7}$$

where the operator $c_{k,r}$ annihilates an electron with momentum $\vartheta_r k$ on the branch r. By exploiting this relation, H_0 is rewritten as

$$H_0 = v_F \sum_{r=R,L} \sum_{k=-\infty}^{+\infty} k \, c_{k,r}^\dagger c_{k,r}, \tag{2.8}$$

from which we immediately recognize that the expectation value of this operator on its ground state (all levels with energy below E_F filled) is divergent. This is an unphysical effect due to the introduction of an infinite number of negative-energy states and we can deal with this issue by considering normal ordered operators, obtained from the bare ones by subtracting their expectation value on a reference state, which is usually the ground state $|GS\rangle$. For instance, the normal ordered number operator is

$$N_r = \sum_{k=-\infty}^{+\infty} :c_{k,r}^\dagger c_{k,r}: = \sum_{k=-\infty}^{+\infty} \left[c_{k,r}^\dagger c_{k,r} - \left\langle GS \left| c_{k,r}^\dagger c_{k,r} \right| GS \right\rangle \right] \tag{2.9}$$

and counts the number of electrons on the branch r, *with respect to the ground state*. In the same way, the expression for H_0 has to be normal ordered to obtain meaningful results in calculations.

The Hamiltonian (2.5) describes a system composed of two counterpropagating channels hosting spinless fermions, as sketched in Fig.

2.3. For this reason the model we are describing is called the spinless LL. We anticipate, however, that the very same Hamiltonian can also be used to describe another important system of spinful fermions which we will investigate in Chapter 4. As we will see, this system is related to a topological phase of matter called Quantum Spin Hall Effect (QSHE) and has the very peculiar property that the spin projection of electrons is directly related to their propagation direction, this effect being known as spin-momentum locking. In order to describe such a system it is sufficient to assume that R-branch (L-branch) electrons have spin up (down). This system in the presence of interactions is called Helical Luttinger Liquid (HLL) and has first been studied in Ref. [132].
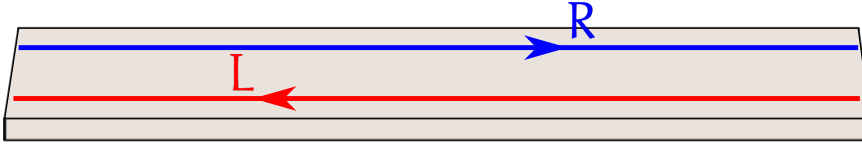
Figure 2.3: Sketch of a spinless LL: the system is composed of two counter-propagating channels, associated with the linearized dispersions (2.4). Notice that here we have drawn the two channels in separate space positions for graphical purposes, but, unlike what happens in the IQHE, they are not spatially separated in reality.

2.2.2 *Bosonization*

The free Hamiltonian H_0 in Eq. (2.5) can be converted in a different but completely equivalent language, by using the bosonization identity [22, 123, 133], which expresses fermionic operators in terms of bosonic ones:

$$\Psi_r(x) = \frac{F_r}{\sqrt{2\pi a}}\, e^{i\vartheta_r k_F x} e^{-i\sqrt{2\pi}\Phi_r(x)}\,. \tag{2.10}$$

Here, $a \sim k_F^{-1}$ is a short length cutoff, F_r are called Klein factors[1] and bosonic fields $\Phi_r(x)$ are represented as[2]

$$\Phi_r(x) = \frac{i}{\sqrt{L}} \sum_{q>0} \frac{e^{-aq/2}}{\sqrt{q}} \left(b_{q,r} e^{iq\vartheta_r x} - b_{q,r}^\dagger e^{-iq\vartheta_r x} \right) = \Phi_r^\dagger(x)\,, \tag{2.11}$$

with creation and annihilation operators satisfying

$$\left[b_{q,r}, b_{q',r'} \right] = \left[b_{q,r}^\dagger, b_{q',r'}^\dagger \right] = 0\,, $$
$$\left[b_{q,r}, b_{q',r'}^\dagger \right] = \delta_{q,q'}\delta_{r,r'}\,. \tag{2.12}$$

---

1 We are going to discuss their role in the following.
2 From the exponential factor $e^{-aq/2}$ in (2.11), we see that the inverse of the cutoff, a^{-1}, plays the role of an upper bound to the momentum q associated with particle-hole pairs created by operators $b_{q,r}^\dagger$; see also Eq. (2.13).

They are related to the fermionic operators by

$$b_{q,r}^\dagger = \sqrt{\frac{2\pi}{Lq}} \sum_{k=-\infty}^{+\infty} c_{k+q,r}^\dagger c_{k,r},$$

$$b_{q,r} = \sqrt{\frac{2\pi}{Lq}} \sum_{k=-\infty}^{+\infty} c_{k-q,r}^\dagger c_{k,r},$$

(2.13)

which show that $b_{q,r}^\dagger$ creates a superposition of particle-hole pairs with momentum q on the branch r. From the definition (2.11) and the commutators (2.12), the following commutation rules for fields $\Phi_r(x)$ can be obtained[3]

$$\left[\Phi_r(x), \Phi_{r'}(x')\right] = \frac{i\vartheta_r}{\pi}\delta_{r,r'}\tan^{-1}\left(\frac{x-x'}{a}\right) \to \frac{i\vartheta_r}{2}\delta_{r,r'}\mathrm{sgn}(x-x').$$

(2.14)

We now discuss the role of Klein factors F_r appearing in the bosonization identity (2.10). They are essential for a proper representation of fermionic fields in terms of bosonic ones. As a matter of fact, $\Psi_r(x)$ removes an electron from the system, whereas $\Phi_r(x)$ cannot modify the particle number because

$$\left[b_{q,r}^\dagger, N_r\right] = \sqrt{\frac{2\pi}{Lq}} \sum_{k,k'} \left[c_{k+q,r}^\dagger c_{k,r}, :c_{k',r}^\dagger c_{k',r}:\right]$$

$$= \sqrt{\frac{2\pi}{Lq}} \sum_{k,k'} \left(c_{k+q,r}^\dagger \left[c_{k,r}, c_{k',r}^\dagger\right] c_{k',r} + c_{k',r}^\dagger \left[c_{k+q,r}^\dagger, c_{k',r}\right] c_{k,r}\right)$$

$$= \sqrt{\frac{2\pi}{Lq}} \sum_{k} \left(c_{k+q,r}^\dagger c_{k,r} - c_{k+q,r}^\dagger c_{k,r}\right) = 0.$$

(2.15)

This is why Klein factors are needed in (2.10). They are unitary operators, $F_r^\dagger F_r = F_r F_r^\dagger = \mathbb{1}$, which obey the algebra [123]

$$\left\{F_r, F_{r'}^\dagger\right\} = 2\delta_{r,r'}$$

$$\left\{F_r^\dagger, F_{r'}^\dagger\right\} = \{F_r, F_{r'}\} = 0 \quad \text{for } r \neq r'$$

(2.16)

and ensure that the canonical anticommutation relations (2.6) are satisfied. Moreover, Klein factors commute with operators $b_{q,r}$, $b_{q,r}^\dagger$ and

$$\left[F_r^\dagger, N_{r'}\right] = -\delta_{r,r'}F_r^\dagger, \quad [F_r, N_{r'}] = \delta_{r,r'}F_r,$$

(2.17)

showing that $F_r^\dagger$ (F_r) adds (removes) a particle to (from) the branch r. Notice, however, that they are not fermionic operators because $F_r^2 \neq 0$.

---

3 In obtaining this result, the limit $|x-x'| \ll L$ has to be taken.

By using the above introduced machinery, we can rewrite all fermionic operators in a bosonized form. In what follows we focus on three of them we are particularly interested in.

DENSITY OPERATOR   The particle density operator of the branch r is defined as[4]

$$\rho_r^{(e)}(x) = \; :\Psi_r^\dagger(x)\Psi_r(x): \tag{2.18}$$

By using Eq. (2.7) we can write

$$\begin{aligned}\rho_r^{(e)}(x) &= \frac{1}{L}\sum_{k,k'} :c_{k',r}^\dagger c_{k,r}: e^{i\vartheta_r(k-k')x}\\ &= \frac{N_r}{L} + \frac{1}{L}\sum_{q>0}\sum_k \left(c_{k+q,r}^\dagger c_{k,r}e^{-iq\vartheta_r x} + c_{k-q,r}^\dagger c_{k,r}e^{iq\vartheta_r x}\right).\end{aligned} \tag{2.19}$$

Thus, from Eqs. (2.13) and (2.11), the following representation in terms of the bosonic field $\Phi_r(x)$ follows

$$\rho_r^{(e)}(x) = \frac{N_r}{L} - \frac{\vartheta_r}{\sqrt{2\pi}}\partial_x\Phi_r(x), \tag{2.20}$$

which describes density fluctuations on top of a constant background term.

FREE HAMILTONIAN   It is possible to show that the Hamiltonian H_0 becomes [123, 130]

$$\begin{aligned}H_0 &= v_F\sum_{r=R,L}\int_{-L/2}^{L/2} dx \; :\Psi_r^\dagger(x)(-i\vartheta_r\partial_x)\Psi_r(x):\\ &= \frac{v_F}{2}\sum_{r=R,L}\int_{-L/2}^{L/2} dx \; :[\partial_x\Phi_r(x)]^2: + \frac{v_F\pi}{L}\sum_{r=R,L}N_r(N_r+1).\end{aligned} \tag{2.21}$$

The second term is usually referred to as the zero-mode contribution, while the first one is associated with bosonic excitations at fixed particle number. In the zero-mode part, the linear term in N_r can be reabsorbed in a shift of the chemical potential and will thus be dropped.

INTERACTION HAMILTONIAN   The great advantage of the bosonization technique is that it allows to express the four-fermion-operator Hamiltonian (2.3) as a *quadratic* form of the bosonic fields. In particular, by assuming a contact interaction potential

$$U(x-y) = U_0\delta(x-y), \tag{2.22}$$

---

4 We use the notation $\rho_r^{(e)}(x)$ for the particle density operator in order to distinguish it from the *charge* density operator $\rho_r(x) = -e\rho_r^{(e)}(x)$.

it can be shown that the most relevant terms are such that Eq. (2.3) becomes $H_{int} \simeq H_2 + H_4$, where H_2 and H_4 are density-density couplings [119, 130]:

$$H_2 = g_2 \int_{-L/2}^{L/2} dx \; :\rho_R^{(e)}(x)\rho_L^{(e)}(x):, \tag{2.23a}$$

$$H_4 = \frac{g_4}{2} \sum_{r=R,L} \int_{-L/2}^{L/2} dx \; :\left[\rho_r^{(e)}(x)\right]^2: . \tag{2.23b}$$

Here, the notation for the coupling constants is chosen according to the classification of interaction processes knows as the g-ology [119]. The two terms H_2 and H_4 describe inter- and intra-channel interactions respectively. By using the relation (2.20) into (2.23) and taking (2.21) into account, the complete Hamiltonian assumes the form

$$H = H_0 + H_2 + H_4 = H_N + H_B, \tag{2.24}$$

with

$$H_N = \frac{v_F \pi}{L}\left[\left(1 + \frac{g_4}{2\pi v_F}\right)\sum_{r=R,L} N_r^2 + \frac{g_2}{v_F \pi}N_R N_L\right] \tag{2.25}$$

and

$$H_B = \int_{-L/2}^{L/2} dx \left[\left(\frac{v_F}{2} + \frac{g_4}{4\pi}\right)\sum_{r=R,L} :[\partial_x \Phi_r(x)]^2: + \frac{g_2}{2\pi} :\partial_x \Phi_R(x)\partial_x \Phi_L(x):\right] . \tag{2.26}$$

Here, H_B describes bosonic excitations, while H_N is the zero-mode Hamiltonian. As we can see, the intra-channel coupling g_4 simply results in a renormalization of the Fermi velocity and, in the absence of g_2, the model describes a system of free fermions with a velocity $v_F + g_4/(2\pi)$.

2.2.3 Diagonalization

Since the Hamiltonian is quadratic in the bosonic fields, it can now be easily diagonalized by means of a Bogoliubov transformation

$$\begin{pmatrix} \Phi_R(x) \\ \Phi_L(x) \end{pmatrix} = \begin{pmatrix} \cosh\gamma & \sinh\gamma \\ \sinh\gamma & \cosh\gamma \end{pmatrix}\begin{pmatrix} \Phi_+(x) \\ \Phi_-(x) \end{pmatrix} . \tag{2.27}$$

This is a canonical transformation and preserves the commutation rules of bosonic fields: in other words, by assuming (2.14) and using (2.27) one obtains

$$\left[\Phi_\eta(x), \Phi_{\eta'}(x')\right] = \frac{i\eta}{2}\mathrm{sgn}(x-x') \quad \text{(with } \eta = \pm\text{)}. \tag{2.28}$$

In doing the calculation it is easy to realize that the transformation (2.27) has indeed to be parametrized with hyperbolic functions for the above commutation rules to be ensured. This is a because we are describing a system with counterpropagating channels. In Sec. 2.3 we will see that a different transformation has to be employed in the case of copropagating modes.

By substituting Eq. (2.27) into (2.26), one finds that the condition for the Hamiltonian H_B to be diagonal with respect to the new fields $\Phi_\eta(x)$ is

$$\tanh 2\gamma = \frac{g_2}{2\pi v_F + g_4} \implies \gamma = -\frac{1}{2}\ln K, \tag{2.29}$$

where we introduced the Luttinger parameter

$$K = \sqrt{\frac{2\pi v_F - g_2 + g_4}{2\pi v_F + g_2 + g_4}} \tag{2.30}$$

which measures the interaction strength. In the case of free fermions $K = 1$, while for repulsive (attractive) interactions $K < 1$ ($K > 1$).

The Hamiltonian H_B in diagonal form reads

$$H_B = \frac{u}{2}\sum_{\eta=\pm}\int_{-L/2}^{L/2} dx : [\partial_x\Phi_\eta(x)]^2:, \tag{2.31}$$

where u is a renormalized velocity

$$u = \frac{1}{2\pi}\sqrt{(2\pi v_F + g_4)^2 - g_2^2}, \tag{2.32}$$

which simplifies to $u = v_F/K$ if $g_2 = g_4$. The Bogoliubov transformation (2.27) expressed in terms of the Luttinger parameter K becomes

$$\Phi_r(x) = \sum_{\eta=\pm} A_{\eta\vartheta_r}\Phi_\eta(x), \tag{2.33}$$

where we introduced the coefficients[5]

$$A_+ = \cosh\gamma = \frac{1}{2}\left(\frac{1}{\sqrt{K}} + \sqrt{K}\right), \tag{2.34a}$$

$$A_- = \sinh\gamma = \frac{1}{2}\left(\frac{1}{\sqrt{K}} - \sqrt{K}\right). \tag{2.34b}$$

They obviously satisfy the relation

$$A_+^2 = 1 + A_-^2 \geqslant 1 \tag{2.35}$$

for every value of K. For completeness, we also diagonalize the zero-mode term H_N in (2.25), even if it will not be considered in the forthcoming Chapters. This is achieved very simply by introducing the operators $N_\pm = N_R \pm N_L$, in terms of which

$$H_N = \frac{\pi u}{2L}\left(\frac{1}{K}N_+^2 + KN_-^2\right). \tag{2.36}$$

[5] The notation $A_{\eta\vartheta_r}$ in (2.33) does not mean that the coefficients $A_{\eta\vartheta_r}$ form a matrix. Indeed, the subscript index appearing in (2.34) is simply given by the product of the values of indices η and ϑ_r. Thus, $A_{++} = A_{--} \to A_+$ and $A_{+-} = A_{-+} \to A_-$.

CHIRAL OPERATORS   It is important to stress that, in the presence of interactions, the original fields $\Phi_{R/L}(x)$ are no more right- and left-moving, respectively. This is because, unlike in the non-interacting case, the Hamiltonian is not diagonal with respect to these fields. This property is instead verified by the new fields $\Phi_\eta(x)$, which therefore evolve chirally. Indeed, their Heisenberg's equations of motion obtained from (2.31) read

$$(\partial_t + \eta u \partial_x)\Phi_\eta(x, t) = 0 \tag{2.37}$$

and are solved by

$$\Phi_\eta(x, t) = \Phi_\eta(x - \eta u t, 0) = \Phi_\eta\left(0, t - \frac{\eta x}{u}\right). \tag{2.38}$$

These fields can be used to define chiral density operators: by neglecting zero-mode contributions, the time evolution of the total particle density can indeed be expressed as

$$
\begin{aligned}
\rho^{(e)}(x, t) &= \rho_R^{(e)}(x, t) + \rho_L^{(e)}(x, t) \\
&= \frac{1}{\sqrt{2\pi}} [\Phi_L(x, t) - \Phi_R(x, t)] \\
&= \frac{A_+ - A_-}{\sqrt{2\pi}} \partial_x [\Phi_-(x, t) - \Phi_+(x, t)] \\
&= \rho_+^{(e)}(x, t) + \rho_-^{(e)}(x, t),
\end{aligned}
\tag{2.39}
$$

where we have introduced

$$\rho_\eta^{(e)}(x, t) = -\eta \sqrt{\frac{K}{2\pi}} \partial_x \Phi_\eta(x, t) \tag{2.40}$$

and Eqs. (2.20), (2.34) have been used. Thus, the total density has been written as a sum of two chiral operators which describe excitations propagating in opposite directions. The following important relations are also satisfied

$$\rho_\eta^{(e)}(x) = \frac{1 + \eta K}{2} \rho_R^{(e)}(x) + \frac{1 - \eta K}{2} \rho_L^{(e)}(x), \tag{2.41a}$$

$$\rho_r^{(e)}(x) = \frac{\vartheta_r}{K} \left[\frac{1 + \vartheta_r K}{2} \rho_+^{(e)}(x) - \frac{1 - \vartheta_r K}{2} \rho_-^{(e)}(x) \right] \tag{2.41b}$$

and can be obtained directly from Eqs. (2.20), (2.34) and (2.40). While in the non-interacting case $\rho_{R/L}^{(e)}(x) = \rho_\pm^{(e)}(x)$, in the presence of interactions the particle density operator on channel r is a combination of the two chiral densities. This fact already suggests that if a r-branch electron is injected into the system, it will split up into two counterpropagating excitations which, as a consequence, have a fractional charge. This phenomenon is generally referred to as charge fractionalization [134–140] and we are now going to briefly review it.

2.2.4 *Charge fractionalization*

If we denote by $|GS\rangle$ the ground state of the LL, the state obtained by adding an electron at position x_0 in the branch r is $\Psi_r^\dagger(x_0)|GS\rangle$. By exploiting the bosonization identity (2.10), together with Eq. (2.34), the time evolution of the fermionic operator is expressed as

$$\Psi_r^\dagger(x_0, t) = \frac{F_r}{\sqrt{2\pi a}} e^{i\vartheta_r k_F x_0} e^{-i\sqrt{2\pi}[A_+ \Phi_+(x_0 - ut, 0) + A_- \Phi_-(x_0 + ut, 0)]},$$

(2.42)

which clearly shows that the action of $\Psi_r^\dagger(x_0)$ on the ground state results in the creation of two excitations with different chiralities, associated with the action of the bosonic fields $\Phi_\pm(x_0)$.

Further and more precise information can be obtained in the following way [134]. Consider the commutator

$$\left[\rho^{(e)}(x), \Psi_r^\dagger(x_0)\right] = \sum_{r'} \left[:\Psi_{r'}^\dagger(x)\Psi_{r'}(x):, \Psi_r^\dagger(x_0)\right] = \delta(x - x_0)\Psi_r^\dagger(x_0),$$

(2.43)

which is directly obtained from the anticommutation relations (2.6). The above equation is a manifestation of the fact that $\Psi_r^\dagger(x_0)$ indeed creates an electron at position x_0 in the LL. What happens at later times? We can answer the question by looking at the commutator

$$\begin{aligned}
\left[\rho^{(e)}(x, t), \Psi_r^\dagger(x_0, 0)\right] &= \sum_{\eta=\pm} \left[\rho_\eta^{(e)}(x - \eta ut, 0), \Psi_r^\dagger(x_0, 0)\right] \\
&= \sum_{\eta=\pm} \sum_{r'=R,L} \frac{1 + \eta\vartheta_r K}{2} \left[\rho_{r'}(x - \eta ut, 0), \Psi_r^\dagger(x_0, 0)\right] \\
&= \sum_{\eta=\pm} \frac{1 + \eta\vartheta_r K}{2} \delta[(x - x_0) - \eta ut] \Psi_r^\dagger(x_0, 0),
\end{aligned}$$

(2.44)

whose result has been obtained with the help of Eqs. (2.39), (2.41a), (2.43) and by exploiting the chirality of density operators $\rho_\pm^{(e)}(x, t)$. From this result we then come to the following conclusion: the injection of an electron on the branch r creates two excitations moving in opposite directions with respect to the injection point x_0 and bearing a *fraction* of the initial electron charge. Explicitly, the fractionalization factors are given by

$$f_+ = \frac{1 + \vartheta_r K}{2},$$

(2.45a)

$$f_- = \frac{1 - \vartheta_r K}{2}.$$

(2.45b)

Importantly, as clearly emphasized in Ref. [134], these fractional values are not a result of a quantum average, as they come from Eq. (2.44) which is an operator identity.
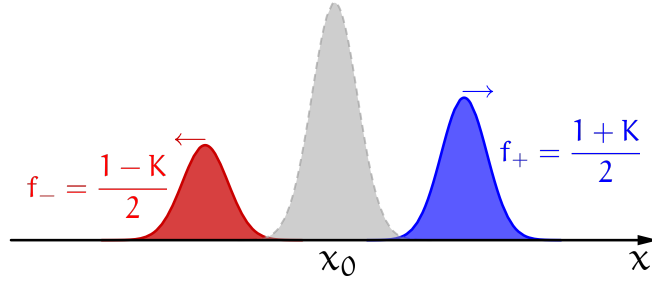
Figure 2.4: Sketch of the charge fractionalization process in a LL. An electron on the R-branch is injected into the LL at position x_0 (grey packet) and splits into two counterpropagating excitations carrying a fraction of its charge (f_+ and f_-, depending on the direction of propagation, as indicated in the picture). The majority of the charge travels to the right for every value of K.

In Fig. 2.4 we sketch the fractionalization process for the injection of an electron on the branch R: a fraction $f_+ = (1 + K)/2$ of the initial charge travels to the right, while a fraction $f_- = (1 - K)/2$ propagates to the left. In the absence of interactions $f_+ = 1$ and $f_- = 0$, as expected because in that case excitations on the R-branch are truly right-moving. Notice also that $f_+ \geqslant 1/2$ and $f_- \leqslant 1/2$ when a R-electron is injected, while the opposite is true if a L-electron is added to the system. Therefore, the majority of the charge always travels in a direction which is in agreement with the "original character" of the injected electron.

ENERGY PARTITIONING   Before closing this Section, we would like to mention that, in LL theory, charge is not the only quantity subject to fractionalization processes. As an example, if we refer again to Fig. 2.4, we can ask how the energy of the injected electron is divided into the two emerging fractional excitations. The answer, first provided in [141], turns out to be non universal and depends also on the detailes of the injection process. In particular, the behavior in the case of a localized injection is quite different from what happens for an extended tunneling. In the first situation, the fraction ε_η of the energy propagating in the η-direction is [141, 142]

$$\varepsilon_\eta = \frac{(1 + \eta K)^2}{2(1 + K^2)},$$ (2.46)

where the injection of a R-electron has been assumed. Since $\varepsilon_+ \geqslant 1/2$, this means that the majority of the energy travels to the right. On the contrary, when a completely non-local injection is considered, it is possible that the energy mainly flows to the left. In [142] we studied the energy partitioning problem by considering the injection of a

single electron from the mesoscopic capacitor into a LL. In particular, we derived the time-resolved profile of energy wave packets and characterized the crossover between the two limiting cases considered in [141] (namely a completely local injection and a fully delocalized one).

2.3   LUTTINGER MODEL FOR COPROPAGATING CHANNELS

In this Section we present the LL theory for describing interactions in copropagating chiral channels. The system we have in mind is sketched in Fig. 2.5(a), representing the IQHE state at filling factor $\nu = 2$. In this state, two Landau levels are filled and, therefore, two channels are present at each edge of the sample. There is only one possible direction of propagation along the edges, which is determined by the sign of the applied orthogonal magnetic field B needed to bring the system in the IQHE regime. Importantly, as discussed in Sec. 1.2.2, the copropagating edge channels are *spatially separated* and thus it perfectly makes sense to talk about inner and outer channels. The theory we are going to present was proposed in Ref. [143] and is a chiral version of the LL we have previously described. However, we prefer to avoid using the term "chiral Luttinger liquid", as this usually refers to Wen's theory [144] for FQHE states in the Laughlin's sequence, which will not be considered in this thesis.

2.3.1   *The model and its diagonalization*

Let us now discuss the model. For the sake of simplicity, here we will just consider a single edge: in particular, we describe the right-moving channels in the upper edge of Fig. 2.5(a). These channels emerge in the system because at filling factor $\nu = 2$ the Fermi energy E_F intersects the Landau levels in two pairs of points, as sketched in Fig. 2.5(b). Here, we have taken the Zeeman coupling into account. Therefore, besides the separation $\hbar\omega_c = \epsilon_{n+1} - \epsilon_n$ between two consecutive Landau levels, the spin degeneracy is lifted and each level ϵ_n is split into two levels $\epsilon_{n,\uparrow}$ and $\epsilon_{n,\downarrow}$, separated by the Zeeman energy $\hbar\omega_Z$. The typical experimental situation is such that $\omega_Z \approx 0.1\omega_c$ [145]: as a result, the two edge channels depicted in Fig. 2.5(a) have opposite spin polarizations, as they come from the two lowest-energy levels $\epsilon_{0,\downarrow}$ and $\epsilon_{0,\uparrow}$, as shown in Fig. 2.5(b). The propagation velocities along the two edge channels are obtained in the usual way

$$
\begin{aligned}
v_1 &= \left.\frac{\partial \epsilon_{0,\downarrow}(k)}{\partial k}\right|_{k=k_{F,\downarrow}}, \\
v_2 &= \left.\frac{\partial \epsilon_{0,\uparrow}(k)}{\partial k}\right|_{k=k_{F,\uparrow}},
\end{aligned}
\tag{2.47}
$$
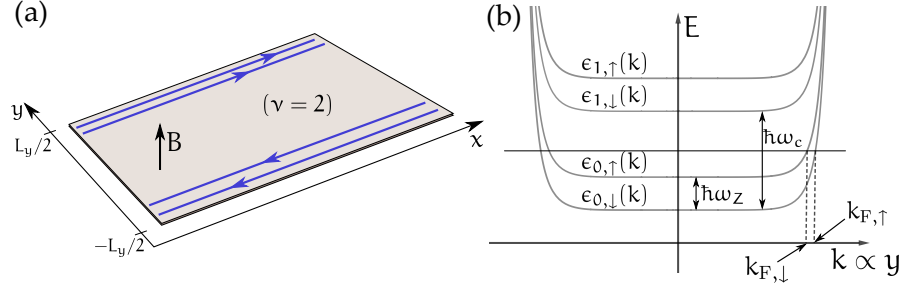
Figure 2.5: The IQHE state at filling factor $\nu = 2$. Panel (a): two chiral edge channels emerge at the edges of the sample, the propagation direction along which is determined by the sign of the applied magnetic field B. Panel (b): energy levels of the system. Each Landau level $\epsilon_n(k)$ is split by the Zeeman coupling which lifts the spin degeneracy by an amount $\hbar\omega_Z$. As a result, the edge modes sketched in (a) have opposite spin polarizations.

where ν_1 (ν_2) refers to the outer (inner) channel and the momenta $k_{F,\downarrow\uparrow}$ are those in correspondence of which the levels $\epsilon_{0,\downarrow\uparrow}$ cross the Fermi energy E_F, as shown in Fig. 2.5(b). These velocities are in general different due to the different slope of the energy levels at the Fermi energy.

The starting point of the model is the linear-dispersion Hamiltonian

$$H_0 = \sum_{\beta=1,2} \nu_\beta \int_{-L/2}^{L/2} dx \; :\Psi_\beta^\dagger(x)(-i\partial_x)\Psi_\beta(x): , \qquad (2.48)$$

where L is the length of the system, the index $\beta = 1$ ($\beta = 2$) labels the outer (inner) channel on the edge and $\Psi_\beta(x)$ is the fermionic field operator annihilating an electron at position x on channel β. Moreover, the velocities ν_β are assumed to be already taking into account possible intra-channel density-density interactions. As a matter of fact, we showed in Sec. 2.2.2 that the intra-channel coupling described by the Hamiltonian (2.23b) simply renormalizes the free propagation velocity. Next, we consider a density-density short-range inter-channel interaction term

$$H_2 = 2\pi V_{12} \int_{-L/2}^{L/2} dx \; :\rho_1^{(e)}(x)\rho_2^{(e)}(x): , \qquad (2.49)$$

where V_{12} is the coupling constant between the two channels and

$$\rho_\beta^{(e)}(x) = :\Psi_\beta^\dagger(x)\Psi_\beta(x): \qquad (2.50)$$

is the particle density operator on channel β. As discussed in the previous Section, bosonic fields $\Phi_\beta(x)$ are introduced via the bosonization identity

$$\Psi_\beta(x) = \frac{F_\beta}{\sqrt{2\pi a}} e^{ik_F x} e^{-i\sqrt{2\pi}\Phi_\beta(x)} \qquad (2.51)$$

where we recall that a is a short-length cutoff and F_β a Klein factor. Bosonic fields can be used to express the particle density operators, which become[6]

$$\rho_\beta^{(e)}(x) = -\frac{1}{\sqrt{2\pi}}\, \partial_x \Phi_\beta(x)\,. \tag{2.52}$$

If we compare this expression with Eq. (2.20), we notice that here the sign is the same for both channels $\beta = 1, 2$, while a sign difference was present in the former case. This is because now we are dealing with copropagating channels and not counterpropagating ones. This difference is also reflected in the commutator

$$\left[\Phi_\beta(x), \Phi_{\beta'}(x')\right] = \frac{i}{2}\, \delta_{\beta,\beta'} \mathrm{sgn}(x - x')\,, \tag{2.53}$$

where, again, the sign of the r.h.s. is the same for both values of β, unlike in (2.14).

The bosonized version of the full Hamiltonian $H = H_0 + H_2$ reads

$$H = \frac{1}{2}\int_{-L/2}^{L/2} dx\; :\!\begin{pmatrix} \partial_x \Phi_1(x) & \partial_x \Phi_2(x) \end{pmatrix} \begin{pmatrix} v_1 & V_{12} \\ V_{12} & v_2 \end{pmatrix} \begin{pmatrix} \partial_x \Phi_1(x) \\ \partial_x \Phi_2(x) \end{pmatrix}\!:\,, \tag{2.54}$$

where the off-diagonal terms are obtained directly by substituting (2.52) into (2.49), while the diagonal ones follow from the bosonized form (2.21) discussed in the previous Section. The Hamiltonian can be straightforwardly diagonalized by the following transformation

$$\begin{pmatrix} \Phi_1(x) \\ \Phi_2(x) \end{pmatrix} = \begin{pmatrix} \cos\chi & -\sin\chi \\ \sin\chi & \cos\chi \end{pmatrix} \begin{pmatrix} \Phi_+(x) \\ \Phi_-(x) \end{pmatrix}\,, \tag{2.55a}$$

$$\begin{pmatrix} \Phi_+(x) \\ \Phi_-(x) \end{pmatrix} = \begin{pmatrix} \cos\chi & \sin\chi \\ -\sin\chi & \cos\chi \end{pmatrix} \begin{pmatrix} \Phi_1(x) \\ \Phi_2(x) \end{pmatrix}\,, \tag{2.55b}$$

which introduces two new bosonic fields $\Phi_\pm(x)$ satisfying the commutation relations

$$\left[\Phi_\eta(x), \Phi_{\eta'}(x')\right] = \frac{i}{2}\, \delta_{\eta,\eta'} \mathrm{sgn}(x - x') \qquad (\eta = \pm)\,. \tag{2.56}$$

Notice that the transformation (2.55) is different from (2.27) and is parametrized by trigonometric functions instead of hyperbolic ones. This is because here we are dealing with copropagating channels and the transformation must preserve the commutation relations (2.53) instead of (2.14). The parameter χ is called the *mixing angle* and it is determined by the requirement that the Hamiltonian be diagonal in the basis of the new fields. This leads to the equation

$$\tan 2\chi = \frac{2V_{12}}{v_1 - v_2}\,. \tag{2.57}$$

---

6 Zero modes are neglected in this Section.

The mixing angle ranges in $\chi \in [0, \pi/2]$; in the non-interacting case $\chi = 0$ and $\Phi_{1,2}(x) = \Phi_{\pm}(x)$ so the two edge channels do not mix, as expected. On the contrary, the maximal mixing is achieved at $\theta = \pi/4$, which is usually referred to as the "strongly interacting" limit and seems to be the relevant case in different experimental implementations [3, 26, 114]. Notice, however, that Eq. (2.57) indicates that this situation can be achieved for any finite value of the inter-channel coupling V_{12}, provided that the difference $v_1 - v_2$ is small enough.

The Hamiltonian in diagonal form reads

$$H = \frac{1}{2} \sum_{\eta=\pm} v_\eta \int_{-L/2}^{L/2} dx \; :[\partial_x \Phi_\eta(x)]^2:, \tag{2.58}$$

where the renormalized velocities are given by

$$v_\pm = \frac{v_1 + v_2}{2} \pm \frac{v_1 - v_2}{2 \cos 2\chi} = \frac{v_1 + v_2}{2} \pm \frac{V_{12}}{\sin 2\chi}$$
$$= \frac{1}{2} \left[v_1 + v_2 \pm \sqrt{(v_1 - v_2)^2 + 4V_{12}^2} \right]. \tag{2.59}$$

Here $v_+ > v_-$, so the Hamiltonian (2.58) describes slow and fast bosonic modes, propagating at velocities v_- and v_+ respectively. Moreover, from the chirality of the system, we have the constraint $v_\pm > 0$ as all excitations must propagate in the right direction. This gives the following bound on the inter-channel coupling strength [146]

$$V_{12} \leqslant \sqrt{v_1 v_2}. \tag{2.60}$$

This relation further strengthen the previous comment about the "strongly interacting" limit ($\chi = \pi/4$): it is a situation which cannot arise from an arbitrarily strong inter-channel interaction and, for this reason, we prefer to refer to it as maximal mixing.

2.3.2 *Charge fractionalization*

Just like in the spinless LL described in Sec. 2.2, charge fractionalization is also predicted to occur in copropagating channels as an interaction effect [147–149]. In order to see how this happens, we follow the same reasoning as in Sec. 2.2.4. Suppose that an electron is injected into the outer channel ($\beta = 1$) at position x_0. This is described by the action of the operator $\Psi_1^\dagger(x_0)$, which indeed satisfies the commutators

$$\left[\rho_1^{(e)}(x), \Psi_1^\dagger(x_0) \right] = \delta(x - x_0)\Psi_1^\dagger(x_0),$$
$$\left[\rho_2^{(e)}(x), \Psi_1^\dagger(x_0) \right] = 0. \tag{2.61}$$

In order to understand what happens at later times, one has to calculate again the above commutators with the time-evolved operators

$\rho_{1,2}^{(e)}(x,t)$. The latter can be simply evaluated by relying on the fact that the transformation (2.55) implies

$$\begin{pmatrix} \rho_1^{(e)}(x) \\ \rho_2^{(e)}(x) \end{pmatrix} = \begin{pmatrix} \cos\chi & -\sin\chi \\ \sin\chi & \cos\chi \end{pmatrix} \begin{pmatrix} \rho_+^{(e)}(x) \\ \rho_-^{(e)}(x) \end{pmatrix}, \tag{2.62a}$$

$$\begin{pmatrix} \rho_+^{(e)}(x) \\ \rho_-^{(e)}(x) \end{pmatrix} = \begin{pmatrix} \cos\chi & \sin\chi \\ -\sin\chi & \cos\chi \end{pmatrix} \begin{pmatrix} \rho_1^{(e)}(x) \\ \rho_2^{(e)}(x) \end{pmatrix}, \tag{2.62b}$$

where we defined

$$\rho_\eta^{(e)}(x) = -\frac{1}{\sqrt{2\pi}} \partial_x \Phi_\eta(x). \tag{2.63}$$

Now, bosonic operators $\Phi_\eta(x)$ have a simple time evolution as their Heisenberg's equations of motion, deduced from Eq. (2.58), read

$$(\partial_t + v_\eta \partial_x)\Phi_\eta(x,t) = 0 \tag{2.64}$$

and are solved by

$$\Phi_\eta(x,t) = \Phi_\eta(x - v_\eta t, 0) = \Phi_\eta\left(0, t - \frac{x}{v_\eta}\right). \tag{2.65}$$

As a consequence, $\rho_\eta^{(e)}(x,t) = \rho_\eta^{(e)}(x - v_\eta t, 0)$. Therefore we can easily calculate the commutators

$$\mathscr{C}_\beta \equiv \left[\rho_\beta^{(e)}(x,t), \Psi_1^\dagger(x_0,0)\right], \tag{2.66}$$

with $\beta = 1,2$. By repeatedly using Eq. (2.62) we find

$$\begin{aligned} \mathscr{C}_1 &= \cos\chi \left[\rho_+^{(e)}(x - v_+ t, 0), \Psi_1^\dagger(x_0,0)\right] \\ &\quad - \sin\chi \left[\rho_-^{(e)}(x - v_- t, 0), \Psi_1^\dagger(x_0,0)\right] \\ &= \cos^2\chi \left[\rho_1^{(e)}(x - v_+ t, 0), \Psi_1^\dagger(x_0,0)\right] \\ &\quad + \sin^2\chi \left[\rho_1^{(e)}(x - v_- t, 0), \Psi_1^\dagger(x_0,0)\right] \\ &= \left\{\cos^2\chi\, \delta[(x - x_0) - v_+ t] + \sin^2\chi\, \delta[(x - x_0) - v_- t]\right\} \Psi_1^\dagger(x_0,0) \end{aligned} \tag{2.67}$$

and, in the same way,

$$\mathscr{C}_2 = \frac{\sin 2\chi}{2}\left\{\delta[(x - x_0) - v_+ t] - \delta[(x - x_0) - v_- t]\right\}\Psi_1^\dagger(x_0,0). \tag{2.68}$$

The meaning of these commutators is that two different excitations propagating at different velocities emerge on both the outer and the inner channel. Once again, they carry a fraction of the initial electron charge, which can be read directly from the above equations:

$$\begin{aligned} f_{1,-} &= \sin^2\chi, & f_{1,+} &= \cos^2\chi, \\ f_{2,-} &= -\frac{\sin 2\chi}{2}, & f_{2,+} &= \frac{\sin 2\chi}{2}. \end{aligned} \tag{2.69}$$
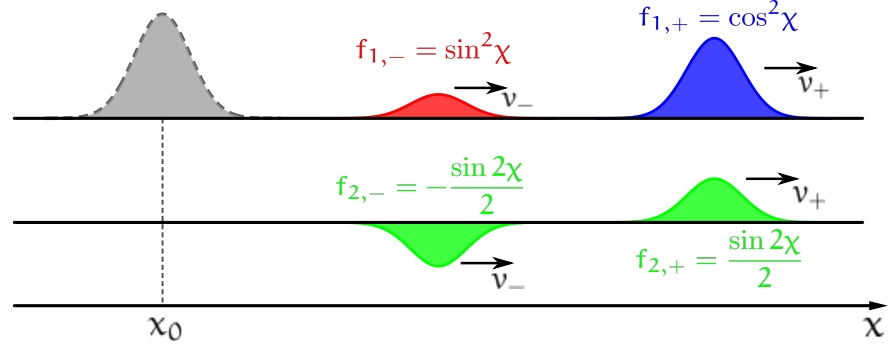
Figure 2.6: Charge fractionalization in copropagating channels. An electron injected into the outer channel at position x_0 splits into fractional excitations, propagating in the same direction (due to the chirality of the system) but with different velocities.

Here, $f_{\beta,\eta}$ denotes the fraction carried by the excitation propagating at velocity v_η on channel β. The above equations correctly reproduce the non-interacting limit when $\chi = 0$, in which case we have $f_{1,+} = 1$ and $f_{1,-} = f_{2,\pm} = 0$, as expected because the channels are decoupled. In Fig. 2.6 we have sketched the fractionalization process just described. It is worth noting that $f_{1,-} + f_{1,+} = 1$ for every value of the mixing angle. This is of course due to charge conservation, because these excitations originate from the electron injected at $x = x_0$. Likewise, $f_{2,+} = -f_{2,-}$, meaning that no net charge is transferred from the outer to the inner channel. Indeed, the two channels are capacitively coupled via Coulomb interactions, which cannot lead to a variation of the particle number on each channel.

We also note that at maximal mixing ($\chi = \pi/4$) the injected electron splits into two identical excitations as the fractionalization factors for the outer channel reduce to $f_{1,+} = f_{1,-} = 1/2$. Moreover, the situation is the same also on the inner channel: $f_{2,\pm} = \pm 1/2$. As a consequence, the mode made of the two fast excitations (those propagating with velocity v_+) has exactly the same charge as the injected electron, while the slow mode (made of the two excitations propagating at v_-) carries no charge on the whole. This is why in the literature it is common to encounter the terms "charged" and "neutral modes" [23] associated with fractionalization in integer quantum Hall channels: they refer precisely at the scenario depicted in Fig. 2.6 at the mixing angle $\chi = \pi/4$. Last, but not least, evidence for the presence of fractional charges in copropagating quantum Hall channels has been recently reported by different groups [23, 26, 150, 151], demonstrating that the LL theory for copropagating quantum Hall edge states is successful in explaining experimental results [152]. In addition, a behavior consistent with the LL model was also observed in very recent measurements of non-equilibrium energy distributions [153].

SINGLE-ELECTRON EXCITATIONS IN COPROPAGATING INTERACTING CHANNELS

In this Chapter we address the problem of generating single-electron excitations in the IQHE regime at filling factor $\nu = 2$, in the presence of interactions between the two copropagating edge channels. We consider the case in which excitations are created by means of a voltage pulse. Based on what we discussed in Sec. 2.3.2, we expect these excitations to undergo a fractionalization process, which we are going to show explicitly by calculating the charge density in the presence of the drive. We also go beyond this picture, by analyzing the fractional excitations in momentum space and discussing their particle-hole content. We also obtain complementary information by addressing the time evolution of the Wigner function. Finally, we consider a QPC geometry and demonstrate that it is possible to extract the mixing angle characterizing the interaction between the edge channels from noise measurements. The material presented in this Chapter includes our original findings discussed in Refs. [29, 30].

3.1 MODEL AND EQUATIONS OF MOTION

We consider a quantum Hall bar at filling factor $\nu = 2$, as sketched in Fig. 3.1. The system is described according to the LL model for copropagating channels presented in the previous Chapter. Here, due to the geometry of the bar, there is an additional edge that has to be taken into account. As a result, the Hamiltonian we are going to use is composed of two copies of the single-edge Hamiltonian discussed in Sec. 2.3.1. In particular

$$H_0 = \sum_{r=R,L} \sum_{\beta=1,2} v_\beta \int_{-\infty}^{+\infty} dx \; :\Psi_{r,\beta}^\dagger(x)(-i\partial_x)\Psi_{r,\beta}(x): \qquad (3.1)$$

is the free part and[1]

$$H_2 = 2\pi V_{12} \sum_{r=R,L} \int_{-\infty}^{+\infty} dx \; :\rho_{r,1}^{(e)}(x)\rho_{r,2}^{(e)}(x): \qquad (3.2)$$

is the interaction term. In these expressions, the index $r = R$ ($r = L$) refers to the right-moving (left-moving) channels on the upper (lower) edge, while the index $\beta = 1$ ($\beta = 2$) labels the outer (inner) channel on each edge. As we have seen in Sec. 2.3.1, by using the

---

[1] The notation H_2 for inter-channel interactions is the same as in Chapter 2.
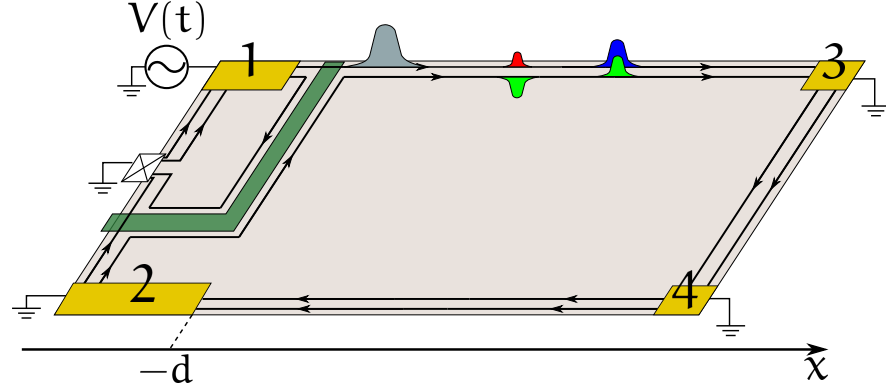
Figure 3.1: Sketch of the setup: a quantum Hall bar at filling factor $\nu = 2$ is coupled to a voltage pulse source $V(t)$, creating excitations at terminal 1. By means of a tunable gate, only outer channel excitations are actually transferred at $x = -d$ (grey pulse). Due to interactions, the original pulse is split into fractional excitations (blue, red and green pulses).

bosonization identity it is possible to introduce bosonic fields $\Phi_{r,\beta}(x)$ and subsequently diagonalize the Hamiltonian, which becomes

$$H_0 + H_2 = \frac{1}{2} \sum_{r=R,L} \sum_{\eta=\pm} v_\eta \int_{-\infty}^{+\infty} dx \, :[\partial_x \Phi_{r,\eta}(x)]^2:, \tag{3.3}$$

where $\Phi_{r,\eta}(x)$ are the bosonic fields related to the original ones by the transformation (2.55):

$$\begin{pmatrix} \Phi_{r,+}(x) \\ \Phi_{r,-}(x) \end{pmatrix} = \begin{pmatrix} \cos\chi & \sin\chi \\ -\sin\chi & \cos\chi \end{pmatrix} \begin{pmatrix} \Phi_{r,1}(x) \\ \Phi_{r,2}(x) \end{pmatrix}, \tag{3.4}$$

χ being the mixing angle.

Next, we want to describe a voltage-pulse-generated excitation on the upper-edge outer channel. In the case of a mesoscopic capacitor, this would have been the natural scenario, since the quantum dot used for injecting the electron would have been coupled to the outer channel (see, e. g., the setup in Fig. 1.7a). Here, the situation is a bit trickier as there is no particular reason why a voltage drive would be selectively coupled only to one channel. It is possible to circumvent this problem by considering the additional presence of a gate (green part of Fig. 3.1) acting as a filter right after terminal 1, in the same spirit of what was implemented in Ref. [151]. By acting on the gate, only the excitation created on the outer channel is transmitted at $x = -d$. Therefore, in the described situation, everything goes as if the drive $V(t)$ was only coupled to the outer channel. Thus, we introduce the Hamiltonian

$$H_g = -e \int_{-\infty}^{+\infty} dx \, U(x,t) \rho_{R,1}^{(e)}(x), \tag{3.5}$$

with

$$U(x,t) = \Theta(-x-d)V(t) \tag{3.6}$$

and, as usual, $\rho_{R,1}^{(e)}(x)$ denotes the particle density operator on channel 1 and edge R. By writing this operator in terms of the bosonic field $\Phi_{R,1}(x)$ with the help of Eq. (2.52) and subsequently using the inverse of the transformation (3.4), the full Hamiltonian $H = H_0 + H_2 + H_g$ can be expressed in terms of the chiral fields $\Phi_{r,\eta}(x)$:

$$H = \frac{1}{2} \sum_{r=R,L} \sum_{\eta=\pm} v_\eta \int_{-\infty}^{+\infty} dx \; :[\partial_x \Phi_{r,\eta}(x)]^2:$$
$$+ \frac{e}{\sqrt{2\pi}} \int_{-\infty}^{+\infty} dx \, U(x,t) \left[\cos\chi \, \partial_x \Phi_{R,+}(x) - \sin\chi \, \partial_x \Phi_{R,-}(x)\right]. \tag{3.7}$$

Starting from this Hamiltonian, we solve the equations of motion for $\phi_{r,\eta}$ and obtain their time evolution, which reads (see App. A.2)

$$\Phi_{R,+}(x,t) = \phi_{R,+}(x-v_+t,0) - \frac{e\cos\chi}{\sqrt{2\pi}} \int_{-\infty}^{t} dt' \, U(x-v_+(t-t'),t'),$$

$$\Phi_{R,-}(x,t) = \phi_{R,-}(x-v_-t,0) + \frac{e\sin\chi}{\sqrt{2\pi}} \int_{-\infty}^{t} dt' \, U(x-v_-(t-t'),t'),$$

$$\Phi_{L,+}(x,t) = \phi_{L,+}(x-v_+t,0),$$

$$\Phi_{L,-}(x,t) = \phi_{L,-}(x-v_-t,0). \tag{3.8}$$

Here, low-case fields denote the free time evolution in the absence of the drive. Notice that L-fields evolve freely, since $V(t)$ acts only on the upper edge and thus the lower one is at equilibrium. Finally, the bosonization identity (2.51) allows us to express the time evolution of fermionic fields as (we set $k_F = 0$)

$$\Psi_{R,1}(x,t) = \psi_{R,1}(x,t)e^{ie\left[\cos^2\chi \, \varphi_+(x,t)+\sin^2\chi \, \varphi_-(x,t)\right]},$$

$$\Psi_{R,2}(x,t) = \psi_{R,2}(x,t)e^{ie\sin\chi\cos\chi\left[\varphi_+(x,t)-\varphi_-(x,t)\right]},$$

$$\Psi_{L,1}(x,t) = \psi_{L,1}(x,t),$$

$$\Psi_{L,2}(x,t) = \psi_{L,2}(x,t), \tag{3.9}$$

where we have defined the functions

$$\varphi_\pm(x,t) = \int_{-\infty}^{t} dt' \, U(x-v_\pm(t-t'),t') \tag{3.10}$$

and, once again, $\psi_{r,\beta}(x,t)$ denotes the time evolution with respect to the Hamiltonian $H_0 + H_2$.

At this point, the dynamics of the system is completely determined by the above results, which allow us to calculate any expectation value we are interested in. Recall that, since we adopt the Heisenberg

picture, such quantum averages are calculated with respect to the time-independent equilibrium density matrix at $t = -\infty$, which stems from the Hamiltonian $H_0 + H_2$. We will denote these averages with $\langle \ldots \rangle$ and omit the standard subscript 0 on the average symbol, because we will only compute expectation values with respect to the equilibrium density matrix and thus there is no ambiguity. In what follows we are going to study different quantities in order to characterize the wave packets excited by the drive.

3.2 CHARGE DENSITY

The simplest observable to address is the charge density, because it can be computed with little effort. The first thing to do is to evaluate the time evolution of particle density operators, which is easily done by using the inverse of (3.4):

$$
\rho_{r,1}^{(e)}(x,t) = -\frac{\vartheta_r}{\sqrt{2\pi}} \partial_x \Phi_{r,1}(x,t)
$$
$$
= -\frac{\vartheta_r}{\sqrt{2\pi}} \left[\cos\chi \, \partial_x \Phi_{r,+}(x - \vartheta_r v_+ t, 0) - \sin\chi \, \partial_x \Phi_{r,-}(x - \vartheta_r v_- t, 0) \right],
$$
(3.11a)

$$
\rho_{r,2}^{(e)}(x,t) = -\frac{\vartheta_r}{\sqrt{2\pi}} \partial_x \Phi_{r,2}(x,t)
$$
$$
= -\frac{\vartheta_r}{\sqrt{2\pi}} \left[\sin\chi \, \partial_x \Phi_{r,+}(x - \vartheta_r v_+ t, 0) + \cos\chi \, \partial_x \Phi_{r,-}(x - \vartheta_r v_- t, 0) \right].
$$
(3.11b)

Starting from these expressions, it is also immediate to write down the charge current densities $J_{r,\beta}(x,t)$, which are determined by the continuity equations

$$
-e\partial_t \rho_{r,\beta}^{(e)}(x,t) + \partial_x J_{r,\beta}(x,t) = 0
$$
(3.12)

and we report here for a later use:

$$
J_{r,1}(x,t) = \frac{e}{\sqrt{2\pi}} \left[v_+ \cos\chi \, \partial_x \Phi_{r,+}(x - \vartheta_r v_+ t, 0) \right.
$$
$$
\left. - v_- \sin\chi \, \partial_x \Phi_{r,-}(x - \vartheta_r v_- t, 0) \right],
$$
(3.13a)
$$
J_{r,2}(x,t) = \frac{e}{\sqrt{2\pi}} \left[v_+ \sin\chi \, \partial_x \Phi_{r,+}(x - \vartheta_r v_+ t, 0) \right.
$$
$$
\left. + v_- \cos\chi \, \partial_x \Phi_{r,-}(x - \vartheta_r v_- t, 0) \right].
$$
(3.13b)

Coming now back to the particle density, since we are interested in the non-equilibrium effects due to the drive $V(t)$, we define the *excess* density by subtracting the equilibrium contribution:

$$
\Delta\rho_{r,\beta}^{(e)}(x,t) = -\frac{\vartheta_r}{\sqrt{2\pi}} \left(\langle \partial_x \Phi_{r,\beta}(x,t) \rangle - \langle \partial_x \phi_{r,\beta}(x,t) \rangle \right).
$$
(3.14)

Given the solution in Eq. (3.8), the equilibrium terms cancel and the particle density is expressed as a combination of derivatives of the functions defined in Eq. (3.10). By expliciting the form of $U(x,t)$ according to (3.6) and recalling that the excess charge densities are

$$\Delta\rho_{r,\beta}(x,t) = -e\Delta\rho_{r,\beta}^{(e)}(x,t), \tag{3.15}$$

we readily arrive this result for the upper-edge excitations:

$$\Delta\rho_{R,1}(x,t) = \frac{e^2}{2\pi}\Theta(x+d)\left[\frac{\cos^2\chi}{v_+}V\left(t_+ - \frac{d}{v_+}\right) + \frac{\sin^2\chi}{v_-}V\left(t_- - \frac{d}{v_-}\right)\right] \tag{3.16a}$$

$$\Delta\rho_{R,2}(x,t) = \frac{e^2\sin 2\chi}{4\pi}\Theta(x+d)\left[\frac{1}{v_+}V\left(t_+ - \frac{d}{v_+}\right) - \frac{1}{v_-}V\left(t_- - \frac{d}{v_-}\right)\right] \tag{3.16b}$$

having defined the chiral combinations $t_\pm = t - x/v_\pm$. Concerning the lower edge, it is immediate to see that $\Delta\rho_{L,\beta}(x,t) = 0$, meaning that no excitation with respect to equilibrium is present. In the same way we can obtain the excess charge currents, which read

$$\Delta J_{R,1}(x,t) = \frac{e^2}{2\pi}\Theta(x+d)\left[\cos^2\chi V\left(t_+ - \frac{d}{v_+}\right) + \sin^2\chi V\left(t_- - \frac{d}{v_-}\right)\right], \tag{3.17a}$$

$$\Delta J_{R,2}(x,t) = \frac{e^2\sin 2\chi}{4\pi}\Theta(x+d)\left[V\left(t_+ - \frac{d}{v_+}\right) - V\left(t_- - \frac{d}{v_-}\right)\right], \tag{3.17b}$$

while the lower-edge excess currents vanish. Both results (3.16) and (3.17) describe a situation which is fully consistent with the charge fractionalization phenomenon we have described in Sec. 2.3.2 and sketched in Fig. 2.6: two excitations propagating at different velocities emerge on each upper-edge channel. Moreover, they are weighted with the fractionalization factors we derived in (2.69), as it should be. Finally, the excess particle densities and currents are nonvanishing only for $x > -d$, which is due to the chirality of the system, and retain the same shape of the drive $V(t)$, thanks to the linear dispersion.

Before proceeding further, we give in Fig. 3.2 an illustrative example of Eqs. (3.16) and (3.17). We consider a single-pulse Gaussian drive

$$V(t) = -V_0\, e^{-t^2/w^2}, \tag{3.18}$$

where V_0 is a positive amplitude and w parametrizes the width of the Gaussian. Let us focus at the moment on the outer channel. In Fig. 3.2a we plot the excess particle density as a function of position and at different times. In the four snapshots we can observe how the wave packets start to form and progressively separate from each other during the propagation along the channel due to their different
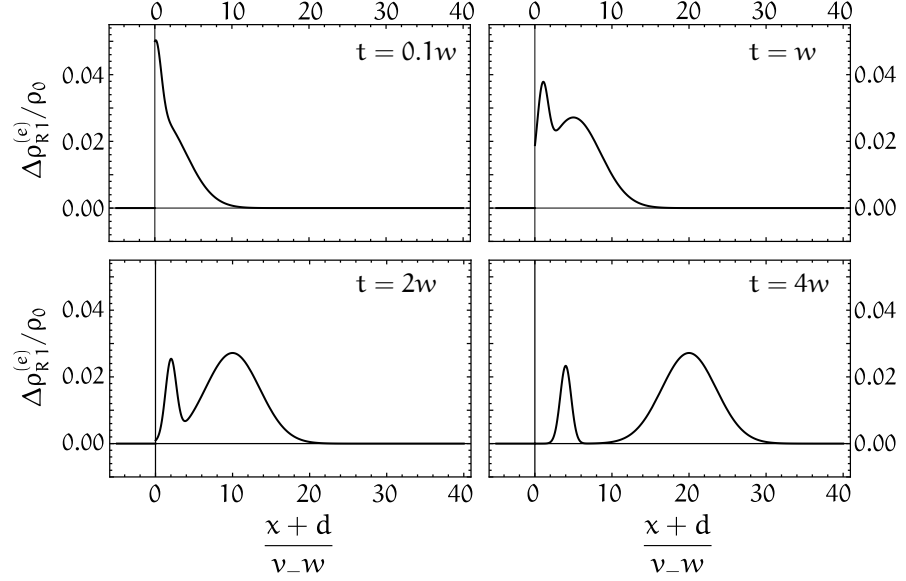
(a) Real-space time evolution of the outer-channel excess particle density, in units of $\rho_0 = eV_0/v_-$, for the Gaussian drive (3.18). The different panels are snapshots referring to the time indicated in the embedded labels. From these plots we clearly observe the phase where the wave packets are created, followed by the separation due to the different velocities along the edge.
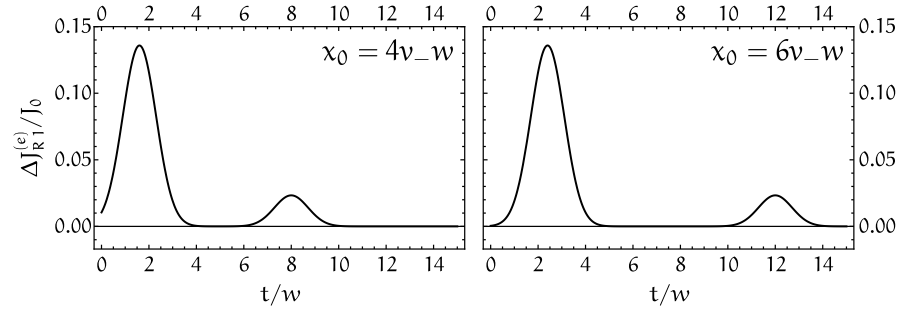
(b) Time resolved excess particle current on the outer channel, in units of $J_0 = eV_0$, for the Gaussian drive (3.18). Different panels refer to the detection point x_0 specified in the embedded labels. The bigger pulse observed at earlier times corresponds to the fast excitation and is followed by a smaller signal associated with the slow one. The ratio of the peaks height is determined by $\tan^2\chi$. The farther the detection point, the larger the time interval between the arrival of the two current pulses.

Figure 3.2: Excess particle density and current on the outer channel. In all plots we set $\chi = \pi/8$ and $v_+ = 5v_-$.

velocities. A similar process happens on the inner channel, where two wave packets with opposite sign are excited. The plots are obtained for a mixing angle $\chi = \pi/8$ and a velocity ratio $v_+/v_- = 5$. The different spatial extension of the two wave packets is a consequence of the terms $x/v_\pm$ entering the expression (3.16a) and the relative height of the two pulses is influenced not only by the fractionalization factors $\cos^2\chi$ and $\sin^2\chi$, but also by the presence of $v_\pm^{-1}$ multiplying $V(t)$.

In Fig. 3.2b we look instead at the excess particle current (i. e. the charge current divided by the electron charge $-e$) as a function of time, for two different detection points x_0 which must be located away enough from the point $x = -d$ where excitations are generated. Differently from what is observed in Fig. 3.2a, here the temporal extension of the two pulses is the same, because no velocity factor multiplies the variable t in (3.17a). Likewise, the relative height of the pulses is simply determined by the fractionalization factors. Moreover, since the faster pulse arrives first at the detection point, a bigger spike is observed in the current, followed by a lower one related to the slower excitation. Finally, the time at which the peaks are observed clearly depends on the distance between the injection point $x = -d$ and the detection point $x = x_0$.

What is the excited charge on each channel? As the above example should help visualize, there are two equivalent ways of computing this quantity. The first is to integrate the charge density at time t over all space. The second is to integrate the charge current detected at a given point x_0 over time, from $-\infty$ to t. In either way we find

$$
\begin{aligned}
\mathcal{C}_1(t) &= \int_{-\infty}^{+\infty} dx\, \Delta\rho_{R,1}(x,t) = \frac{e^2}{2\pi} \int_{-\infty}^{t} d\tau\, V(\tau)\,, \\
\mathcal{C}_2(t) &= \int_{-\infty}^{+\infty} dx\, \Delta\rho_{R,2}(x,t) = 0\,.
\end{aligned}
\tag{3.19}
$$

If we wait until the injection is over[2], which in practice means $t \gg w$, with w the typical time scale of the drive $V(t)$, we obtain the total excited charge

$$
\mathcal{C}_1 = \lim_{t\to\infty} \mathcal{C}_1(t) = \frac{e^2}{2\pi} \int_{-\infty}^{+\infty} d\tau\, V(\tau)\,.
\tag{3.20}
$$

By introducing the parameter

$$
q = -\frac{e}{2\pi} \int_{-\infty}^{+\infty} dt\, V(t)\,,
\tag{3.21}
$$

we clearly have $\mathcal{C}_1 = -eq$. This parameter then represents the number of electronic charges injected into the system by the drive $V(t)$. Even if q is a number, with a little abuse of language it is customary to refer

---

2 Of course this is not possible if the drive is periodic, in which case the meaningful quantity to define is the charge per period. We will deal with this situation later in the Chapter.

to it also as a charge, by meaning a charge in units of $-e$. The number of charges $q_{\beta,\pm}$ carried by the fractionalized pulse moving at velocity $v_\pm$ on channel β is expressed in terms of q as

$$q_{1,-} = q\sin^2\chi, \qquad q_{1,+} = q\cos^2\chi,$$
$$q_{2,-} = -q\frac{\sin 2\chi}{2}, \qquad q_{2,+} = q\frac{\sin 2\chi}{2}. \qquad (3.22)$$

These expressions can be easily derived by integrating over space the terms in the charge density (3.16) associated with the different excitations.

The above description of fractionalization relies on integrated quantities and, as such, does not give any information on the detailed structure of the excitations. In particular, it is not sensitive to their particle-hole content. In order to investigate these features, we have to go beyond the charge density and consider correlations in space or time, which are encoded in the coherence functions. In particular, we are going to investigate the non-equilibrium momentum distribution and the Wigner function, through which a microscopic investigation of the interplay between non-equilibrium dynamics and interaction effects can be performed. In the following two Sections, we will consider only the dynamics of the upper edge, where the voltage is applied and excitations are generated. We therefore fix the edge index to $r = R$ and drop it for notational convenience.

3.3 MOMENTUM DISTRIBUTION

The excess momentum distribution on channel β is defined as

$$\Delta n_\beta(k, t) = \left\langle c_\beta^\dagger(k, t)c_\beta(k, t) \right\rangle - n_\beta^{(0)}(k), \qquad (3.23)$$

with $n_\beta^{(0)}(k)$ the stationary equilibrium distribution and $c_\beta(k)$ the operator annihilating an electron with momentum k on channel β. Just as happens for the particle current, also this observable can be expressed in terms of the coherence functions defined in Eqs. (1.49) and (1.50). In particular (we set $k_F = 0$)

$$\Delta n_\beta(k, t) = \frac{1}{2\pi} \int_{-\infty}^{+\infty} dx \int_{-\infty}^{+\infty} d\xi\, e^{-ik\xi} \Delta \mathcal{G}_\beta^< \left(x + \frac{\xi}{2}, x - \frac{\xi}{2}; t, t \right). \qquad (3.24)$$

Thus, the momentum distribution is linked to spatial correlations at different points. It is important to remark that, in general, it has a non-trivial time dependence, due to the fact that $V(t)$ drives the system out of equilibrium. Moreover, since $\Delta n_\beta(k, t)$ is defined as a *variation* with respect to equilibrium, positive values in the excess momentum distribution indicate the presence of additional electronic excitations in the system. Conversely, negative values are a signature of a reduced number of electrons and are thus associated with the presence of holes.

The calculation of the excess coherence function appearing in (3.24) relies on bosonization techniques: by using the results (3.9) and (3.10) in order to express the time evolution of fermionic fields we find

$$\Delta \mathcal{G}_1^< \left(x + \frac{\xi}{2}, x - \frac{\xi}{2}; t, t \right) = \frac{e^{2\pi[\cos^2\chi \, G_+(-\xi) + \sin^2\chi \, G_-(-\xi)]}}{2\pi a}$$
$$\times \left\{ \exp\left[-ie \left(\cos^2\chi \, \Delta\varphi_+(x, \xi; t) + \cos^2\chi \, \Delta\varphi_-(x, \xi; t) \right) + \right] - 1 \right\},$$
$$(3.25a)$$

$$\Delta \mathcal{G}_2^< \left(x + \frac{\xi}{2}, x - \frac{\xi}{2}; t, t \right) = \frac{e^{2\pi[\sin^2\chi \, G_+(-\xi) + \cos^2\chi \, G_-(-\xi)]}}{2\pi a}$$
$$\times \left\{ \exp\left[-ie \cos\chi \sin\chi \left(\Delta\varphi_+(x, \xi; t) + \Delta\varphi_-(x, \xi; t) \right) + \right] - 1 \right\},$$
$$(3.25b)$$

where we have defined the differences

$$\Delta\varphi_\pm(x, \xi; t) = \varphi_\pm \left(x - \frac{\xi}{2}, t \right) - \varphi_\pm \left(x + \frac{\xi}{2}, t \right) \tag{3.26}$$

with $\varphi_\pm(x, t)$ given in Eq. (3.10). Moreover, we also introduced the equilibrium bosonic Green functions

$$G_\pm(x) = \langle \phi_\pm(x, 0)\phi_\pm(0, 0) \rangle - \langle \phi_\pm^2(0, 0) \rangle, \tag{3.27}$$

which are calculated in App. D and read [cf. Eq. (D.23)]

$$G_\pm(x) = \frac{1}{2\pi} \ln \left[\frac{a}{a - ix} \frac{\pi k_B \theta x / v_\pm}{\sinh(\pi k_B \theta x / v_\pm)} \right], \tag{3.28}$$

where θ is the temperature of the edge channels. The above results are completely general and allows us to calculate the momentum distribution for any drive $V(t)$. However, we are particularly interested in the Lorentzian drive, in order to investigate how Levitons are affected by interactions. Therefore, in the following we are mainly going to consider

$$V(t) = -\frac{q}{e} \frac{2w}{w^2 + t^2}, \tag{3.29}$$

where w parametrizes the width of the pulse. As we have seen in Sec. 1.4, when q is a positive (negative) integer, this drive generates pure electron-like (hole-like) excitations in non-interacting systems [5–8]. The evaluation of coherence functions (3.25) in the presence of the drive (3.29) leads to

$$\Delta \mathcal{G}_\beta^< \left(x + \frac{\xi}{2}, x - \frac{\xi}{2}; t, t \right) = \frac{1}{2\pi i \xi} \prod_{\eta = \pm} \left[\frac{\pi k_B \theta \xi / v_\eta}{\sinh(\pi k_B \theta \xi / v_\eta)} \right]^{\zeta_{\beta,\eta}}$$
$$\times \left\{ \prod_{\eta = \pm} \prod_{\varepsilon = \pm} \left[\frac{i v_\eta w - \varepsilon (v_\eta t_\eta + \varepsilon \xi / 2)}{i v_\eta w + \varepsilon (v_\eta t_\eta + \varepsilon \xi / 2)} \right]^{q_{\beta,\eta}} - 1 \right\},$$
$$(3.30)$$

with $q_{\beta,\eta}$ given in (3.22), $t_\eta = t - x/v_\eta$, $\zeta_{1,+} = \zeta_{2,-} = \cos^2\chi$ and $\zeta_{1,-} = \zeta_{2,+} = \sin^2\chi$. In obtaining this expression, the approximation $t \gtrsim w$ was used. This means that we wait until the injection process is over. We are now going to consider two different regimes.

3.3.1   *Regime of full spatial separation*

As we have seen in Sec. 3.2, the pulses excited on the edge channels become more and more spatially separated as they propagate along the edge, due to the fact that $v_+ > v_-$ (see Fig. 3.2). In this subsection, we assume that enough time has elapsed since the application of $V(t)$ for the excitations to be very well separated. Explicitly, if we assume that $V(t)$ is a pulse centered around $t = 0$, we have the condition

$$t \gg w \frac{v_+ + v_-}{v_+ - v_-} \,. \tag{3.31}$$

Indeed, fast/slow pulses are centered around $x_\pm = v_\pm t$ and have a spatial extension $\delta x_\pm = w v_\pm$. Then, the separation condition $|x_+ - x_-| \gg |\delta x_+ + \delta x_-|$ yields the above relation. In this regime, the expression (3.30) greatly simplifies and, consequently, the evaluation of momentum distributions is easier. Indeed, it was proved in Refs. [154, 155] that a function with the structure of (3.30) can be separated as

$$\Delta \mathcal{G}_\beta^< \left(x + \frac{\xi}{2}, x - \frac{\xi}{2}; t, t\right) \to \Delta \mathcal{G}_{\beta+}^< (t_+, \xi) + \Delta \mathcal{G}_{\beta-}^< (t_-, \xi), \tag{3.32}$$

where

$$\Delta \mathcal{G}_{\beta,\eta}^< (t_\eta, \xi) = \frac{1}{2\pi i \xi} \prod_{\varepsilon=\pm} \left[\frac{\pi k_B \theta \xi / v_\varepsilon}{\sinh(\pi k_B \theta \xi / v_\varepsilon)} \right]^{\zeta_{\beta,\varepsilon}}$$
$$\times \left\{ \prod_{\varepsilon=\pm} \left[\frac{i v_\eta w - \varepsilon(v_\eta t_\eta + \varepsilon \xi/2)}{i v_\eta w + \varepsilon(v_\eta t_\eta + \varepsilon \xi/2)} \right]^{q_{\beta,\eta}} - 1 \right\}, \tag{3.33}$$

Thus, the coherence function (3.30) has been converted from a product into a *sum* of two terms depending on the combinations $t - x/v_\pm$. In practice, the separation (3.32) means that fast and slow excitations on a given channel β are treated independently from one another, which is reasonable when their overlap in space is negligible.

As a consequence of Eq. (3.32), we see from the definition (3.24) that

$$\Delta n_\beta(k, t) \to \Delta n_{\beta+}(k) + \Delta n_{\beta-}(k) \,. \tag{3.34}$$

where

$$\Delta n_{\beta,\pm}(k) = \frac{1}{2\pi} \int_{-\infty}^{+\infty} dx \int_{-\infty}^{+\infty} d\xi \, e^{-ik\xi} \Delta \mathcal{G}_{\beta,\pm}^< (t_\pm, \xi) \tag{3.35}$$

are time-independent distributions because the functions $\Delta \mathcal{G}_{\beta\pm}^<$ depend on space and time only via the combinations $x - v_\pm t$ and thus any dependence on t is lost when computing the integral over x in (3.35). This shows that the non-equilibrium distribution $\Delta n_\beta(k, t)$ actually reaches a stationary limit when the excitations are spatially well separated. Moreover, the functions $\Delta n_{\beta,\pm}(k)$ defined in (3.35) can

be considered as the momentum distributions of the single excitations taken independently from each other. Finally, they satisfy the following symmetry relations [which follow from (3.35) and (3.33)]

$$v_- \Delta n_{1,+}(k/v_+) = v_+ \Delta n_{1,-}(k/v_-), \tag{3.36a}$$

$$v_- \Delta n_{2,+}(k/v_+) = -v_+ \Delta n_{2,-}(-k/v_-). \tag{3.36b}$$

MINIMAL EXCITATIONS FOR INTEGER CHARGES   Let us now consider the zero-temperature case. By investigating the momentum distributions in this regime, it is possible to have information about the particle-hole content of the excitations propagating in the system, excluding thermal particle-hole pairs. We now show that the condition for having "clean" excitations (purely electron-like or hole-like) is that the numbers $q_{\beta,\pm}$ defined in (3.22) be integer. Thus, it is not the charge q [cf. Eq. (3.21)] carried by the original pulse $V(t)$ the quantity that matters, but rather the charges renormalized by interactions. In order to see that this is indeed the case, it is sufficient to notice that when $q_{\beta,\pm}$ are integer numbers, the zero-temperature expressions of the correlators (3.33) become identical to Eq. (1.82). As a result, they admit the representation

$$\Delta \mathcal{G}_{1,\pm}^<(t_\pm, \xi) = \frac{1}{v_\pm} \sum_{j=1}^{m_\pm} \Pi_j \left(t_\pm - \frac{\xi}{2v_\pm} \right) \Pi_j^* \left(t_\pm + \frac{\xi}{2v_\pm} \right), \tag{3.37a}$$

$$\Delta \mathcal{G}_{2,\pm}^<(t_\pm, \xi) = \frac{\pm 1}{v_\pm} \sum_{j=1}^{n} \Pi_j^{(\pm)} \left(t_\pm - \frac{\xi}{2v_\pm} \right) \Pi_j^{(\mp)} \left(t_\pm + \frac{\xi}{2v_\pm} \right),$$

$$\tag{3.37b}$$

where we have assumed $q_{1+} = m_+$, $q_{1-} = m_-$ and $q_{2\pm} = \pm n$, with $m_\pm, n \in \mathbb{N}$. Moreover $\Pi_j^{(+)} \equiv \Pi_j$ and $\Pi_j^{(-)} \equiv \Pi_j^*$. The functions Π_j have been defined in Eq. (1.84) and here are denoted differently not to make confusion with the bosonic fields $\phi_{\beta,\pm}$. By using the Fourier representation (1.86) it is finally straightforward to show that the zero-temperature momentum distributions obtained from (3.35) read

$$\Delta n_{1\pm}(k) = 2wv_\pm \Theta(k) \sum_{j=0}^{m_\pm - 1} \left| L_j(2wv_\pm k) \right|^2 e^{-2wv_\pm k},$$

$$\tag{3.38}$$

$$\Delta n_{2\pm}(k) = \pm 2wv_\pm \Theta(\pm k) \sum_{j=0}^{n-1} \left| L_j(\pm 2wv_\pm k) \right|^2 e^{\mp 2wv_\pm k},$$

where L_j are Laguerre polynomials. It is easy to verify that the total charge of each wave packet is recovered by integrating its distribution over k.

The result (3.38) shows that both wave packets on channel 1 and the fast one on channel 2 are made only of electron-like excitations above the Fermi level, while the slow wave packet on the inner channel is
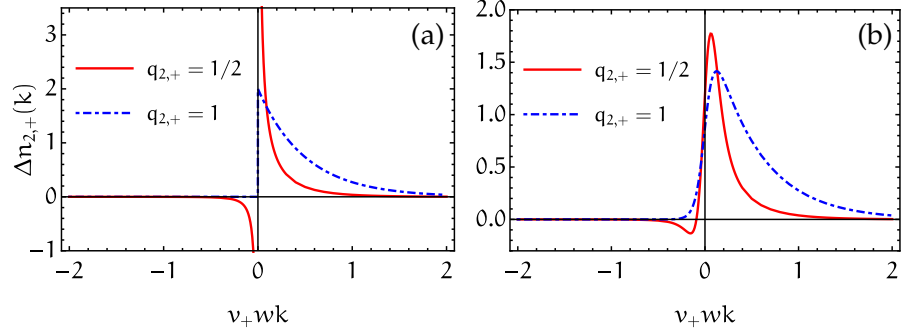
Figure 3.3: Distribution $\Delta n_{2,+}(k)$ (in units of wv_+) at fixed interaction angle parameter $\chi = \pi/4$. In this case the charge carried by the fractional excitation is $-eq_{2,+} = -eq/2$, which is an integer multiple of $-e$ for $q \in 2\mathbb{N}$. Panel (a): zero temperature result; for integer charges, the distribution is given by (3.38) and describes a purely electronic excitation, with no associated holes. In contrast, when $q_{2,+}$ is not an integer, a divergence appears near $k = 0$. Panel (b): finite temperature distributions for $k_B \theta w = 0.05$. The divergence near the Fermi momentum is washed out. Still, hole contributions do appear in the case of non integer charges, while in the integer case the distribution is always positive.

made only of hole-like excitations below the Fermi level. It is worth underlining that this feature is peculiar of Lorentzian voltage pulses and it is not shared by generic wave packets generated by other drives, which would contain electron-hole pair contributions. As a last comment, we note that the charges of the outer-channel excitations can be simultaneously integer only if q itself is. Indeed

$$\begin{aligned} m_+ = q_{1,+} = q\cos^2\chi \\ m_- = q_{1,-} = q\sin^2\chi \end{aligned} \implies q = m_+ + m_- \in \mathbb{N}. \qquad (3.39)$$

This condition, however, can be achieved only for particular values of the mixing angle, such that $\tan^2\chi = m_-/m_+$, in agreement with Ref. [114]. On the inner channel, instead, given any interaction strength it is possible to have both excitations with integer charge if

$$q = \frac{2n}{\sin 2\chi}, \qquad (3.40)$$

with $n \in \mathbb{N}$ and no further constraints. Thus, even starting from a non-integer q, which describes a non-minimal excitation, two clean pulses with opposite charges can be created on the inner channel, due to interactions. By building upon this observation, we will show in Sec. 3.5 that it is possible to construct a quantity from which the mixing angle χ can be extracted.

GENERIC CHARGES AND FINITE TEMPERATURE   We now describe what happens when the charge of a given excitation is not an in-

teger multiple of $-e$. In this situation the momentum distribution features particle-hole pair contributions, indicating that the excitation is not clean. An example is shown in Fig. 3.3(a), where we plot the zero-temperature distribution $\Delta n_{2,+}(k)$ for $\chi = \pi/4$ and compare the case of integer ($q_{2,+} = 1$) and non-integer ($q_{2,+} = 1/2$) charges. In the latter case the distribution is evaluated numerically and clearly features a divergence around $k = 0$, with negative contributions for $k < 0$ signaling the presence of hole excitations.

We can actually prove that the divergence around $k = 0$ is common to all distributions $\Delta n_{\beta\pm}$. In order to evaluate the small-k behavior of $\Delta n_{\beta,\pm}(k)$, we have to consider the dominant contribution in the integral (3.35) as $|\xi| \to \infty$. It is possible to show that the leading order is (at zero temperature)

$$\int_{-\infty}^{+\infty} dx \, \Delta \mathcal{G}_{\beta,\pm}^{<}(t_{\pm}, \xi) \underset{|\xi| \to \infty}{\approx} \frac{|\xi|}{2\pi i \xi} \left[e^{2\pi i q_{\beta,\pm} \mathrm{sgn}(\xi)} - 1 \right]. \tag{3.41}$$

Thanks to this estimate we find

$$\Delta n_{\beta\pm}(k \to 0) \approx \frac{1 - \cos(2\pi q_{\beta,\pm})}{2\pi^2} \frac{1}{k}. \tag{3.42}$$

Thus, for non-integer $q_{\beta\pm}$, particle-hole pairs distributed as $1/k$ near the Fermi momentum arise in $\Delta n_{\beta,\pm}(k)$. Notice that the previous expression vanishes for integer charges. This does not mean that the distributions vanish near $k = 0$, but simply that sub-leading orders in the expansion (3.41) have to be kept. By integrating Eq. (3.42) over k, we see that the number of particle-hole pairs is logarithmically divergent [6–8], a manifestation of the orthogonality catastrophe [6]. Finally, in Fig. 3.3(b) we present finite-temperature results, showing that the zero-temperature divergence disappears and the distributions are smeared around $k = 0$.

3.3.2 *Transient regime*

When the wave packets are not completely separated in space, some effects due to their overlap can modify the picture we have presented above. In this subsection we investigate this regime, by focusing on the dynamics of the inner channel (for the sake of simplicity and also because in Sec. 3.5 we will calculate the noise due to the partitioning of inner-channel excitations). Since in this transient regime the separation (3.32) cannot be made, the momentum distribution acquires a time dependence. We can decompose it as

$$\Delta n_2(k, t) = \Delta n_{2,+}(k) + \Delta n_{2,-}(k) + \Delta n_{2,\chi}(k, t), \tag{3.43}$$

where the whole time dependence is encoded in the term $\Delta n_{2,\mathcal{X}}(k,t)$, associated with the overlap of the fast and slow wavapackets. It is defined as

$$
\Delta n_{2,\mathcal{X}}(k,t) = \frac{1}{2\pi} \int_{-\infty}^{+\infty} dx \int_{-\infty}^{+\infty} d\xi\, e^{-ik\xi}
$$
$$
\times \left[\Delta \mathcal{G}_{2}^{<}\left(x + \frac{\xi}{2}, x - \frac{\xi}{2}; t, t \right) - \sum_{\eta=\pm} \Delta \mathcal{G}_{2,\eta}^{<}(t_{\eta}, \xi) \right].
\tag{3.44}
$$

Notice that if the separation (3.32) can be made, the above expression vanishes. Thus $\Delta n_{2,\mathcal{X}}$ is really associated with the transient regime where the wave packets are overlapping. Eq. (3.44) must be evaluated numerically, in general, but can be simplified in the case of integer charges, i. e. $q_{2,+} = n$. Indeed, with the help of (3.37), one obtains [29]

$$
\Delta n_{2,\mathcal{X}}(k,t) = \int_{-\infty}^{+\infty} \frac{dx}{v_+ v_-} \int_{-\infty}^{+\infty} d\xi (-i\xi) e^{-ik\xi}
$$
$$
\times \sum_{s,p=1}^{n} \prod_{\eta=\pm} \Pi_s^{(\eta)}\left(t_\pm - \frac{\eta\xi}{2v_\pm} \right) \Pi_p^{(\eta)}\left(t_\pm + \frac{\eta\xi}{2v_\pm} \right)
$$
$$
= \gamma \sum_{s,p=1}^{n} \partial_k \left| \int_{-\infty}^{+\infty} \frac{d\omega}{2\pi} \tilde{\Pi}_s(\omega) \tilde{\Pi}_p^*(\gamma\omega - v_- k) e^{i\omega t(\gamma-1)} \right|^2,
\tag{3.45}
$$

where

$$
\gamma = \frac{v_-}{v_+} < 1
\tag{3.46}
$$

and $\tilde{\Pi}_s(\omega)$ is the Fourier transform of $\Pi_s(t)$ [cf. Eq. (1.86)]. The simplest case is represented by the choice $q_{2,+} = 1$, for which the above general expression reduces to

$$
\Delta n_{2,\mathcal{X}}(k,t) = -\frac{8w\gamma(\gamma+1)^{-2}}{1 + \frac{t^2}{w^2}\left(\frac{1-\gamma}{1+\gamma} \right)^2} \sum_{\eta=\pm} \eta v_\eta \Theta(\eta k) e^{-2\eta v_\eta wk}.
\tag{3.47}
$$

As shown in Fig. 3.4, this mixed term describes electron excitations ($\Delta n_{2,\mathcal{X}} > 0$) at $k < 0$ and hole excitations ($\Delta n_{2,\mathcal{X}} < 0$) at $k > 0$. This means that the effect of the overlap between the two oppositely-charged pulses carrying integer charges results in an effective reduction of the overall number of electron and hole excitations, with respect to the case of completely separated wave packets. Note that the time-dependent overlap contribution (3.47) becomes negligible at times $t \gg w\frac{1+\gamma}{1-\gamma}$, which is precisely the condition (3.31) discussed in the stationary regime.

We conclude this Section by addressing the number $\Delta N_h(t)$ of excited holes at time t due to the effect of the drive. At zero temperature, this quantity is given by

$$
\Delta N_h(t) = -\int_{-\infty}^{0} dk\, \Delta n_2(k,t).
\tag{3.48}
$$
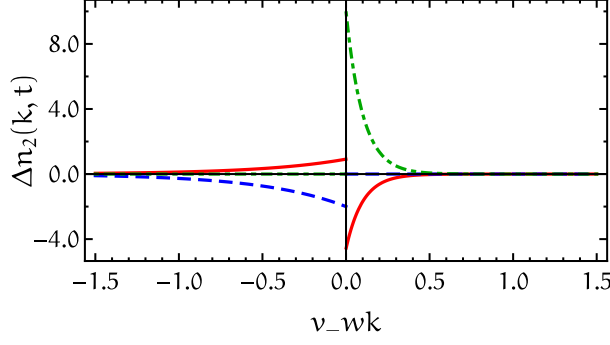
Figure 3.4: The different components of the momentum distribution $\Delta n_2(k,t)$, in the case $q_{2,+} = 1$. The blue (green) dashed (dot-dashed) line represents $\Delta n_{2,-}$ ($\Delta n_{2,+}$), while the full red line is $10\Delta n_{2,\chi}$ for $t/w = 5$. In this plot we have used $\gamma = 1/5$.
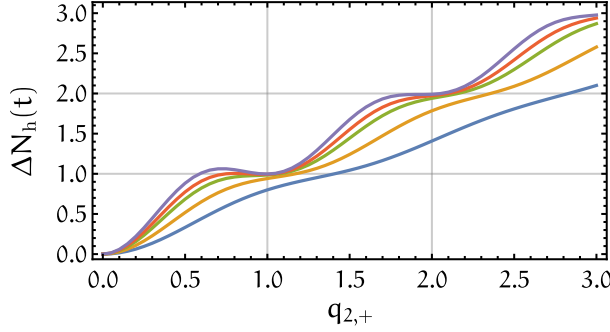
Figure 3.5: Total number of injected holes as a function of $q_{2,+} = q\cos\chi\sin\chi$ at zero temperature, in the case of a Lorentzian drive. Different curves refer to (from bottom to top) $t/w = 5, 10, 20, 30, 50$. The ratio between slow and fast velocities is $\gamma = 1/5$.

The calculation is performed in Appendix E.1 and yields

$$\Delta N_h(t) = \frac{1}{(2\pi)^2} \int_{-\infty}^{+\infty} dx \int_{-\infty}^{+\infty} dy \frac{1}{(a+iy)^2}$$
$$\times \cos\left[e\frac{q_{2,+}}{q} \left(\int_{t_+ + \frac{y}{2v_+}}^{t_+ - \frac{y}{2v_+}} dt'V(t') - \int_{t_- + \frac{y}{2v_-}}^{t_- - \frac{y}{2v_-}} dt'V(t') \right) \right]. \tag{3.49}$$

This quantity is plotted in Fig. 3.5, for different values of t/w. By increasing t/w, $\Delta N_h(t) \to q_{2,+}$ when $q_{2,+}$ is integer, as expected from the previous analysis in the regime of well-separated pulses. Indeed in this situation the slow excitation is purely hole-like and carries a charge $q_{2,-} = -q_{2,+}$. For intermediate times, instead, this quantity reflects the effective charge reduction discussed above due to the overlap contribution $\Delta n_{2,\chi}(k,t)$. Moreover, for non-integer values of $q_{2,+}$, we clearly see that $\Delta N_h(t)$ grows upon increasing t/w. By choosing a non-integer charge value and considering several times,

one realizes that (for sufficiently large t/w), this increase is logarithmic in t or, equivalently, in the propagation distance along the edge. This feature is in agreement with the scaling behavior (3.42), appearing in the stationary regime: Eq. (3.42) indeed results in a logarithmic divergence of the number of produced holes.

3.4   WIGNER FUNCTION

As we have seen in Sec. 1.5.1, the Wigner function is a very powerful tool to access the energy content of an excitation, while keeping track of its time evolution. It is then perfectly suited to investigate the fractionalization problem we are dealing with in this Chapter. Therefore, in this Section we give results for the Wigner function of the fractionalized excitations, confirming from another perspective what we previously discussed.

The excess (electron) Wigner function of channel β is defined as

$$\Delta W_\beta^< (x, t; \omega) = \frac{1}{2\pi} \int_{-\infty}^{+\infty} d\tau \, \Delta \mathcal{G}_\beta^< \left(x, x; t + \frac{\tau}{2}, t - \frac{\tau}{2} \right) e^{i\omega\tau} \quad (3.50)$$

and it is thus related to time correlations rather than spatial ones as in the case of the momentum distribution, [cf. Eq. (3.24)]. We have already all we need in order to evaluate $\Delta W_\beta^<$. Indeed, the excess coherence appearing in the integral (3.50) can be calculated along the lines of what has been done in Sec. 3.3 and the result is similar to Eq. (3.30):

$$\Delta \mathcal{G}_\beta^< \left(x, x; t + \frac{\tau}{2}, t - \frac{\tau}{2} \right) = \frac{i}{2\pi i \tau} \frac{\pi k_B \theta \tau}{\sinh(\pi k_B \theta \tau)} \prod_{\eta = \pm} \left(\frac{1}{v_\eta} \right)^{\zeta_{\beta,\eta}}$$
$$\times \left\{ \prod_{\eta = \pm} \prod_{\varepsilon = \pm} \left[\frac{iw - \varepsilon(x_\eta/v_\eta - \varepsilon\tau/2)}{iw + \varepsilon(x_\eta/v_\eta - \varepsilon\tau/2)} \right]^{q_{\beta,\eta}} - 1 \right\}, \quad (3.51)$$

with $q_{\beta,\eta}$ given in (3.22), $x_\eta = x - v_\eta t$ and we recall that $\zeta_{1,+} = \zeta_{2,-} = \cos^2\chi$ and $\zeta_{1,-} = \zeta_{2,+} = \sin^2\chi$. Just as we have done in Eq. (3.32), it is possible to separate the above correlator into a sum of terms depending only on $x - v_\eta t$, when the condition (3.31) is met. In this way, one obtains

$$\Delta W_\beta^< (x, t; \omega) = \sum_{\eta = \pm} \Delta W_{\beta,\eta}^< (x - v_\eta t; \omega), \quad (3.52)$$

where $\Delta W_{\beta,\eta}^<$ is the excess Wigner function of the excitation propagating at velocity v_η on channel β. It is also possible to derive analytic expressions when $q_{\beta,\eta}$ are integer numbers, by repeating a calculation which is essentially the same as the one presented in Appendix B.2. However, here we will directly show and comment some results in the transient regime, where the Wigner function has to be numerically computed from Eqs. (3.50) and (3.51).
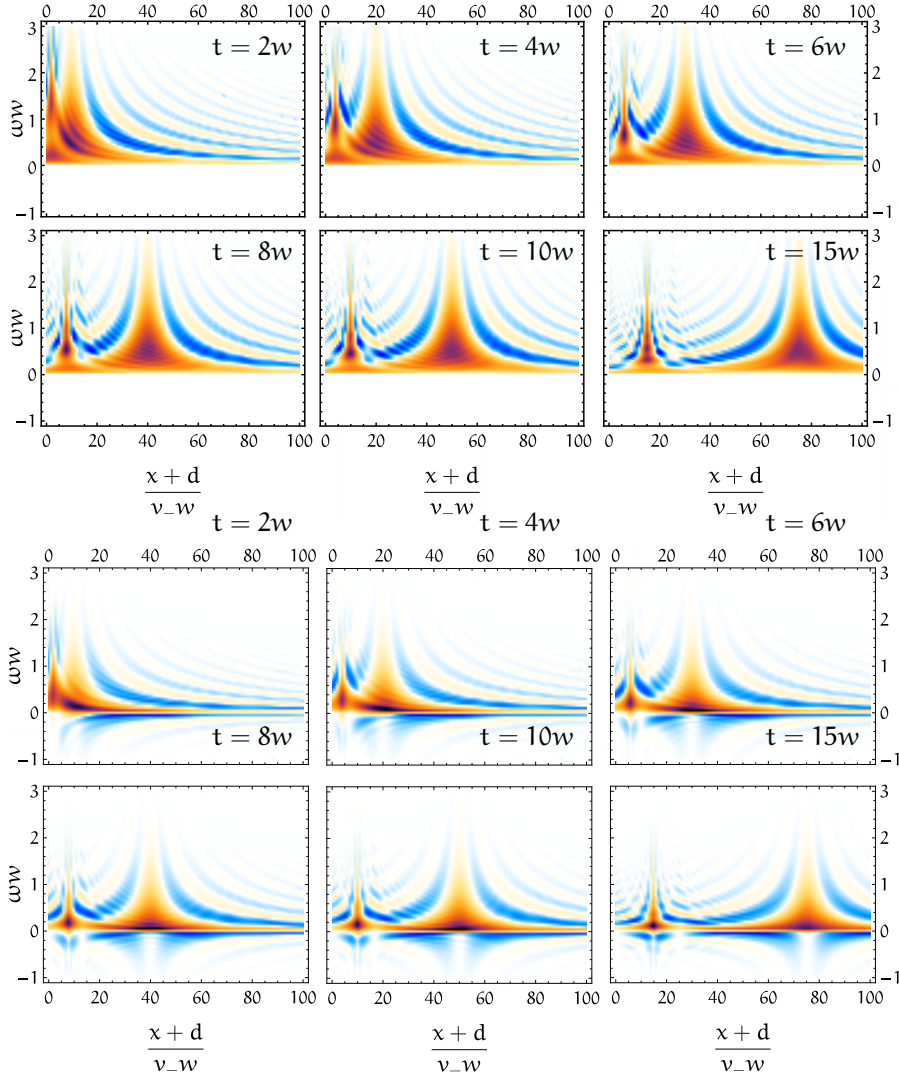
Figure 3.6: Time evolution of the outer-channel excess Wigner function $\Delta W_1^<(x, t; \omega)$, in the case of a Lorentzian drive. All panels are snapshots at a given time, as indicated on each density plot. The mixing angle is fixed to $\chi = \pi/4$ and the velocity ratio is $v_+/v_- = 5$. The upper group of plots refer to the situation $q_{1,+} = q_{1,-} = 1$. In this case both excitations are clean Levitons and no holes are created. The lower group of plots refers instead to the case $q_{1,+} = q_{1,-} = 1/2$. Here, the charge being non-integer, the excitations are not clean and hole contributions emerge at $\omega < 0$. From these plots the charge fractionalization process is transparent.

In Fig. 3.6 we show some density plots of the outer-channel excess Wigner function $\Delta W_1^<(x, t; \omega)$, as a function of x and ω, for different times. We have chosen the mixing angle $\chi = \pi/4$, corresponding to maximal coupling, and we have considered $v_+/v_- = 5$. We recall that, at maximal coupling, the charges of the outer-channel excitations are $q_{1,+} = q_{1,-} = q/2$ [see Eq. (3.22)], where q is defined in (3.21) and is determined by the drive $V(t)$ [see Eq. (3.29)]. In the Figure we have put two groups of panels, corresponding to different situations. Before describing the differences between them, let us immediately notice that the charge fractionalization process is evident from both groups: we can observe how excitations are generated and how they split and separate as they propagate along the edge channel.

The upper group refers to $q = 2$, as an example of the case where the charge of each excitation is integer (here $q_{1,+} = q_{1,-} = 1$). It shows that even in this interacting system a superposition[3] of Lorentzian pulses carrying integer charges of the same sign is a clean excitation. Indeed, from the plots of the Wigner function we clearly observe no signal at $\omega < 0$, indicating that no holes are excited in the system. It is intuitive to understand from the picture that, by waiting long enough, the two pulses will be eventually very well separated and the Wigner function of the system would be the sum of two independent contributions looking exactly as the Wigner function for a single-Leviton state we plotted in Fig. 1.11 (top left). On the contrary, in the lower group of panels we have considered the situation $q = 1$, meaning that $q_{1,+} = q_{1,-} = 1/2$. In this case hole contributions at negative energy are clearly visible.

In Fig. 3.7 we report the very same plots, but this time for the inner-channel excess Wigner function $\Delta W_2^<(x, t; \omega)$. In all plots, the main positive peak represents the fast pulse with positive charge, while the main negative peak is associated with the hole-like slow excitation. In Fig. 3.7 it is not immediate to see the difference between the case $q = 2$ and $q = 1$, unlike for Fig. 3.6. This is because the excitations on the inner channel always have an opposite charge and thus paricle and hole contributions must be present somewhere. However, with a more attentive look at the fast pulse, we can see that the signal at $\omega < 0$ right below it is suppressed in the upper group of plots, corresponding to the integer case $q_{2,+} = -q_{2,-} = 1$. This is because the more the pulses are separated from each other, the more the situation on the channel is described by a purely electron-like excitation followed by a purely hole-like one. On the other hand, negative values at $\omega < 0$ below the fast peak in the case $q_{2,+} = -q_{2,-} = 1/2$ indicate that excitations are not clean.

---

3 The term superposition refers to the fact that two pulses emerge due to fractionalization and does not indicate that the original drive $V(t)$ is made of multiple pulses.
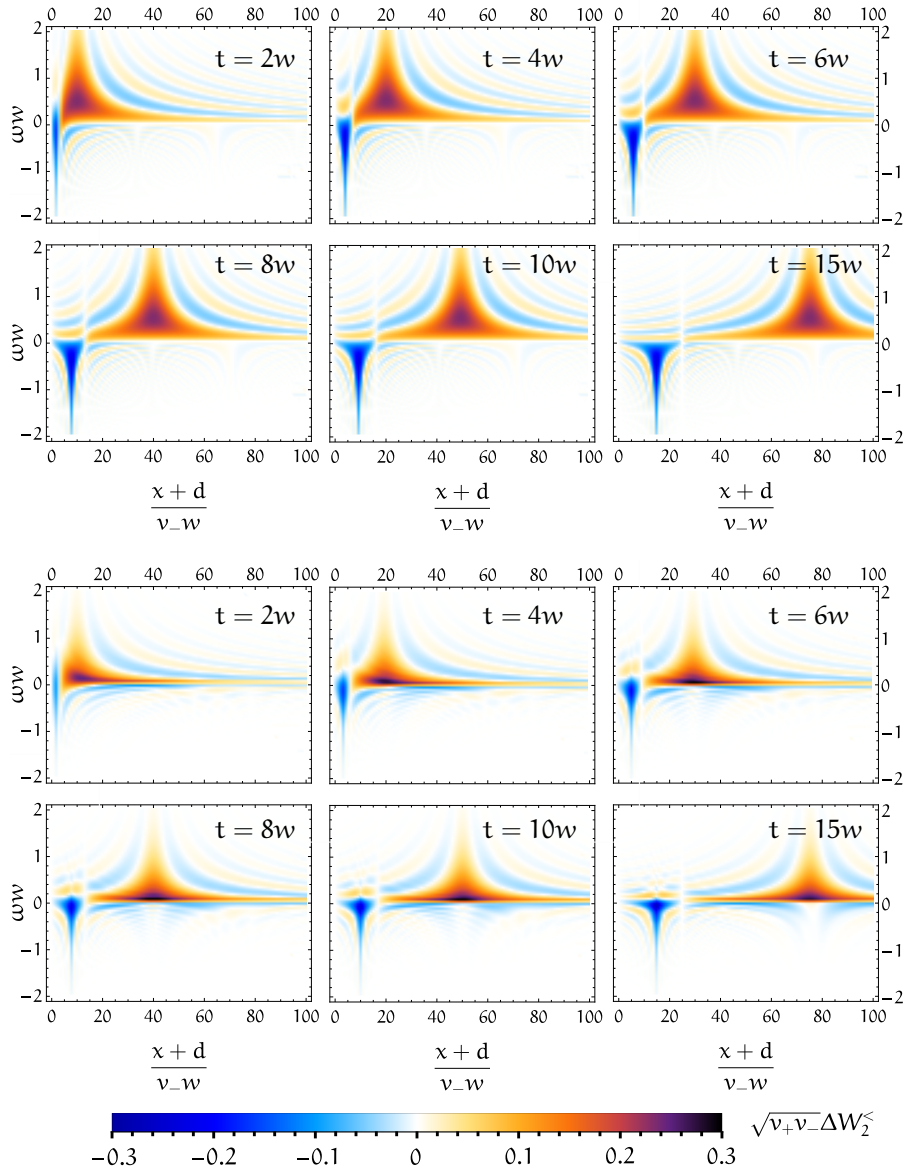
Figure 3.7: Time evolution of the inner-channel excess Wigner function $\Delta W_2^<(x, t; \omega)$. All panels are snapshots at a given time, as indicated on each density plot. The mixing angle is fixed to $\chi = \pi/4$ and the velocity ratio is $v_+/v_- = 5$. The upper group of plots refers to the situation $q_{2,+} = -q_{2,-} = 1$. The lower group of plots refers instead to the case $q_{2,+} = -q_{2,-} = 1/2$.
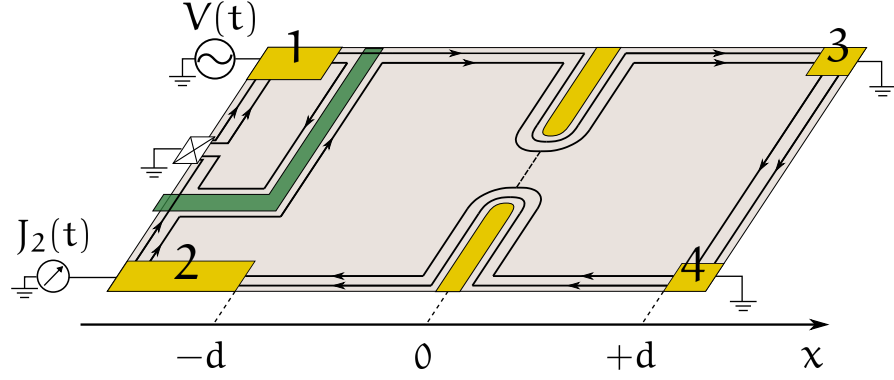
Figure 3.8: HBT setup for partitioning inner-channel excitations. A QPC is polarized in such a way that the outer channel is completely transmitted, while the inner one is partially reflected. The system is driven by $V(t)$ at terminal 1 and the excitations are partitioned after having travelled for a distance d along the edge. The backscattered current $J_2(t)$ entering terminal 2 is measured and used to compute the noise.

3.5 NOISE IN A QPC GEOMETRY

Having discussed in detail the properties of the excitations generated by the Lorentzian drive (3.29), we now turn our attention to the noise produced when they are partitioned at an electronic beamsplitter. As we will show in this Section, the inner-channel partitioning noise turns out to be very useful to extract the mixing angle χ.

We consider the setup sketched in Fig. 3.8, which is the same as in Fig. 3.1 except for the addition of a QPC at $x = 0$, acting as a beamsplitter. The system being only driven at terminal 1, this setup is known as the HBT configuration [2]. The noise generated by partitioning outer-channel excitations at a QPC has been considered in some works in the literature [114, 149, 150]. Here, we focus on the inner channel, since it is more suitable to probe interactions. To this end, the QPC is assumed to be polarized so as to completely transmit the outer channel and weakly reflect the inner one.

We will then consider the following Hamiltonian

$$H_t = \Lambda \Psi_{R,2}^\dagger(0)\Psi_{L,2}(0) + \text{H.c.}, \tag{3.53}$$

accounting for tunneling processes between the upper- to lower-edge inner channel, and assume that the tunnel amplitude Λ is small (weak backscattering regime). The Hamiltonian (3.53) will be thus considered as a perturbation with respect to the Hamiltonian H defined in (3.7).

3.5.1 *Relation with the number of holes*

We want to calculate the zero-frequency autocorrelation noise in terminal 2. It is defined as

$$S = 2 \int_{-\infty}^{+\infty} dt \int_{-\infty}^{+\infty} d\tau \left[\langle J_2(t+\tau)J_2(t) \rangle - \langle J_2(t+\tau) \rangle \langle J_2(t) \rangle \right], \quad (3.54)$$

where $J_2(t) = J_{L,2}(-d, t)$ is the backscattered current entering in the terminal and $J_{L,2}(x, t)$ is given in Eq. (3.13b). Within the perturbative approach, the time evolution $O(t)$ of a generic operator is built as a power series in the tunnel amplitude Λ. In particular, up to second order one finds

$$O(t) = O^{(0)}(t) - i \int_{-\infty}^{t} d\tau \left[O^{(0)}(t), H_t^{(0)}(\tau) \right]$$
$$- \int_{-\infty}^{t} dt' \int_{-\infty}^{t'} dt'' \left[H_t^{(0)}(t''), \left[H_t^{(0)}(t'), O^{(0)}(t) \right] \right], \quad (3.55)$$

where the superscript (0) denotes the time evolution with respect to the Hamiltonian H in (3.7). By applying this formula to $J_{L,2}(-d, t)$ and plugging the result into (3.54), we arrive at the result

$$S = \frac{4e^2 |\Lambda|^2}{(2\pi a)^2} \int_{-\infty}^{+\infty} dt \int_{-\infty}^{+\infty} d\tau \left(\frac{a}{a + i v_- \tau} \frac{\pi \theta \tau}{\sinh \pi \theta \tau} \right)^2$$
$$\times \cos \left[e \frac{q_{2,+}}{q} \left(\int_{t-\tau}^{t} dt' V(t') - \int_{t-\tau+\tau_d}^{t+\tau_d} dt' V(t') \right) \right], \quad (3.56)$$

where

$$\tau_d = d \left(\frac{1}{v_+} - \frac{1}{v_-} \right). \quad (3.57)$$

The calculation leading to this formula is detailed in App. E.2. The first thing to note about Eq. (3.56) is that it is formally equivalent to the HBT noise obtained with the modified voltage

$$\tilde{V}(t) = V(t) - V(t - \tau_d), \quad (3.58)$$

describing the arrival from the left side of the QPC of two identical but oppositely-charged excitations, separated by a time delay τ_d, which is controlled by the propagation distance and the velocity mismatch between fast and slow modes. As discussed in App. C.2, this situation is equivalent to the HOM noise obtained when two identical and *equally-charged* pulses arrive at the QPC from *opposite* sides, after having been excited at terminals 1 and 4. Our HBT setup thus simulates a HOM interferometry of fractional excitations.

As a second remark, we notice that the formula (3.56) at zero temperature is very similar, though not identical, to the result (3.49) for the number of excited holes at time t. This resemblance then suggests
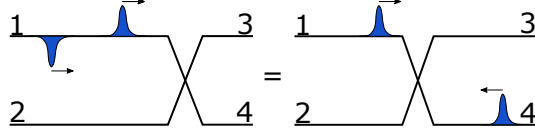
Figure 3.9: Equivalence between the investigated HBT setup at $\nu = 2$ (left) and a non-interacting HOM setup at $\nu = 1$ (right). In the first one, the two oppositely-charged excitations on the inner channel arrive at a QPC from the left side and are separated due to the fractionalization phenomena. In the second one, two excitations with the same charge arrive at a QPC from opposite sides and are separated due to the time delay between the drive applied at terminal 1 and the one at terminal 4.

that a relation between the t and τ_d can be found in such a way that S and ΔN_h be proportional. As a matter of fact, by evaluating Eqs. (3.56) and (3.49) in the case of a Lorentzian drive such that $q_{2,+}$ is integer, the following relation is found[4]

$$\frac{S}{S_0} = 2N_h(t^\star), \quad \frac{t^\star}{w} = \sqrt{\frac{\gamma}{(\gamma-1)^2}\left(\frac{\tau_d}{w}\right)^2 - 1},\tag{3.59}$$

where $S_0 = 2e^2|\Lambda|^2/v_-^2$ and γ is given in (3.46). The noise as a function of $q_{2,+}$ behaves in the same way as in Fig. 3.5. In particular, S/S_0 approaches the value $2q_{2,+}$ at integer $q_{2,+}$, upon increasing the propagation distance d. This can be very easily interpreted from the HOM perspective: the greater the propagation distance, the better the two wave packets are separated and the greater is τ_d. Therefore, in this regime two Levitons of charge $q_{2,+}$ arrive at the QPC separated by a very long time, thus contributing independently to the noise, which becomes twice as big as what a single Leviton would produce. On the contrary, the anti-bunching effect is responsible for a noise reduction in the regime of non-negligible overlap [117].

3.5.2 *Periodic pulses*

In this final part of the Chapter we want to investigate whether it is possible from noise measurements to obtain information about the mixing angle χ describing electronic interactions in the model we are considering. In order to be closer to an experimental situation, we address the case of a *periodic* stream of pulses, $V(t) = V(t+T)$. As discussed in Sec. 1.6, this calls for slightly different definitions of some quantities. First of all, the t-integration in (3.54) is replaced by an average over the drive period, because the correlators are now

---

4 Of course this relation is not general and depends on the particular drive, as the presence of the parameter w in (3.59) shows.

periodic functions of t and cannot be integrated on the whole real axis. In this way the definition of the noise becomes

$$S = 2 \int_{-T/2}^{T/2} \frac{dt}{T} \int_{-\infty}^{+\infty} d\tau \left[\langle J_2(t+\tau)J_2(t) \rangle - \langle J_2(t+\tau) \rangle \langle J_2(t) \rangle \right] . \quad (3.60)$$

Secondly, instead of (3.21), we now define a charge *per period*, as in (1.93).

$$q = -\frac{e}{2\pi} \int_{-T/2}^{T/2} dt\, V(t) . \quad (3.61)$$

Thirdly, and most importantly, the periodic voltage drive $V(t)$ is decomposed be relying on the photoassisted coefficients as in Eq. (1.100)

$$e^{ie \int_0^t d\tau\, V(\tau)} = e^{-iq\Omega t} \sum_{\ell \in \mathbb{Z}} p_\ell(q)\, e^{-i\ell\Omega t} , \quad (3.62)$$

where $\Omega = 2\pi T^{-1}$. Finally, the overlap between two consecutive pulses is controlled by the ratio $\eta = w/T$ between the typical temporal extension of each pulse composing the periodic train and the period of the drive. For instance, a periodic train built from Lorentzian pulses (3.29) can be written as

$$V(t) = -\frac{q\Omega}{e\pi} \sum_{p=-\infty}^{+\infty} \frac{\eta}{\eta^2 + (t/T - p)^2} , \quad (3.63)$$

and its photoassisted coefficients read [81, 117]

$$p_\ell(q) = q e^{-2\pi\eta\ell} \sum_{s=0}^{+\infty} \frac{\Gamma(q+\ell+s)}{\Gamma(q+1-s)} \frac{(-1)^s e^{-4\pi\eta s}}{s!(\ell+s)!} , \quad (3.64)$$

where $\Gamma(z)$ is Euler's Gamma function. For a detailed derivation of this formula, see the PhD thesis of L. Vannucci [52] or F. Ronetti [156].

By using the decomposition (3.62) into (3.56) and following the lines of the calculation presented in App. C.1, it can be straightforwardly shown that

$$\frac{S}{S_0} = \frac{1}{T} \sum_{\ell=-\infty}^{+\infty} |\tilde{p}_\ell(q_{2,+}, \tau_d)|^2\, \ell \coth\left(\frac{\ell\Omega}{2k_B\theta} \right) , \quad (3.65)$$

where the modified photoassisted coefficients are the same as in a HOM setup and read [cf. Eq. (C.20)]

$$\tilde{p}_\ell(q_{2,+}, \tau_d) = \sum_{m=-\infty}^{+\infty} p_{\ell+m}(q_{2,+}) p_\ell^*(q_{2,+}) e^{2\pi i m \tau_d/T} . \quad (3.66)$$

As we can see, unlike (3.56), this result is periodic in τ_d/T, so that τ_d cannot be increased at will and the maximal separation between consecutive pulses is achieved at $\tau_d/T = 1/2$. In this context, the
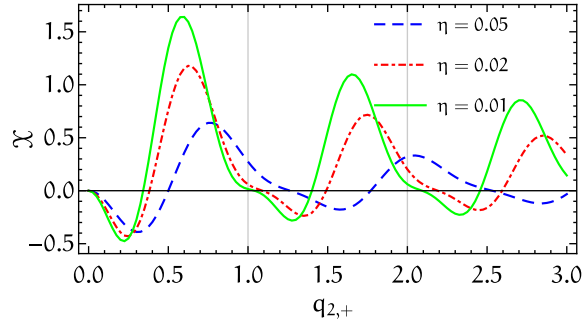
Figure 3.10: The function $\mathcal{X}$ in Eq. (3.67) at zero temperature and with $\tau_d = T/2$ for the Lorentzian drive (3.63). We note that the zeros (in the neighborhood of which $\mathcal{X}$ is decreasing) are more and more precisely localized at integer values of $q_{2,+}$ when η is decreased.

overlap at a given period can be reduced by diminishing the width of the pulse, namely the ratio $\eta = w/T$.

We now argue that the quantity

$$\mathcal{X}(q) = 2\pi \frac{2S(q) - S(2q)}{S_0 \Omega} \tag{3.67}$$

can be used to extract the mixing angle χ. Consider indeed the Lorentzian drive: from what we have discussed in Sec. 3.3.2, we expect that $S(q_{2,+}) \to q_{2,+}$ for integer values of $q_{2,+}$, provided that η is small enough (negligible overlap between consecutive pulses). Thus $\mathcal{X}(q_{2,+})$ would vanish whenever $q_{2,+} \in \mathbb{N}$. By recalling that $q_{2,+} = q \sin \chi \cos \chi$, it would be then possible to recover the value of χ by looking at the positions of the zeros of the quantity $\mathcal{X}$ as a function of the experimentally tunable parameter q. Explicitly, if $q = q_n$ is the position of the n-th zero of $\mathcal{X}(q)$, then χ would be obtained by solving $q_n = n \cos \chi \sin \chi$.

Fig. 3.10 shows the quantity $\mathcal{X}$ as a function of $q_{2,+}$ in the case of a Lorentzian drive (3.63), for different values of η. We can see that $\mathcal{X}(q_{2,+})$ does not vanish only at integer values of $q_{2,+}$, but this is not the only problem. While it is clearly visible that, by decreasing η, the zeros we are interested in are more and more precisely localized at integer values of $q_{2,+}$, we note that significant deviations from this ideal situation already appear for $\eta = 0.05$, which is a quite small value. Therefore, the Lorentzian drive is not well suited for the purpose of extracting χ from a practical point of view.

However, one may wonder whether other drives do exhibit more stable signatures. This happens to be the case for the rectangular wave. Within a period, this signal reads

$$V(t) = -\frac{q\Omega}{2e\eta} \left[\Theta(t) + \Theta(\eta T - t) \right], \quad t \in [0, T) \tag{3.68}$$
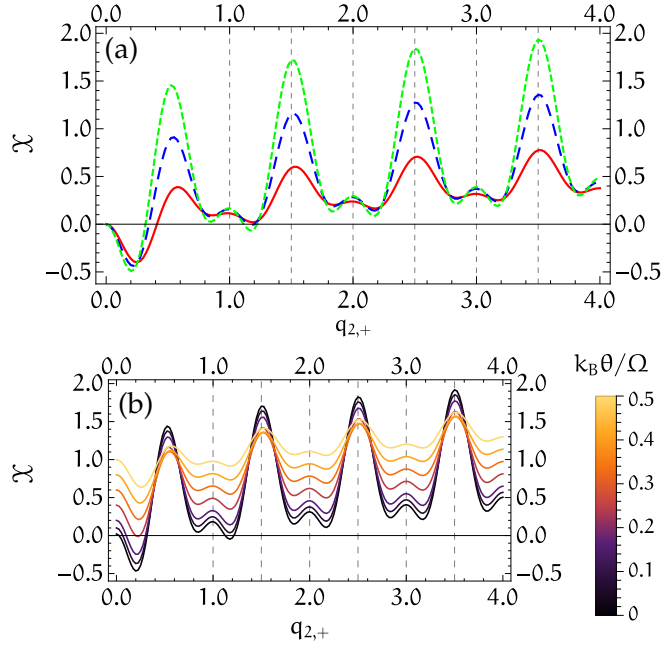
Figure 3.11: The quantity $\mathcal{X}$, defined in (3.67), as a function of $q_{2,+}$ for the rectangular wave (3.68). Panel (a): zero-temperature result for different values of $\eta = 0.2$, 0.1, 0.05 (from bottom to top). Principal maxima are very well located at half-integer $q_{2,+}$ already for $\eta = 0.1$. In addition, the smaller η the bigger the amplitude of oscillations. Panel (b): different curves for temperatures ranging from zero to $k_B\theta = \Omega/2$ and $\eta = 0.05$. In both panels the time delay is set to $\tau_d = T/2$.

and its photoassisted coefficients are calculated in Ref. [157] and read

$$p_\ell(q) = \frac{q}{\pi} \frac{e^{i\pi[\eta\ell + q(\eta-1)]} \sin\{\pi[\eta\ell + q(\eta-1)]\}}{(q+\ell)[\eta\ell + q(\eta-1)]}. \tag{3.69}$$

In Fig. 3.11(a) we show $\mathcal{X}(q)$ for this drive, in the case of optimal maximal time delay $\tau_d = T/2$ and at zero temperature. We observe, after a transient at small values of $q_{2,+}$, a regular oscillating pattern, with local maxima in correspondence of integer $q_{2,+}$ and principal maxima better and better located at half-integer values of $q_{2,+}$ the more η is decreased. Finite-temperature effects are taken into account in Fig. 3.11(b), and are shown to progressively reduce the amplitude of oscillations, but have very little influence on the position of the maxima, which is the feature of interest for our purpose. We can also investigate what happens if the time delay is not the maximum possible. This is shown in Fig. 3.12, where we can see that a change in τ_d has two effects. First of all, it slightly reduces the amplitude of the oscillations, the maximum amplitude being achieved at the optimal value $\tau_d = T/2$. Secondly, it also shifts the positions of the maxima, which are therefore less precisely localized at integer and half-integer values of $q_{2,+}$. We stress, however, that this effect is quite small and
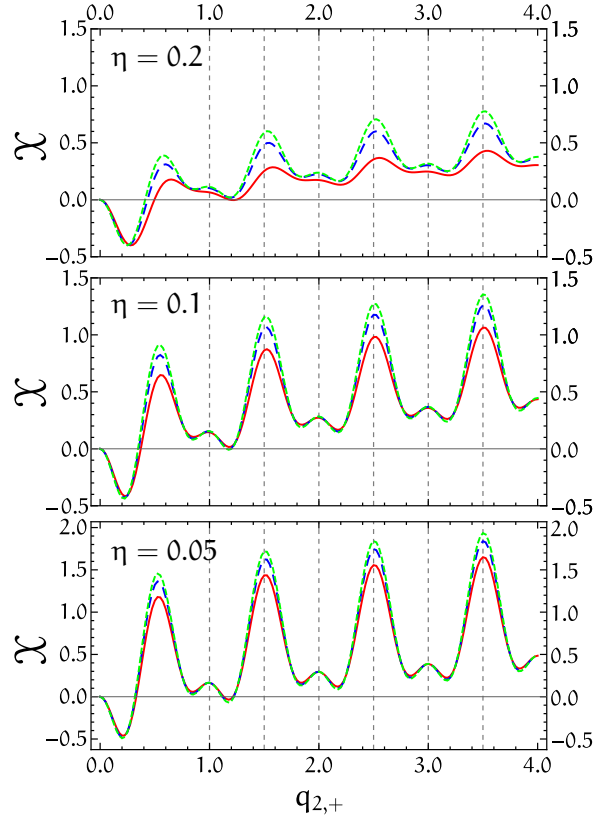
Figure 3.12: Effect of the time delay. In each panel we plot the quantity $\mathfrak{X}(q)$, at a given value of η as specified in the pictures, for three different values of the delay $\tau_d/T = 0.25, 0.35, 0.5$ (from the bottom to the top curve). As we can see, the main effect a non-maximal time delay is to reduce a little the amplitude of the oscillations and to induce a less precise localization of the maxima at integer and half-integer values of $q_{2,+}$. The latter effect is weakened by decreasing η (cf. top and bottom panel).

becomes more and more irrelevant as the value of η is decreased, as it clearly emerges by comparing the top and bottom panels of Fig. 3.12.

This discussion shows that the rectangular wave (3.68) enables to determine the value of the mixing angle χ from the quantity $\mathfrak{X}$ introduced in (3.67), by plotting it as a function of the tunable external parameter q and looking for the values of q at which $\mathfrak{X}$ has principal or secondary maxima. For those values the charge number $q_{2,+} = q \cos\chi \sin\chi$, must be integer or half-integer, thus allowing to extract the parameter χ.

INTERACTING HELICAL CHANNELS DRIVEN BY PERIODIC VOLTAGE PULSES

In this Chapter we turn our attention to a different interacting system, namely we investigate the dynamics of Lorentzian pulses in a couple of counterpropagating helical channels. This system will be described by means of the LL theory presented in Sec. 2.2 and some physical effects are conceptually similar to what has been discussed in the previous Chapter. In particular, based on what we have seen in Sec. 2.2.4, we expect a fractionalization process to occur also in helical channels as a result of interactions. We are going to show that this is indeed the case and we will investigate the properties of fractional excitations by computing their spectral functions. Finally, we propose a possible setup, based on scanning tunneling spectroscopy, which enables to probe the different features of the spectral function, as well as to extract the Luttinger parameter encoding the interaction strength. The results presented in this Chapter are based on our publication [31].

Before entering the description of the model, it is worth reviewing briefly how helical channels emerge at the edge of 2DTIs and why they are topologically protected in a similar way as chiral edge states in the IQHE.

4.1 TWO-DIMENSIONAL TOPOLOGICAL INSULATORS

After the discovery of the IQHE and FQHE – and their interpretation as topological phases [53, 158, 159] – no such new phases were discovered for a long time. Things changed in the mid 2000's when the QSHE was theoretically predicted, first in graphene [160, 161] and then in HgTe/CdTe quantum wells [17]. Quite amazingly, the latter prediction was experimentally confirmed soon after by L. Molenkamp's group [18]; it was the first evidence of a 2DTI. Since these pioneering works, it was understood that maybe topological phases are not so rare as one could think at first and this stimulated a veritable quest for topological materials. Just to mention an example, QSHE was also predicted in InAs/GaSb composite quantum wells [162] and soon after experimentally observed [163, 164]. But 2DTIs are just the beginning of the story and by now we are aware of several different classes of topological materials [165–168].

For the purpose of this thesis, however, we will limit here to the QSHE state. In the following, we describe how it can emerge and how time reversal symmetry protects it.

4.1.1 *Time reversal symmetry and Kramer's theorem*

The effect of time reversal operator Θ is to reverse the arrow of time. Then, positions in space are left unchanged, while momenta are reversed. This means that the action of Θ on position and momentum operators x and p must be

$$\Theta x \Theta^{-1} = x, \quad \Theta p \Theta^{-1} = -p. \tag{4.1}$$

As a consequence we obtain

$$\Theta i\hbar \Theta^{-1} = \Theta[x, p]\Theta^{-1} = -[x, p] = -i\hbar, \tag{4.2}$$

or $\Theta i \Theta^{-1} = -i$. Therefore time reversal must involve complex conjugation and is an anti-unitary operator. It can be then represented as

$$\Theta = U\mathcal{K}, \tag{4.3}$$

where $\mathcal{K}$ is complex conjugation and U a unitary operator, satisfying $UU^\dagger = \mathbb{1}$. By applying Θ twice we obtain

$$\Theta^2 = U\mathcal{K}U\mathcal{K} = UU^* = U(U^T)^{-1} = \Phi, \tag{4.4}$$

where Φ cannot be anything else than a diagonal matrix of phases, since by applying time reversal twice we must come back to the initial state, up to a phase. By taking the transpose of the previous equation we readily find $U^T = U\Phi$ and $U = \Phi U^T$, hence

$$U = \Phi U^T = \Phi U\Phi, \tag{4.5}$$

and this can only happen if $\Phi = \pm\mathbb{1}$. In conclusion, $\Theta^2 = \pm\mathbb{1}$.

We can further show that the first sign applies to bosons, while the second to fermions. In order to see why, we start from the observation that, since the spin of a particle is like an angular momentum, it must be flipped under time reversal. This request, together with the constraint that Θ be proportional to $\mathcal{K}$, fixes the representation of time reversal to be [14]

$$\Theta = e^{-i\pi S_y}\mathcal{K}, \tag{4.6}$$

where S_y is the y component of the particle's spin (the choice of the y direction is just conventional). By squaring this expression, one obtains

$$\Theta^2 = e^{-2i\pi S_y} \tag{4.7}$$

and this tells us that $\Theta^2 = +\mathbb{1}$ for integer spins, while $\Theta^2 = -\mathbb{1}$ for half-integer spins, as announced.

The minus sign appearing in the case of fermions has an important consequence i.e. the Kramer's theorem. Its statement is: in a time

reversal invariant system of fermions, the spectrum must be always doubly degenerate. To prove the theorem we note that in the presence of time reversal symmetry $[\Theta, H] = 0$ so that, for every eigenstate $|\phi\rangle$, also $\Theta|\phi\rangle$ is an eigenstate with the same energy. Consider now the overlap between these two states:

$$
\begin{aligned}
\langle\phi|\Theta\phi\rangle &= \sum_{mn} \phi_m^* U_{mn} \mathcal{K}\phi_n = \sum_{mn} \phi_m^* U_{mn} \phi_n^* \\
&= \sum_{mn} [\phi_m^* U_{mn} \phi_n^*]^T = \sum_{mn} \phi_n^* (-U_{nm}) \phi_m^* \\
&= -\sum_{mn} \phi_n^* U_{nm} \mathcal{K}\phi_m = -\langle\phi|\Theta\phi\rangle = 0.
\end{aligned}
\tag{4.8}
$$

Therefore, the two states are orthogonal and this completes the proof. The crucial step is the second equality in the second line, where we used $U = -U^T$, as Eq. (4.4) requires when $\Phi = -\mathbb{1}$. This rather simple theorem is very important, as it protects the existence of edge states in 2DTIs, as we will see in the next Section.

4.1.2 *Quantum Spin Hall Effect*

Here, we just want to give an intuitive picture of what the QSHE is, without giving basically any details, for which the reader is referred to the extensive literature on the topic (e. g. [15, 16] and references therein). We can think of the QSHE as two copies of an IQHE state at filling factor 1 with different chiralities, as schematically depicted in Fig. 4.1. As a result, edge states where the chirality is related to
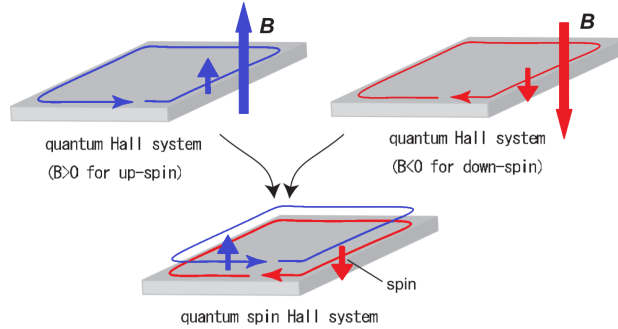
Figure 4.1: QSHE as a combination of two IQHE states with opposite chiralities. Image adapted from [169].

the spin projection can be obtained and the total magnetic field in the system vanishes, thus preventing time reversal symmetry from being broken. The direct relation between spin projection and chirality has been called spin-momentum locking [132]. In 2005, Kane and Mele [160] realized that such a system can be actually obtained in
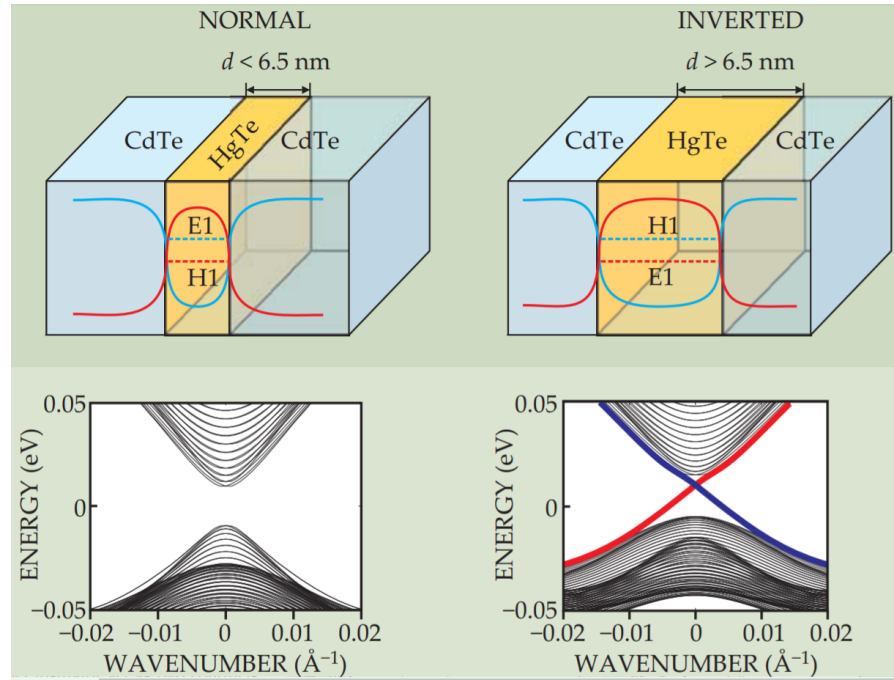
Figure 4.2: Band structure of the BHZ model. In the normal regime, the system is gapped and is a trivial insulator. In the inverted regime, a couple of helical states emerges in the bulk gap. The crossing of these states is protected by time reversal symmetry. Figure taken from [170].

graphene, as a result of spin-orbit interaction[1]. However, this was a proof of concept since the spin orbit coupling in graphene is too weak for the effect to be observed. Soon after the work of Kane and Mele, a proposal for observing the QSHE in a realistic material was put forward by Bernevig, Hughes and Zhang (BHZ model) [17] and later experimentally confirmed [18].

The BHZ model describes the low-energy properties of a CdTe/HgTe quantum well, depicted in Fig. 4.2. CdTe is a normal semiconductor, where the conduction band arising from electrons in s-orbitals is above the valence band arising from electrons in p-orbitals. On the contrary, in heavy materials such as HgTe, the s-like and p-like bands are inverted due to the effect of a very large spin-orbit coupling. By relying on an effective model built with these two bands, the authors were able to show that a phase transition occurs due to the band inversion induced when a quantum well with a thick enough HgTe component is realized. As we can see in Fig. 4.2, when the thickness of the HgTe is $d < 6.5$ nm, the quantum well is in the normal regime and the system is an insulator. However, for $d > 6.5$ nm, the quantum well enters the inverted regime and a couple of gapless states emerges in the bulk gap.

---

1 In the derivation of their model, they also showed that the system can be actually seen as composed of two copies of the Haldane model for the Chern insulator [67].

Moreover, states with different slopes (i.e. with opposite velocities along the edge of the quantum well) are associated with opposite spin projections. Therefore, we obtain a very peculiar 1D conductor along the edge of the system (see Fig. 4.1), where the propagation direction of electrons is directly related to their spin projection: this property is known as spin-momentum locking. However, until now the two spin sectors of the Hamiltonian are considered as independent and one would expect that any coupling between them would open a gap at the level crossing, eventually destroying the edge modes. But this is impossible because of Kramer's theorem, as we now discuss.

Time reversal symmetry requires that the Bloch Hamiltonian satisfies $\Theta H(k)\Theta^{-1} = H(-k)$, where the momentum k takes values in the Brillouin zone and Θ is the time-reversal operator. In other words, the spectrum must be symmetric with respect to $k = 0$. As we have seen, Kramer's theorem further requires a double degeneracy, with the consequence that level crossing must happen at $k = 0$ and at the edge of the Brillouin zone (because due to Bloch periodicity the momenta at the edge of the Brillouin zone have to be identified). We then understand that the crossing inside the bulk gap in Fig. 4.2 is protected by time reversal symmetry and cannot be gapped without violating Kramer's theorem.

From the point of view of the bulk topological properties, the Chern number introduced in Sec. 1.2.1 vanishes (because of time reversal symmetry), but there is still a $\mathbb{Z}_2$ topological invariant μ. Differently from the Chern number, μ can assume only the values 0 or 1. The existence of only two different topological classes can be understood by a simple argument, relying on the bulk-boundary correspondence [15]. It has to do with the possible ways in which bands can be connected at the time reversal invariant momenta. In particular, supposing the
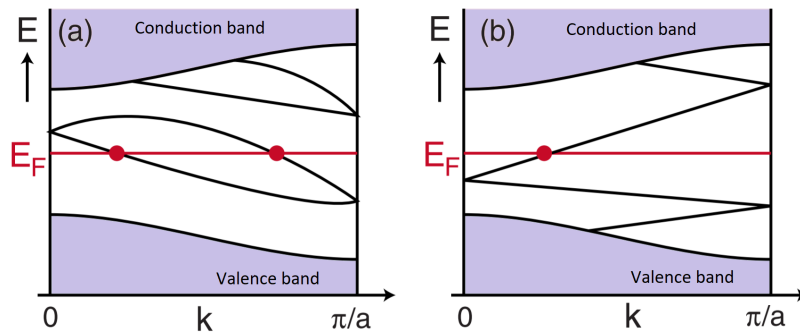
Figure 4.3: The two possibile ways of connecting the Kramer-degenerate points $k = 0$ and $k = \pi/a$ (degeneracies at other momenta are always split by the spin-orbit interaction). Image adapted from [15].

presence of edge states, there are only two ways to connect the two-fold degenerate states at $k = 0$ and $k = \pi/a$ (here a is the spacing of

the underlying lattice). This is shown in Fig. 4.3, where only half of the Brillouin zone is drawn, as the other half is mirror symmetric. If the states are pairwise connected as in panel (a), it is then possible to push them upwards or downwards into the conduction or valence bands, thus connecting the spectrum to the one of a trivial insulator. This is why the configuration with an even pair of helical edge modes is equivalent to no edge modes at all. This is the situation in which the topological invariant is $\mu = 0$. On the other hand, if the states are connected as in panel (b), there is no way of getting rid of the edge modes without violating Kramer's theorem. In this case, the system is topologically non-trivial and the invariant $\mu = 1$. Being no other possibilities, this explains why there is a $\mathbb{Z}_2$ classification of the system.

In conclusion, the QSHE is a topological phase of matter where helical modes emerge at the boundaries of the system. These states are characterized by the spin-momentum locking – relating the spin degree of freedom to the chirality of the mode – and are topologically protected.

4.2 MODEL AND CHARGE FRACTIONALIZATION

We consider a pair of interacting helical channels, capacitively coupled to an external voltage source, as schematically depicted in Fig. 4.4. Due to the spin-momentum locking, electrons on channel R are associated with spin up, while electrons on channels L have an opposite spin projection. Short range interactions between channels R and L are considered (represented by the wiggly lines in Fig. 4.4). As shown in Chapter 2, the Hamiltonian describing the helical system reads

$$H_{\text{HLL}} = \frac{u}{2} \sum_{\eta = \pm} \int_{-\infty}^{+\infty} dx \, [\partial_x \Phi_\eta(x)]^2 \,, \tag{4.9}$$
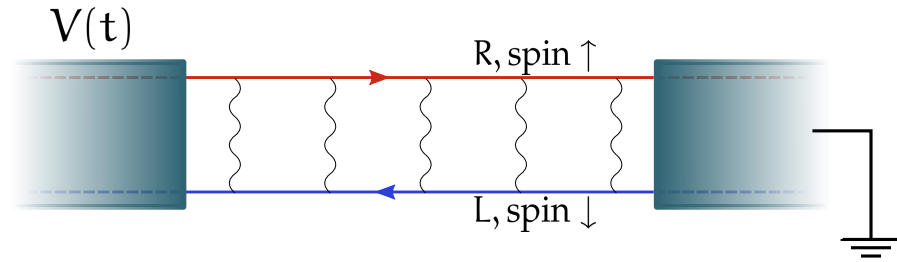
Figure 4.4: Sketch of a couple of interacting helical channels coupled to an external drive. Wiggly lines represent the interaction between the two channels.

where $\Phi_\eta(x)$ are the chiral bosonic fields defined in Sec. 2.2.3, which are related to the bosonic fields $\Phi_r(x)$ associated with channel r via the relation (2.33), which we rewrite here:

$$\Phi_r(x) = \sum_{\eta=\pm} A_{\eta\vartheta_r} \Phi_\eta(x), \qquad A_\pm = \frac{1}{2}\left(\frac{1}{\sqrt{K}} \pm \sqrt{K}\right). \qquad (4.10)$$

Recall that K is the Luttinger parameter [cf. (2.30)] quantifying the interaction strength and it assumes the value $K = 1$ in the non-interacting case, while $K < 1$ for repulsive interactions.

Although interesting in itself, the investigation of electronic correlations in the QSHE state can be important also from an experimental point of view. Recent results do indeed indicate that interaction effects can be relevant in QSHE systems: a Luttinger parameter $K = 0.42$ was reported in Bismuthene on SiC substrate [28]. In addition, evidence for interaction effects in the QSHE state realized in an InAs/GaSb quantum well was also reported in a previous work, claiming that $K = 0.22$ in that system [27]. Despite a later theoretical interpretation demonstrated that the experimental data could also be consistent with a value $K = 0.8$ [171], indicating weak electronic correlations, interaction effects still seem to be relevant.

The last ingredient present in Fig. 4.4 is the external drive, which is modeled by the Hamiltonian

$$H_g = -e \int_{-\infty}^{+\infty} dx\, U(x,t)[\rho_R^{(e)}(x) + \rho_L^{(e)}(x)], \qquad (4.11)$$

where $U(x,t)$ encodes the spatial and temporal profile of the external voltage. Hereafter we assume

$$U(x,t) = \Theta(-x)V(t) \qquad (4.12)$$

so that the drive $V(t)$ is applied in the region $(-\infty, 0)$. Moreover, we consider a periodic train of pulses with period T,

$$V(t) = \sum_{j\in\mathbb{Z}} V^{(0)}(t - jT), \qquad (4.13)$$

specifying only later the precise form of the pulse $V^{(0)}(t)$. The charge per period of the pulse (in units of $-e$) is

$$q = \int_{-T/2}^{T/2} \frac{-e}{2\pi} V(t)\, dt. \qquad (4.14)$$

As shown in detail in App. A.2, the equations of motion for fields Φ_η (obtained from $H_{HLL} + H_g$) are

$$(\partial_t + u\eta\partial_x)\Phi_\eta(x,t) = -e\sqrt{\frac{K}{2\pi}}\Theta(-x)V(t) \qquad (4.15)$$

and their solution reads

$$\Phi_+(x,t) = \phi_+(x-ut,0)$$
$$- e\sqrt{\frac{K}{2\pi}}\left[\Theta(x)\int_{-\infty}^{t-\frac{x}{u}}dt'V(t') + \Theta(-x)\int_{-\infty}^{t}dt'V(t')\right]$$
(4.16a)

$$\Phi_-(x,t) = \phi_-(x+ut,0) - e\sqrt{\frac{K}{2\pi}}\Theta(-x)\int_{t+\frac{x}{u}}^{t}dt'V(t'). \quad (4.16b)$$

Here, as in the previous Chapter, $\phi_\pm(x \mp ut, 0)$ denotes the chiral evolution of bosonic fields when no drive is applied. The time evolution of fermion operators $\Psi_r(x,t)$ is thus obtained by using (4.10) and the bosonization identity (2.10). Finally, a generic expectation value of an operator $O(t)$, is obtained as $\langle O(t)\rangle = \text{Tr}[\hat{\rho}O(t)]$. Here, $\hat{\rho}$ is the time-independent equilibrium density matrix at $t = -\infty$ when no voltage is applied and thus originating only from the Hamiltonian H_{HLL}.

4.2.1 *Excess particle density*

The expectation value of the particle density

$$\left\langle \rho^{(e)}(x,t)\right\rangle = \left\langle \rho_R^{(e)}(x,t) + \rho_L^{(e)}(x,t)\right\rangle \quad (4.17)$$

give us immediate information about the space profile of the excitations generated by the drive. In particular, we are interested in the deviations from the equilibrium situation

$$\Delta\rho^{(e)}(x,t) = \left\langle \rho^{(e)}(x,t)\right\rangle - \left\langle \rho_0^{(e)}(x,t)\right\rangle, \quad (4.18)$$

with $\rho_0^{(e)}(x,t)$ denoting the time evolution of the particle density operator in the absence of the drive. The evaluation of (4.18) is straightforward by writing $\rho^{(e)}(x,t) = \rho_+^{(e)}(x,t) + \rho_-^{(e)}(x,t)$, where the chiral density operators have been defined in (2.40):

$$\rho_\eta^{(e)}(x,t) = -\eta\sqrt{\frac{K}{2\pi}}\partial_x\Phi_\eta(x,t). \quad (4.19)$$

Thus, from (4.16) we readily find

$$\Delta\rho^{(e)}(x,t) = \sum_{\eta=\pm}\Delta\rho_\eta^{(e)}(x,t) = -e\sum_{\eta=\pm}\frac{\eta K}{2\pi u}V\left(t-\eta\frac{x}{u}\right)\Theta(\eta x). \quad (4.20)$$

This shows that the effect of the drive is to induce excitations propagating both to the right ($\eta = +$) and to the left ($\eta = -$). Notice that this expression is independent of the temperature and that the chiral
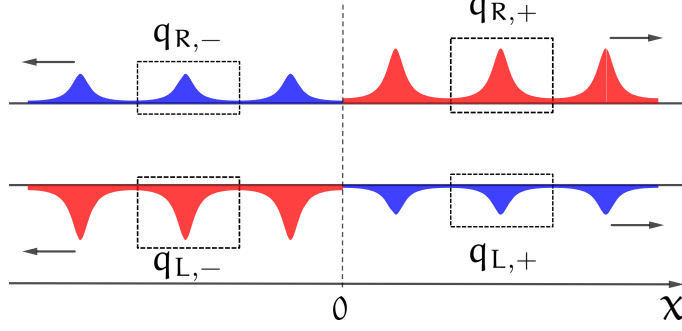
Figure 4.5: Sketch of the space profile of the excess charge density due to the periodic voltage $V(t)$, with $q > 0$. Excitations originating at $x = 0$ on both channels $r = R, L$ propagate in the positive or negative direction of the x axis, depending on the value of the index η. The charge per period (in units of $-e$) carried by each excitation is $q_{r,\eta}$, as given in (4.23). Red pulses indicate excitations which are also present in the non-interacting case, while blue ones refer to those originating only as a result of interactions.

right- (left-) moving excitation contributes only at $x > 0$ ($x < 0$), as shown in Fig. 4.5. Moreover, from the relation [cf. Eq. (2.41b)]

$$\Delta\rho_r^{(e)}(x,t) = \frac{\vartheta_r}{K}\left[\frac{1+\vartheta_r K}{2}\Delta\rho_+^{(e)}(x,t) - \frac{1-\vartheta_r K}{2}\Delta\rho_-^{(e)}(x,t)\right], \quad (4.21)$$

we understand that excitations for each chirality η are composed of contributions coming from both channels $r = R, L$. Finally, by combining (4.20) and (4.21), the spatial profile of the excitation on channel r moving in the η direction is

$$\Delta\rho_{r,\eta}^{(e)}(x,t) = \frac{-e\vartheta_r}{2\pi u}\frac{1+\eta\vartheta_r K}{2}V\left(t - \eta\frac{x}{u}\right)\Theta(\eta x), \quad (4.22)$$

as schematically depicted in Fig. 4.5. All the contributions described by the above formula can be distinguished, since R and L channels have opposite spin projections.

When $K = 1$, only $\Delta\rho_{R,+}^{(e)}$ and $\Delta\rho_{L,-}^{(e)}$ are present (red pulses), consistently with the fact that for free fermions R and L channels do not mix and are right- and left-moving, respectively. On the contrary, in the interacting case also the $(R, -)$ and $(L, +)$ channels are involved (blue pulses), due to charge fractionalization phenomena [25, 125, 126, 134, 138, 139]. The charge[2] per period $q_{r,\eta}$ carried on each channel is obtained by integrating over one period the corresponding contribution to the current flowing away from the point $x = 0$. Thus, by fixing a detection point $d > 0$, we find

$$q_{r,\eta} = u\int_{-T/2}^{T/2}\Delta\rho_{r,\eta}^{(e)}(\eta d, t)\,dt = \vartheta_r\frac{1+\eta\vartheta_r K}{2}q = \vartheta_r\sqrt{K}A_{\eta\vartheta_r}q, \quad (4.23)$$

---

2 With a little abuse of language, we shall systematically refer to $q_{r,\eta}$ as the charge of the excitations, actually meaning the charge in units of $-e$.

where (4.14) has been used and coefficients $A_{\eta\vartheta_r}$ are defined in (4.10). The charge $q_{r,\eta}$ carried by each excitation is an interaction-dependent fraction of the charge q injected by the drive $V(t)$, which is the experimentally tunable parameter. Notice that $\pm q$ would be the charge carried in the non-interacting system $(K = 1)$ by the excitation on channel $(R, +)/(L, -)$. We emphasize that the effect of interactions goes well beyond the simple renormalization of the charge carried on each channel. Indeed, interacting correlation functions contain interaction-dependent power-laws which are not present in the K=1 case [119, 130]. As detailed in the next Section, this leads to qualitative differences in the spectral properties between interacting and non-interacting systems.

4.3   NON-EQUILIBRIUM SPECTRAL FUNCTION

Following the same logic adopted in Chapter 3, we now go beyond the description of excitations in terms of their spatial profile – given by the excess particle density – and we investigate their energy content. While in the previous Chapter we considered both the momentum distribution (Sec. 3.3) and the Wigner function (Sec. 3.4), here we address the spectral functions of the fractionalized excitations, which can be directly probed via scanning tunneling spectroscopy, as we will show in Sec. 4.4.

4.3.1   *General properties*

Unlike the momentum distribution, which is related to correlations at equal time and different space points, the spectral function is obtained from the coherence function at different times and the same space point. Since we are interested in the non-equilibrium effects induced by the drive, we consider the excess coherence functions

$$\Delta \mathcal{G}_r^<(x, x; t_1, t_2) = \left\langle \Psi_r^\dagger(x, t_2)\Psi_r(x, t_1) \right\rangle e^{ie \int_{t_1}^{t_2} U(x,t')dt'}$$
$$- \left\langle \psi_r^\dagger(x, t_2)\psi_r(x, t_1) \right\rangle , \tag{4.24a}$$

$$\Delta \mathcal{G}_r^>(x, x; t_1, t_2) = \left\langle \Psi_r(x, t_1)\Psi_r^\dagger(x, t_2) \right\rangle e^{ie \int_{t_1}^{t_2} U(x,t')dt'}$$
$$- \left\langle \psi_r(x, t_1)\psi_r^\dagger(x, t_2) \right\rangle . \tag{4.24b}$$

Here, $\psi_r(x, t)$ denotes the time evolution of the fermion operator for r-electrons in the absence of the drive. The exponential factor appearing in the previous equation is a Wilson line, ensuring that coherence functions are gauge-invariant [172, 173]. Due to $V(t)$, the Green functions depend both on the difference $\tau = t_1 - t_2$ and on the average time $t = (t_1 + t_2)/2$. Therefore, we define the local (excess) spectral

functions as a Fourier transform with respect to τ, accompanied by an average over the period of the drive T:

$$\Delta \mathcal{A}_r^{\gtrless}(\omega; x) = \int_{-T/2}^{T/2} \frac{dt}{T} \int_{-\infty}^{+\infty} \frac{d\tau}{2\pi} e^{i\omega\tau} \Delta \mathcal{G}_r^{\gtrless}\left(x, x; t + \frac{\tau}{2}, t - \frac{\tau}{2}\right). \quad (4.25)$$

By resorting to standard bosonization techniques [119, 123], the excess coherence functions can be written as (see App. F.1)

$$\Delta \mathcal{G}_r^{\gtrless}\left(x, x; t + \frac{\tau}{2}, t - \frac{\tau}{2}\right) = \sum_{\eta = \pm} \Theta(\eta x) \Delta \mathcal{G}_{r,\eta}^{\gtrless}\left(t_\eta + \frac{\tau}{2}, t_\eta - \frac{\tau}{2}\right), \quad (4.26)$$

where $t_\eta = t - \eta x/u$ and the contribution of the excitation on the channel (r, η) has the structure

$$\Delta \mathcal{G}_{r,\eta}^{\gtrless}\left(t_\eta + \frac{\tau}{2}, t_\eta - \frac{\tau}{2}\right) = G_0^{\gtrless}(\tau) P_{r,\eta}^{\gtrless}(\tau) \Xi_{r,\eta}(t_\eta, \tau), \quad (4.27)$$

which we now comment step by step. Firstly, due to the function $\Theta(\eta x)$, the term related to the excitation with $\eta = +(-)$ contributes only at positive (negative) values of x. Taking advantage of this fact, we can write the relation

$$\Delta \mathcal{A}_r^{\gtrless}(\omega; x) = \sum_{\eta = \pm} \Theta(\eta x) \Delta \mathcal{A}_{r,\eta}^{\gtrless}(\omega), \quad (4.28)$$

which defines the greater/lesser spectral function $\Delta \mathcal{A}_{r,\eta}^{\gtrless}(\omega)$ associated with the excitation (r, η) as[3]

$$\Delta \mathcal{A}_{r,\eta}^{\gtrless}(\omega) = \int_{-T/2}^{T/2} \frac{dt}{T} \int_{-\infty}^{+\infty} \frac{d\tau}{2\pi} e^{i\omega\tau} G_0^{\gtrless}(\tau) P_{r,\eta}^{\gtrless}(\tau) \Xi_{r,\eta}(t, \tau). \quad (4.29)$$

Moreover, the factor

$$G_0^<(\tau) = \left\langle \psi_r^\dagger(x, 0) \psi_r(x, \tau) \right\rangle = \frac{1}{2\pi(a - iu\tau)} \left[\frac{a}{a - iu\tau} \right]^{2A_-^2} = G_0^>(-\tau) \quad (4.30)$$

represents the equilibrium coherence function at zero temperature and is independent of the channel index r (see App. D for the derivation of this expression). The term

$$P_{r,\eta}^<(\tau) = \frac{i\eta u\tau - a\vartheta_r}{i\eta u\tau} = P_{r,\eta}^>(-\tau) \quad (4.31)$$

stems from the point splitting procedure and ensures that the excess particle density

$$\Delta \rho_r^{(e)}(x, t) = \lim_{\tau \to 0} \Delta \mathcal{G}_r^<\left(x, x; t + \frac{\tau}{2}, t - \frac{\tau}{2}\right) \quad (4.32)$$

---

3 Notice that, thanks to the integration with respect to t (and the fact that the integrand function depends on this variable only via the combination $t_\eta = t - \eta x/u$), any dependence on x is lost. This is why we directly wrote $\Xi_{r,\eta}(t, \tau)$ in Eq. (4.29), instead of $\Xi_{r,\eta}(t_\eta, \tau)$.

is correctly reproduced in the diagonal limit. This point is discussed in detail in App. F.2 and (in a different context) in Ref. [154]. We emphasize that the factor (4.31) is only relevant at small values of τ and thus affects the corresponding spectral function $\Delta A_{r,\eta}^{\gtrless}(\omega)$ only at high energies.

The last term appearing in (4.27) is the phase factor $\Xi_{r,\eta}(t,\tau)$, which encodes all the dependence on the external drive and can be written as

$$\Xi_{r,\eta}(t,\tau) = \exp\left[-ie\eta\sqrt{K}A_{\eta\vartheta_r}\int_{t+\tau/2}^{t-\tau/2} V(t')\,dt'\right] - 1\,, \qquad (4.33)$$

where we recognize the fractionalization factors $\sqrt{K}A_{\eta\vartheta_r}$ already encountered when discussing the excess particle density [cf. also (4.10)].

By combining Eqs. (4.30), (4.31), (4.33) and plugging them into (4.29) we thus obtain an expression for the excess spectral functions $\Delta A_{r,\eta}^{\gtrless}(\omega)$ which is entirely general. From this expression it is then possible to derive some general properties which we now discuss.

SYMMETRY RELATIONS   The excess spectral functions obtained for the different possible combination of indices r and η are not independent. It is indeed straightforward to see from the above results that

$$\Delta A_{r,\eta}^{<}(\omega)\big|_q = \Delta A_{-r,-\eta}^{<}(\omega)\big|_{-q} = \Delta A_{r,\eta}^{>}(-\omega)\big|_{-q}\,. \qquad (4.34)$$

Here, we have explicitly indicated the dependence on the parameter q: the notation $\Delta A_{r,\eta}^{\gtrless}(\omega)\big|_q$ means that the spectral function is evaluated with a voltage $V(t)$ bearing a charge q [see Eq. (4.14)]. Thus, going from positive to negative q simply means flipping the sign of $V(t)$. Concerning instead the index r, it has to be understood that $-R = L$ and viceversa. Thanks to (4.34) we can simply focus on two spectral functions and obtain from those all other contributions by properly changing the sign of q and ω. In particular, we will investigate in detail $\Delta A_{R,\pm}^{<}(\omega, q)$.

In addition to Eq. (4.34), other symmetries are present in the non-interacting case $K = 1$:

$$\begin{aligned}
\Delta A_{r,\eta}^{<}(\omega)\big|_q &= -\,\Delta A_{r,\eta}^{>}(\omega)\big|_q = -\,\Delta A_{r,\eta}^{<}(-\omega)\big|_{-q}\,, \\
(r,\eta) &= (R,+) \text{ or } (L,-)\,.
\end{aligned} \qquad (4.35)$$

As a consequence, the total excess spectral function, defined as

$$\begin{aligned}
\Delta A_{r,\eta}(\omega)\big|_q &= \Delta A_{r,\eta}^{<}(\omega)\big|_q + \Delta A_{r,\eta}^{>}(\omega)\big|_q \\
&= \Delta A_{r,\eta}^{<}(\omega)\big|_q + \Delta A_{r,\eta}^{<}(-\omega)\big|_{-q}\,,
\end{aligned} \qquad (4.36)$$

vanishes when $K = 1$ independently of the drive. In the presence of interactions, instead, $\Delta A_{r,\eta}(\omega) \neq 0$. Therefore, a measure sensitive to

$\Delta\mathcal{A}_{r,\eta}(\omega)$ would be able to clearly distinguish between an interacting and a non-interacting system. Such a possibility will be addressed in Sec. 4.4.

SUM RULE AND MINIMALITY   The next general property is an important sum rule obtained by integrating the excess spectral functions over ω. By looking at (4.27) it is obvious that such an integration yields a $\delta(\tau)$. Thanks to this Dirac delta function, the remaining integrals are then easily computed: the small-τ expansion of the phase factor (4.33) for small τ compensates the divergence arising from the factor (4.31) and the final result reads

$$q_{r,\eta} = uT \int_{-\infty}^{+\infty} \Delta\mathcal{A}_{r,\eta}^{<}(\omega)\,d\omega = -uT \int_{-\infty}^{+\infty} \Delta\mathcal{A}_{r,\eta}^{>}(\omega)\,d\omega\,. \quad (4.37)$$

This indicates that the integral over energies of the lesser excess spectral function on channel r,η gives the charge per period carried by the excitation on that channel, in the same way as the integral over time of the excess charge density in Eq. (4.23).

Due to (4.37), we can introduce the notion of minimality of an excitation, by requiring that the corresponding excess spectral function has everywhere the same sign as the one dictated by its sum rule. The motivation for this definition lies in the fact that every $\Delta\mathcal{A}_{r,\eta}^{\gtrless}(\omega)$ physically represents a perturbation (with respect to equilibrium) which is globally larger if the function has somewhere a different sign compared to what (4.37) requires. As an example, if the excess spectral function $\Delta\mathcal{A}_{R,+}^{<}(\omega)$ of an excitation carrying a charge $q_{R,+} > 0$ is somewhere negative, this negativity region shows the presence of negative charges, which must be compensated because the integral over all energies is fixed to be $q_{R,+} > 0$. Thus the perturbation represented by $\Delta\mathcal{A}_{R,+}^{<}(\omega)$ is globally larger with respect to the case of a positive-definite excess spectral function.

PERIODIC DRIVE   As discussed in previous Chapters, in the presence of a periodic drive, it is possible to exploit the Fourier decomposition [117, 157]

$$e^{ie\int_0^t V(t')\,dt'} = e^{-iq\Omega t} \sum_{\ell \in \mathbb{Z}} p_\ell(q)\,e^{-i\ell\Omega t}\,, \quad (4.38)$$

where we recall that $\Omega = 2\pi/T$. By using (4.38) it is easy to show that

$$\int_{-T/2}^{T/2} \frac{dt}{T}\,\Xi_{r,\eta}(t,\tau) = -1 + \sum_{\ell \in \mathbb{Z}} |p_\ell(q_{r,\eta})|^2 e^{-i\eta\vartheta_r \tau(\ell+q_{r,\eta})\Omega}\,. \quad (4.39)$$

Moreover, if we let $\tau = 0$ in this expression and consider that Eq. (4.33) implies $\Xi_{r,\eta}(t,0) = 0$, we find the following very useful relation

$$\sum_{\ell \in \mathbb{Z}} |p_\ell(q_{r,\eta})|^2 = 1\,. \quad (4.40)$$

This result can be intuitively understood from the physical meaning of the photoassisted coefficients. Indeed, since p_ℓ is a probability amplitude for the process where an electron emits or absorbs ℓ energy quanta, the l.h.s. of (4.40) then represents the sum of the probabilities of all possible processes, which then have to sum up to one. Another useful sum rule is

$$\sum_{\ell \in \mathbb{Z}} \ell \, |p_\ell(q_{r,\eta})|^2 = 0 \tag{4.41}$$

and can be obtained by taking the τ-derivative of both sides of (4.39) and calculating the result for $\tau = 0$.

By plugging (4.39) into (4.29) for $\Delta \mathcal{A}_{r,\eta}^<(\omega)$, we finally obtain the following expression:

$$\Delta \mathcal{A}_{r,\eta}^<(\omega) = \frac{a^{2A_-^2}}{4\pi^2} \sum_{\ell \in \mathbb{Z}} |p_\ell(q_{r,\eta})|^2$$
$$\times \int_{-\infty}^{+\infty} d\tau \frac{e^{i\tau(\omega - \eta \vartheta_r \Omega_\ell)} - e^{i\omega\tau}}{(a - iu\tau)^{1+2A_-^2}} \frac{i\eta u\tau - a\vartheta_r}{i\eta u\tau}, \tag{4.42}$$

with $\Omega_\ell = (\ell + q_{r,\eta})\Omega$. Notice that the photoassisted coefficients depend on the charge $q_{r,\eta}$ of the different excitations.

4.3.2 Lorentzian pulses

As thoroughly discussed in Secs. 1.4–1.6, periodic trains of properly quantized Lorentzian pulses play a special role in the context of EQO [5, 116] and are currently the object of intense investigation due to their peculiar properties [30, 33, 34, 81, 85, 108, 117, 157, 174–182]. Here, we will thus focus on this particular kind of drive, so as to better highlight which differences arise due to the presence of repulsive interactions. The real-time shape of a single Lorentzian pulse is

$$V^{(0)}(t) = \frac{q}{-e} \frac{2w}{w^2 + t^2} \tag{4.43}$$

and its photoassisted coefficients have been reported in (3.64). By plugging them into (4.42) it is thus possible to obtain the spectral functions by computing the integral (in general numerically).

As a first step, we now address the situation where the charge $q_{r,\eta}$ of the excitation on channel (r, η) assumes an integer value[4]. As a consequence of the particular form of the photoassisted coefficients of the Lorentzian drive, the spectral function shows some remarkable properties for these integer values. The behavior of the excess lesser spectral function $\Delta \mathcal{A}_{R,+}^<$ for right-moving wave packets is shown in

---

4 Since these charges depend on the interaction strength K according to (4.23), it is not possible that all $q_{r,\eta}$ be simultaneously integer, unless for very specific values of K. The case of a non-integer charge will be consider later in this Section.
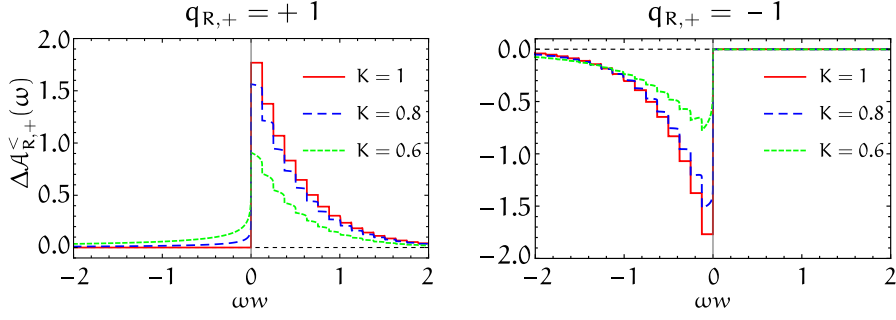
Figure 4.6: Lesser spectral function $\Delta\mathcal{A}_{R,+}^{<}(\omega)$, in units of $w(uT)^{-1}$, as a function of ωw. Charges are $q_{R,+} = \pm 1$, as specified on each panel and different values of the interaction strength K are indicated in the label. In all plots we set a representative value for the period $T = 50w$ and $a = 0.01uw$.

Fig. 4.6 for different values of the interaction strength K. Note that this contribution is present also in the non-interacting case ($K = 1$), where $q_{R,+} = q$. Different panels correspond to integer but opposite values of the injected charge $q_{R,+} = \pm 1$ [we recall that $q_{R,+} = q\sqrt{K}A_+$, according to (4.23)]. In the absence of interactions ($K = 1$), (4.35) dictates that the spectral function with $q_{R,+} = -1$ can be obtained by reversing the one with $q_{R,+} = +1$ with respect to both axes. This results in a vanishing total spectral function $\Delta\mathcal{A}_{R,+} = \Delta\mathcal{A}_{R,+}^{<} + \Delta\mathcal{A}_{R,+}^{>} = 0$. On the other hand, a manifest asymmetry appears in the presence of interactions ($K < 1$), where the excess lesser spectral functions for positive and negative charges become independent. Another clear feature in Fig. 4.6(b) is that $\Delta\mathcal{A}_{R,+}^{<}(\omega) \propto \Theta(-\omega)$ when $q_{R,+} = -1$, independently of interactions. This behavior is uniquely due to the specific shape of integer Lorentzian pulses and, in particular, to the following peculiar property of their photoassisted coefficients:

$$p_\ell(q) = 0 \qquad \forall\, \ell\, \text{sign}(q) < -|q|, \quad q \in \mathbb{Z}. \tag{4.44}$$

In the non-interacting case, $K = 1$, the additional symmetry relation (4.35) is responsible for the appearance of a $\Theta(+\omega)$ also at the positive charge value $q_{R,+} = +1$, a feature which disappears when $K < 1$, where $\Delta\mathcal{A}_{R,+}^{<}(\omega)$ is finite for both $\omega \gtrless 0$ [Fig. 4.6(a)].

Importantly, in the non-interacting case only the channels $(R, +)$ and $(L, -)$ have a finite spectral weight, while for $K < 1$ other two channels are also present. The presence of these additional contributions in the non-equilibrium spectral function and in its variation are thus a unique fingerprint of interactions. The variation $\Delta\mathcal{A}_{R,-}^{<}(\omega)$ is shown for different interaction strengths $K < 1$ in Fig. 4.7, where, again, the two panels refer to opposite injected integer charges $q_{R,-} = \pm 1$ [we recall that $q_{R,-} = q\sqrt{K}A_-$, according to (4.23)]. The plots show that $\Delta\mathcal{A}_{R,-}^{<}(\omega)$ is nonvanishing for both $\omega \gtrless 0$ when its charge is negative, while a $\Theta(-\omega)$ appears for a positive charge. This shows once more

Figure 4.7: Lesser spectral function $\Delta \mathcal{A}_{R,-}^{<}(\omega)$, in units of $w(uT)^{-1}$, as a function of ωw. Charges are $q_{R,-} = \pm 1$, as specified on top of each panel and different values of the interaction strength K are indicated in the label. In all plots we set a representative value $T = 50w$ for the period and $a = 0.01uw$.

that the presence of interactions results in an asymmetric behavior of the non-equilibrium spectral function in response to positive or negative excitations.

Further information can be obtained from Figures 4.6 and 4.7 by looking at the sign of the spectral functions. We have already pointed out in (4.37) that the integral of $\Delta \mathcal{A}_{r,\eta}^{<}(\omega)$ yields the charge $q_{r,\eta}$. By inspecting the plots, we see that for the channel $(R,+)$ in Fig. 4.6 the sign of $\Delta \mathcal{A}_{R,+}^{<}$ is everywhere the same as the one of its integral. We actually prove in App. F.3 that the spectral function is always positive-definite for integer and positive $q_{R,+}$. This shows that, as far as the channel $(R,+)$ is concerned, Lorentzian pulses with associated integer charges remain minimal even in the presence of interactions. On the contrary, when we look at $\Delta \mathcal{A}_{R,-}$, we immediately notice that at low ω its sign is actually the opposite of the one required by the sum rule, meaning that a change of sign at high energies must take place in order for (4.37) to be fulfilled. This is explicitly shown in App. F.3 too. For this reason, the function $\Delta \mathcal{A}_{R,-}^{<}$ is not minimal also in the case of associated integer charges. The main properties of the spectral functions $\Delta \mathcal{A}_{R,\pm}^{<}$ are summarized in Table 4.1.

Having described the peculiarities of Lorentzian pulses with associated integer charges $q_{r,\eta}$, a comment on a generic situation of non-integer charge is in order. In this case qualitative differences appear and have to be considered, since it is in general not possible to have all charges $q_{r,\eta}$ simultaneously integer, unless for very specific values of the interaction strength. As an example, in Fig. 4.8 we plot the function $\Delta \mathcal{A}_{R,+}^{<}(\omega)$ for $q_{R,+} = \pm 0.6$, directly obtained from (4.42). The main difference to be appreciated with respect to the integer case in Fig. 4.6 is the absence of the $\Theta(-\omega)$ and that the sign of $\Delta \mathcal{A}_{R,+}^{<}(\omega)$ is not defined, showing a non-minimal character.

Properties of $\Delta \mathcal{A}^<_{R,+}(\omega)$			Properties of $\Delta \mathcal{A}^<_{R,-}(\omega)$		
$q_{R,+}$	$K = 1$	$K < 1$	$q_{R,-}$	$K = 1$	$K < 1$
$+1$	$\propto \Theta(+\omega)$ minimal	always finite minimal	$+1$	zero	$\propto \Theta(-\omega)$ non-minimal
-1	$\propto \Theta(-\omega)$ minimal	$\propto \Theta(-\omega)$ minimal	-1	zero	always finite non-minimal

Table 4.1: Summary of the main properties of the spectral functions for integer charges. In the non-interacting case $K = 1$, no charge is injected on the $(R, -)$ channel and therefore $\Delta \mathcal{A}^<_{R,-}(\omega)$ vanishes everywhere. The properties of the other spectral functions can be obtained by using the symmetry relations (4.34).
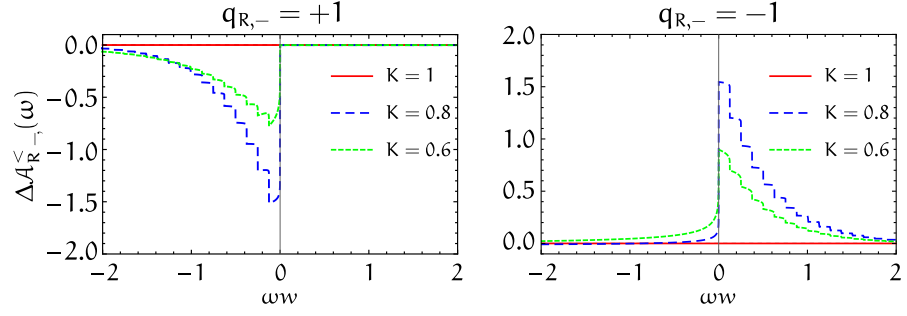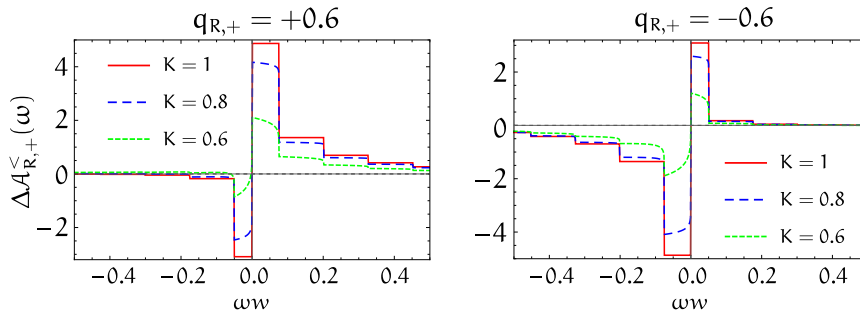

Figure 4.8: Excess lesser spectral fuction $\Delta \mathcal{A}^<_{R,+}(\omega)$, in units of $w(uT)^{-1}$, as a function of ωw. Here, we show an example of non-integer charge, with $q_{R,+} = \pm 0.6$. We set $T = 50w$ and $a = 0.01uw$.
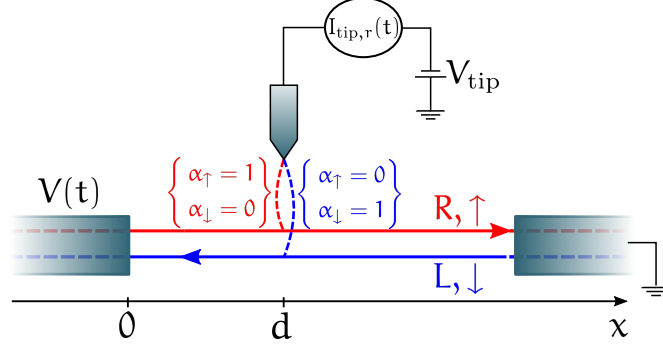
Figure 4.9: Sketch of the proposed setup. The interacting helical channels are driven by the periodic time-dependent voltage $V(t)$, applied in the region $x < 0$. A spin-polarized tip is placed at $d > 0$ and allows the spin-preserving tunneling of electrons, selecting their spin according to its polarization. The tip is modeled as a non-interacting system and is biased with a voltage V_{tip} with respect to the chemical potential of the helical channels. This setup measures the tunnel current between the system and the tip.

4.4   POSSIBLE EXPERIMENTAL SIGNATURES

In this Section we show how the intrinsic properties of the spectral functions can be probed by relying on a scanning tunneling setup with a spin-polarized tip, kept at a given (but tunable) bias V_{tip} with respect to the helical channels. As a result of this coupling, a tunnel current flows between the tip and the system. The spin polarization of the tip allows us to access all possible channels of the helical liquid, by exploiting the spin-momentum locking [183, 184]. Recently, this technique has been successfully used to probe the surface states of three-dimensional topological insulators [185–187].

We consider a spin-polarized tip, placed at a fixed position $d > 0$, as sketched in Fig. 4.9. The tip is coupled to the system via the tunneling Hamiltonian

$$H_t = \sum_{\sigma=\uparrow,\downarrow} \left[\lambda \left(\alpha_\uparrow \Psi_R^\dagger(d)\xi_\uparrow + \alpha_\downarrow \Psi_L^\dagger(d)\xi_\downarrow \right) + \text{H.c.} \right] , \qquad (4.45)$$

where ξ_σ is the annihilation operator for electrons of the tip with spin projection σ. The spin-up polarization of the tip is described by $\alpha_\uparrow = 1$ and $\alpha_\downarrow = 0$, the spin-down one by $\alpha_\uparrow = 0$ and $\alpha_\downarrow = 1$. Notice that $\xi_\uparrow$ and $\xi_\downarrow$ are only coupled to Ψ_R and Ψ_L, respectively, because we only include spin-preserving tunneling [183].

The tunnel current flowing between the system and the tip, when the latter is polarized with spin $\uparrow$ or $\downarrow$, can be written as

$$I_{tip,R/L} = ie\lambda \Psi_{R/L}^\dagger(d)\xi_{\uparrow/\downarrow} + \text{H.c.} \qquad (4.46)$$

The noise associated with its fluctuations is

$$S_{tip,r} = 2 \int_{-T/2}^{T/2} \frac{dt}{T} \int_{-\infty}^{+\infty} d\tau \left\langle \delta I_{tip,r} \left(t + \frac{\tau}{2} \right) \delta I_{tip,r} \left(t - \frac{\tau}{2} \right) \right\rangle, \quad (4.47)$$

where $\delta I_{tip,r}(t) = I_{tip,r}(t) - \langle I_{tip,r}(t) \rangle$.

Both quantities $\bar{I}_{tip,r} = \int_{-T/2}^{T/2} \frac{dt}{T} \langle I_{tip,r}(t) \rangle$ and $S_{tip,r}$ are evaluated by assuming that the tunneling Hamiltonian is a small perturbation. This allows one to use the perturbative expansion (3.55) and calculate the average current and noise to lowest order in the coupling constant λ. The calculation is essentially the same as the one presented in App. E.2, but it is shorter. The result, expressed by means of coherence functions, reads[5]

$$\bar{I}_{tip,r} = \frac{e|\lambda|^2}{T} \int_{-T/2}^{T/2} dt \int_{-\infty}^{+\infty} d\tau \left[\mathcal{G}_r^< \left(d, d; t + \frac{\tau}{2}, t - \frac{\tau}{2} \right) \mathcal{G}_{tip}^>(-\tau) \right.$$
$$\left. - \mathcal{G}_{tip}^<(\tau) \mathcal{G}_r^> \left(d, d; t - \frac{\tau}{2}, t + \frac{\tau}{2} \right) \right],$$

$$S_{tip,r} = \frac{2e^2|\lambda|^2}{T} \int_{-T/2}^{T/2} dt \int_{-\infty}^{+\infty} d\tau \left[\mathcal{G}_r^< \left(d, d; t + \frac{\tau}{2}, t - \frac{\tau}{2} \right) \mathcal{G}_{tip}^>(-\tau) \right.$$
$$\left. + \mathcal{G}_{tip}^<(\tau) \mathcal{G}_r^> \left(d, d; t - \frac{\tau}{2}, t + \frac{\tau}{2} \right) \right],$$

$$(4.48)$$

where the tip coherence functions,

$$\mathcal{G}_{tip}^<(\tau) = \langle \xi_\sigma^\dagger(0) \xi_\sigma(\tau) \rangle \tag{4.49a}$$

$$\mathcal{G}_{tip}^>(\tau) = \langle \xi_\sigma(0) \xi_\sigma^\dagger(-\tau) \rangle \tag{4.49b}$$

are independent of the spin σ. By taking the Fourier transform, it is now easy to relate the average current and the zero frequency noise to an overlap of spectral functions:

$$\bar{I}_{tip,r} = 2\pi e|\lambda|^2 \int_{-\infty}^{+\infty} d\omega \left[\mathcal{A}_r^<(\omega; d) \mathcal{A}_{tip}^>(\omega - eV_{tip}) \right.$$
$$\left. - \mathcal{A}_r^>(\omega; d) \mathcal{A}_{tip}^<(\omega - eV_{tip}) \right], \quad (4.50)$$

$$S_{tip,r} = 4\pi e^2|\lambda|^2 \int_{-\infty}^{+\infty} d\omega \left[\mathcal{A}_r^<(\omega; d) \mathcal{A}_{tip}^>(\omega - eV_{tip}) \right.$$
$$\left. + \mathcal{A}_r^>(\omega; d) \mathcal{A}_{tip}^<(\omega - eV_{tip}) \right]. \quad (4.51)$$

Here, $\mathcal{A}_r^{\gtrless}(\omega, d) = \mathcal{A}_0^{\gtrless}(\omega) + \Delta \mathcal{A}_r^{\gtrless}(\omega, d)$, with $\Delta \mathcal{A}_r^{\gtrless}(\omega, d)$ defined in (4.25) and the equilibrium term $\mathcal{A}_0^{\gtrless}(\omega)$ is the Fourier transform of (4.30):

$$\mathcal{A}_0^{\gtrless}(\omega) = \int_{-\infty}^{+\infty} \frac{d\tau}{2\pi} e^{i\omega\tau} G_0^{\gtrless}(\tau) = \frac{1}{2\pi u} \frac{e^{-\frac{a|\omega|}{u}}}{\Gamma(1 + 2A_-^2)} \Theta(\pm\omega) \left[\frac{a|\omega|}{u} \right]^{2A_-^2}.$$

---

[5] Notice that the expression for the noise has the same formal structure of the second term in (C.7). This is a general structure when current and noise are calculated at second order in the tunneling (or at all orders with scattering matrix theory in a non-interacting system).

$$(4.52)$$

Since $d > 0$, spectral functions are only related to the excitation on the channel $(r, +)$ [see Eq. (4.26)]. For notational convenience, we will not include the index $+$ in this Section, since there is no ambiguity. The equilibrium spectral functions of the tip are defined as

$$\mathcal{A}_{\text{tip}}^{\gtrless}(\omega) = \frac{1}{2\pi} \int_{-\infty}^{+\infty} d\tau \, \mathcal{G}_{\text{tip}}^{\gtrless}(\tau) \, e^{i\omega\tau}, \qquad (4.53)$$

and can be calculated from from (4.52), with $A_- = 0$ and $u = v_F$, because the tip is considered as non-interacting. Then, for $a \to 0$, $\mathcal{A}_{\text{tip}}^{\gtrless}(\omega) = (2\pi v_F)^{-1} \Theta(\pm\omega)$. Therefore, the deviations $\Delta \bar{I}_{\text{tip},r}$ in the current (4.50) due to the only effect of the drive $V(t)$ can be expressed as

$$\Delta \bar{I}_{\text{tip},r}(V_{\text{tip}}) = \frac{e|\lambda|^2}{v_F} \left[\int_{eV_{\text{tip}}}^{+\infty} d\omega \Delta \mathcal{A}_r^<(\omega) \big|_q - \int_{-\infty}^{eV_{\text{tip}}} d\omega \Delta \mathcal{A}_r^<(-\omega) \big|_{-q} \right]. \qquad (4.54)$$

Similarly, the deviations $\Delta S_{\text{tip},r}$ in the noise (4.51) read

$$\Delta S_{\text{tip},r}(V_{\text{tip}}) = \frac{2e^2|\lambda|^2}{v_F} \left[\int_{eV_{\text{tip}}}^{+\infty} d\omega \Delta \mathcal{A}_r^<(\omega) \big|_q + \int_{-\infty}^{eV_{\text{tip}}} d\omega \Delta \mathcal{A}_r^<(-\omega) \big|_{-q} \right]. \qquad (4.55)$$

It is important emphasizing that $\Delta \bar{I}_{\text{tip},r} \neq 0$ even at zero static bias ($V_{\text{tip}} = 0$), because the system is driven out of equilibrium by the presence of $V(t)$, which has a non-zero dc component. In addition, while in general the deviations $\Delta \bar{I}_{\text{tip},r}$ and $\Delta S_{\text{tip},r}$ are different from $\bar{I}_{\text{tip},r}$ and $S_{\text{tip},r}$ obtained in (4.50) and (4.51), the difference disappears at $V_{\text{tip}} = 0$. Finally, we introduce the excess noises by combining the last two equations:

$$\begin{aligned} \Delta S_{\text{exc},r}^{(\pm)}(V_{\text{tip}}) &= \Delta S_{\text{tip},r}(V_{\text{tip}}) \mp 2e\Delta \bar{I}_{\text{tip},r}(V_{\text{tip}}) \\ &= \pm \frac{4e^2|\lambda|^2}{v_F} \int_{\mp\infty}^{eV_{\text{tip}}} d\omega \, \Delta \mathcal{A}_r^{\gtrless}(\omega) \big|_q. \end{aligned} \qquad (4.56)$$

These quantities represent the deviations of the noise from its Poissonian limiting value.

We have now defined all the quantities we need in order to probe the spectral properties of the helical channels that we have discussed in detail in Sec. 4.3. First of all, the variation of the total spectral distribution $\Delta \mathcal{A}_r(\omega) = \Delta \mathcal{A}_r^<(\omega) + \Delta \mathcal{A}_r^>(\omega)$ can be obtained from the excess differential conductance, namely

$$\Delta \mathcal{A}_r(\omega) = -\frac{v_F}{e^2|\lambda|^2} \frac{\partial \Delta \bar{I}_{\text{tip},r}(V_{\text{tip}})}{\partial V_{\text{tip}}} \bigg|_{eV_{\text{tip}}=\omega}. \qquad (4.57)$$
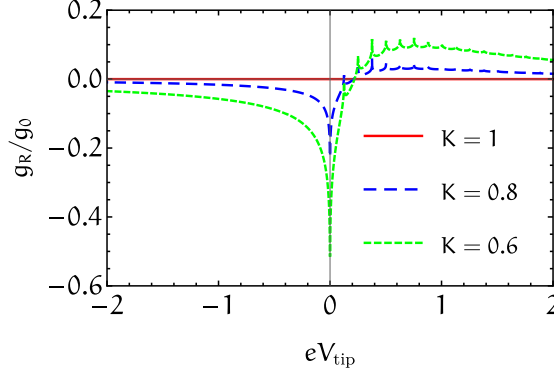
Figure 4.10: Excess differential conductance $g_R = \frac{\partial \Delta \bar{I}_{tip,R}(V_{tip})}{\partial V_{tip}}$ in units of $g_0 = \frac{e^2|\lambda|^2 w}{v_F u T}$, as a function of eV_{tip}, in units of w^{-1}. These plots are obtained for a Lorentzian drive with $q_{R,+} = 1$ and $T = 50w$ and directly give, up to a sign, the total excess spectral function $\Delta A_R(\omega)$, as established by (4.57). Notice that in the non-interacting case, the result is zero, due to the symmetry (4.35) of the spectral functions.

This quantity behaves differently depending whether the system is interacting or not. Indeed, recall that (4.36) implies that $\Delta A_r(\omega) = 0$ in the absence of interactions, regardless the shape of the drive. This does not hold anymore as soon as interactions are present. As an example, by considering a Lorentzian drive, we show in Fig. 4.10 the variation of the differential conductance for different values of the interaction strength, in the case where the tip is polarized with $\sigma = \uparrow$. Thanks to the sharply different behavior between interacting and non-interacting case, it is thus possible from a measurement of the current $\Delta I_{tip,r}$ to probe whether the system is interacting or not.

Additional information can be obtained by taking the derivative of the excess noise introduced in (4.56):

$$\Delta A_r^{\gtrless}(\omega, q) = \pm \frac{v_F}{4e^3|\lambda|^2} \frac{\partial \Delta S_{exc,r}^{(\pm)}(V_{tip})}{\partial V_{tip}} \Bigg|_{eV_{tip}=\omega} . \qquad (4.58)$$

This relation makes it possible, by varying V_{tip}, to reconstruct both the greater and lesser spectral functions and access all the features presented in Sec. 4.3. Notice also that the spectral functions of both channels R and L can be investigated by changing the polarization of the tip.

Further information about the excess noise can be extracted from (4.56). At $V_{tip} = 0$, the two quantities $\Delta S_{exc,R}^{(\pm)}(0)$ vanish when the excitation on the channel $(R, +)$ is a Lorentzian with integer charge. In particular $\Delta S_{exc,R}^{(+)}(0) = 0$ when $q_{R,+}$ is a positive integer (electron-like excitation, with $q > 0$), while $\Delta S_{exc,R}^{(-)}(0) = 0$ when $q_{R,+}$ is a negative integer (hole-like excitation, with $q < 0$). This is due to the fact that
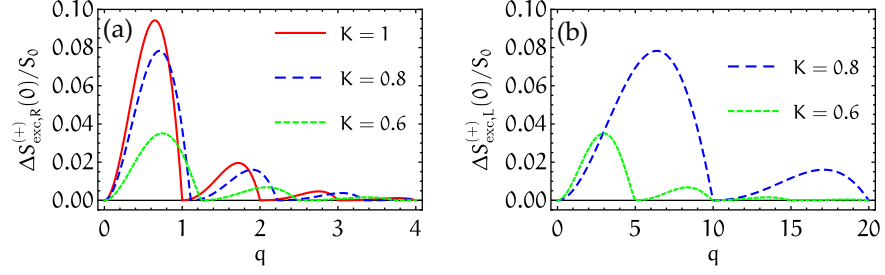
Figure 4.11: Panel (a): excess noise $\Delta S^{(+)}_{\text{exc,R}}(0)$, in units of $S_0 = e^2\Omega|\lambda|^2/(\pi u^2)$, as a function of q, for different values of the interaction K. The zeros are located at the points given by (4.59), namely when $q_{R,+}$ is a positive integer. Panel (b): excess noise $\Delta S^{(+)}_{\text{exc,L}}(0)$, in units of S_0. Here, the zeros are located according to (4.60). Note that no signal is present at $K = 1$. In both panels we set $w = 0.1T$ and $u(a\Omega)^{-1} = 10$.

$\Delta\mathcal{A}^{>}_R(\omega)|_{q_{R,+}=+1} \propto \Theta(\omega)$, while $\Delta\mathcal{A}^{<}_R(\omega)|_{q_{R,+}=-1} \propto \Theta(-\omega)$ (see Fig. 4.6). Through the same reasoning we see that $\Delta S^{(\pm)}_{\text{exc,L}}(0) = 0$ when $q_{L,+}$ is a negative [$q > 0$, see (4.23)] or positive ($q < 0$) integer, respectively. Let us focus on $\Delta S^{(+)}_{\text{exc,r}}(0)$ and analyze the conditions for it to vanish. When $r = R$, we need $q_{R,+} = n$, with $n \in \mathbb{N}^+$. In terms of the initial injected value q, this means

$$q = \frac{2n}{1+K}. \tag{4.59}$$

Likewise, when $r = L$, we need $q_{L,+} = -m$, with $m \in \mathbb{N}^+$, namely

$$q = \frac{2m}{1-K}. \tag{4.60}$$

In Fig. 4.11 we present the behavior of excess noise $\Delta S^{(+)}_{\text{exc,R/L}}(0)$ as a function of the externally tunable parameter q, showing that the zeros are indeed located at the points given by (4.59) and (4.60). By varying the interaction, the zeros in panel (a) move to higher values of q, as required by (4.59), while the opposite is true in panel (b), according to (4.60). In the latter case we do not have any signal at $K = 1$, since the spectral function on the L channel vanishes. This discussion demonstrates that a measurement of the excess noise could be used to extract the value of the interaction strength. Indeed, by looking for instance at the value of q at which the n-th zero in Fig. 4.11(a) occurs, the Luttinger parameter can be determined by solving (4.59) for K.

As a side comment, it is perhaps useful to recall that a vanishing excess noise in the case of Lorentzian pulses producing excitations with integer charge has been already reported in a QPC geometry for non-interacting systems [5, 8, 117] as well as in the integer [29, 114] and fractional quantum Hall effect [81]. Indeed, one can recognize

that expressions for the excess noise of a QPC are equivalent to the ones in (4.50) and (4.51). We emphasize however that interactions in counterpropagating helical channels result in a richer phenomenology in the excess noise, as the positions of the zeros depend on K.

We conclude this Chapter by underlining an important point concerning the relation between the concept of minimality and a vanishing excess noise. As it is clear from the above discussion, a vanishing excess noise is only due to the presence of proper Θ functions in the spectral functions. This property is uniquely determined by the Lorentzian drive and is therefore robust with respect to the presence of interactions. Indeed a vanishing excess noise can be achieved at any interaction strength, provided that the conditions in (4.59) or (4.60) are met.

In a non-interacting system a vanishing excess noise directly implies that $\Delta \mathcal{A}_R^<(\omega)$ has a definite sign, because the excess noise can be directly related to the number the unwanted particle-hole pairs. In other words, we have a one-to-one correspondence between the concept of minimal excitation and a vanishing excess noise. This is not anymore true if $K \neq 1$. To be more precise, it is still true as far as the "dominant" channels $(R, +)$ and $(L, -)$ are concerned, while this is not the case for channels $(R, -)$ and $(L, +)$. As an example, when a Lorentzian pulse with $q_{L,+}$ a negative integer is generated on the channel $(L, +)$, both $\Delta \mathcal{A}_{L,+}^{\gtrless}(\omega)$ do not have a definite sign, but still $\Delta S_{\mathrm{exc},L}^{(+)}(0) = 0$, as we see in Fig. 4.11. Similar considerations can be also done when $q_{L,+}$ is a positive integer. We conclude that, apart from the case $K = 1$, a vanishing excess noise is not necessarily related to a minimal spectral function (in the sense of absence of additional positive/negative charge). Phenomena related to this observation were already noticed in a different context [188].

LEVITONS IN A SUPERCONDUCTING BACKGROUND

In this Chapter we investigate the effect of superconducting correlations on Leviton-like excitations. For this purpose we consider the nonequilibrium transport properties of a junction between two superconductors, where one terminal is driven by an arbitrary periodic voltage. The main result we will show is that the excess noise due to quasiparticle transfers across the junction is again minimized by properly quantized Lorentzian pulses, which shows that this property is very robust as it survives in different kind of interacting systems. The model we use for describing the system relies on earlier studies in the literature of superconducting weak links, whose revision is well beyond the scope of this thesis. Therefore, we will just present this model as a starting point for our calculations, referring to the literature for details and thorough discussions. The work presented in this Chapter is based on our publication [32] and can be seen as a preliminary study towards the extension of EQO ideas to superconducting systems.

5.1 INTRODUCTION

The interest of the scientific community in transport properties of weakly coupled superconductors [189–191] dates back to the very first years following Josephson's famous prediction [192] that a nondissipative supercurrent can flow in a junction of two superconductors separated by an insulating layer as a result of a coherent tunneling of Cooper pairs. With the experimental advances in nanofabrication processes, it became possible to realize the so-called Superconducting Quantum Point Contact (SQPC) [193–198], i.e. a system where two superconducting regions are connected by a narrow constriction whose length is much smaller than the superconducting coherence length. The breaking junction technique [199–202] has turned out to be the most effective way of implementing SQPCs and paved the way to the realization of several experiments in this field [203–207]. Alternatively, the split gate technology in 2DEGs proximitized by superconducting electrodes [208] or in more exotic two-dimensional materials [209] exhibiting superconductivuty can also be emplyed.

From a theoretical point of view, a unified approach to the description of superconducting junctions under the effect of a constant voltage bias was developed in the mis 90s [210]. In this context, multiple Andreev reflections [211, 212] were identified as the key ingredient to

explain the subgap structure experimentally observed in the current-voltage characteristic. Other interesting effects arise when such junctions are subject to microwave radiations, a situation which has been extensively investigated, from early experiments by Shapiro [213] until much more recent research activity [214–218], witnessing a renewed interest in this topic.

Before going presenting our calculations, it is worth recalling (very briefly and without any aim for completeness) some basic aspects related to superconductivity and the Josephson effect, which will be useful in order to better understand our results.

ORDER PARAMETER AND COOPER PAIRS A superconductor is described by a complex order parameter [219], which is decomposed as $\Delta\,e^{i\vartheta}$, where Δ is called the superconducting gap and ϑ is the phase. The gap Δ is related to the binding energy of a Cooper pair [220]. The latter is the fundamental building block of a superconductor and is a bound state of two electrons which feel an effective attractive interaction mediated by phonons (at energies close to the Fermi level).

JOSEPHSON'S RELATIONS In 1962 Josephson derived the basic relations which describe the behaviour of a junction between two superconductors [192]. They are summarized by these two formulas

$$I(t) = I_J(t) + I_0(t) = I_c \sin[\phi(t)] + I_0(t), \tag{5.1a}$$
$$\dot{\phi}(t) = 2eV(t). \tag{5.1b}$$

Here, $I_0(t) \sim V(t)/R$ is a normal dissipative current, while $I_J(t)$ is called supercurrent because it is dissipationless. The amplitude I_c is called critical current and is proprotional to the gap Δ. Finally, ϕ is the phase *difference* between the two superconductors forming the junction and $V(t)$ is the voltage bias across it.

DC JOSEPHSON EFFECT The first surprising prediction arising from the previous relations is that a Josephson junction carries a current even in the absence of an external bias: indeed even for $V(t) = 0$, if a phase difference ϕ_0 is present, we have

$$I = I_c \sin \phi_0 \tag{5.2}$$

This current is dissipationless and is due to a coherent tunneling of Cooper pairs.

AC JOSEPHSON EFFECT Another striking prediction is that a Josephson junction biased with a constant potential V_0 develops an alternating current response. This is clearly seen by integrating (5.1b) and substituting the result into (5.1a):

$$I_J(t) = I_c \sin(\phi_0 + 2eV_0t). \tag{5.3}$$

The frequency $\omega_J = 2eV_0$ entering this expression is called the Josephson frequency. Of course, in any dc measure, the alternating supercurrent (5.3) would average to zero.

INVERSE AC JOSEPHSON EFFECT   When a combination of a dc bias and an alternating drive,

$$V(t) = V_0 + V_S \cos(\omega_S t), \tag{5.4}$$

is applied to a Josephson junction, dc supercurrent peaks appear at particular values of the bias V_0. Indeed, by integrating (5.1b) we have $\phi(t) = \phi_0 + \omega_J t + (2eV_S/\omega_S)\sin(\omega_S t)$. By plugging this result into (5.1a) one finds

$$I_J(t) = I_c \sum_{n\in\mathbb{Z}} (-1)^n J_n\left(\frac{2eV_S}{\omega_S}\right) \sin(\omega_J t + n\omega_S t + \phi_0), \tag{5.5}$$

where J_n are Bessel functions. This expression shows that the interplay of the dc bias V_0 and the alternating cosine drive results in a dc supercurrent

$$I_J = I_c \sum_{n\in\mathbb{Z}} (-1)^n J_n\left(\frac{2eV_S}{\omega_S}\right) \sin\phi_0 \tag{5.6}$$

whenever $\omega_J = n\omega_S$ or, equivalently,

$$V_0 = \frac{n\omega_S}{2e}, \quad n \in \mathbb{Z}. \tag{5.7}$$

Thus, the current-voltage characteristics of a junction driven by a signal (5.4) exhibits supercurrent spikes at voltages V_0 which are commensurate with the driving frequency ω_S according to (5.7). These are known as Shapiro spikes (if the junction is voltage biased) or Shapiro steps (if the junction is current biased) [213].

5.2   MODEL AND SETUP

We now start illustrating our calculation. The system we are interested in is a driven SQPC [194, 197], schematically depicted in Fig. 5.1, representing a junction between two superconducting regions, the left one being subject to a periodic but otherwise arbitrary time-dependent voltage

$$V(t) = V_{dc} + V_{ac}(t) = V(t + T), \tag{5.8}$$

with angular frequency $\Omega = 2\pi T^{-1}$. Here V_{dc} is the dc contribution and $V_{ac}(t)$ the ac part satisfying

$$\int_{-T/2}^{T/2} dt\, V_{ac}(t) = 0. \tag{5.9}$$
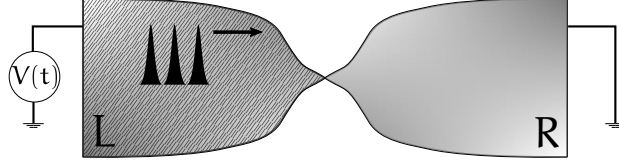
Figure 5.1: Sketch of the considered setup. A narrow constriction between two superconducting electrodes implements a quantum point contact geometry. A time-dependent voltage $V(t)$ is applied to the left side of the junction (shaded region), while the right electrode is grounded. Note that the schematic peaks depicted in the left contact refer to the applied voltage bias.

The starting point of our calculations is the model developed in Ref. [210], according to which the essential features of our system can be described by considering a single quantum channel, with the following Hamiltonian: [210, 221, 222]

$$H(t) = H_L + H_R + \lambda \sum_{\sigma=\uparrow,\downarrow} \left(e^{i\phi(t)} c_{L\sigma}^\dagger c_{R\sigma} + \text{H.c.} \right) . \tag{5.10}$$

Here, H_L and H_R are the BCS Hamiltonians of the uncoupled superconducting electrodes [223] and the tunnel term accounts for electron transfers between them. As shown in [221]

We consider a symmetric junction, meaning that the modulus of the superconducting gap Δ is equal in both right and left parts. The presence of an external bias can be included in the hopping amplitudes, which acquire a time dependence [224, 225] (see also App. G.1) and can be written as

$$\phi(t) = -\frac{\phi_0}{2} + e \int_0^t dt' \, V(t'), \tag{5.11}$$

where ϕ_0 is the bare superconducting phase difference between the electrodes.

The average current across the junction is given by

$$I(t) = ie\lambda \sum_{\sigma=\uparrow,\downarrow} \left(e^{i\phi(t)} \left\langle c_{L\sigma}^\dagger(t) c_{R\sigma}(t) \right\rangle - \text{H.c.} \right), \tag{5.12}$$

whereas the zero-frequency noise is defined as

$$S(t) = 2 \int_{-\infty}^{+\infty} dt' C(t+t', t), \tag{5.13}$$

with $C(t, t') = \langle I(t)I(t') \rangle - \langle I(t) \rangle \langle I(t') \rangle$. Both current and noise can be expressed via nonequilibrium Keldysh Green functions [226–228]. In particular, the relevant Keldysh components we need are expressed as matrices in the Nambu representation [229]:

$$\hat{G}_{i,j}^{+-}(t, t') = i \begin{pmatrix} \left\langle c_{j\uparrow}^\dagger(t') c_{i\uparrow}(t) \right\rangle & \left\langle c_{j\downarrow}(t') c_{i\uparrow}(t) \right\rangle \\ \left\langle c_{j\uparrow}^\dagger(t') c_{i\downarrow}^\dagger(t) \right\rangle & \left\langle c_{j\downarrow}(t') c_{i\downarrow}^\dagger(t) \right\rangle \end{pmatrix} \tag{5.14}$$

with $i, j = R, L$ and $\hat{G}_{i,j}^{-+}(t, t') = [\hat{G}_{j,i}^{+-}(t, t')]^\dagger$. Starting from the definition (5.12) it is straightforward to show that

$$I(t) = e\text{Tr}[\hat{\sigma}_3 \hat{W}(t)\hat{G}_{RL}^{+-}(t, t) - \hat{\sigma}_3 \hat{G}_{LR}^{+-}(t, t)\hat{W}^\dagger(t)], \tag{5.15}$$

where $\hat{\sigma}_3$ is the third Pauli matrix and the hopping matrix $\hat{W}(t)$ is defined as

$$\hat{W}(t) = \begin{pmatrix} \lambda e^{i\phi(t)} & 0 \\ 0 & -\lambda e^{-i\phi(t)} \end{pmatrix}. \tag{5.16}$$

As far as the noise is concerned, an equally straightforward though longer calculation relying on the repeated application of Wick's theorem allows one to derive the following result: [210, 230]

$$\begin{aligned} C(t, t') = 2e^2 \text{Tr}\Big[&\hat{\sigma}_3 \hat{W}(t)\hat{G}_{RR}^{-+}(t, t')\hat{\sigma}_3 \hat{W}^\dagger(t')\hat{G}_{LL}^{+-}(t', t) \\ &- \hat{\sigma}_3 \hat{W}(t)\hat{G}_{RL}^{-+}(t, t')\hat{\sigma}_3 \hat{W}(t')\hat{G}_{RL}^{+-}(t', t) \\ &+ \hat{\sigma}_3 \hat{W}^\dagger(t)\hat{G}_{LL}^{-+}(t, t')\hat{\sigma}_3 \hat{W}(t')\hat{G}_{RR}^{+-}(t', t) \\ &- \hat{\sigma}_3 \hat{W}^\dagger(t)\hat{G}_{LR}^{-+}(t, t')\hat{\sigma}_3 \hat{W}^\dagger(t')\hat{G}_{LR}^{+-}(t', t)\Big]. \end{aligned} \tag{5.17}$$

In a perturbative scheme regarding the coupling term λ in Eq. (5.10) as a small parameter, the full Green functions $\hat{G}$ are obtained from the unperturbed ones $\hat{g}$ describing the uncoupled electrodes via Dyson's equations (see App. G.2 for more details). In the energy domain, the advanced and retarded components of the latter are [210]

$$\hat{g}^{a/r}(\omega) = \frac{1}{\mathcal{E}\sqrt{\Delta^2 - (\omega \mp i\epsilon)^2}} \begin{pmatrix} -\omega \mp i\epsilon & \Delta \\ \Delta & -\omega \mp i\epsilon \end{pmatrix}, \tag{5.18}$$

where $\epsilon = 0^+$ and the energy scale $\mathcal{E} \sim 1/\pi\mathcal{D}(E_F)$ is related to the normal density of states $\mathcal{D}(E_F)$ at the Fermi energy [210]. Other components of Green functions are related to the above ones by

$$\hat{g}^{+-}(\omega) = 2i\,\text{Im}[\hat{g}^a(\omega)]n_F(\omega), \tag{5.19a}$$
$$\hat{g}^{-+}(\omega) = -2i\,\text{Im}[\hat{g}^a(\omega)]n_F(-\omega), \tag{5.19b}$$

with $n_F(\omega)$ the Fermi function.

5.3 DC CURRENT AND NOISE

We now come to the evaluation of the dc current and noise. They are defined as

$$I = \mathscr{T}^{-1} \int_{-\mathscr{T}/2}^{\mathscr{T}/2} dt\, I(t), \tag{5.20a}$$

$$S = \mathscr{T}^{-1} \int_{-\mathscr{T}/2}^{\mathscr{T}/2} dt\, S(t), \tag{5.20b}$$

where $\mathscr{T}$ is a measurement time, much longer than all the other time scales in the system. We consider the tunnel regime where the transmission of the junction is very small, so that current and noise can be evaluated to lowest order in the tunneling amplitude λ. The result can be expressed as:

$$I = I_0 + \zeta_{2q}(I_1 + I_J), \tag{5.21a}$$

$$S = S_0 + \zeta_{2q}S_1. \tag{5.21b}$$

As already seen in several instances, we recall that $q\Omega = -eV_{dc}$, with $V_{dc} = T^{-1}\int_0^T dt\, V(t)$ the dc component of the drive, while the factor ζ_x is defined as

$$\zeta_x = \begin{cases} 1 & \text{if } x \in \mathbb{Z}, \\ 0 & \text{if } x \notin \mathbb{Z}. \end{cases} \tag{5.22}$$

All contributions in Eq. (5.21) can be expressed in terms of the photoassisted amplitudes which we encountered several times. Here, however, we write the decomposition (3.62) in a slightly more general fashion [117, 157]

$$e^{ie\int_0^t dt'\,V(t')} = e^{-iq\Omega t}\sum_{\ell \in \mathbb{Z}} p_\ell(\alpha)e^{-i\ell\Omega t}. \tag{5.23}$$

In this expression, by analogy with the definition of q, we introduced a parameter $\alpha = -eV_{ac}^0/\Omega$, where V_{ac}^0 is the characteristic amplitude of the ac component of the drive $V_{ac}(t)$, see Eq. (5.8). As an example, for a harmonic drive we have $V(t) = V_{dc} + V_{ac}^0\cos(\Omega t)$. The difference with respect to the decomposition (3.62) used in the previous Chapters is that now the photoassisted amplitudes depend on α and not on q. The reason for keeping $\alpha \neq q$ is that the dc and ac parts of the drive can obviously be separately tuned and this possibility will turn out to be useful in order to perform a spectroscopic analysis of the p_ℓ coefficients, as we discuss in Sec. 5.5.

When the temperature θ is low enough for the gap Δ to be considered independent of it, i.e. $\Delta \gg k_B\theta$, all terms in Eq. (5.21) can be expressed as a single integral over energies (see App. G.2). Moreover, at zero temperaure it is possible to obtain analytical results, which we report below. The terms appearing in the current Eq. (5.21a) read

$$I_0 = \frac{4e\lambda^2}{\pi w^2}\sum_{\ell \in \mathbb{Z}}|p_\ell|^2\Theta(1 - |\Delta_\ell|)\,\Omega_\ell\,\mathcal{J}(\Delta_\ell) \tag{5.24}$$

$$\frac{I_1}{\Delta} = -\frac{4e\lambda^2}{\pi w^2}\sum_{\ell \in \mathbb{Z}}\text{Re}[e^{i\phi_0}p_\ell p_{-\ell-2q}]\Theta(1 - |\Delta_\ell|)\Delta_\ell K(\tilde{\Delta}_\ell) \tag{5.25}$$

$$\frac{I_J}{\Delta} = \frac{4e\lambda^2}{\pi w^2}\sum_{\ell \in \mathbb{Z}}\text{Im}[e^{i\phi_0}p_\ell p_{-\ell-2q}]|\Delta_\ell|$$
$$\times\left[\Theta(1 - |\Delta_\ell|)K(\Delta_\ell) - i\Theta(|\Delta_\ell| - 1)F\left(\varphi_\ell, \tilde{\Delta}_\ell\right)\right] \tag{5.26}$$
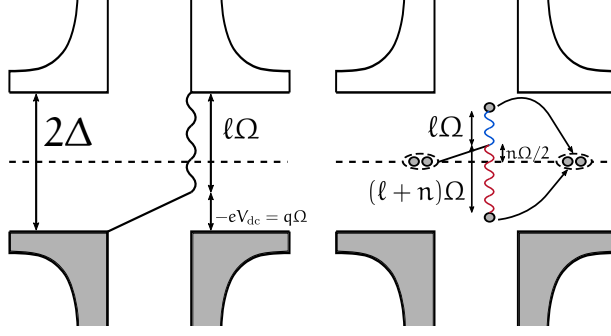
Figure 5.2: Sketch of typical processes involved in the dc current. Left panel: out-of gap process contributing to I_0. A quasiparticle gains an energy $q\Omega = -eV_{dc}$ (straight line) from the dc part of the drive and absorbs ℓ photons (wiggly line) to overcome the energy gap, thanks to the additional energy contribution $\ell\Omega$. This process is weighted by the probability $|p_\ell|^2$, appearing in the expression for I_0. Right panel: sub-gap process contributing to I_J. This process globally results in a transfer of a Cooper pair. Both electrons gain from the dc part of the drive an energy $q\Omega$, with $q = n/2$, $n \in \mathbb{N}$. Then the process is an interference between one electron absorbing ℓ photons (with amplitude p_ℓ, $\ell > 0$) and the other emitting $\ell + n$ photons (with amplitude $p_{-\ell-2q} = p_{-\ell-n}$). Finally the two electrons recombine to form a Cooper pair.

where $\Theta(x)$ is the Heaviside step function and we have defined the quantities

$$\Omega_\ell = (\ell + q)\Omega, \quad \Delta_\ell = \frac{2\Delta}{\Omega_\ell},$$
$$\tilde{\Delta}_\ell = \sqrt{1 - \Delta_\ell^2}, \quad \varphi_\ell = \arcsin\left(\frac{1}{\tilde{\Delta}_\ell}\right). \tag{5.27}$$

Moreover, $F(\varphi, x)$ is the incomplete elliptic integral of the first kind and $\mathcal{J}(x) = E(\sqrt{1-x^2}) - x^2 K(\sqrt{1-x^2})/2$, with $K(x)$ and $E(x)$ the complete elliptic integrals of the first and second kind, respectively [70, 231]. Expressions for noise contributions in Eq. (5.21b) are quite similar:

$$S_0 = \frac{8e^2\lambda^2}{\pi w^2} \sum_{\ell \in \mathbb{Z}} |p_\ell|^2 \Theta(1 - |\Delta_\ell|) |\Omega_\ell| \mathcal{J}(\Delta_\ell), \tag{5.28}$$

$$\frac{S_1}{\Delta} = -\frac{8e^2\lambda^2}{\pi w^2} \sum_{\ell \in \mathbb{Z}} \mathrm{Re}[e^{i\phi_0} p_\ell p_{-\ell-2q}] \Theta(1 - |\Delta_\ell|) |\Delta_\ell| K(\tilde{\Delta}_\ell). \tag{5.29}$$

All the above expressions are general and apply to any periodic drive as different signals are simply distinguished by their photoassisted amplitudes p_ℓ but, apart from that, no other dependence on the drive enters the formulas we have derived.

Let us now comment on results in Eq. (5.21) and their explicit expressions given below. Both the current and the noise contain a continuous contribution as a function of q (I_0 and S_0) and terms
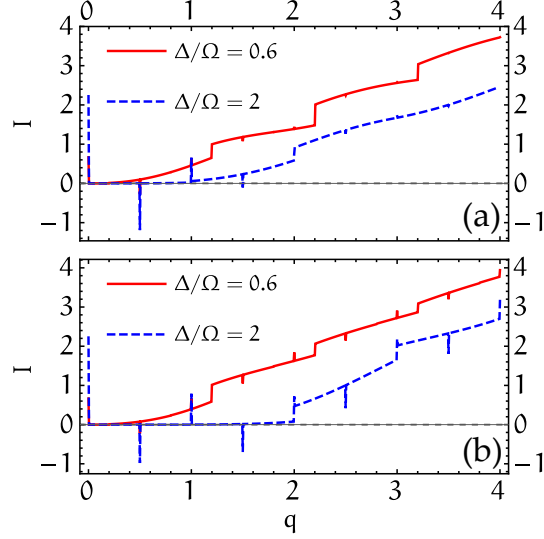
Figure 5.3: Total current I, in units of $e\mathcal{T}\Omega/\pi$, as a function of q and for two values of Δ/Ω, as indicated in the plots. $\mathcal{T} = 4\lambda^2/\mathcal{E}^2$ is the transmission of the junction. (a): the case of a Lorentzian drive with $\eta = 0.1$ [see Eq. (5.38)]. (b): the case of a sine drive $V(t) = V_{dc}[1 - \cos(\Omega t)]$. In both panels we set $\phi_0 = \pi/4$.

appearing only at discrete values of the dc voltage, namely when $2q$ is integer. The latter are Shapiro step contributions [190, 213] and are due to the interplay of the ac Josephson effect and the frequency Ω of the external drive, that together give rise to a dc contribution (see the discussion about the inverse ac Josephson effect on page 109). The external bias appears in all terms via the combination $\Omega_\ell = (\ell + q)\Omega$, a typical signature of photoassisted transport.

The current I_0 is due to quasiparticle transfers across the junction; it involves only out-of-gap processes (due to the Θ function enforcing the "effective voltage" $\Omega_\ell = (\ell + q)\Omega$ to be greater than gap width 2Δ) and is independent of the superconducting phase difference ϕ_0. A typical process contributing to I_0 is depicted in Fig. 5.2 (left panel). It is easy to see that, in the metallic limit $\Delta = 0$, I_0 is the only surviving contribution to the current and reduces to the well known result $I_0 = \mathcal{T}(2e^2/h)V_{dc}$ [117], where $\mathcal{T} = 4\lambda^2/\mathcal{E}^2$ is the transmission of the junction in the tunnel limit [210] and $2e^2/h$ is the conductance of a spinful quantum channel.

Concerning the phase-dependent terms, I_J is the only contribution involving also sub-gap processes [second Θ function in Eq. (5.26)] and is a generalization of the dc Josephson current in the presence of an arbitrary periodic drive. It involves a transfer of Cooper pairs across the junction. From the dependence $p_\ell p_{-\ell-2q}$ (see Eq. (5.26)), we can interpret each transfer as an interference between processes where an electron absorbs ℓ photons, with amplitude p_ℓ and another

one emits $(\ell + n)$ photons, with amplitude $p_{-\ell-2q}$ and $2q = n$, which is the condition enforced by the factor ζ_{2q} in Eq. (5.21). Since both electrons also gain an energy $q\Omega = n\Omega/2$ from the dc part of the voltage, we then see that the final energies of the two electrons are equal and opposite, so that they recombine into a Cooper pair. This kind of process is also sketched in Fig. 5.2 (right panel). In the limit of a purely dc bias, which is obtained by replacing $p_\ell = \delta_{\ell,0}$, I_J reduces to

$$I_J = \delta_{q,0} \mathcal{T} \frac{e\Delta}{2} \sin(\phi_0) \tag{5.30}$$

and we recover the dc Josephson effect, with supercurrent flowing at zero bias [192, 225]. Of course, I_J is the only surviving contribution if no drive is applied to the system. The remaining term, I_1, has the same origin as the contribution proportional to $\cos\phi_0$ in the ac Josephson effect and can be interpreted as describing quasiparticle processes involving a superimposed pair transfer [190, 225, 232] (this term has not been discussed in the introduction in Sec. 5.1 and we refer the reader to the cited References for more information).

In Fig. 5.3 we show a representative behavior of the total current I as a function of q. We chose a Lorentzian and a sine drive, which will be discussed in detail in Sec. 5.4 in relation to the excess noise. From the plots in Fig. 5.3 we clearly observe the continuous contribution I_0, characterized by some discontinuities due to the Θ functions in the sum in Eq. (5.24). On top of that, Shapiro spikes at half-integer values of q appear. They come almost completely from I_J, since I_1 is found to be negligible for a wide range of parameters.

Finally, concerning the noise, S_0 and S_1 are the counterparts to I_0 and I_1, respectively, and are generated by the same processes contributing to I_0 and I_1. In particular, S_0 is associated with the partitioning of quasiparticles excited above the gap by the driving voltage. There is however no term in the noise associated with sub-gap processes appearing in I_J, which are therefore noiseless [224, 225]. In the following we analyze the above general results in two different regimes.

5.4   EXCESS NOISE AND LORENTZIAN DRIVE

As we have seen in several instances across this thesis, Lorentzian pulses play a special role in the context of EQO and are being extensively studied [5, 29, 33–35, 82, 85, 117, 175, 233–235]. For such a reason it is then natural to ask whether their peculiar properties survive in the presence of superconducting correlations. One of the most important of them, is the minimization of the noise, which is the main point we are now going to address. In this Section we consider the ac and dc amplitudes of the drive to be equal, namely $\alpha = q$.

For a generic drive, the excess noise can be defined as [81, 117]:

$$\Delta S = S - 2eI. \tag{5.31}$$

The above definition involves the total current and noise and can be decomposed as

$$\Delta S = \Delta S_0 + \Delta S_1 - 2eI_J, \tag{5.32}$$

with $\Delta S_{0,1} = S_{0,1} - 2eI_{0,1}$. In particular, ΔS_0 only refers to quasiparticle terms and will constitute the main focus of our discussion. As a matter of fact, S_1, I_1 and I_J are defined only for half-integer values of q and depend on the superconducting phase difference ϕ_0. Therefore, in a setup where ϕ_0 is not fixed, it is in principle possible to isolate S_0 and I_0. Indeed, I_1 and S_1 will vary as $\cos(\phi_0)$, while I_J as $\sin(\phi_0)$ and then these contributions can be subtracted by averaging over different measurements. For these reasons we focus our attention on ΔS_0. We also mention that Eq. (5.31) can be considered as a rewriting of the Fano factor $F \equiv S/2eI$. Indeed if the latter quantity is used instead of our definition, we obtain $F = 1$ for Levitons carrying an integer charge. This constitutes a signature that quasiparticles with unit charge tunnel at the QPC. In the tunnel limit which we are considering here, this is the only relevant process as multiple Andreev reflections are absent (higher order processes in λ would be needed in order to access them). From Eq. (5.24) and Eq. (5.28) we immediately find:

$$\Delta S_0 = \frac{16e^2\lambda^2}{\pi w^2} \sum_{\ell < -q} |p_\ell|^2 \Theta(1 - |\Delta_\ell|)\Omega|\ell + q|\mathcal{J}(\Delta_\ell). \tag{5.33}$$

Before moving to the discussion of Lorentzian pulses, it is instructive to highlight a deeper connection between the excess noise and single-electron properties, which we have already encountered in the previous Chapter. Very generally, by starting from Eq. (5.17) and using Dyson's equations (G.11) and (G.13), one can show that the excess noise ΔS_0 can be written in terms of Green function as

$$\Delta S_0 = \frac{4e^2\lambda^2}{\pi} \int_{-\infty}^{+\infty} d\omega\, g_0^{+-}(\omega) \sum_{\ell \in \mathbb{Z}} |p_\ell|^2 g_0^{-+}(\omega - \Omega_\ell). \tag{5.34}$$

Here, the subscript 0 in Green functions denotes the term proportional to the identity matrix $\hat{\sigma}_0$ in Nambu space. Recall also that $\Omega_\ell = (\ell + q)\Omega$. This formula has the typical structure of the Tien-Gordon effect [236] and involves an overlap between two Green functions: $g_0^{+-}(\omega)$ at equilibrium and $g_0^{-+}(\omega)$, shifted by the dc bias $q\Omega$ as well as all energies $\ell\Omega$ corresponding to photoassisted processes and weighted by the probability $|p_\ell|^2$.

It is possible to link Eq. (5.34) to electron energy distributions which are usually employed in the context of EQO [1, 113]. In particular, here
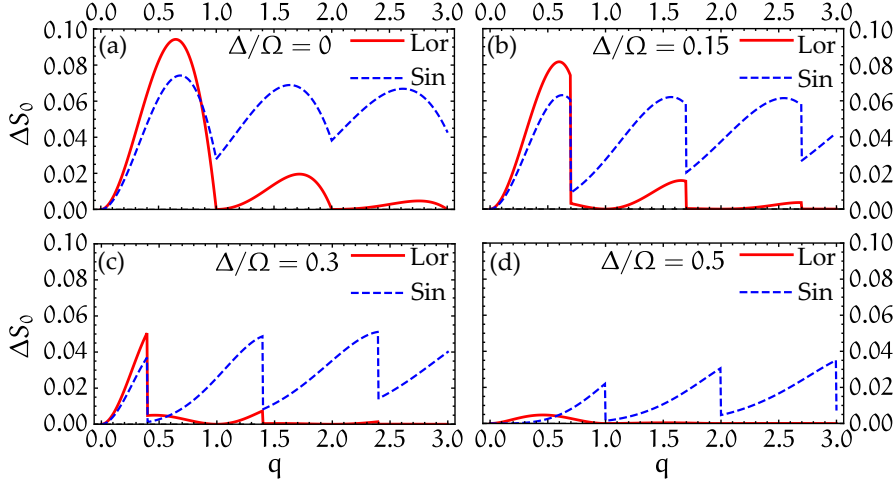
Figure 5.4: Excess noise ΔS_0 for different values of Δ/Ω as a function of q, in units of $2e^2 \mathcal{T}\Omega/\pi$. The width of Lorentzian pulses is $\eta = 0.1$. Full red curves refer to Lorenzian pulses, dashed blue ones to a sine drive $V(t) = V_{dc}[1 - \cos(\Omega t)]$, with $q\Omega = eV_{dc}$.

we refer to nonequilibrium energy distribution of the left side of the SQPC. We refer to Appendix G.1 for the details and here we simply state the result:

$$\Delta S_0 \propto \int_{-\infty}^{+\infty} d\omega \, f_{eq}^<(\omega) f^>(\omega) \,. \tag{5.35}$$

This formula is essentially the same as Eq. (4.51), which we derived in the previous Chapter. It is a general result that, at lowest order in the tunneling, the noise can be written as an overlap between two spectral distributions. Roughly speaking, $g_0^{+-}(\omega)$ gives the electron energy distribution at equilibrium $f_{eq}^<(\omega)$, while the sum in (5.34) containing $g_0^{-+}(\omega - \Omega_\ell)$ represents the hole energy distribution $f^>(\omega)$ in the presence of the drive. Their explicit expressions at zero temperature are

$$f_{eq}^<(\omega) = \frac{-2\omega}{\mathcal{E}\sqrt{\omega^2 - \Delta^2}} \Theta(-\omega - \Delta) \,,$$

$$f^>(\omega) = \sum_{\ell \in \mathbb{Z}} \frac{|p_\ell|^2}{\mathcal{E}} \frac{2(\omega - \Omega_\ell)}{\sqrt{(\omega - \Omega_\ell)^2 - \Delta^2}} \Theta(\omega - \Omega_\ell - \Delta) \,. \tag{5.36}$$

As a final remark, we notice that a similar procedure can be followed for ΔS_1. Indeed, despite this term is not relevant to our discussion, it can be shown that (assuming that $p_\ell \in \mathbb{R}$, which can be always done by a proper choice of the time origin)

$$\Delta S_1 \propto \cos\phi_0 \int_{-\infty}^{+\infty} d\omega \, g_1^{+-}(\omega) \sum_{\ell \in \mathbb{Z}} p_\ell p_{-\ell-2q} g_1^{-+}(\omega - \Omega_\ell) \,, \tag{5.37}$$

where g_1 is the off-diagonal component of the Green function in Nambu space. The above expression can be obtained by starting from

anomalous correlators of the form $\langle c_{L\downarrow}(t')c_{L\uparrow}(t)\rangle$ and following the calculation which is presented in Appendix G.1.

Let us now discuss in detail the relevant case of a Lorentzian drive. A train of Lorentzian-shaped pulses has the form (3.63)

$$V(t) = \frac{V_{dc}}{\pi} \sum_{k\in\mathbb{Z}} \frac{\eta}{\eta^2 + (t/T - k)^2} \, , \tag{5.38}$$

where η is the ratio between the width of a pulse and the period T of the drive. Its photoassisted coefficients p_ℓ are given by (3.64) and have the peculiar property that they vanish for $\ell < -q$ in the case of quantized pulses, i.e. for integer values of q [cf. Eq. (4.44)]. Consequently, I_1 and S_1 vanish for integer Levitons. This is because the combination of photoassisted coefficients appearing in Eq. (5.25) and Eq. (5.29) becomes in this case

$$p_\ell p_{-\ell-2q} = \zeta_q \delta_{\ell,-q} p_{-q}^2, \tag{5.39}$$

enforcing $\ell = -q$ and, eventually, $I_1 = S_1 = 0$ due to the action of the Θ functions. This means that, unlike any other drive, the noise for quantized Lorentzian pulses is independent of the bare superconducting phase difference ϕ_0. Moreover, another interesting property is that the I_J contribution reduces to

$$I_J = \mathcal{T}\frac{e\Delta}{2}p_{-q}^2 \sin(\phi_0) \tag{5.40}$$

for integer Levitons. This is a very simple Josephson-like relation, where the supercurrent peaks occurring at integer q are weighted by the photoassisted amplitude p_{-q}^2.

Concerning the behavior of the excess noise, Eq. (5.33) shows that it vanishes for Levitons with integer charge, in the same way as in the free-electron case [5, 117]. This is a direct consequence of the properties of their p_ℓ coefficients. In Fig. 5.4 we plot the excess noise ΔS_0 for different values of the ratio Δ/Ω, comparing Lorentzian and cosine drives. In the metallic limit $\Delta = 0$ [Fig. 5.4(a)] we recover well-known behaviors (cf. Fig. C.2 in App. C.1), while at finite gap we observe the appearence of sharp discontinuities [Figs. 5.4(b)–(d)] which are due to the BCS density of states, as we will argue in the following. Still, we clearly observe that quantized Lorentzian pulses minimize the excess noise, in contrast to the harmonic voltage.

By increasing the ratio Δ/Ω, we observe a progressive overall suppression of the signal for both drives. This can be understood by noticing that, in the adiabatic limit $\Delta \gg \Omega, eV_{dc}$, no contribution other than I_J can survive, since no transport across the gap is possible anymore and I_J is the only term involving also sub-gap processes (see Sec. 5.5 for a more thorough discussion). For this reason, even though only quantized Levitons minimize the excess noise (strictly speaking), the major differences between integer Lorentzian pulses and any other
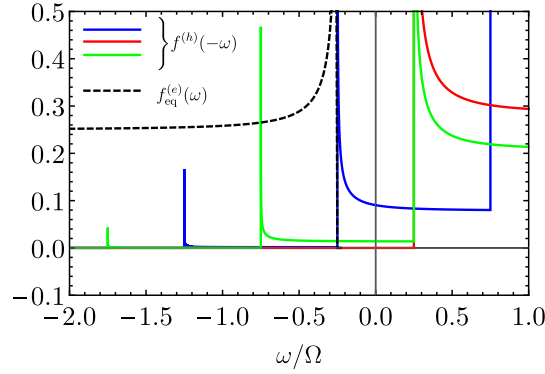
Figure 5.5: Overlap between equilibrium distribution $f_{eq}^<(\omega)$ (black dashed curve) and out-of-equilibrium distribution $f^>(\omega)$ (both in units of $2/\mathcal{E}$) for $\Delta/\Omega = 0.25$ and: Lorentzian drive at $q = 1$ (red curve), Lorentzian drive at $q = 0.5$ (blue curve) and sine drive at $q = 1$ (green curve). The width of Lorentzian pulses is $\eta = 0.1$. Notice that the equilibrium distribution has been reduced by a factor of 4 to better appreciate the contributions from $f^>(\omega)$, which are quite small in the region $\omega < -\Delta$.

drive are best appreciated if the ratio Δ/Ω is at most of the order of unity. We comment about this constraint in Sec. 5.6. By increasing Δ/Ω, we progressively enter the adiabatic regime and the transport properties of the junction become qualitatively similar for any drive, as we will discuss in the following Section.

Finally, we illustrate the behavior of the distribution functions in Eq. (5.36), which are related to the excess noise by Eq. (5.35). Fig. 5.5 shows the overlap of these distributions for some values of q and a fixed Δ/Ω. It is always zero for quantized Levitons because in this case $p_\ell = 0$ for $\ell < -q$. This means that $f^>(\omega)$ is nonzero only for $\omega > \Delta + \ell\Omega$, with $\ell \geqslant 0$ and the overlap vanishes because $f_{eq}^<(\omega)$ is nonzero for $\omega < -\Delta$. This is no longer the case for non-quantized Lorentzians or any other drive, for which $f^>(\omega)$ is nonvanishing also in the region $\omega < -\Delta$. The structure of functions in Eq. (5.36) also allows us to understand the discontinuities observed in Fig. 5.4. Indeed, both $f_{eq}^<$ and $f^>$ show signatures of the square root singularity of the BCS density of states. The singularity of the equilibrium distribution is at $\omega = -\Delta$, while those of $f^>$ depend on the values of ℓ and q. When a singularity of $f^>(\omega)$ enters/leaves the region $\omega < -\Delta$, an abrupt increase/decrease of the overlap between the two distribution occurs. At a given ℓ, this happens when $q = -\ell - 2\Delta/\Omega$, which are precisely the values where discontinuities in ΔS_0 are observed (see Fig. 5.4).

As a concluding comment, it is worth mentioning that a complete characterization of the excitations induced in the system by the drive would require the investigation of complementary quantities such as the electron distribution and the anomalous correlator in the k-space,

which are beyond the purpose of this Chapter, where we simply investigate the transport properties of the SQPC. Unfortunately, such quantities are difficult to be addressed experimentally. This constitutes the main motivation to investigate current fluctuations – in particular ΔS_0 – which is directly connected to the photo-assisted (out of equilibrium) energy distribution $f^>(\omega)$. Although less transparent from the point of view of fully characterizing the induced excitations, this quantity is still very interesting and routinely investigated in experiments.

5.5   LARGE GAP: ADIABATIC LIMIT

Let us now analyze the situation where the superconducting gap is the most relevant energy scale in the problem. This, in particular, means that both the excitation frequency Ω and eV_{dc} have to be much smaller than the gap Δ. In this limit all contributions to the current and noise but I_J are progressively suppressed. Mathematically, this is because the bigger the gap, the higher the value that the index ℓ has to assume to prevent Θ functions from vanishing. Although ℓ can assume any value in principle, in practice contributions at high ℓ are strongly suppressed due to the p_ℓ coefficients. More physically and intuitively, this means that when Δ is by far the biggest energy scale, the drive cannot provide enough energy to the system for out-of-gap processes to be possible, even with the photoassisted tunneling mechanism. Therefore the relevant quantity in the adiabatic regime is the part of I_J involving sub-gap processes. Thanks to the limit $\Delta \gg \Omega, eV_{dc}$, Eq. (5.26) for I_J considerably simplifies and becomes

$$I_J = \mathcal{T}\frac{e\Delta}{2}\sum_{\ell\in\mathbb{Z}}\text{Im}[p_\ell p_{-\ell-2q}e^{i\phi_0}] = \mathcal{T}\frac{e\Delta}{2}p_{-2q}(2\alpha)\sin(\phi_0), \quad (5.41)$$

where we assumed, without loss of generality, that photoassisted coefficients are real and we used the general property

$$\sum_{\ell\in\mathbb{Z}}p_\ell(\alpha)p_{-\ell+x}(\alpha) = p_x(2\alpha). \quad (5.42)$$

This result has the same structure of Eq. (5.40), to which it reduces in the case of a Lorentzian drive, since $p_{-2q}(2q) = p^2_{-q}(q)$ for integer q. We emphasize, though, that in the case of integer Levitons Eq. (5.40) holds for any value of the ratio Ω/Δ, without restrictions. Eq. (5.41) describes a series of supercurrent spikes appearing whenever $2q$ is integer, whose amplitude is determined by the photoassisted coefficient $p_{-2q}(2\alpha)$ (recall that α is related to the ac amplitude of the drive). The condition $2q \in \mathbb{Z}$ means that the dc amplitude of the drive has to satisfy $V_{dc} = n\Omega/2e$, with integer n. This is nothing buth the condition fo the appearance of Shapiro spikes in the current-voltage characteristics, as discussed on page 109 in the case of a harmonic

drive. Here, we recover the same kind of effect, but in the presence of an arbitrary periodic drive. The photoassisted coefficient $p_{-2q}(2\alpha)$ replaces and generalizes the Bessel functions appearing in (5.6).

We also notice that the relation in Eq. (5.41) could be used as a tool to operate a "spectroscopy" of photoassisted absorption and emission probabilities by varying independently α and q, in the same spirit of what has been proposed in Ref. [117]. It is indeed possible to vary the ac amplitude of the drive (and hence α) in correspondence of the fixed dc amplitudes where Shapiro spikes occur, thus recovering p_ℓ coefficients from the amplitude of the spike.

5.6 SUMMARY

The results presented in this Chapter can be regarded as a preliminary study for the extension of EQO ideas to systems with superconducting correlations. In particular, here we characterized the transport properties (current and noise) of a SQPC in the tunnel limit, under the effect of a generic periodic drive.

When the angular frequency of the drive Ω is comparable to the superconducting gap Δ, sharp differences between quantized Lorentzian pulses and every other signal occur. Indeed, the former drive is the only one for which the excess noise associated with quasiparticle processes vanishes. Remarkably enough, this well known property of ballistic metallic systems still persist when entering the superconducting regime. Moreover, the total noise becomes independent of the bare superconducting phase difference ϕ_0.

From the experimental point of view, the constraint $\Delta/\Omega \lesssim 1$ is quite challenging but not unreachable. In SQPCs realized with the break junction technique, the typical regime is more towards the opposite case [206] (with the gap in the range of hundreds of μeV and $\nu = \Omega/2\pi$ in the range of a few tens of GHz). However, some recent experiments [209] are extremely promising for the investigation of regime $\Delta/\Omega \lesssim 1$, due to the quite small superconducting gap achievable at the interface $LaAlO_3/SrTiO_3$. Indeed, in the split gate SQPC geometry implemented in Ref. [209], a gap $\Delta \approx 22$μeV was observed, corresponding to a frequency $\nu \approx 5.3$ GHz, which perfectly fits the typical range where measurements in the electron quantum optics domain have been performed [5]. For more conventional superconducting materials it is in principle possible to reduce the gap by applying a magnetic field.

Finally, in the adiabatic limit (large gap) we obtain a very simple Josephson-like relation for the supercurrent, describing Shapiro spikes whose height is proportional to the photoassisted amplitude of the drive considered. All other contributions to current and noise are strongly suppressed and ultimately vanish in this regime, since they involve quasiparticle transfers across the gap.

CONCLUSIONS AND PERSPECTIVES

In this thesis, we have investigated the role of electron-electron correlations in electron quantum optics setups. In Chapter 1 we have reviewed the main ideas of electron quantum optics in non-interacting systems. In particular, we have focused our attention on the single-electron excitations known as Levitons, the properties of which we have presented from the theoretical point of view and also from an experimental side, with a brief description of the measurements which have confirmed their existence.

Chapter 2 has been devoted to the introduction of the theoretical tools which are needed in order to describe electron-electron interactions in one-dimensonal systems, which are the playground of the analysis carried out in the thesis. The subsequent Chapters constitute the original part of the thesis and are dedicated to the investigation of how the properties of Levitons are influenced by interactions in different systems. Two of them, namely the integer quantum Hall effect and the quantum spin Hall effect states are an example of topological systems, where the non-trivial topological properties of the bulk result in the emergence of one-dimensional conducting edge channels, where backscattering is forbidden. They are thus an ideal playground for implementing electron quantum optics setups.

In Chapter 3 we have considered a quantum Hall system with two interacting copropagating channels, where a voltage-pulse-generated excitation is introduced on the outer one. As a result of interactions, the initial pulse fractionalizes and creates smaller excitations carrying an interaction-dependent fraction of the original charge. By resorting to nonequilibrium momentum distributions and the Wigner functions, we have carefully studied the properties of these fractionalized excitations, showing that when they are generated by a Lorentzian drive and carry an integer charge, they are minimal excitations. Moreover, the inner-channel excitations always having equal and opposite charges, we showed that it is possible to extract the mixing angle describing the interaction strength from the noise generated when they are partitioned at a quantum point contact.

Chapter 4 presents the analysis of the properties of voltage-pulse generated excitations in an interacting helical liquid, namely a quantum spin Hall state where electron-electron interactions between counterpropagating channels are taken into account. As in the previous case of co-propagating channels, the presence of interactions induces a fractionalization process, making the initially excited pulse split into smaller ones, the properties of which we investigated by evaluating their non-equilibrium spectral functions. In contrast to what happens

in a non-interacting situation, Lorentzian pulses carrying an integer charge are not necessarily associated with a spectral function with definite sign, a fact that shows that care has to be taken in extending the concept of minimal excitation. Nevertheless, the excess noise for such pulses always vanishes and it is possible to take advantage of this fact in order to extract the Luttinger parameter describing the interaction strength in the system.

In Chapter 5 we have investigated the effect of superconducting correlations on Levitons, by considering a superconducting quantum point contact in the presence of an arbitrary periodic drive. In particular, we showed how a train of Lorentzian pulses with quantized area minimizes the noise also in this system, thus strengthening the result of the previous Chapters, namely that this peculiar property of Levitons is uniquely due to the particular shape of the drive and does not suffer from the presence of an interacting background.

Finally, we would like to mention some possible developments in the field of electron quantum optics. As we have seen, the properties of Levitons are well established in non-interacting systems, both theoretically [7, 8, 117] and experimentally [5]. Very recent experimental results in the fractional quantum Hall regime [237] are very promising in order to eventually test the theoretical predictions for filling factors in the Laughlin's sequence which have been put forward in the past few years [81, 82, 85, 87]. Moreover, the exotic physics of the fractional quantum Hall effect makes it possible to address composite-edge structures, where neutral upstream modes [238], propagating in opposite direction with respect to the charged ones, could lead to new interesting effects related to the energy flow associated with single-electron excitations.

Concerning the domain of two-dimensional topological insulators, a recent experimental breakthrough [19, 20] has demonstrated that quantum point contacts can be integrated in systems supporting helical edge channels, thus opening the possibility of conceiving interferometric measurements of single-electron excitations in these systems.

Concerning the properties of Levitons in the presence of superconductivity, a natural extension to what we have discussed in Chapter 5 would be to consider topological superconductors, where the emergence of Majorana zero modes [239] could give rise to interesting effects in the transport properties of the superconducting quantum point contact.

A

TIME EVOLUTION OF FERMIONIC AND BOSONIC OPERATORS

In this Appendix we evaluate the time evolution of fermionic and bosonic operators due to the effect of a voltage drive in different configurations.

A.1 NON-INTERACTING CASE

This is the case we considered in Sec. 1.4, where a drive was applied to a right-moving chiral channel. Here, we will address at the same time the case of right- and left-moving channels. The free Hamiltonian is

$$H_{0,r} = \int_{-\infty}^{+\infty} dx \, \Psi_r^\dagger(x)(-iv_F \vartheta_r \partial_x)\Psi_r(x) \,, \tag{A.1}$$

where $r = R/L$ for right/left-movers and $\vartheta_{R/L} = \pm 1$. Next, we consider a time-dependent voltage $V(t)$ applied in the region $x < -d$, with $d > 0$. This is described by the Hamiltonian

$$H_{g,r} = -e \int_{-\infty}^{+\infty} dx \, U(x,t)\rho_r^{(e)}(x) \,, \tag{A.2}$$

with $U(x,t) = \Theta(-x-d)V(t)$ and $\rho_r^{(e)}(x) =: \Psi_r^\dagger(x)\Psi_r(x):$ the particle density operator on channel r.

The equations of motion determining the time evolution $\Psi_r(x,t)$ operators are obtained by calculating the commutator $[H_{0,r} + H_{g,r}, \Psi_r]$. This is easily done by using the identity $[A, BC] = \{A, B\}C - B\{A, C\}$, as well as the canonical anticommutation relations. We have

$$[\Psi_r(x), H_{0,r}] = -i\vartheta_r v_F \partial_x \Psi_r(x) \,, \tag{A.3a}$$

$$[\Psi_r(x), H_{g,r}] = -eU(x,t)\Psi_r(x) \,, \tag{A.3b}$$

resulting in the equation of motion

$$i(\partial_t + \vartheta_r v_F \partial_x)\Psi_r(x,t) = -eU(x,t)\Psi_r(x,t) \,. \tag{A.4}$$

This equation can be solved by the Green function method as follows: define the differential operator $\mathcal{L}_r = i(\partial_t + \vartheta_r v_F \partial_x)$ and look for a solution of the form

$$\Psi_r(x,t) = \psi_r(x,t)e^{\beta_r(x,t)} \,, \tag{A.5}$$

such that $\mathcal{L}_r \psi_r(x, t) = 0$. Then Eq. (A.4) is converted in an equation for the function $\beta_r(x, t)$:

$$\mathcal{L}_r \Psi_r(x, t) = \psi_r(x, t) e^{\beta_r(x,t)} \mathcal{L}_r \beta_r(x, t) = -e U(x, t) \psi_r(x, t) e^{\beta_r(x,t)},$$
$$\implies \mathcal{L}_r \beta_r(x, t) = -e U(x, t). \tag{A.6}$$

By introducing the Green function $G_r(x, x'; t, t')$ of the operator $\mathcal{L}_r$, satisfying

$$\mathcal{L}_r G_r(x, x'; t, t') = \delta(x - x') \delta(t - t'), \tag{A.7}$$

we can write the solution to (A.6) in the form

$$\beta_r(x, t) = -e \int_{\mathbb{R}^2} dx' \, dt' \, G_r(x, x'; t, t') U(x', t'). \tag{A.8}$$

Indeed, by acting with $\mathcal{L}_r$ on this expression and using the property (A.7), we readily obtain (A.6). The Green function for $\mathcal{L}_r$ is

$$G_r(x, x'; t, t') = -i \Theta(t - t') \delta[v_F(t - t') - \vartheta_r(x - x')]. \tag{A.9}$$

As a matter of fact

$$\begin{aligned} \mathcal{L}_r G_r(x, x'; t, t') &= \delta(t - t') \delta(x - x') \\ &\quad + \Theta(t - t') \partial_t \delta[v_F(t - t') - \vartheta_r(x - x')] \\ &\quad + v_F \Theta(t - t') \partial_x \delta[v_F(t - t') - \vartheta_r(x - x')] \\ &= \delta(t - t') \delta(x - x'). \end{aligned} \tag{A.10}$$

By using (A.9) into (A.8) we obtain

$$\beta_r(x, t) = ie \int_{-\infty}^{t} dt' \, U[x - \vartheta_r v_F(t - t'), t']. \tag{A.11}$$

The last ingredient is the solution to the homogeneous equation $\mathcal{L}_r \psi_r(x, t) = 0$, which is any function of the form $\psi_r(x - \vartheta_r v_F t, 0)$. Therefore we conclude

$$\Psi_r(x, t) = \psi_r(x - \vartheta_r v_F t, 0) \, e^{ie \int_{-\infty}^{t} dt' \, U[x - \vartheta_r v_F(t - t'), t']}, \tag{A.12}$$

which reduces to Eq. (1.36) for $r = R$. In particular, by expliciting the form $U(x, t) = \Theta(-x - d) V(t)$, we find

$$\Psi_r(x, t) = \psi_r(x - \vartheta_r v_F t, 0) e^{i\alpha\left(t - \vartheta_r \frac{x+d}{v_F}\right)} \quad (\text{for } \vartheta_r x > -\vartheta_r d), \tag{A.13}$$

with the function $\alpha(t)$ defined as

$$\alpha(t) = e \int_{-\infty}^{t} d\tau \, V(\tau). \tag{A.14}$$

The above result reduces to Eq. (1.37) for $r = R$ and $d = 0$.

Here, we derive the equations of motion in the case of interacting fermions. Let us start by considering the system at $\nu = 2$ addressed in Chapter 3. In this case the Hamiltonian which describes the coupled edge channels in the presence of an applied voltage is given by (3.7). The free bosonic part is

$$H' = \frac{1}{2} \sum_{r=R,L} \sum_{\eta=\pm} v_\eta \int_{-\infty}^{+\infty} dx \; :[\partial_x \Phi_{r,\eta}(x)]^2:, \tag{A.15}$$

while the effect of the drive is encoded in

$$H_g = \frac{e}{\sqrt{2\pi}} \int_{-\infty}^{+\infty} dx \, U(x,t) \left[\cos\chi \, \partial_x \Phi_{R,+}(x) - \sin\chi \, \partial_x \Phi_{R,-}(x)\right]. \tag{A.16}$$

Here, bosonic fields satisfy the commutators

$$\left[\Phi_{r,\eta}(x), \Phi_{r',\eta'}(x')\right] = \frac{i\vartheta_r}{2} \delta_{r,r'} \delta_{\eta,\eta'} \mathrm{sgn}(x-x'). \tag{A.17}$$

It is thus easy to obtain

$$[H', \Phi_{r,\eta}(x)] = i\vartheta_r v_\eta \partial_x \Phi_{r,\eta}(x), \tag{A.18}$$

$$[H_g, \Phi_{r,\eta}(x)] = \delta_{r,R} \frac{ie}{\sqrt{2\pi}} U(x,t)(\delta_{\eta,+} \cos\chi - \delta_{\eta,-} \sin\chi), \tag{A.19}$$

resulting in the equations of motion

$$(\partial_t + \vartheta_r v_\eta \partial_x)\Phi_{r,\eta}(x,t) = \frac{\zeta_{r,\eta}}{\sqrt{2\pi}} U(x,t), \tag{A.20}$$

where $\zeta_{R,+} = -e\cos\chi$, $\zeta_{R,-} = e\sin\chi$ and $\zeta_{L,\pm} = 0$. Now, the above equation has the very same structure of Eq. (A.6) and therefore its solution is analogous to what we found in Eq. (A.11). By making the due modifications we then find

$$\Phi_{r,\eta}(x,t) = \phi_{r,\eta}(x - \vartheta_r v_\eta t, 0) + \frac{\zeta_{r,\eta}}{\sqrt{2\pi}} \int_{-\infty}^{t} dt' \, U[x - \vartheta_r v_\eta(t-t'), t'], \tag{A.21}$$

which is exactly Eq. (3.8) of the main text.

Finally, we briefly mention that the calculation for obtaining the equations of motion (4.15) considered in Chapter 4 is almost identical to what we have just done (apart for some differences in the signs of the commutators of bosonic fields). In particular, the solution (4.16) follows from the exact same method as illustrated above.

WIGNER FUNCTION

In this Appendix we provide some basic notions about the Wigner function and prove the formula (1.88) for a multi-Leviton state.

B.1 WEYL TRANSFORM AND WIGNER FUNCTION

Consider a quantum-mechanical particle in one dimension. Once the quantum state $|\phi\rangle$ is known, we have complete information about the system. In particular, the probability density $\varpi(x)$ of finding the particle at a given position x is given by

$$\varpi(x) = |\langle x | \phi \rangle|^2 = |\phi(x)|^2\,, \tag{B.1}$$

where $\phi(x)$ is the wavefunction in the position basis. In the same way, the probability density in momentum space is obtained by going to the momentum basis

$$\tilde{\varpi}(p) = |\langle p | \phi \rangle|^2 = |\tilde{\phi}(p)|^2\,, \tag{B.2}$$

where $\tilde{\phi}(p)$ is the Fourier-transformed wavefunction[1]

$$\tilde{\phi}(p) = \frac{1}{\sqrt{h}} \int_{-\infty}^{+\infty} dx\, e^{-i\frac{px}{\hbar}} \phi(x)\,. \tag{B.3}$$

Finally, the time evolution of the system is obtained by solving the Schrödinger equation for $\phi(x,t)$.

There is, however, an alternative and completely equivalent formulation of quantum mechanics which relies on distribution functions defined on the phase space. In this formulation, one deals with constant-number equations instead of operators. Moreover, it provides a conceptually simpler way of obtaining the classical limit, as classical mechanics deals with trajectories in the phase space. In what follows, we present a very brief introduction to this formulation, focusing on the Wigner distribution function [111]. This discussion is extensively based on Ref. [240]. For a broader discussion about general quantum phase-space distribution functions see, e. g., Ref. [241]. We also refer the interested reader to the review [242] for an overview of recent applications of Wigner function approaches to different areas of quantum physics.

---

[1] In this Section we restore the Planck's constant h. Moreover, quantum operators will be denoted by the superscript "^" in order to distinguish them from ordinary variables.

Consider an operator $\hat{O}$ depending on the position and momentum operators: $\hat{O} = O(\hat{x}, \hat{p})$. Its Weyl transform is defined as

$$O_W(x, p) = \int_{-\infty}^{+\infty} dy \left\langle x + \frac{y}{2} \left| \hat{O} \right| x - \frac{y}{2} \right\rangle e^{-i\frac{py}{\hbar}} \tag{B.4}$$

$$= \int_{-\infty}^{+\infty} dq \left\langle p + \frac{q}{2} \left| \hat{O} \right| p - \frac{q}{2} \right\rangle e^{+i\frac{qx}{\hbar}}. \tag{B.5}$$

As we can see, the Weyl transform is a map which converts an operator into a scalar function of the variables x and p. The Weyl transform allows us to express a trace of two operators as an integral over the phase space:

$$\mathrm{Tr}[\hat{A}\hat{B}] = \frac{1}{h} \iint_{-\infty}^{+\infty} dx\, dp\, A_W(x, p) B_W(x, p). \tag{B.6}$$

Indeed

$$\iint_{-\infty}^{+\infty} dx\, dp\, A_W(x, p) B_W(x, p) = \iint_{-\infty}^{+\infty} dx\, dp \iint_{-\infty}^{+\infty} dy\, dy'\, e^{-i\frac{p}{\hbar}(y+y')}$$

$$\times \left\langle x + \frac{y}{2} \left| \hat{A} \right| x - \frac{y}{2} \right\rangle \left\langle x + \frac{y'}{2} \left| \hat{B} \right| x - \frac{y'}{2} \right\rangle$$

$$= 2\pi\hbar \iint_{-\infty}^{+\infty} dx\, dy \left\langle x + \frac{y}{2} \left| \hat{A} \right| x - \frac{y}{2} \right\rangle \left\langle x - \frac{y}{2} \left| \hat{B} \right| x + \frac{y}{2} \right\rangle$$

$$= h \iint_{-\infty}^{+\infty} du\, dv \left\langle u \left| \hat{A} \right| v \right\rangle \left\langle v \left| \hat{B} \right| u \right\rangle$$

$$= h \int_{-\infty}^{+\infty} du \left\langle u \left| \hat{A}\hat{B} \right| u \right\rangle = \mathrm{Tr}[\hat{A}\hat{B}].$$

In particular, when we take $\hat{B}$ to be the density operator $\hat{\rho}$, from the previous formula we can write the expectation value of $\hat{A}$ as

$$\left\langle \hat{A} \right\rangle = \mathrm{Tr}[\hat{\rho}\hat{A}] = \iint_{-\infty}^{+\infty} dx\, dp\, A_W(x, p) W(x, p), \tag{B.7}$$

where we defined the Wigner function $W(x, p) = h^{-1}\rho_W(x, p)$. In particular, for a pure state $\hat{\rho} = |\phi\rangle\langle\phi|$ we have

$$W(x, p) = \frac{1}{h} \int_{-\infty}^{+\infty} dy\, e^{-i\frac{py}{\hbar}} \phi\left(x + \frac{y}{2}\right) \phi^*\left(x - \frac{y}{2}\right). \tag{B.8}$$

From this expression it is immediate to see that $W(x, p)$ is real (we just have to take the complex conjugate and change the integration variable $y \to -y$). Eq. (B.7) expresses the expectation value of an operator as an integral over phase space of its Weyl transform weighted by the Wigner function. Since the following normalization holds

$$\iint_{-\infty}^{+\infty} dx\, dp\, W(x, p) = 1 \tag{B.9}$$

(due to the normalization of the wavefunction), it then seems that $W(x, p)$ could be interpreted as a phase-space probability density. Unfortunately, this is not the case as the Wigner function can be negative. However, position and momentum probability densities are marginal distributions of $W(x, p)$:

$$\varpi(x) = \int_{-\infty}^{+\infty} dp\, W(x, p)\,, \tag{B.10a}$$

$$\tilde{\varpi}(p) = \int_{-\infty}^{+\infty} dx\, W(x, p)\,. \tag{B.10b}$$

The following argument shows that indeed Wigner functions can be negative. Consider two pure states $\hat{\rho}_a = |\phi_a\rangle\langle\phi_a|$ and $\hat{\rho}_b = |\phi_b\rangle\langle\phi_b|$ and the corresponding Wigner functions W_a and W_b. Then,

$$|\langle\phi_a\,|\,\phi_b\rangle|^2 = \text{Tr}[\hat{\rho}_a\hat{\rho}_b] = h\iint_{-\infty}^{+\infty} dx\, dp\, W_a(x, p)W_b(x, p)\,. \tag{B.11}$$

If $|\phi_a\rangle$ and $|\phi_b\rangle$ are orthogonal, the above integral has to vanish, showing that W_a or W_b (or both) must be negative somewhere.

A further important aspect is that the Wigner function cannot assume arbitrarily large values, unlike what happens for classical probability densities over the phase space, which are typically δ-like. This is a manifestation of the uncertainty principle. In order to show that the Wigner function is bounded, let us consider the two wavefunctions

$$\phi_1(y) = \frac{1}{\sqrt{2}}e^{+i\frac{py}{2\hbar}}\phi\left(x - \frac{y}{2}\right)\,, \tag{B.12a}$$

$$\phi_2(y) = \frac{1}{\sqrt{2}}e^{-i\frac{py}{2\hbar}}\phi\left(x + \frac{y}{2}\right)\,, \tag{B.12b}$$

which are obviously normalized due to the normalization of $\phi(x)$. By using these, the Wigner function is expressed as

$$W(x, p) = \frac{2}{h}\int_{-\infty}^{+\infty} dy\, \phi_1^*(y)\phi_2(y) = \frac{2}{h}\langle\phi_1\,|\,\phi_2\rangle\,. \tag{B.13}$$

It then follows from the Cauchy-Schwarz inequality that

$$|\langle\phi_1\,|\,\phi_2\rangle|^2 \leqslant \langle\phi_1\,|\,\phi_1\rangle\langle\phi_2\,|\,\phi_2\rangle \implies -\frac{2}{h} \leqslant W(x, p) \leqslant +\frac{2}{h}\,. \tag{B.14}$$

Notice that this bound is removed when the classical limit $h \to 0$ is considered. A simple and instructive example in this sense is provided by the simple harmonic oscillator

$$\hat{H} = \frac{\hat{p}^2}{2m} + \frac{1}{2}m\omega^2\hat{x}^2\,. \tag{B.15}$$

The ground-state wavefunction is

$$\phi_0(x) = \left(\frac{1}{\pi a^2}\right)^{1/4} e^{-\frac{x^2}{2a^2}}\,, \qquad a = \sqrt{\frac{\hbar}{m\omega}}\,, \tag{B.16}$$

from which the following Wigner function is obtained:

$$W_0(x, p) = \frac{2}{h} \exp\left[-\frac{1}{\hbar}\left(\frac{p^2}{m\omega} + m\omega x^2\right)\right].\tag{B.17}$$

In the classical limit one finds

$$W_0(x, p) = \frac{1}{\sqrt{\pi \hbar m \omega}} e^{-\frac{p^2}{m\omega \hbar}} \sqrt{\frac{m\omega}{\pi \hbar}} e^{-\frac{m\omega x^2}{\hbar}} \rightarrow \delta(p)\delta(x),\tag{B.18}$$

which is the expected result as the minimal-energy configuration of the classical harmonic oscillator corresponds to $x = p = 0$. This example also shows that, while it is certainly true that any classical state has a positive Wigner function (and hence any negativity in $W(x, p)$ is a signature of quantumness), the converse is not true: quantum states can have an always-positive Wigner function and when this happens they are also referred to as quasi-classical [243]. An example is provided by coherent states.

Another very interesting example is shown in Fig. B.1, where the Wigner function of a cat state built from two Gaussian wavefunctions centered at different space points is drawn. Explicitly, the cat state is $|\phi\rangle = (|\phi_\xi\rangle + |\phi_{-\xi}\rangle)/\sqrt{N}$, where

$$\langle x | \phi_{\pm\xi}\rangle = \phi_{\pm\xi}(x) = \sqrt[4]{\frac{2}{\pi a^2}} e^{-\frac{(x\pm\xi)^2}{a^2}}\tag{B.19}$$

and

$$N = 2\left(1 + e^{-\frac{2\xi^2}{a^2}}\right)\tag{B.20}$$

is a normalization factor. It is easy to show that the Wigner function W_ϕ of the cat state $|\phi\rangle$ can be written as [243]

$$W_\phi(x, p) = W_\xi(x, p) + W_{-\xi}(x, p) + W_{int}(x, p),\tag{B.21}$$

where

$$W_{\pm\xi}(x, p) = \frac{1}{2\pi\hbar N} \exp\left[-\frac{2(x\pm\xi)^2}{a^2} - \frac{a^2 p^2}{2\hbar^2}\right]\tag{B.22}$$

are the Wigner functions associated with the states $|\phi_{\pm\xi}\rangle$, while

$$W_{int}(x, p) = \frac{1}{\pi\hbar N} \exp\left[-\frac{2x^2}{a^2} - \frac{a^2 p^2}{2\hbar^2}\right] \cos\left(\frac{2p\xi}{\hbar}\right)\tag{B.23}$$

is an interference term, which would be absent if the state $|\phi\rangle$ was a statistical mixture built from $|\phi_\xi\rangle$ and $|\phi_{-\xi}\rangle$. The result is shown in Fig. B.1, where the interference fringes related to the entanglement of the cat state $|\phi\rangle$ can be clearly observed in the region between the spatial points at which the two states $|\phi_{\pm\xi}\rangle$ are localized.

So far we have seen that Weyl transforms and Wigner functions provide a way to express expectation values of observables as integrals

over phase space through (B.7). However, $W(x, p)$ has been introduced by relying on the wavefunction $\phi(x)$ and, thus, assuming that the Schrödinger equation has been solved in order to find the latter. It is actually possible to derive the time evolution equation for $W(x, p)$ and the analog of the time-independent Schrödinger eigenvalue equation for stationary states [244–248]. We do not report these equations here as they lie beyond the scope of this brief introduction. From these equations, the Wigner function can be directly determined without having to solve the Schrödinger equation and, once $W(x, p)$ is known, the wavefunction can be recovered. Thus, the phase-space formulation of quantum mechanics in terms of the Wigner function is completely equivalent to the usual formulation in terms of wavefunctions and operators.
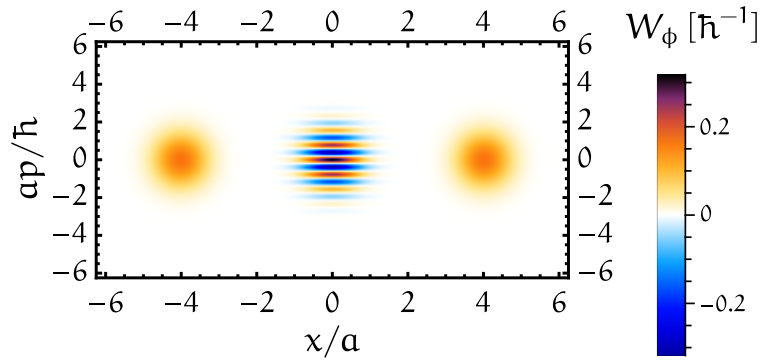
Figure B.1: Wigner function (B.21) for a Schrödinger cat state obtained from the two Gaussian wavefunctions (B.19) centered at $\xi = \pm 4a$.

B.2   CALCULATION OF THE WIGNER FUNCTION FOR A MULTI-LEVITON STATE

We now show the derivation of Eq. (1.88). The starting point is the expression (1.83) of the excess electron coherence, which we report here for convenience

$$\Delta \mathcal{G}^{<}(t_1, t_2) = \frac{1}{v_F} \sum_{j=1}^{n} \phi_j(t_1)\phi_j^*(t_2),$$ (B.24)

as well as the definition (1.62) of the Wigner function[2]

$$\Delta W^{<}(t, \omega) = \frac{1}{2\pi} \int_{-\infty}^{+\infty} d\tau \, \Delta \mathcal{G}^{<} \left(t + \frac{\tau}{2}, t - \frac{\tau}{2} \right) e^{i\omega\tau}.$$ (B.25)

---

2 Notice that, unfortunately, here a different convention is taken for the sign of the exponential with respect to what was presented in Sec. B.1. This is the choice usually made in the context of EQO [113].

By substituting (B.24) into the definition (B.25) and using the Fourier representation of wavefunctions $\phi_j(t)$ we obtain

$$
\begin{aligned}
\Delta W^<(t, \omega) &= \frac{1}{2\pi v_F} \sum_{j=1}^{n} \int_{-\infty}^{+\infty} d\tau\, e^{i\omega\tau} \phi_j\left(t + \frac{\tau}{2}\right) \phi_j^*\left(t - \frac{\tau}{2}\right) \\
&= \frac{1}{4\pi^2 v_F} \sum_{j=1}^{n} \int_{-\infty}^{+\infty} d\omega_1 \int_{-\infty}^{+\infty} d\omega_2\, \tilde{\phi}_j(\omega_1) \tilde{\phi}_j^*(\omega_2) e^{-i(\omega_1 - \omega_2)t} \\
&\quad \times \int_{-\infty}^{+\infty} \frac{d\tau}{2\pi}\, e^{i\tau\left(\omega - \frac{\omega_1 + \omega_2}{2}\right)} \\
&= \frac{1}{2\pi^2 v_F} \sum_{j=1}^{n} \int_{-\infty}^{+\infty} d\omega_1\, \tilde{\phi}_j(\omega_1) \tilde{\phi}_j^*(2\omega - \omega_1) e^{-2i(\omega_1 - \omega)t}.
\end{aligned}
$$

$$(B.26)$$

We now substitute the explicit expression (1.86) of the Fourier-transformed wavefunctions $\tilde{\phi}_j(\omega)$:

$$
\begin{aligned}
\Delta W^<(t, \omega) &= \frac{2w}{\pi v_F} \sum_{j=0}^{n-1} \int_{-\infty}^{+\infty} d\omega_1\, \Theta(\omega_1) \Theta(2\omega - \omega_1) e^{-2\omega w} \\
&\quad \times L_j(2\omega_1 w) L_j[(4\omega - 2\omega_1)w] e^{-2i(\omega_1 - \omega)t} \\
&= \frac{2w}{\pi v_F} \Theta(\omega) e^{-2\omega w} \sum_{j=0}^{n-1} I_j,
\end{aligned}
$$

$$(B.27)$$

where we defined the integral

$$
I_j = \int_0^{2\omega} d\omega_1\, L_j(2\omega_1 w) L_j[(4\omega - 2\omega_1)w] e^{-2i(\omega_1 - \omega)t}. \tag{B.28}
$$

By a change of variable $\Omega = \omega_1 - \omega$ the previous expression becomes

$$
I_j = \int_{-\omega}^{+\omega} d\Omega\, L_j[2w(\omega + \Omega)] L_j[2w(\omega - \Omega)] e^{-2i\Omega t}. \tag{B.29}
$$

In order to proceed further, we exploit the following identity involving the product of two Laguerre polynomials [249]

$$
L_j(x) L_j(y) = \frac{1}{(p!)^2} \sum_{p=0}^{j} (xy)^p L_{j-p}^{(2p)}(x + y), \tag{B.30}
$$

where $L_{j-p}^{(2p)}$ denotes a generalized Laguerre polynomial. By using this identity the expression for I_j becomes

$$
I_j = \sum_{p=0}^{j} \frac{(2w)^{2p}}{(p!)^2} L_{j-p}^{(2p)}(4\omega w) \int_{-\omega}^{+\omega} d\Omega\, (\omega^2 - \Omega^2)^p e^{-2i\Omega t}. \tag{B.31}
$$

Since the integration domain is symmetric, only the even part of the integrand (with respect to Ω) survives, so that

$$
\begin{aligned}
I_j &= 2\sum_{p=0}^{j} \frac{(2w)^{2p}}{(p!)^2} L_{j-p}^{(2p)}(4\omega w) \int_0^{\omega} d\Omega \, (\omega^2 - \Omega^2)^p \cos(2\Omega t) \\
&= 2\omega \sum_{p=0}^{j} \frac{(2\omega w)^{2p}}{(p!)^2} L_{j-p}^{(2p)}(4\omega w) \int_0^{1} du \, (1-u^2)^p \cos(2\omega t u) \quad \text{(B.32)} \\
&= \frac{\omega\sqrt{\pi}}{p!} \sum_{p=0}^{j} \frac{(2\omega w)^{2p}}{(\omega t)^{p+1/2}} L_{j-p}^{(2p)}(4\omega w) J_{p+\frac{1}{2}}(2\omega t) \, ,
\end{aligned}
$$

where in the last step we used the integral representation of the Bessel function $J_\nu(z)$ [70]

$$
\int_0^{1} du \, (1-u^2)^{\nu-1/2} \cos(zt) = \frac{\sqrt{\pi}\,\Gamma(\nu+1/2)}{2(z/2)^\nu} J_\nu(z) \, , \qquad \text{(B.33)}
$$

with $\nu = p + 1/2$, $z = 2\omega t$ and Γ the Euler gamma function. Finally, by substituting (B.32) into (B.27) we arrive at

$$
\begin{aligned}
\Delta W^<(t,\omega) = \Theta(\omega)\frac{1}{v_F\sqrt{\pi}} e^{-2\omega w} \\
\times \sum_{j=0}^{n-1}\sum_{p=0}^{j} \frac{1}{p!} \left[\frac{2\omega w}{\sqrt{\omega t}}\right]^{2p+1} L_{j-p}^{(2p)}(4\omega w) J_{p+\frac{1}{2}}(2\omega t) \, ,
\end{aligned} \qquad \text{(B.34)}
$$

which is precisely Eq. (1.88) presented in the main text.

NOISE IN INTERFEROMETRIC SETUPS

In this Appendix we provide some complementary details about noise calculations performed in the main text of the thesis.

C.1 HBT NOISE IN THE NON-INTERACTING CASE

Let us start by considering the setup presented in Sec. 1.6, which we report here in Fig. C.1 (top). For the sake of completeness, we
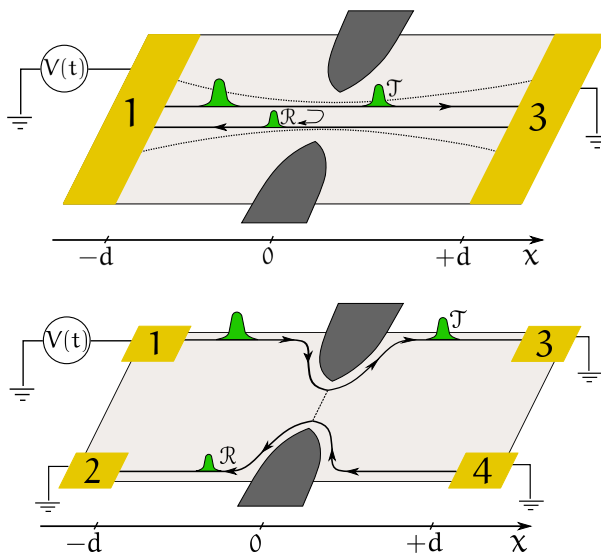
Figure C.1: HBT setup in a non-interacting system. Top: two-terminal geometry in a 2DEG where a conduction channel is formed due to a QPC which also acts as a beamsplitter. Bottom: four-terminal geometry in the IQHE regime at filling factor $\nu = 1$. Here, the QPC allows the tunneling between the two edges of the sample.

also sketched the equivalent setup in the IQHE regime at filling factor $\nu = 1$ (bottom panel). Apart from the different number of terminals, we can formally describe the two cases in a unified way. Indeed, in both situations right- and left-moving fermionic species are present: in the first case, they both lie within the conduction channel created by the QPC, while in the second one the right/left-moving fermions are associated with the upper/lower edge state in the system. The setup in the IQHE system is more closely resemblant to an actual interferometer whose input arms are represented by the channels originating from terminals 1 and 4, which are then "mixed" at the QPC, from which, in turn, the output arms go towards terminals 2 and 3.

We are interested in calculating the correlators

$$S_{ab} = \int_{-T/2}^{T/2} \frac{dt}{T} \int_{-\infty}^{+\infty} dt' \left\langle \delta J_a(t) \delta J_b(t+t') \right\rangle, \qquad (C.1)$$

where the indices can assume the values $a, b = 2, 3$ and, of course, only $a = b = 3$ in the top setup of Fig. C.1. The operator $J_a(t)$ denotes the electric current flowing into terminal a. In order to express these operators, we first have to characterize the partitioning at the QPC. In a non-interacting system, this can be conveniently modeled via the scattering matrix theory [250–252]. Basically, the QPC is modeled as a scatterer and fields outcoming from the scattering region are conncted to the incoming ones via a matrix relation:

$$\begin{pmatrix} \Psi_R(x,t) \\ \Psi_L(x,t) \end{pmatrix}_{out} = \begin{pmatrix} \sqrt{\mathcal{T}} & i\sqrt{\mathcal{R}} \\ i\sqrt{\mathcal{R}} & \sqrt{\mathcal{T}} \end{pmatrix} \begin{pmatrix} \Psi_R(x,t) \\ \Psi_L(x,t) \end{pmatrix}_{in}, \qquad (C.2)$$

where $\Psi_{R/L,out}$ are the fields after the QPC. In the above formula, $\mathcal{T}$ and $\mathcal{R} = 1 - \mathcal{T}$ are the transmission and reflection probabilities, respectively. Now, current operators $J_a(t)$ are simply expressed as a difference between currents incoming into and outcoming from terminal a. Thus we write

$$J_2(t) = ev_F \left[:\Psi_{R,in}^\dagger(-d,t)\Psi_{R,in}(-d,t): - :\Psi_{L,out}^\dagger(-d,t)\Psi_{L,out}(-d,t): \right],$$
$$(C.3a)$$

$$J_3(t) = ev_F \left[:\Psi_{L,in}^\dagger(+d,t)\Psi_{L,in}(+d,t): - :\Psi_{R,out}^\dagger(+d,t)\Psi_{R,out}(+d,t): \right].$$
$$(C.3b)$$

By using (C.2) they are expressed in terms of incoming fields as

$$J_2(t) = -ev_F \left[\mathcal{T} \left(\Psi_{L,in}^\dagger(-d,t)\Psi_{L,in}(-d,t) - \Psi_{R,in}^\dagger(-d,t)\Psi_{R,in}(-d,t) \right) \right.$$
$$\left. +i\sqrt{\mathcal{RT}} \left(\Psi_{L,in}^\dagger(-d,t)\Psi_{R,in}(-d,t) - \Psi_{R,in}^\dagger(-d,t)\Psi_{L,in}(-d,t) \right) \right],$$
$$(C.4a)$$

$$J_3(t) = -ev_F \left[\mathcal{T} \left(\Psi_{R,in}^\dagger(+d,t)\Psi_{R,in}(+d,t) - \Psi_{L,in}^\dagger(+d,t)\Psi_{L,in}(+d,t) \right) \right.$$
$$\left. +i\sqrt{\mathcal{RT}} \left(\Psi_{R,in}^\dagger(+d,t)\Psi_{L,in}(+d,t) - \Psi_{L,in}^\dagger(+d,t)\Psi_{R,in}(+d,t) \right) \right].$$
$$(C.4b)$$

Now we have to use these expressions into (C.1) and perform the calculation. In order to do so, recall that the time evolution of incoming fields is [cf. App. A.1, in particular Eq. (A.13)]

$$\Psi_{R,in}(x,t) = e^{i\alpha(t-x/v_F-d/v_F)} \psi_R(0, t-x/v_F), \qquad (C.5a)$$
$$\Psi_{L,in}(x,t) = \psi_L(0, t+x/v_F), \qquad (C.5b)$$

where $\psi_{R/L}(0, t \mp x/v_F)$ is the equilibrium time evolution when no drive is applied and

$$\alpha(t) = e \int_{-\infty}^{t} d\tau\, V(\tau). \qquad (C.6)$$

Notice that the incoming field for left-movers has a free evolution, as in the HBT setup we are considering the drive is applied only to right-movers. By using the above expressions, after a straightforward though not so short calculation, we arrive at

$$
S_{33} = e^2 v_F^2 \mathcal{R}\mathcal{T} \left[\frac{\mathcal{T}}{\mathcal{R}} \int_{-T/2}^{T/2} \frac{dt}{T} \int_{-\infty}^{+\infty} dt' \sum_{r=R,L} \mathcal{G}_{0,r}^<(t',t)\mathcal{G}_{0,r}^>(t,t') \right.
$$
$$
\left. + \int_{-T/2}^{T/2} \frac{dt}{T} \int_{-\infty}^{+\infty} dt' \left(\mathcal{G}_R^<(t',t)\mathcal{G}_{0,L}^>(t,t') + \mathcal{G}_{0,L}^<(t',t)\mathcal{G}_R^>(t,t') \right) \right],
$$
(C.7)

where it is understood that the coherence functions are evaluated with the incoming fields (C.5). In the same way it is possible to show that $S_{22} = S_{33} = -S_{23} = -S_{32}$. In obtaining the expression (C.7), the chirality of fields and the time integration were used in order to get rid of the positions $\pm d$ appearing in (C.4). This is almost the result in Eq. (1.95) in Sec. 1.6. There is indeed in the first line of Eq. (C.7) an additional term made of purely equilibrium coherence functions. By expressing them with the help of Eq. (1.98) we find

$$
\int_{-T/2}^{T/2} \frac{dt}{T} \int_{-\infty}^{+\infty} dt' \mathcal{G}_{0,r}^<(t',t)\mathcal{G}_{0,r}^>(t,t')
$$
$$
= \int_{-T/2}^{T/2} \frac{dt}{T} \int_{-\infty}^{+\infty} dt' \int_{-\infty}^{+\infty} d\omega \int_{-\infty}^{+\infty} d\omega' \frac{e^{i(\omega-\omega')(t-t')}}{(2\pi v_F)^2} n_F(\omega)n_F(-\omega')
$$
$$
= \frac{1}{2\pi v_F^2} \int_{-T/2}^{T/2} \frac{dt}{T} \int_{-\infty}^{+\infty} d\omega \, n_F(\omega)n_F(-\omega) = \frac{k_B\theta}{2\pi v_F^2} .
$$
(C.8)

This is a purely thermal contribution and vanishes at zero temperature: Eq. (1.95) is therefore proved.

We can now proceed futher and prove Eq. (1.102). To this aim, we exploit the Fourier decomposition (1.100) to express the coherence functions for right movers, which become

$$
\mathcal{G}_R^<(t,t') = \sum_{\ell m \in \mathbb{Z}} p_m^* p_\ell e^{-i(\ell+q)\Omega t} e^{i(m+q)\Omega t'} \mathcal{G}_{0,R}^<(t,t'), \quad \text{(C.9a)}
$$
$$
\mathcal{G}_R^>(t,t') = \sum_{\ell m \in \mathbb{Z}} p_m p_\ell^* e^{i(\ell+q)\Omega t'} e^{-i(m+q)\Omega t} \mathcal{G}_{0,R}^>(t,t'), \quad \text{(C.9b)}
$$

$\Omega = 2\pi T^{-1}$ being the angular frequency of the drive. By using these relations, we can evaluate the two terms in the second line of Eq. (C.7). The first one is

$$
\int_{-T/2}^{T/2} \frac{dt}{T} \int_{-\infty}^{+\infty} dt' \mathcal{G}_R^<(t',t)\mathcal{G}_{0,L}^>(t,t')
$$

$$
= \int_{-T/2}^{T/2} \frac{dt}{T} \int_{-\infty}^{+\infty} dt' \sum_{\ell m} p_m^* p_\ell e^{-i(\ell+q)\Omega t'} e^{i(m+q)\Omega t} \mathcal{G}_{0,R}^<(t',t)\mathcal{G}_{0,L}^>(t,t')
$$

$$
= \sum_{\ell m} p_m^* p_\ell \int_{-T/2}^{T/2} \frac{dt}{T} \int_{-\infty}^{+\infty} dt' e^{-i(\ell+q)\Omega t'} e^{i(m+q)\Omega t}
$$

$$
\times \int_{-\infty}^{+\infty} d\omega \int_{-\infty}^{+\infty} d\omega' \frac{e^{i(\omega-\omega')(t-t')}}{(2\pi v_F)^2} n_F(\omega) n_F(-\omega')
$$

$$
= \sum_{\ell m} \frac{p_m^* p_\ell}{2\pi v_F^2} \int_{-T/2}^{T/2} \frac{dt}{T} e^{i(m-\ell)\Omega t} \int_{-\infty}^{+\infty} d\omega\, n_F(\omega) n_F[-(\omega+(\ell+q)\Omega)]
$$

$$
= \frac{1}{2\pi v_F^2} \sum_\ell |p_\ell|^2 (\ell+q)\Omega \left(1 + \frac{1}{e^{\frac{(\ell+q)\Omega}{k_B \theta}} - 1} \right) , \tag{C.10}
$$

where we have used the relation

$$
\int_{-T/2}^{T/2} \frac{dt}{T} e^{i(\ell-m)\Omega t} = \delta_{\ell,m} , \tag{C.11}
$$

which can be easily demonstrated. Along the lines of the previous calculation we also find

$$
\int_{-T/2}^{T/2} \frac{dt}{T} \int_{-\infty}^{+\infty} dt' \mathcal{G}_{0,L}^<(t',t)\mathcal{G}_R^>(t,t')
$$

$$
= -\frac{1}{2\pi v_F^2} \sum_\ell |p_\ell|^2 (\ell+q)\Omega \left(1 + \frac{1}{e^{-\frac{(\ell+q)\Omega}{k_B \theta}} - 1} \right) . \tag{C.12}
$$

By combining Eqs. (C.10) and (C.12) we thus obtain

$$
\int_{-T/2}^{T/2} \frac{dt}{T} \int_{-\infty}^{+\infty} dt' \left[\mathcal{G}_R^<(t',t)\mathcal{G}_{0,L}^>(t,t') + \mathcal{G}_{0,L}^<(t',t)\mathcal{G}_R^>(t,t') \right]
$$

$$
= \frac{1}{2\pi v_F^2} \sum_\ell |p_\ell|^2 (\ell+q)\Omega \coth \left(\frac{(\ell+q)\Omega}{2k_B \theta} \right) . \tag{C.13}
$$

Finally, by substituting this result in Eq. (C.7), together with (C.8), we have the following expression

$$
S_{33} = \frac{e^2}{2\pi} \left[2\mathcal{T}^2 k_B \theta + \mathcal{R}\mathcal{T} \sum_\ell |p_\ell|^2 (\ell+q)\Omega \coth \left(\frac{(\ell+q)\Omega}{2k_B \theta} \right) \right] . \tag{C.14}
$$

The zero-temperature limit of the above result is Eq. (1.102) presented in the main text.

We conclude this Section by giving the formula for the excess noise at finite temperature. The only thing to do is to evaluate the dc noise
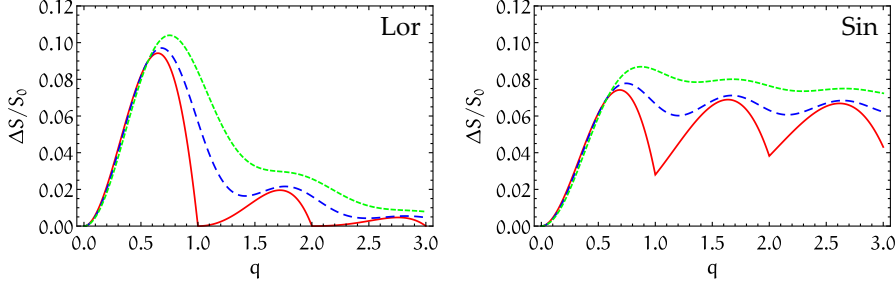
Figure C.2: Comparison of the excess noise ΔS, Eq. (C.15), in the case of two drives, for different temperatures. Left: Lorentzian drive with width-to-period ratio $\eta = 0.1$. Right: sine drive. In both panels the different curves refer to (from bottom to top) zero temperature, $k_B\theta = 0.1\Omega$ and $k_B\theta = 0.15\Omega$. The excess noise is plotted in units of $S_0 = e^2\mathcal{RT}/T$.

S_{dc}, which can be easily done by setting $p_\ell = \delta_{\ell,0}$. Therefore, the finite-temperature expression we are looking for reads

$$\Delta S = \frac{e^2\mathcal{RT}}{T}\left[\sum_\ell |p_\ell|^2(\ell+q)\coth\left(\frac{(\ell+q)\Omega}{2k_B\theta}\right) - q\coth\left(\frac{q\Omega}{2k_B\theta}\right)\right].$$
(C.15)

This is the formula that was used in order to estimate the finite-temperature corrections in the experiment [5] which we described in Sec. 1.6. Of course, its zero-temperature limit yields Eq. (1.104). In Fig. C.2 we show the excess noise calculated with Eq. (C.15) for a Lorentzian (left panel) and a sine drive (right panel). We observe that the zero-temperature excess noise vanishes for the Lorentzian drive, while it is finite for the sine signal. Finite temperature effects cause the minima at integer values of q to shift rightwards and an overall smearing of the curves. These theoretical predictions are in good agreement with the experimental measurements presented in Fig. 1.14, page 37.

C.2 NOISE IN THE HOM SETUP

The HOM setup is represented in Fig. C.3: here, in addition to terminal 1, a voltage drive $V_4(t)$ is also applied to terminal 4. As a result, excitations are generated on both edges and sent towards the QPC, where they collide. The goal is again to compute the autocorrelation noise $S_{22} = S_{33}$. The calculation is almost identical to what we have shown in the previous Section, the only difference being that now the time evolution of fermionic fields reads

$$\Psi_{R,in}(x,t) = e^{i\alpha_1(t-x/v_F-d/v_F)}\psi_R(0,t-x/v_F), \qquad (C.16a)$$

$$\Psi_{L,in}(x,t) = e^{i\alpha_4(t+x/v_F-d/v_F)}\psi_L(0,t+x/v_F), \qquad (C.16b)$$
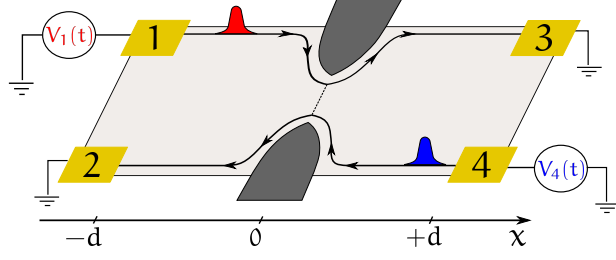
Figure C.3: HOM setup in a quantum Hall bar at $\nu = 1$. Both terminals 1 and 4 are driven, so that excitations are generated on both edges, and sent towards the QPC where they collide. The resulting current and noise signals are measured at terminals 2 and 3.

where $\alpha_{1/4}(t)$ is given by (C.6), with the appropriate voltage $V_{1/4}(t)$. Since terminal 4 is now driven, also the left-moving fermionic field $\Psi_{L,in}$ acquires a non-trivial time evolution. Thus, Eq. (C.7) is modified into

$$S_{33} = e^2 v_F^2 \mathcal{R}\mathcal{T} \left[\frac{\mathcal{T}}{\mathcal{R}} \int_{-T/2}^{T/2} \frac{dt}{T} \int_{-\infty}^{+\infty} dt' \sum_{r=R,L} \mathcal{G}_{0,r}^<(t',t)\mathcal{G}_{0,r}^>(t,t') \right.$$
$$\left. + \int_{-T/2}^{T/2} \frac{dt}{T} \int_{-\infty}^{+\infty} dt' \left(\mathcal{G}_R^<(t',t)\mathcal{G}_L^>(t,t') + \mathcal{G}_L^<(t',t)\mathcal{G}_R^>(t,t') \right) \right],$$

(C.17)

where the coherence functions for the lower edge are no more evaluated at equilibrium. By using the time evolution (C.16) in order to express the coherence functions, it is then easy to realize that (C.17) is completely equivalent to the result (C.7) for the HBT noise, but with a *modified* voltage

$$\tilde{V}(t) = V_1(t) - V_4(t). \tag{C.18}$$

In the simplest HOM configuration the voltage drives are chosen as $V_1(t) = V(t)$ and $V_4(t) = V(t + t_d)$, where t_d is a constant time delay. In this case the expression (C.14) becomes

$$S_{33} = \frac{e^2}{2\pi} \left[2\mathcal{T}^2 k_B \theta + \mathcal{R}\mathcal{T} \sum_\ell |\tilde{p}_\ell|^2 \ell\Omega \coth\left(\frac{\ell\Omega}{2k_B\theta} \right) \right], \tag{C.19}$$

where the photoassisted coefficients $\tilde{p}_\ell$ are expressed in terms of the p_ℓ associated with the drive $V(t)$ as

$$\tilde{p}_\ell = \sum_{m \in \mathbb{Z}} p_{\ell+m} p_m^* e^{im\Omega t_d}. \tag{C.20}$$

More general results about the HOM noise are beyond the scope of this thesis and we refer the interested reader to Refs. [52, 86, 156].

D

BOSONIC GREEN FUNCTIONS

In this Appendix we calculate the equilibrium bosonic Green function

$$\mathcal{G}_\eta(x,t) = \langle \phi_\eta(x,t)\phi_\eta(0,0) \rangle - \langle \phi_\eta^2(0,0) \rangle . \tag{D.1}$$

We first consider the case where $\phi_\eta(x,t)$ are fields with opposite chiralities evolving as $\phi_\eta(x,t) = \phi_\eta(x - \eta u t, 0)$, according to the Hamiltonian

$$H = \frac{u}{2} \sum_{\eta=\pm} \int_{-\infty}^{+\infty} dx : [\partial_x \phi_\eta(x)]^2 := \sum_{\eta=\pm} \sum_{q>0} u q b_{q,\eta}^\dagger b_{q,\eta} . \tag{D.2}$$

Recall that b's are bosonic operators, in terms of which the fields are expressed as

$$\phi_\eta(x,t) = \frac{i}{\sqrt{L}} \sum_{q>0} \frac{e^{-aq/2}}{\sqrt{q}} \left(b_{q,\eta} e^{iq(\eta x - ut)} - b_{q,\eta}^\dagger e^{-iq(\eta x - ut)} \right) . \tag{D.3}$$

Moreover, they satisfy the equilibrium averages (here θ is the temperature)

$$\left\langle b_{q,\eta}^\dagger b_{q',\eta'} \right\rangle = \delta_{\eta,\eta'} \delta_{q,q'} \frac{1}{e^{\frac{uq}{k_B\theta}} - 1} , \tag{D.4a}$$

$$\left\langle b_{q,\eta} b_{q',\eta'}^\dagger \right\rangle = \delta_{\eta,\eta'} \delta_{q,q'} \frac{e^{\frac{uq}{k_B\theta}}}{e^{\frac{uq}{k_B\theta}} - 1} . \tag{D.4b}$$

By putting (D.3) into (D.1) and using the above result, it is easy to obtain

$$\mathcal{G}_\eta(x,t) = \int_0^{+\infty} dq \, \frac{e^{-aq}}{2\pi q} \left[\coth\left(\frac{uq}{k_B\theta}\right) [\cos(qx_\eta) - 1] + i\eta \sin(qx_\eta) \right] , \tag{D.5}$$

where we have defined the chiral variables $x_\eta = x - \eta u t$ and performed the continuum limit

$$\sum_{q>0} \rightarrow \frac{L}{2\pi} \int_0^{+\infty} dq . \tag{D.6}$$

It is convenient to split Eq. (D.5) as $\mathcal{G}_\eta(x,t) = \mathcal{G}_\eta^{(0)}(x,t) + \mathcal{G}_\eta^{(\theta)}(x,t)$, where

$$\mathcal{G}_\eta^{(0)}(x,t) = \int_0^{+\infty} dq \, \frac{e^{-aq}}{2\pi q} \left(e^{iq\eta x_\eta} - 1 \right) \tag{D.7}$$

is independent of temperature and

$$\mathscr{G}_\eta^{(\theta)}(x,t) = \int_0^{+\infty} dq \, \frac{e^{-aq}}{2\pi q} \left[\coth\left(\frac{uq}{k_B\theta}\right) - 1 \right] [\cos(qx_\eta) - 1] \quad \text{(D.8)}$$

is a purely thermal contribution vanishing in the limit $\theta \to 0$.

Let us now focus on the zero-temperature term. By introducing the variable $y = aq$ and writing the exponential in (D.7) as a power series we get

$$\mathscr{G}_\eta^{(0)}(x,t) = \frac{1}{2\pi} \sum_{n=1}^{\infty} \frac{1}{n!} \left(\frac{i\eta x_\eta}{a}\right)^n \int_0^{+\infty} dy \, e^{-y} y^{n-1}. \quad \text{(D.9)}$$

The integral is equal to $\Gamma(n-1) = (n-1)!$ (Γ is Euler's Gamma function). Thus we obtain

$$\mathscr{G}_\eta^{(0)}(x,t) = \frac{1}{2\pi} \sum_{n=1}^{\infty} \frac{1}{n} \left(\frac{i\eta x_\eta}{a}\right)^n = \frac{1}{2\pi} \ln\left(\frac{1}{1 - i\eta x_\eta/a}\right). \quad \text{(D.10)}$$

The calculation of the thermal contribution (D.8) is more difficult. We begin by rearranging it as

$$\mathscr{G}_\eta^{(\theta)}(x,t) = \frac{1}{2\pi} \int_0^{+\infty} dy \, \frac{1}{y(1 - e^{-y})}$$
$$\times \left[e^{-\left(1 + \frac{\omega_c}{k_B\theta} + i\frac{k_B\theta x_\eta}{u}\right)y} + e^{-\left(1 + \frac{\omega_c}{k_B\theta} - i\frac{k_B\theta x_\eta}{u}\right)y} - 2e^{-\left(1 + \frac{\omega_c}{k_B\theta}\right)y} \right],$$
$$\text{(D.11)}$$

where $y = uq/(k_B\theta)$ and $\omega_c = u/a$ is the cutoff energy. Next, by introducing the Hurwitz zeta function [70]

$$\zeta(\gamma,z) = \frac{1}{\Gamma(\gamma)} \int_0^{+\infty} dt \frac{e^{-zt}}{t^{1-\gamma}(1 - e^{-t})}, \quad \text{(D.12)}$$

we write (D.11) as

$$\mathscr{G}_\eta^{(\theta)}(x,t) = \frac{1}{2\pi} \lim_{\gamma \to 0} \Gamma(\gamma) \left[\zeta\left(\gamma, 1 + \frac{\omega_c}{k_B\theta} + i\frac{k_B\theta x_\eta}{u}\right) \right.$$
$$\left. \times \zeta\left(\gamma, 1 + \frac{\omega_c}{k_B\theta} - i\frac{k_B\theta x_\eta}{u}\right) - 2\zeta\left(\gamma, 1 + \frac{\omega_c}{k_B\theta}\right) \right]. \quad \text{(D.13)}$$

Finally, by using the expansions [70]

$$\Gamma(\gamma) = \frac{1}{\gamma} + \mathcal{O}\left(\frac{1}{\gamma^2}\right), \quad \text{(D.14)}$$

$$\zeta(\gamma,z) = \frac{1}{2} - z + \gamma\left(\ln\Gamma(z) + \frac{1}{2}\ln 2\pi\right) + \mathcal{O}(\gamma^2), \quad \text{(D.15)}$$

which are valid for $\gamma \to 0$, we obtain

$$\mathscr{G}_\eta^{(\theta)}(x,t) = \frac{1}{2\pi} \ln\left[\frac{\left|\Gamma\left(1 + \frac{\omega_c}{k_B\theta} - i\frac{k_B\theta x_\eta}{u}\right)\right|^2}{\Gamma^2\left(1 + \frac{\omega_c}{k_B\theta}\right)} \right]. \quad \text{(D.16)}$$

We can now combine this result with (D.10) and write the final expression for the Green function (D.1)

$$\mathcal{G}_\eta(x,t) = \frac{1}{2\pi} \ln \left[\frac{\left| \Gamma\left(1 + \frac{\omega_c}{k_B\theta} - i\frac{k_B\theta x_\eta}{u}\right)\right|^2}{\Gamma^2\left(1 + \frac{\omega_c}{k_B\theta}\right)(1 - i\eta x_\eta/a)} \right]. \tag{D.17}$$

Since ω_c is assumed to be the largest energy scale in the problem, we are always in the condition $\omega_c \gg k_B\theta$. We can take advantage of this regime and of the identity

$$|\Gamma(1 + iy)|^2 = \frac{\pi y}{\sinh(\pi y)}, \tag{D.18}$$

(with $y \in \mathbb{R}$) to simplify (D.17), which becomes

$$\mathcal{G}_\eta(x,t) = \frac{1}{2\pi} \ln \left[\frac{a}{a - i\eta x_\eta} \frac{\pi k_B\theta x_\eta/u}{\sinh(\pi k_B\theta x_\eta/u)} \right]. \tag{D.19}$$

This is the expression we used in the main text. As we can see, the above function does not depend on space and time separately, but only via the chiral combinations $x_\eta = x - \eta u t$. Therefore, we can define a function of a single argument

$$G_\eta(z) = \frac{1}{2\pi} \ln \left[\frac{a}{a - i\eta z} \frac{\pi k_B\theta z/u}{\sinh(\pi k_B\theta z/u)} \right], \tag{D.20}$$

in terms of which we evidently have

$$\mathcal{G}_\eta(x,t) = G_\eta(x - \eta u t). \tag{D.21}$$

The above calculation applies to a system where the bosonic fields $\phi_\eta(x,t)$ have a different chirality but the same propagation velocity u. This is the system we investigated in Chapter 4. The result (D.19) can be easily extended to the case in which $\phi_\eta(x,t)$ have the *same chirality*, but *different velocities*, v_+ and v_-, depending on the index η. This is the system of copropagating channels we considered in Chapter 3. The very same calculation we presented above can be repeated, the only difference being that the starting expression of $\phi_\eta(x,t)$ now reads

$$\phi_\eta(x,t) = \frac{i}{\sqrt{L}} \sum_{q>0} \frac{e^{-aq/2}}{\sqrt{q}} \left(b_{q,\eta} e^{iq(x - v_\eta t)} - b_{q,\eta}^\dagger e^{-iq(x - v_\eta t)} \right), \tag{D.22}$$

instead of (D.3). This brings to the result

$$\mathcal{G}_\eta(x,t) = G_\eta(x - v_\eta t), \qquad G_\eta(z) = \frac{1}{2\pi} \ln \left[\frac{a}{a - iz} \frac{\pi k_B\theta z/v_\eta}{\sinh(\pi k_B\theta z/v_\eta)} \right]. \tag{D.23}$$

COMPLEMENTS TO CHAPTER 3

E.1 NUMBER OF EXCITED HOLES

The purpose of this Section is to derive the expression (3.49) for the number of injected holes at zero temperature due to the voltage pulse $V(t)$. Let us start by a simple observation. We defined in (3.23) the momentum distribution for edge channel 2 as

$$\Delta n_2(k, t) = \left\langle c_2^\dagger(k, t) c_2(k, t) \right\rangle - n_2^{(0)}(k), \tag{E.1}$$

with

$$n_2^{(0)}(k) = \left\langle c_2^{(0)\dagger}(k) c_2^{(0)}(k) \right\rangle \tag{E.2}$$

the equilibrium distribution in the absence of the drive. Now, because of fermionic anticommutation relations we clearly have $\Delta n_2(k, t) = -\Delta \tilde{n}_2(k, t)$, where

$$\Delta \tilde{n}_2(k, t) = \left\langle c_2(k, t) c_2^\dagger(k, t) - c_2^{(0)}(k) c_2^{(0)\dagger}(k) \right\rangle. \tag{E.3}$$

Therefore the number of holes at zero temperature can also be expressed as

$$\Delta N_h(t) = -\int_{-\infty}^{0} dk \, \Delta n_2(k, t) = \int_{-\infty}^{0} dk \, \Delta \tilde{n}_2(k, t), \tag{E.4}$$

with

$$\Delta \tilde{n}_2(k, t) = \frac{1}{2\pi} \int_{-\infty}^{+\infty} dx \int_{-\infty}^{+\infty} d\xi \frac{e^{-ik\xi}}{2\pi} \frac{1}{a - i\xi}$$
$$\left\{ \exp\left[-ie\frac{q_{2,+}}{q} \left(\int_{t-\frac{x}{v_+}-\frac{\xi/2}{v_+}}^{t-\frac{x}{v_+}+\frac{\xi/2}{v_+}} dt' V(t') - \int_{t-\frac{x}{v_-}-\frac{\xi/2}{v_-}}^{t-\frac{x}{v_-}+\frac{\xi/2}{v_-}} dt' V(t') \right) \right] - 1 \right\}.$$

The above expression is obtained by using Eqs. (3.6), (3.10), (3.25b) and (3.26) into the expression (3.24). By using the integral representation $\Theta(-k) = \frac{1}{2\pi} \lim_{a\to 0} \int_{-\infty}^{+\infty} dy \frac{e^{-iky}}{a+iy}$. and $\int_{-\infty}^{+\infty} \frac{dy}{(a+iy)^2} = 0$, we can rewrite the previous formula in the form

$$\Delta N_h(t) = \frac{1}{(2\pi)^2} \int_{-\infty}^{+\infty} dx \int_{-\infty}^{+\infty} dy \frac{1}{(a+iy)^2}$$
$$\times \exp\left[-ie\frac{q_2}{q} \left(\int_{t-\frac{x}{v_+}+\frac{y}{2v_+}}^{t-\frac{x}{v_+}-\frac{y}{2v_+}} dt' V(t') - \int_{t-\frac{x}{v_-}+\frac{y}{2v_-}}^{t-\frac{x}{v_-}-\frac{y}{2v_-}} dt' V(t') \right) \right]. \tag{E.5}$$

Furthermore, one can show that the contribution proportional to the sine function in the last expression (we will denote it by ΔN_h^s) actually vanishes. To that end, we note that

$$\lim_{a\to 0}\frac{1}{(a+iy)^2}=\lim_{a\to 0}\frac{a^2-y^2}{(a^2+y^2)^2}-i\pi\partial_y\delta(y)\equiv A(y)-i\pi\partial_y\delta(y),$$

(E.6)

where evidently $A(y)$ is an even function. Therefore N_h^s becomes

$$\begin{aligned}
N_h^s &= \frac{-i}{(2\pi)^2}\int_{-\infty}^{+\infty}dx\int_{-\infty}^{+\infty}dy[A(y)-i\pi\partial_y\delta(y)]\\
&\times\sin\left[e\frac{q_{2,+}}{q}\left(\int_{t-\frac{x}{v_+}+\frac{y}{2v_+}}^{t-\frac{x}{v_+}-\frac{y}{2v_+}}dt'V(t')-\int_{t-\frac{x}{v_-}+\frac{y}{2v_-}}^{t-\frac{x}{v_-}-\frac{y}{2v_-}}dt'V(t')\right)\right]\\
&= \frac{-i}{(2\pi)^2}\int_{-\infty}^{+\infty}dx\int_0^{+\infty}dy[A(y)-A(-y)]\\
&\times\sin\left[e\frac{q_{2,+}}{q}\left(\int_{t-\frac{x}{v_+}+\frac{y}{2v_+}}^{t-\frac{x}{v_+}-\frac{y}{2v_+}}dt'V(t')-\int_{t-\frac{x}{v_-}+\frac{y}{2v_-}}^{t-\frac{x}{v_-}-\frac{y}{2v_-}}dt'V(t')\right)\right]\\
&+\frac{eq_{2,+}}{4\pi q}\int_{-\infty}^{+\infty}dx\sum_{\eta=\pm}\frac{\eta}{v_\eta}V\left(t-\frac{x}{v_\eta}\right)\int_{-\infty}^{+\infty}dy\,\delta(y)\\
&\times\cos\left[e\frac{q_{2,+}}{q}\left(\int_{t-\frac{x}{v_+}+\frac{y}{v_+}}^{t-\frac{x}{v_+}}dt'V(t')-\int_{t-\frac{x}{v_-}+\frac{y}{v_-}}^{t-\frac{x}{v_-}}dt'V(t')\right)\right]\\
&= \frac{eq_{2,+}}{4\pi q}\int_{-\infty}^{+\infty}dx\left[\frac{1}{v_+}V\left(t-\frac{x}{v_+}\right)-\frac{1}{v_-}V\left(t-\frac{x}{v_-}\right)\right]=0,
\end{aligned}$$

(E.7)

having used the odd parity of the sine and the even parity of $A(y)$. Equation (3.49) in the main text is thus proved.

E.2   NOISE

In this Section we prove the formula (3.56) for the HBT noise due to the partitioning of inner-channel excitations. Recall that it is defined as

$$\begin{aligned}
S &= 2\int_{-\infty}^{+\infty}dt\int_{-\infty}^{+\infty}d\tau\left[\langle J_2(t+\tau)J_2(t)\rangle-\langle J_2(t+\tau)\rangle\langle J_2(t)\rangle\right]\\
&\equiv 2\int_{-\infty}^{+\infty}dt\int_{-\infty}^{+\infty}d\tau\,S(t,\tau),
\end{aligned}$$

(E.8)

with $J_2(t) = J_{L,2}(-d, t)$. The starting point of the calculation is the expression (3.55) for the perturbative expansion of the current operator $J_{L,2}(x, t) = J_{L,2}^{(0)}(x, t) + J_{L,2}^{(1)}(x, t) + J_{L,2}^{(2)}(x, t)$:

$$
\begin{aligned}
J_{L,2}(x, t) = J_{L,2}^{(0)}(x, t) - i \int_{-\infty}^{t} d\tau \left[J_{L,2}^{(0)}(x, t), H_t^{(0)}(\tau) \right] \\
- \int_{-\infty}^{t} dt' \int_{-\infty}^{t'} dt'' \left[H_t^{(0)}(t''), \left[H_t^{(0)}(t'), J_{L,2}^{(0)}(x, t) \right] \right],
\end{aligned}
\tag{E.9}
$$

The 0th order is simply the time evolution in the absence of tunneling, which is obtained from the solution of the equations of motion:

$$
J_{L,2}^{(0)}(x, t) = \frac{e}{\sqrt{2\pi}} \left[v_+ s \, \partial_x \phi_{L,+}(x + v_+ t, 0) + v_- c \, \partial_x \phi_{L,-}(x + v_- t, 0) \right].
\tag{E.10}
$$

In this expression, we have introduced the shorthand notation

$$
c \equiv \cos\chi, \qquad s \equiv \sin\chi.
\tag{E.11}
$$

From the above equation we can calculate the commutator needed for the first order contribution

$$
\left[J_{L,2}^{(0)}(t), H_t^{(0)}(\tau) \right] = \frac{e}{\sqrt{2\pi}} \left(v_+ s \, C_+ + v_- c \, C_- \right),
\tag{E.12}
$$

with

$$
\begin{aligned}
C_+ = \left[\partial_x \phi_{L,+}(x + v_+ t, 0), \Lambda \Psi_{R,2}^{\dagger}(0, \tau) \Psi_{L,2}(0, \tau) + \text{H.c.} \right], \\
C_- = \left[\partial_x \phi_{L,-}(x + v_- t, 0), \Lambda \Psi_{R,2}^{\dagger}(0, \tau) \Psi_{L,2}(0, \tau) + \text{H.c.} \right].
\end{aligned}
\tag{E.13}
$$

By using the bosonization identity and the useful relation

$$
\left[A, e^B \right] = [A, B] e^B,
\tag{E.14}
$$

we arrive at

$$
\begin{aligned}
C_+ = -\frac{\sqrt{2\pi} s}{v_+} \delta \left(\tau - \left(t + \frac{x}{v_+} \right) \right) \Lambda \Psi_{R,2}^{\dagger}(0, \tau) \Psi_{L,2}(0, \tau) - \text{H.c.} \\
C_+ = -\frac{\sqrt{2\pi} c}{v_-} \delta \left(\tau - \left(t + \frac{x}{v_-} \right) \right) \Lambda \Psi_{R,2}^{\dagger}(0, \tau) \Psi_{L,2}(0, \tau) - \text{H.c.}
\end{aligned}
\tag{E.15}
$$

Therefore we have the first order contribution

$$
\begin{aligned}
J_{L,2}^{(1)}(x, t) = i e \left\{ s^2 \left[\Lambda \Psi_{R,2}^{\dagger} \left(0, t + \frac{x}{v_+} \right) \Psi_{L,2} \left(0, t + \frac{x}{v_+} \right) - \text{H.c.} \right] + \right. \\
\left. + c^2 \left[\Lambda \Psi_{R,2}^{\dagger} \left(0, t + \frac{x}{v_-} \right) \Psi_{L,2} \left(0, t + \frac{x}{v_-} \right) - \text{H.c.} \right] \right\}.
\end{aligned}
\tag{E.16}
$$

We are now ready to compute the noise $S(t, \tau)$. We first observe that the separate averages $\left\langle J_{L,2}^{(1)} \right\rangle$ vanish because of Klein factors. Therefore we just have to calculate $\left\langle J_{L,2}^{(1)}(-d, t+\tau) J_{L,2}^{(1)}(-d, t) \right\rangle$. By substituting (E.16) we find eight non vanishing terms:

$$
S(t, \tau) = e^2 |\Lambda|^2 \times
$$
$$
\Big\langle s^4 \, \Psi_{R,2}^\dagger (0, t_+ + \tau) \, \psi_{L,2} (0, t_+ + \tau) \, \Psi_{L,2}^\dagger (0, t_+) \, \Psi_{R,2} (0, t_+)
$$
$$
+ s^2 c^2 \, \Psi_{R,2}^\dagger (0, t_+ + \tau) \, \psi_{L,2} (0, t_+ + \tau) \, \Psi_{L,2}^\dagger (0, t_-) \, \Psi_{R,2} (0, t_-)
$$
$$
+ s^4 \, \Psi_{L,2}^\dagger (0, t_+ + \tau) \, \psi_{R,2} (0, t_+ + \tau) \, \Psi_{R,2}^\dagger (0, t_+) \, \Psi_{L,2} (0, t_+)
$$
$$
+ s^2 c^2 \, \Psi_{L,2}^\dagger (0, t_+ + \tau) \, \psi_{R,2} (0, t_+ + \tau) \, \Psi_{R,2}^\dagger (0, t_-) \, \Psi_{L,2} (0, t_-)
$$
$$
+ s^2 c^2 \, \Psi_{R,2}^\dagger (0, t_- + \tau) \, \psi_{L,2} (0, t_- + \tau) \, \Psi_{L,2}^\dagger (0, t_+) \, \Psi_{R,2} (0, t_+)
$$
$$
+ c^4 \, \Psi_{R,2}^\dagger (0, t_- + \tau) \, \psi_{L,2} (0, t_- + \tau) \, \Psi_{L,2}^\dagger (0, t_-) \, \Psi_{R,2} (0, t_-)
$$
$$
+ s^2 c^2 \, \Psi_{L,2}^\dagger (0, t_- + \tau) \, \psi_{R,2} (0, t_- + \tau) \, \Psi_{R,2}^\dagger (0, t_+) \, \Psi_{L,2} (0, t_+)
$$
$$
+ c^4 \, \Psi_{L,2}^\dagger (0, t_- + \tau) \, \psi_{R,2} (0, t_- + \tau) \, \Psi_{R,2}^\dagger (0, t_-) \, \Psi_{L,2} (0, t_-) \Big\rangle ,
$$
$$
\text{(E.17)}
$$

where $t_\pm = t - d/v_\pm$. Now we use the bosonization identity together with the solution of the equations of motion (A.21) to express the time evolution of the fermion operators. When computing the averages, the results can be expressed by using the bosonic Green functions

$$
\mathscr{G}_{R,\pm}(x, t) = \langle \phi_{R,\pm}(x,t) \phi_{R,\pm}(0,0) \rangle - \langle \phi_{R,\pm}^2(0,0) \rangle , \tag{E.18}
$$
$$
\mathscr{G}_{L,\pm}(x, t) = \langle \phi_{L,\pm}(x,t) \phi_{L,\pm}(0,0) \rangle - \langle \phi_{L,\pm}^2(0,0) \rangle . \tag{E.19}
$$

The space coordinate being zero, the R and L Green function become equal and can be expressed as [cf. Eq. (D.23)]

$$
\mathscr{G}_{R,\pm}(0, t) = \mathscr{G}_{L,\pm}(0, t) = \frac{1}{2\pi} \tilde{G}_\pm(t) = \frac{1}{2\pi} \ln \frac{a}{a + iv_\pm t} \frac{\pi k_B \theta t}{\sinh(\pi k_B \theta t)} . \tag{E.20}
$$

By enumerating from ① to ⑧ the terms appearing in the average (E.17) we find

$$
① = s^4 \, \frac{e^{2s^2 \tilde{G}_+(\tau)} e^{2c^2 \tilde{G}_-(\tau)}}{(2\pi a)^2} e^{iecs \left[\int_{t+\tau-\frac{2d}{v_+}}^{t-\frac{2d}{v_+}} dt' V(t') - \int_{t+\tau-d\left(\frac{1}{v_+}+\frac{1}{v_-}\right)}^{t-d\left(\frac{1}{v_+}+\frac{1}{v_-}\right)} dt' V(t') \right]}
$$
$$
\text{(E.21a)}
$$

$$
② = s^2 c^2 \, \frac{e^{2s^2 \tilde{G}_+\left[\tau - d\left(\frac{1}{v_+} - \frac{1}{v_-}\right)\right]} e^{2c^2 \tilde{G}_-\left[\tau - d\left(\frac{1}{v_+} - \frac{1}{v_-}\right)\right]}}{(2\pi a)^2} \times
$$
$$
\times e^{iecs \left[\int_{t+\tau-\frac{2d}{v_+}}^{t-d\left(\frac{1}{v_+}+\frac{1}{v_-}\right)} dt' V(t') - \int_{t+\tau-d\left(\frac{1}{v_+}+\frac{1}{v_-}\right)}^{t-\frac{2d}{v_-}} dt' V(t') \right]}
$$
$$
\text{(E.21b)}
$$

$$
\text{⑤} = s^2 c^2 \, \frac{e^{2s^2 \tilde{G}_+ \left[\tau + d\left(\frac{1}{v_+} - \frac{1}{v_-}\right)\right]} e^{2c^2 \tilde{G}_- \left[\tau + d\left(\frac{1}{v_+} - \frac{1}{v_-}\right)\right]}}{(2\pi a)^2}
$$
$$
\times e^{iecs\left[\int_{t+\tau-d\left(\frac{1}{v_+}+\frac{1}{v_-}\right)}^{t-\frac{2d}{v_+}} dt' V(t') - \int_{t+\tau-\frac{2d}{v_-}}^{t-d\left(\frac{1}{v_+}+\frac{1}{v_-}\right)} dt' V(t')\right]}
\tag{E.21c}
$$

$$
\text{⑥} = c^4 \, \frac{e^{2s^2 \tilde{G}_+(\tau)} e^{2c^2 \tilde{G}_-(\tau)}}{(2\pi a)^2} e^{-iecs\left[\int_{t+\tau-\frac{2d}{v_-}}^{t-\frac{2d}{v_-}} dt' V(t') - \int_{t+\tau-d\left(\frac{1}{v_+}+\frac{1}{v_-}\right)}^{t-d\left(\frac{1}{v_+}+\frac{1}{v_-}\right)} dt' V(t')\right]}
\tag{E.21d}
$$

We did not write all terms, because they come in pairs as (①,③), (②,④), (⑤,⑦), (⑥,⑧). The missing terms in the above equations are obtained by taking the complex conjugate of the voltage-dependent phase factor of their partner. Therefore $S(t, \tau)$ can be rewritten as

$$
S(t, \tau) = \frac{2e^2 |\Lambda|^2}{(2\pi a)^2} \times
$$
$$
\Bigg\{ s^4 \, e^{2s^2 \tilde{G}_+(\tau)} e^{2c^2 \tilde{G}_-(\tau)}
$$
$$
\times \cos\left[ecs \left(\int_{t+\tau-\frac{2d}{v_+}}^{t-\frac{2d}{v_+}} dt' V(t') - \int_{t+\tau-d\left(\frac{1}{v_+}+\frac{1}{v_-}\right)}^{t-d\left(\frac{1}{v_+}+\frac{1}{v_-}\right)} dt' V(t') \right) \right]
$$
$$
+ s^2 c^2 \, e^{2s^2 \tilde{G}_+ \left[\tau - d\left(\frac{1}{v_+} - \frac{1}{v_-}\right)\right]} e^{2c^2 \tilde{G}_- \left[\tau - d\left(\frac{1}{v_+} - \frac{1}{v_-}\right)\right]}
$$
$$
\times \cos\left[ecs \left(\int_{t+\tau-\frac{2d}{v_+}}^{t-d\left(\frac{1}{v_+}+\frac{1}{v_-}\right)} dt' V(t') - \int_{t+\tau-d\left(\frac{1}{v_+}+\frac{1}{v_-}\right)}^{t-\frac{2d}{v_-}} dt' V(t') \right) \right]
$$
$$
+ s^2 c^2 \, e^{2s^2 \tilde{G}_+ \left[\tau + d\left(\frac{1}{v_+} - \frac{1}{v_-}\right)\right]} e^{2c^2 \tilde{G}_- \left[\tau + d\left(\frac{1}{v_+} - \frac{1}{v_-}\right)\right]}
$$
$$
\times \cos\left[ecs \left(\int_{t+\tau-d\left(\frac{1}{v_+}+\frac{1}{v_-}\right)}^{t-\frac{2d}{v_+}} dt' V(t') - \int_{t+\tau-\frac{2d}{v_-}}^{t-d\left(\frac{1}{v_+}+\frac{1}{v_-}\right)} dt' V(t') \right) \right]
$$
$$
+ \cos\left[ecs \left(\int_{t+\tau-\frac{2d}{v_-}}^{t-\frac{2d}{v_-}} dt' V(t') - \int_{t+\tau-d\left(\frac{1}{v_+}+\frac{1}{v_-}\right)}^{t-d\left(\frac{1}{v_+}+\frac{1}{v_-}\right)} dt' V(t') \right) \right]
$$
$$
\times c^4 \, e^{2s^2 \tilde{G}_+(\tau)} e^{2c^2 \tilde{G}_-(\tau)} \Bigg\} .
\tag{E.22}
$$

This is the farthest point we can arrive at for $S(t, \tau)$. However, once we integrate it over t and τ, the result looks much simpler. Indeed, we can make different changes of variables for each of the four terms in the last equation and show that their t and τ dependence is actually the same. Then we have a common factor, multiplying the combination $s^4 + 2s^2 c^2 + c^4 = (s^2 + c^2)^2 = 1$. In the end we find:

$$
S = \frac{4e^2 |\Lambda|^2}{(2\pi a)^2} \int_{-\infty}^{+\infty} dt \int_{-\infty}^{+\infty} d\tau \, e^{2s^2 \tilde{G}_+(\tau)} e^{2c^2 \tilde{G}_-(\tau)}
$$
$$
\cos\left\{ ecs \left[\int_{t+\tau}^{t} dt' V(t') - \int_{t+\tau+\tau_d}^{t+\tau_d} dt' V(t') \right] \right\},
\tag{E.23}
$$

where we have defined

$$\tau_d \equiv d \left(\frac{1}{v_+} - \frac{1}{v_-} \right) . \tag{E.24}$$

After substituting the expression (E.20) for the Green functions and recalling that $q_{2,+} = qcs$ we arrive at Eq. (3.56) of the main text.

E.2.1 *Backscattered current*

Here the final task is to compute the average backscattered current integrated over time (which is the equivalent of the T-averaged current in the case of a periodic signal), that is

$$\overline{\langle J_{L,2}(-d,t) \rangle} = \int_{-\infty}^{+\infty} dt \, \langle J_{L,2}(-d,t) \rangle . \tag{E.25}$$

In order to compute the average backscattered current, I have to calculate the current operator $J_{L,2}$ at second order. Recalling (E.12), (E.15) and substituting them into the second order term of the perturbative expansion (E.9), we find

$$J_{L,2}^{(2)}(x,t) =$$
$$-e \left\{ \left[\int_{-\infty}^{t+\frac{x}{v_+}} dt' \, s^2 \left[H_t^{(0)}(t'), \Lambda \Psi_{R,2}^\dagger \left(0, t+\frac{x}{v_+} \right) \Psi_{L,2} \left(0, t+\frac{x}{v_+} \right) - \text{H.c.} \right] \right. \right.$$
$$+ \left. \left. \int_{-\infty}^{t+\frac{x}{v_-}} dt' \, c^2 \left[H_t^{(0)}(t'), \Lambda \Psi_{R,2}^\dagger \left(0, t+\frac{x}{v_-} \right) \Psi_{L,2} \left(0, t+\frac{x}{v_-} \right) - \text{H.c.} \right] \right\} . \right.$$
$$\tag{E.26}$$

There are then two very similar contributions, differing only because of $v_+ \leftrightarrow v_-$ and the prefactors s^2 and c^2. When calculating the commutators several terms arise, but many of them vanish because of Klein factors when taking averages. By keeping only those with a non-zero average we arrive at

$$J_{L,2}^{(2)}(-d,t) \equiv J_{L,2}^{(+)}(t) + J_{L,2}^{(-)}(t)$$
$$= -e|\Lambda|^2 \left[s^2 \int_{-\infty}^{t-\frac{d}{v_+}} dt' \, D_+(t,t';d) + c^2 \int_{-\infty}^{t-\frac{d}{v_-}} dt' \, D_-(t,t';d) \right] , \tag{E.27}$$

with

$$D_\pm(t,t';d) = \Psi_{L,2}^\dagger(0,t')\Psi_{R,2}(0,t')\Psi_{R,2}^\dagger \left(0, t_\pm \right) \Psi_{L,2} \left(0, t_\pm \right) + \text{H.c.}$$
$$+ \Psi_{R,2}(0,t')\Psi_{L,2}(0,t')\Psi_{L,2}^\dagger \left(0, t_\pm \right) \Psi_{R,2} \left(0, t_\pm \right) + \text{H.c.} ,$$

where we recall that $t_\pm = t - d/v_\pm$. By computing the averages and the subsequent time integration over t' we find

$$\left\langle J_{L,2}^{(+)}(t) \right\rangle = \int_0^{+\infty} d\tau \left[e^{2s^2 \tilde{G}_+(\tau)} e^{2c^2 \tilde{G}_-(\tau)} - e^{2s^2 \tilde{G}_+(-\tau)} e^{2c^2 \tilde{G}_-(-\tau)} \right]$$

$$\frac{2ie|\Lambda|^2}{(2\pi a)^2 s^2} \sin \left[ecs \left(\int_{t-\tau-\frac{2d}{v_+}}^{t-\frac{2d}{v_+}} dt' V(t') - \int_{t-\tau-d\left(\frac{1}{v_+}+\frac{1}{v_-}\right)}^{t-d\left(\frac{1}{v_+}+\frac{1}{v_-}\right)} dt' V(t') \right) \right]. \tag{E.28}$$

Finally, the integration over t allows us to write

$$\overline{\left\langle J_{L,2}^{(+)}(t) \right\rangle} = \frac{2ie|\Lambda|^2}{(2\pi a)^2} s^2 \int_{-\infty}^{+\infty} dt \int_{-\infty}^{+\infty} d\tau e^{2s^2 \tilde{G}_+(\tau)} e^{2c^2 \tilde{G}_-(\tau)}$$

$$\times \sin \left[ecs \left(\int_{t-\tau}^{t} dt' V(t') - \int_{t-\tau+\tau_0}^{t+\tau_0} dt' V(t') \right) \right]. \tag{E.29}$$

By repeating the same procedure for the term $D_-(t, t'; d)$ we find for $\overline{\left\langle J_{L,2}^{(-)}(t) \right\rangle}$ the same result, apart from a prefactor c^2 instead of s^2. Summing up the two contributions we then have:

$$\overline{\left\langle J_{L,2}(-d, t) \right\rangle} = \frac{2ie|\Lambda|^2}{(2\pi a)^2} \int_{-\infty}^{+\infty} dt \int_{-\infty}^{+\infty} d\tau e^{2s^2 \tilde{G}_+(\tau)} e^{2c^2 \tilde{G}_-(\tau)}$$

$$\times \sin \left[ecs \left(\int_{t-\tau}^{t} dt' V(t') - \int_{t-\tau+\tau_d}^{t+\tau_d} dt' V(t') \right) \right]. \tag{E.30}$$

We can also show the quantity just calculated is actually zero. This is reasonable, since it is nothing but the total charge on channel 2, flowing into the left terminal on the lower edge; this should be zero, because the current is made of two pulses with opposite charges. In order to show that $\overline{\left\langle J_{L,2}(t) \right\rangle} = 0$ it is sufficient to follow the procedure which leads from Eq. (E.5) to (E.7).

E.2.2 *Excess noise*

The excess noise is defined as

$$\Delta S = S - 2e \overline{\left\langle J_{L,2}(-d, t) \right\rangle}. \tag{E.31}$$

Since we have shown that the integrated current (E.30) is zero in our case, then the excess noise is just equal to the noise (in other words the situation is the same as if we were applying a purely ac signal).

COMPLEMENTS TO CHAPTER 4

F.1 DETAILS ON THE DERIVATION OF COHERENCE FUNCTIONS

In this Section we provide the details on the derivation leading to Eqs. (4.26) and (4.27) in the main text. We show in detail the derivation for the excess lesser coherence function $\Delta \mathcal{G}_r^<$; the calculation for the greater contribution is analogous. The starting point is the definition (4.24a), which we report here for convenience:

$$
\begin{aligned}
\Delta \mathcal{G}_r^< (x,x;t_1,t_2) = {} & \left\langle \Psi_r^\dagger(x,t_2)\Psi_r(x,t_1) \right\rangle e^{ie \int_{t_1}^{t_2} U(x,t')dt'} \\
& - \left\langle \psi_r^\dagger(x,t_2)\psi_r(x,t_1) \right\rangle ,
\end{aligned}
\tag{F.1}
$$

where we recall that $\Psi_r(x,t)$ denotes the time evolution in the presence of the external drive $U(x,t) = F(x)V(t)$, while $\psi_r(x,t)$ is evaluated in the absence of the latter.

Two steps are needed to evaluate this coherence function. Firstly, we express fermionic fields by relying on the bosonization identity

$$
\begin{aligned}
\Psi_r(x,t) &= \frac{F_r}{\sqrt{2\pi a}}\, e^{i\vartheta_r k_F x}\, e^{-i\sqrt{2\pi}\Phi_r(x,t)} \\
&= \frac{F_r}{\sqrt{2\pi a}}\, e^{i\vartheta_r k_F x}\, e^{-i\sqrt{2\pi}\sum_{\eta=\pm} A_{\eta\vartheta_r}\Phi_\eta(x-\eta u t,0)},
\end{aligned}
\tag{F.2}
$$

where Eq. (4.10) relating chiral bosonic fields $\Phi_\eta(x,t)$ to the original ones $\Phi_{R/L}(x,t)$ was used. Secondly, the time evolution of bosonic fields in the presence of the drive is obtained by solving the equations of motion (4.15) and reads

$$
\Phi_\eta(x,t) = \phi_\eta(x-\eta u t,0) + \varphi_\eta(x,t),
\tag{F.3}
$$

with

$$
\varphi_\eta(x,t) = -e\sqrt{\frac{K}{2\pi}}\int_{-\infty}^{t} dt'\, V(t')F[x-\eta u(t-t')].
\tag{F.4}
$$

The result (4.16) is obtained for the special case $F(x) = \Theta(-x)$, but here we will keep general for a while. By using Eqs. (F.2), (F.3) and (F.4) in the definition (F.1) we find

$$
\Delta \mathcal{G}_r^< \left(x,x;t+\frac{\tau}{2}, t-\frac{\tau}{2}\right) = G_0^<(\tau)\left(e^{i\Delta\varphi_r(x;t,\tau)} e^{ie\int_{t+\tau/2}^{t-\tau/2} dt'\, U(x,t')} - 1 \right).
\tag{F.5}
$$

Here, we have introduced the equilibrium coherence function

$$
G_0^<(\tau) = \left\langle \psi_r^\dagger(x,0)\psi_r(x,\tau) \right\rangle
\tag{F.6}
$$

and the term $\Delta\varphi_r(x; t, \tau) = \sum_{\eta=\pm} \Delta\varphi_{r,\eta}(x; t, \tau)$, with

$$\Delta\varphi_{r,\eta}(x; t, \tau) = \sqrt{2\pi}A_{\eta\vartheta_r}\left[\varphi_\eta\left(x, t - \frac{\tau}{2}\right) - \varphi_\eta\left(x, t + \frac{\tau}{2}\right)\right] \quad \text{(F.7)}$$

and $\varphi_\eta(x, t)$ given in Eq. (F.4).

As we can see, the coherence function now contains only an equilibrium quantum average, which is evaluated as follows. From the bosonized form of fermionic fields it is easy to show that

$$G_0^<(\tau) = \frac{1}{2\pi a}\prod_{\eta=\pm}\left\langle e^{i\sqrt{2\pi}A_{\eta\vartheta_r}\phi_\eta(x,0)}e^{-i\sqrt{2\pi}A_{\eta\vartheta_r}\phi_\eta(x-\eta u\tau,0)}\right\rangle. \quad \text{(F.8)}$$

Next, we use the identity[1]

$$\left\langle\prod_{j=1}^N e^{O_j}\right\rangle = \exp\left(\frac{1}{2}\sum_{j=1}^N\langle O_j^2\rangle + \sum_{i<j}\langle O_iO_j\rangle\right) \quad \text{(F.9)}$$

(with $N = 2$) which allows us to write

$$G_0^<(\tau) = \frac{1}{2\pi a}\prod_{\eta=\pm}e^{2\pi A_{\eta\vartheta_r}^2[\langle\phi_\eta(x,0)\phi_\eta(x-\eta u\tau,0)\rangle - \langle\phi_\eta^2(0,0)\rangle]}. \quad \text{(F.10)}$$

Finally, the averages appearing in the exponential are evaluated as explained in App. D, leading to the result

$$G_0^<(\tau) = \left\langle\psi_r^\dagger(x, 0)\psi_r(x, \tau)\right\rangle = \frac{1}{2\pi(a - iu\tau)}\left[\frac{a}{a - iu\tau}\right]^{2A_-^2}. \quad \text{(F.11)}$$

Eq. (F.5), together with (F.4), (F.7) and (F.11), gives the most general expression for the excess lesser coherence function in the presence of an arbitrary drive $U(x, t) = F(x)V(t)$. Further progress can be made by specifying the form of $F(x)$, as it has been done in the main text. In particular, we consider now the simple case $F(x) = \Theta(-x)$. In this case, the solution (F.3) reduces to (4.16) and we obtain

$$\Delta\varphi_{r,+}(x; t, \tau) = eA_{\vartheta_r}\sqrt{K}\left[\Theta(x)\int_{t_+ - \frac{\tau}{2}}^{t_+ + \frac{\tau}{2}}dt' V(t') + \Theta(-x)\int_{t - \frac{\tau}{2}}^{t + \frac{\tau}{2}}dt' V(t')\right] \tag{F.12}$$

where we have defined $t_\pm = t \mp x/u$. Similarly, we find

$$\Delta\varphi_{r,-}(x; t, \tau) = eA_{-\vartheta_r}\sqrt{K}\Theta(-x)\left[\int_{t_- + \frac{\tau}{2}}^{t_- - \frac{\tau}{2}}dt' V(t') + \int_{t - \frac{\tau}{2}}^{t + \frac{\tau}{2}}dt' V(t')\right]. \tag{F.13}$$

---

1 This identity holds provided that operators O_i are linear in the bosonic creation and annihilation operators b and $b^\dagger$, $[O_i, O_j] \in \mathbb{C}$, $\forall i, j$ and the Hamiltonian with respect to which the average is evaluated is quadratic in b and $b^\dagger$. For a proof of this relation see Ref. [123]

Finally, the Wilson line term yields the contribution

$$e \int_{t+\tau/2}^{t-\tau/2} dt' \, U(x, t') = -e \, \Theta(-x) \int_{t-\tau/2}^{t+\tau/2} dt' \, V(t'). \tag{F.14}$$

Gathering the results, we can write the phase factor in Eq. (F.5) as

$$e^{i\Delta\varphi_r(x;t,\tau)} e^{ie \int_{t+\frac{\tau}{2}}^{t-\frac{\tau}{2}} dt' \, U(x,t')} = \prod_{\eta=\pm} e^{-ie\eta\sqrt{K} A_{\eta\vartheta_r} \Theta(\eta x) \int_{t_\eta+\frac{\tau}{2}}^{t_\eta-\frac{\tau}{2}} dt' \, V(t')}$$

$$= \sum_{\eta=\pm} \Theta(\eta x) \, e^{-ie\eta\sqrt{K} A_{\eta\vartheta_r} \int_{t_\eta+\frac{\tau}{2}}^{t_\eta-\frac{\tau}{2}} dt' \, V(t')}.$$

$$\tag{F.15}$$

Therefore, the excess coherence function (F.5) can be expressed as

$$\Delta\mathcal{G}_r^< \left(x, x; t + \frac{\tau}{2}, t - \frac{\tau}{2}\right) = \sum_{\eta=\pm} \Theta(\eta x) \Delta\mathcal{G}_{r,\eta}^< \left(t_\eta + \frac{\tau}{2}, t_\eta - \frac{\tau}{2}\right), \tag{F.16}$$

with

$$\Delta\mathcal{G}_{r,\eta}^< \left(t_\eta + \frac{\tau}{2}, t_\eta - \frac{\tau}{2}\right) = G_0^<(\tau) \Xi_{r,\eta}(t_\eta, \tau), \tag{F.17}$$

where $G_0^<(\tau)$ is given in (F.11) and

$$\Xi_{r,\eta}(t_\eta, \tau) = \exp\left[-ie\eta\sqrt{K} A_{\eta\vartheta_r} \int_{t+\tau/2}^{t-\tau/2} dt' \, V(t')\right] - 1. \tag{F.18}$$

The structure of Eqs. (4.26) and (4.27) in the main text is thus proved. The only missing ingredient is the point splitting term appearing in (4.27), which is discussed in the following.

F.2 POINT SPLITTING PROCEDURE

In this Section we give a justification for the point splitting factor (4.31) introduced in the expression (4.27) for the coherence functions. For the sake of generality, here we consider the following form of the external potential $U(x, t) = V(t)F(x)$, in the presence of which the solution of the equations of motion (4.15) is given by the expressions (F.3) and (F.4). The corresponding excess coherence function is written in Eq. (F.5)

As a consistency check of the correctness of this expression, we must verify that its diagonal limit reproduces the correct result for the electron density, namely [cf. also Eq. (2.41b)]:

$$\lim_{\tau\to 0} \Delta\mathcal{G}_r^< \left(x, x; t + \frac{\tau}{2}, t - \frac{\tau}{2}\right) = \Delta\rho_r^{(e)}(x, t) = \frac{-\vartheta_r}{\sqrt{2\pi}} \sum_{\eta=\pm} A_{\eta\vartheta_r} \partial_x \varphi_\eta(x, t)$$

$$= \frac{e\vartheta_r\sqrt{K}}{2\pi} \sum_{\eta=\pm} A_{\eta\vartheta_r} \int_{-\infty}^{t} dt' \, V(t') F'[x - \eta u(t - t')].$$

$$(F.19)$$

We now show that a regularization term – which we called point splitting factor – has to be introduced in the expression for the coherence function for the above result to be true. First of all, an expansion of (F.5) at small τ must be performed in order to compute the limit $\tau \to 0$.

Define the quantity

$$\Upsilon(x; t, \tau) \equiv e^{i\Delta\varphi_r(x;t,\tau)} e^{ie \int_{t+\tau/2}^{t-\tau/2} dt' \, U(x,t')} - 1.$$

$$(F.20)$$

Performing the expansion we have

$$\Upsilon(x; t, \tau) = \underbrace{\Upsilon(x; t, 0)}_{=0} + \frac{\partial\Upsilon}{\partial\tau}(x; t, \tau)\bigg|_{\tau=0} \tau + \mathcal{O}(\tau^2).$$

$$(F.21)$$

The partial derivative can be rewritten in the following way:

$$\frac{\partial\Upsilon}{\partial\tau}(x; t, \tau)\bigg|_{\tau=0} = i \sum_{\eta=\pm} \partial_\tau \Delta\varphi_{r,\eta}(x; t, \tau)\big|_{\tau=0}$$

$$+ ieF(x)\partial_\tau \int_{t+\tau/2}^{t-\tau/2} dt' \, V(t')\bigg|_{\tau=0}.$$

$$(F.22)$$

The first term is computed by expressing $\Delta\varphi_{r,\eta}$ through Eqs. (F.4) and (F.7). The calculation is straightforward, though a bit tedious, and yields

$$i\partial_\tau \Delta\varphi_{r,\eta}(x; t, \tau)\big|_{\tau=0} = -ieA_{\eta\vartheta_r}\sqrt{K}\eta u \int_{-\infty}^{t} dt' \, V(t')F'[x - \eta u(t - t')]$$

$$+ ieA_{\eta\vartheta_r}\sqrt{K}V(t)F(x).$$

$$(F.23)$$

The second term in (F.22) is easily evaluated:

$$ieF(x)\partial_\tau \int_{t+\tau/2}^{t-\tau/2} dt' \, V(t')\bigg|_{\tau=0} = -ieF(x)V(t).$$

$$(F.24)$$

By substituting the last two equations into (F.22), one realizes that the terms involving the product $F(x)V(t)$ cancel out. Notice that this cancellation would not occur without the inclusion of the Wilson line term in the definition (4.24). The final result for the expansion (F.21) reads:

$$\Upsilon(x; t, \tau) \approx -ieu\tau\sqrt{K} \sum_{\eta=\pm} \eta A_{\eta\vartheta_r} \int_{-\infty}^{t} dt' V(t')F'(x - \eta ut + \eta ut').$$

$$(F.25)$$

Gathering the results, we find

$$
\lim_{\tau \to 0} \Delta \mathcal{G}_r^< \left(x, x; t + \frac{\tau}{2}, t - \frac{\tau}{2} \right) = \lim_{\tau \to 0} \frac{\eta u \tau}{u \tau + i a} \left[\frac{a}{a - i u \tau} \right]^{2 A_-^2}
$$
$$
\times \frac{e \sqrt{K}}{2\pi} \sum_{\eta = \pm} A_{\eta \vartheta_r} \int_{-\infty}^t dt' \, V(t') F'[x - \eta u (t - t')].
$$
(F.26)

Now, we know that the limit (F.26) must reproduce the result (F.19) for the electron density, which has been calculated independently by relying on the relation $\rho^{(e)} \sim \partial_x \Phi$, that already takes care of regularization procedures in the bosonization framework. This condition gives a prescription to evaluate the limit in (F.26), which, if evaluated naively, would vanish. Thus we introduce the factor

$$
P_{r,\eta}^< (\tau) = \frac{\eta u \tau + i a \vartheta_r}{\eta u \tau}
$$
(F.27)

in the coherence function (F.5). By doing this, the relation (F.19) is established. Note that $P_{r,\eta}^< (\tau)$ only modifies the short-time behavior of $\Delta \mathcal{G}_r^<$, as it is a regularization prescription.

F.3 SIGN OF THE SPECTRAL FUNCTIONS

Here, we prove what we have stated in Sec. 4.3 about the sign of the spectral functions. Let us start by showing that $\Delta A_{R,+}^<(\omega)$ has a definite sign when evaluated for integer Levitons. For simplicity, it is convenient to consider the case of very long period $T \gg w$ and thus focus on a single Lorentzian pulse, given in (4.43). In this case, the phase factor (4.33) becomes

$$
\Xi_{r,\eta}(t, \tau) = \left[\frac{w + i(t - \tau/2)}{w - i(t - \tau/2)} \right]^{\eta \vartheta_r q_{r,\eta}} \left[\frac{w + i(t + \tau/2)}{w - i(t + \tau/2)} \right]^{-\eta \vartheta_r q_{r,\eta}} - 1.
$$
(F.28)

If $q_{r,\eta}$ is integer, further analytical evaluation is possible. Let us focus on the case where $q_{r,\eta} = n > 0$. We can therefore write [cf. Eq. (1.82) and (1.84)]

$$
\Xi_{r,\eta}(t, \tau) = -2\pi i \tau \sum_{j=1}^n \Pi_j \left(t + \frac{\tau}{2} \right) \Pi_j^* \left(t - \frac{\tau}{2} \right),
$$
(F.29)

where the wavefunctions Π_j are defined as

$$
\Pi_j(t) = \sqrt{\frac{w}{\pi}} \frac{(t + iw)^{j-1}}{(t - iw)^j}.
$$
(F.30)

By relying on these results, the variation of the spectral function becomes

$$\Delta \tilde{A}_{R,+}^{<}(\omega) = \frac{1}{2\pi u} \int_{-\infty}^{+\infty} d\tau\, e^{i\omega\tau} \left[\frac{a}{a - iu\tau} \right]^{2A_-^2}$$
$$\times \int_{-\infty}^{+\infty} dt \sum_{j=1}^{n} \Pi_j \left(t + \frac{\tau}{2} \right) \Pi_j^* \left(t - \frac{\tau}{2} \right).$$

(F.31)

Here, the tilde indicates that we adapted the definition of the spectral function to a single-pulse drive, by replacing the integral $T^{-1} \int_{-T/2}^{T/2} dt$ with $\int_{-\infty}^{+\infty} dt$. By evaluating the previous integral we arrive at

$$\Delta \tilde{A}_{R,+}^{<}(\omega) = \frac{2w}{u} \left(\frac{a}{u} \right)^{2A_-^2} \frac{e^{a\omega/u}}{\Gamma(2A_-^2)} \sum_{j=1}^{n} \left[\Theta(\omega) \mathcal{I}_j(\omega, \omega) + \Theta(-\omega) \mathcal{I}_j(\omega, 0) \right],$$

(F.32)

where Γ is the Gamma function, L_j the Laguerre polynomial of order j and

$$\mathcal{I}_j(\omega_1, \omega_2) = \int_{\omega_2}^{+\infty} d\epsilon\, e^{-2\epsilon w} e^{-\epsilon a/u} |\omega_1 - \epsilon|^{2A_-^2 - 1} L_{j-1}^2(2\epsilon w).$$ (F.33)

This results shows that the spectral function $\Delta A_{R,+}^{<}$ is always positive and nonvanishing for both $\omega \gtrless 0$, precisely as observed in the main text. When $q_{R,+} = m < 0$, by following the same steps as before, we find:

$$\Delta A_{R,+}^{<}(\omega) = -\frac{2w}{u} \left(\frac{a}{u} \right)^{2A_-^2} \frac{e^{a\omega/u}}{\Gamma(2A_-^2)} \sum_{j=1}^{|m|} \Theta(-\omega) \mathcal{J}_j(\omega),$$ (F.34)

with

$$\mathcal{J}_j(\omega) = \int_0^{-\omega} d\epsilon\, e^{-2\epsilon w} e^{\epsilon a/u} L_{j-1}^2(2\epsilon w) |\omega + \epsilon|^{2A_-^2 - 1}.$$ (F.35)

This shows that, in this case, the spectral function is always negative and vanishes for $\omega > 0$.

Concerning the spectral function $\Delta A_{R,-}^{<}(\omega)$, we can repeat a very similar procedure and we find (for $q_{R,-} = n > 0$)

$$\Delta A_{R,-}^{<}(\omega) = -\frac{2w}{u} \left(\frac{a}{u} \right)^{2A_-^2} \frac{e^{a\omega/u}}{\Gamma(2A_-^2)} \sum_{j=1}^{n} \Theta(-\omega) \mathcal{J}_j(\omega)$$
$$+ \frac{4w}{u} \left(\frac{a}{u} \right)^{1+2A_-^2} \frac{e^{a\omega/u}}{\Gamma(1 + 2A_-^2)}$$
$$\times \sum_{j=1}^{n} \Theta(-\omega) \int_0^{-\omega} d\epsilon\, e^{-2\epsilon w} e^{\epsilon a/u} L_{j-1}^2(2\epsilon w) |\omega + \epsilon|^{2A_-^2}.$$

(F.36)

The result is nonvanishing only for $\omega < 0$ and it consists of two terms, each with a definite sign. In particular, the former is negative, while the latter is positive. By looking at the dependence on ω, we realize that the negative term is more relevant at low freqencies, since it contains the power $|\omega + \epsilon|^{2A_-^2 - 1}$, while the positive term, containing $|\omega + \epsilon|^{2A_-^2}$ dominates at large negative frequencies. Therefore, the total distribution does not have a definite sign. This is shown in Fig.
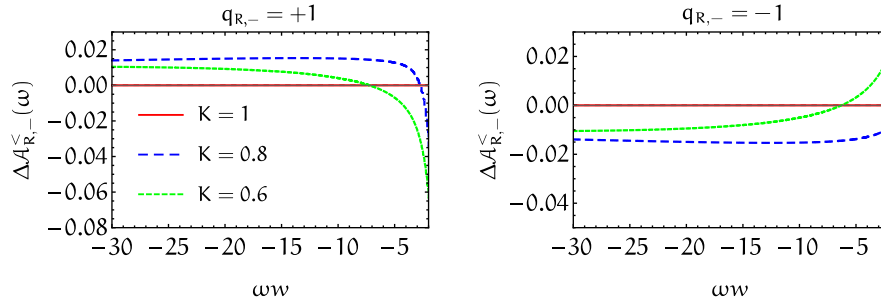
Figure F.1: Behavior of the tails of the spectral function $\Delta A_{R,-}^<(\omega)$, for $q_{R,-} = \pm 1$. Different values of K are indicated in the left panel. We clearly see a change of sign with respect to what happens at values of ω closer to zero, see Fig. 4.7. The units on the axes are the same as in Fig. 4.7.

F.1 (left panel). Similar considerations lead to the conclusion that for $q_{R,-} = m < 0$ the spectral function is negative at large negative values of ω, as illustrated in the right panel of Fig. F.1.

COMPLEMENTS TO CHAPTER 5

G.1 NONEQUILIBRIUM ENERGY DISTRIBUTIONS

In this Appendix we connect the excess noise defined in Eq. (5.31) of the main text to the out-of-equilibrium energy distribution of electrons, commonly used in the context of electron quantum optics [3]. Let us start by writing the model Hamiltonian with the explicit coupling to the external drive:

$$H = H_L + H_R + \lambda \sum_{\sigma=\uparrow\downarrow} (c_{L\sigma}^\dagger c_{R\sigma} + \text{H.c.}) + eV(t)N_L \,. \tag{G.1}$$

Here $c_{L/R\sigma}$ is the annihilation operator for the left/right lead at the point $x = 0$ where the tunneling occurs and N_L is the number operator for electrons in the left lead, the one where the voltage is applied. For our calculations it was convenient to include the effect of $V(t)$ into the tunneling amplitudes, as in Eq. (5.10). In order to do this it is sufficient to apply a unitary transformation generated by the operator

$$U = e^{ieN_L \int_0^t dt' \, V(t')} \,. \tag{G.2}$$

Then the Hamiltonian transforms according to the relation $H \to UHU^\dagger + i\dot{U}U^\dagger$ and becomes

$$H = H_L + H_R + \lambda \sum_{\sigma=\uparrow\downarrow} \left[e^{i\alpha(t)} c_{L\sigma}^\dagger c_{R\sigma} + \text{H.c.} \right] \,, \tag{G.3}$$

with $\alpha(t) = e \int_0^t dt' \, V(t')$. By including also the bare superconducting phase difference ϕ_0 we finally obtain Eq. (5.10). Under the above transformation, electron operators of the left lead become

$$\tilde{c}_{L\sigma} = Uc_{L\sigma}U^\dagger = e^{-i\alpha(t)} c_{L\sigma} \,, \tag{G.4}$$

while $c_{R\sigma}$ is unaffected. This shows that the effect of the external bias on the left lead electron operators can be encoded in the phase $\alpha(t)$.

We are now in position to compute nonequilibrium energy distributions of L-electrons and show how they connect with the excess noise. In the following we consider the effects of the drive $V(t)$ on the *isolated* left electrode (meaning that we do not consider the coupling to the right one consistently with the lowest order perturbation expansion discussed in the main text). The building blocks of the calculation are the electron and hole coherence functions, which are the fundamental ingredients in electron quantum optics [3]. They are defined as [1, 113]

(since there is no dependence on the spin, the index σ will be dropped in the following)

$$\tilde{g}^<(t, t') = \left\langle \tilde{c}_L^\dagger(t') \tilde{c}_L(t) \right\rangle, \tag{G.5a}$$

$$\tilde{g}^>(t, t') = \left\langle \tilde{c}_L(t) \tilde{c}_L^\dagger(t') \right\rangle. \tag{G.5b}$$

Notice that the definition involves $\tilde{c}_L$ operators, since we want to describe nonequilibrium effects due to $V(t)$. By using Eq. (G.4), coherence functions are expressed as

$$\tilde{g}^{\lessgtr}(t, t') = e^{-i[\alpha(t) - \alpha(t')]} g^{\lessgtr}(t, t'), \tag{G.6}$$

where

$$g^<(t, t') = -i\, g_0^{+-}(t - t') = g^>(t', t)$$
$$= \int_{-\infty}^{+\infty} \frac{y\, dy}{w\sqrt{y^2 - \Delta^2}} \Theta(y - \Delta)\, e^{iy(t - t')} \tag{G.7}$$

are zero temperature superconducting coherence functions at equilibrium, with no applied drive. Notice that the conventional free-fermion relation $g^<(\tau) + g^>(\tau) \propto \delta(\tau)$ is recovered in the limit $\Delta \to 0$ as expected. Starting from Eq. (G.5), one can define energy distribution functions [113]

$$f^{\gtrless}(\omega) = \int_{-T/2}^{T/2} \frac{d\bar{t}}{T} \int_{-\infty}^{+\infty} d\tau\, e^{i\omega\tau} \tilde{g}^{\gtrless}\left(\bar{t} + \frac{\tau}{2}, \bar{t} - \frac{\tau}{2}\right), \tag{G.8}$$

where T is the period of the drive. These quantities can be straightforwardly evaluated in terms of photoassisted coefficients. In particular, the equilibrium electron energy distribution is directly given by

$$f_{eq}^<(\omega) = -ig_0^{+-}(\omega) = 2\pi\rho_0(\omega) n_F(\omega) = \frac{-2\omega\Theta(-\omega - \Delta)}{\mathcal{E}\sqrt{\omega^2 - \Delta^2}}, \tag{G.9}$$

with $\rho_0(\omega)$ properly defined in Eq. (G.15) and the last expression being true at zero temperature. Finally, the complete hole energy distribution is found to be

$$f^>(\omega) = i\sum_{\ell \in \mathbb{Z}} |p_\ell|^2 g_0^{-+}(\omega - \Omega_\ell)$$
$$= 2\pi \sum_{\ell \in \mathbb{Z}} |p_\ell|^2 \rho_0(\omega - \Omega_\ell) n_F(\Omega_\ell - \omega) \tag{G.10}$$
$$= \frac{2}{\mathcal{E}} \sum_{\ell \in \mathbb{Z}} |p_\ell|^2 \frac{(\omega - \Omega_\ell)\Theta(\omega - \Omega_\ell - \Delta)}{\sqrt{(\omega - \Omega_\ell)^2 - \Delta^2}}.$$

Thus the connection in Eq. (5.35) of the main text is established.

We now provide general expressions for dc current and noise at low but finite temperature, in terms of a single integral over energy. In order to do so, we first have to introduce Dyson's equations relating full Green functions $\hat{G}$ to unperturbed ones $\hat{g}$. The simplest equation reads:

$$\hat{G}^{a/r}(t, t') = \hat{g}^{a/r}(t - t') + \int_{-\infty}^{+\infty} d\tau \hat{g}^{a/r}(t - \tau)\hat{\Sigma}^{a/r}(\tau)\hat{G}^{a/r}(\tau, t')$$

(G.11)

where $\hat{\Sigma}^{a/r}$ are the self-energy matrices. In our case, they are simply $\hat{\Sigma}_{LL}^{a/r} = \hat{\Sigma}_{RR}^{a/r} = 0$ and $= \hat{\Sigma}_{LR}^{a/r} = [\hat{\Sigma}_{RL}^{a/r}]^\dagger = \hat{W}$, with the matrix $\hat{W}$ given in (5.16). The equation for $\hat{G}^{+-}$ is more complicated:

$$\hat{G}^{+-} = \hat{g}^{+-} + \hat{G}^r\hat{\Sigma}^r\hat{g}^{+-} + \hat{G}^{+-}\hat{\Sigma}^a\hat{g}^a,$$

(G.12)

where a convolution over intermediate time arguments is assumed, like in Eq. (G.11). From this expression we obtain

$$\hat{G}_{LR}^{+-} = \hat{g}^{+-}\hat{W}\hat{G}_{RR}^a + \hat{g}^r\hat{W}\hat{G}_{RR}^{+-},$$

(G.13a)

$$\hat{G}_{RL}^{+-} = \hat{G}_{RR}^r\hat{W}^\dagger\hat{g}^{+-} + \hat{G}_{RR}^{+-}\hat{W}^\dagger\hat{g}^a.$$

(G.13b)

We can now use these relations into Eqs. (5.15)–(5.17) in the main text and truncate the expansion at lowest order in λ to obtain the following general expressions:

$$I_0 = 4\pi e\lambda^2 \sum_{\ell \in \mathbb{Z}} |p_\ell|^2 \int_{-\infty}^{+\infty} d\omega \rho_0(\omega)\rho_0(\omega - \Omega_\ell)[n_F(\omega - \Omega_\ell) - n_F(\omega)],$$

$$I_1 = 4\pi e\lambda^2 \sum_{\ell \in \mathbb{Z}} \text{Re}\left[e^{i\phi_0}p_\ell p_{-\ell-2q}\right] \int_{-\infty}^{+\infty} d\omega \rho_1(\omega)\rho_1(\omega - \Omega_\ell)$$
$$\times [n_F(\omega - \Omega_\ell) - n_F(\omega)],$$

$$I_J = -4\pi e\lambda^2 \sum_{\ell \in \mathbb{Z}} \text{Im}\left[e^{i\phi_0}p_\ell p_{-\ell-2q}\right] \int_{-\infty}^{+\infty} d\omega \rho_1(\omega)n_F(\omega)$$
$$\times [\rho_2(\omega + \Omega_\ell) + \rho_2(\omega - \Omega_\ell)],$$

$$S_0 = 8\pi e^2\lambda^2 \sum_{\ell \in \mathbb{Z}} |p_\ell|^2 \int_{-\infty}^{+\infty} d\omega \rho_0(\omega)\rho_0(\omega - \Omega_\ell)$$
$$\times [n_F(\omega)n_F(\Omega_\ell - \omega) + n_F(-\omega)n_F(\omega - \Omega_\ell)],$$

$$S_1 = 8\pi e^2\lambda^2 \sum_{\ell \in \mathbb{Z}} \text{Re}\left[e^{i\phi_0}p_\ell p_{-\ell-2q}\right] \int_{-\infty}^{+\infty} d\omega \rho_1(\omega)\rho_1(\omega - \Omega_\ell)$$
$$\times [n_F(\omega)n_F(\Omega_\ell - \omega) + n_F(-\omega)n_F(\omega - \Omega_\ell)].$$

(G.14)

The functions appearing in the above integrals are defined in terms of the unperturbed Green functions $\hat{g}^{a/r}(\omega) = g_0^{a/r}(\omega)\hat{\sigma}_0 + g_1^{a/r}(\omega)\hat{\sigma}_1$ given in Eq. (5.18) and are

$$
\begin{aligned}
\rho_0(\omega) &= \frac{1}{\pi}\text{Im}[g_0^a(\omega)] = \frac{|\omega|}{\pi\mathcal{E}\sqrt{\omega^2 - \Delta^2}}\Theta(|\omega| - \Delta)\,, \\
\rho_1(\omega) &= \frac{1}{\pi}\text{Im}[g_1^a(\omega)] = \frac{-\Delta\,\text{sgn}(\omega)}{\pi\mathcal{E}\sqrt{\omega^2 - \Delta^2}}\Theta(|\omega| - \Delta)\,, \\
\rho_2(\omega) &= \frac{1}{\pi}\text{Re}[g_1^a(\omega)] = \frac{\Delta}{\pi\mathcal{E}\sqrt{\Delta^2 - \omega^2}}\Theta(\Delta - |\omega|)\,.
\end{aligned}
\tag{G.15}
$$

Notice that in the above results, the dependence on temperature is confined to Fermi functions. Indeed, the temperature is assumed to be low enough for the gap Δ to be considered constant. The evaluation of integrals in Eq. (G.14) at zero temperature yields the results presented in the main text, see Eqs. (5.24)–(5.29).

BIBLIOGRAPHY

[1] C. Grenier, R. Hervé, G. Fève, and P. Degiovanni, "Electron quantum optics in quantum Hall edge channels," Mod. Phys. Lett. B **25**, 1053 (2011) (cit. on pp. xxv, 1, 24, 116, 163).

[2] E. Bocquillon, F. D. Parmentier, C. Grenier, J.-M. Berroir, P. Degiovanni, D. C. Glattli, B. Pla çais, A. Cavanna, Y. Jin, and G. Fève, "Electron Quantum Optics: Partitioning Electrons One by One," Phys. Rev. Lett. **108**, 196803 (2012) (cit. on pp. xxv, 1, 3, 17, 76).

[3] E. Bocquillon et al., "Electron quantum optics in ballistic chiral conductors," Ann. Phys. **526**, 1 (2014) (cit. on pp. xxv, xxvi, 1, 17, 54, 163).

[4] G. Fève, A. Mahé, J.-M. Berroir, T. Kontos, B. Plaçais, D. C. Glattli, A. Cavanna, B. Etienne, and Y. Jin, "An On-Demand Coherent Single-Electron Source," Science **316**, 1169 (2007) (cit. on pp. xxv, 15, 16).

[5] J. Dubois, T. Jullien, F. Portier, P. Roche, A. Cavanna, Y. Jin, W. Wegscheider, P. Roulleau, and D. C. Glattli, "Minimal-excitation states for electron quantum optics using levitons," Nature **502**, 659 (2013) (cit. on pp. xxv, 3, 15, 19, 20, 34, 37, 65, 96, 104, 115, 118, 121, 124, 141).

[6] L. S. Levitov, H. Lee, and G. B. Lesovik, "Electron counting statistics and coherent states of electric current," J. Math. Phys. **37**, 4845–4866 (1996) (cit. on pp. xxv, 19, 65, 69).

[7] D. A. Ivanov, H. W. Lee, and L. S. Levitov, "Coherent states of alternating current," Phys. Rev. B **56**, 6839–6850 (1997) (cit. on pp. xxv, 19, 36, 65, 69, 124).

[8] J. Keeling, I. Klich, and L. S. Levitov, "Minimal Excitation States of Electrons in One-Dimensional Wires," Phys. Rev. Lett. **97**, 116403 (2006) (cit. on pp. xxv, 19, 36, 65, 69, 104, 124).

[9] K. v. Klitzing, G. Dorda, and M. Pepper, "New Method for High-Accuracy Determination of the Fine-Structure Constant Based on Quantized Hall Resistance," Phys. Rev. Lett. **45**, 494 (1980) (cit. on pp. xxv, 4).

[10] R. B. Laughlin, "Quantized Hall conductivity in two dimensions," Phys. Rev. B **23**, 5632–5633 (1981) (cit. on pp. xxv, 11).

[11] B. I. Halperin, "Quantized Hall conductance, current-carrying edge states, and the existence of extended states in a two-dimensional disordered potential," Phys. Rev. B **25**, 2185–2190 (1982) (cit. on pp. xxv, 11, 13).

[12] R. E. Prange and S. M. Girvin, *The Quantum Hall Effect* (Springer-Verlag, 1990) (cit. on pp. xxv, 11).

[13] M. O. Goerbig, "Quantum Hall Effects," arXiv:0909.1998 (cit. on pp. xxv, 11).

[14] B. A. Bernevig, *Topological insulators and topological superconductors* (Cambridge University Press, 2013) (cit. on pp. xxv, 7–9, 84).

[15] M. Z. Hasan and C. L. Kane, "Colloquium: Topological insulators," Rev. Mod. Phys. **82**, 3045 (2010) (cit. on pp. xxv, 9, 85, 87).

[16] X.-L. Qi and S.-C. Zhang, "Topological insulators and superconductors," Rev. Mod. Phys. **83**, 1057 (2011) (cit. on pp. xxv, 85).

[17] B. A. Bernevig, T. L. Hughes, and S.-C. Zhang, "Quantum Spin Hall Effect and Topological Phase Transition in HgTe Quantum Wells," Science **314**, 1757 (2006) (cit. on pp. xxvi, 14, 83, 86).

[18] M. König, S. Wiedmann, C. Brüne, A. Roth, H. Buhmann, L. W. Molenkamp, X.-L. Qi, and S.-C. Zhang, "Quantum Spin Hall Insulator State in HgTe Quantum Wells," Science **318**, 766 (2007) (cit. on pp. xxvi, 83, 86).

[19] K. Bendias, S. Shamim, O. Herrmann, A. Budewitz, P. Shekhar, P. Leubner, J. Kleinlein, E. Bocquillon, H. Buhmann, and L. W. Molenkamp, "High Mobility HgTe Microstructures for Quantum Spin Hall Studies," Nano Letters **18**, 4831 (2018) (cit. on pp. xxvi, 124).

[20] J. Strunz et al., "Interacting topological edge channels," Nature Physics (2019) 10.1038/s41567-019-0692-4 (cit. on pp. xxvi, 124).

[21] L. D. Landau, "The theory of a Fermi liquid," Sov. Phys. JETP **3**, 920 (1956) (cit. on pp. xxvii, 39).

[22] F. D. M. Haldane, "'Luttinger liquid theory' of one-dimensional quantum fluids. I. Properties of the Luttinger model and their extension to the general 1D interacting spinless Fermi gas," Journal of Physics C: Solid State Physics **14**, 2585 (1981) (cit. on pp. xxvii, 40, 43).

[23] E. Bocquillon, V. Freulon, J.-M. Berroir, P. Degiovanni, B. Plaçais, A. Cavanna, Y. Jin, and G. Fève, "Separation of neutral and charge modes in one-dimensional chiral edge channels," Nature Communications **4**, 1839 (2013) (cit. on pp. xxvii, 17, 56).

[24] H. Kamata, N. Kumada, M. Hashisaka, K. Muraki, and T. Fujisawa, "Fractionalized wave packets from an artificial Tomonaga–Luttinger liquid," Nature Nanotechnology **9**, 177 (2014) (cit. on pp. xxvii, 40).

[25] Y. Jompol, C. J. B. Ford, J. P. Griffiths, I. Farrer, G. A. C. Jones, D. Anderson, D. A. Ritchie, T. W. Silk, and A. J. Schofield, "Probing Spin-Charge Separation in a Tomonaga-Luttinger Liquid," Science **325**, 597–601 (2009) (cit. on pp. xxvii, 40, 91).

[26] V. Freulon, A. Marguerite, J.-M. Berroir, B. Plaçais, A. Cavanna, Y. Jin, and G. Fève, "Hong-Ou-Mandel experiment for temporal investigation of single-electron fractionalization," Nature Communications **6**, 6854 (2015) (cit. on pp. xxvii, 17, 18, 54, 56).

[27] T. Li et al., "Observation of a Helical Luttinger Liquid in InAs/-GaSb Quantum Spin Hall Edges," Phys. Rev. Lett. **115**, 136804 (2015) (cit. on pp. xxvii, 89).

[28] R. Stühler, F. Reis, T. Müller, T. Helbig, T. Schwemmer, R. Thomale, J. Schäfer, and R. Claessen, "Tomonaga-Luttinger liquid in the edge channels of a quantum spin Hall insulator," Nature Physics (2019) 10.1038/s41567-019-0697-z (cit. on pp. xxvii, 89).

[29] M. Acciai, M. Carrega, J. Rech, T. Jonckheere, T. Martin, and M. Sassetti, "Probing interactions via nonequilibrium momentum distribution and noise in integer quantum Hall systems at $\nu = 2$," Phys. Rev. B **98**, 035426 (2018) (cit. on pp. xxviii, 57, 70, 104, 115).

[30] M. Acciai, M. Carrega, J. Rech, T. Jonckheere, D. Ferraro, T. Martin, and M. Sassetti, "Single-electron excitations and interactions in integer quantum Hall systems at $\nu = 2$," Journal of Physics: Conference Series **1182**, 012003 (2019) (cit. on pp. xxviii, 57, 96).

[31] M. Acciai, A. Calzona, M. Carrega, T. Martin, and M. Sassetti, "Spectral properties of interacting helical channels driven by lorentzian pulses," New Journal of Physics **21**, 103031 (2019) (cit. on pp. xxviii, 83).

[32] M. Acciai, F. Ronetti, D. Ferraro, J. Rech, T. Jonckheere, M. Sassetti, and T. Martin, "Levitons in superconducting point contacts," Phys. Rev. B **100**, 085418 (2019) (cit. on pp. xxviii, 107).

[33] D. Dasenbrook and C. Flindt, "Dynamical generation and detection of entanglement in neutral leviton pairs," Phys. Rev. B **92**, 161412 (2015) (cit. on pp. 1, 96, 115).

[34] D. Dasenbrook, J. Bowles, J. B. Brask, P. P. Hofer, C. Flindt, and N. Brunner, "Single-electron entanglement and nonlocality," New Journal of Physics **18**, 043036 (2016) (cit. on pp. 1, 96, 115).

[35] D. C. Glattli and P. Roulleau, "Pseudorandom binary injection of levitons for electron quantum optics," Phys. Rev. B **97**, 125407 (2018) (cit. on pp. 1, 115).

[36]   N. Gisin, G. Ribordy, W. Tittel, and H. Zbinden, "Quantum cryptography," Rev. Mod. Phys. **74**, 145–195 (2002) (cit. on p. 1).

[37]   A. Shenoy-Hejamadi, A. Pathak, and S. Radhakrishna, "Quantum Cryptography: Key Distribution and Beyond," Quanta **6**, 1–47 (2017) (cit. on p. 1).

[38]   A. Bertoni, P. Bordone, R. Brunetti, C. Jacoboni, and S. Reggiani, "Quantum Logic Gates based on Coherent Electron Transport in Quantum Wires," Phys. Rev. Lett. **84**, 5912–5915 (2000) (cit. on p. 1).

[39]   C. Bäuerle, D. C. Glattli, T. Meunier, F. Portier, P. Roche, P. Roulleau, S. Takada, and X. Waintal, "Coherent control of single electrons: a review of current progress," Reports on Progress in Physics **81**, 056503 (2018) (cit. on pp. 1, 14, 15, 18).

[40]   C. C. Dean and M Pepper, "The transition from two- to one-dimensional electronic transport in narrow silicon accumulation layers," Journal of Physics C: Solid State Physics **15**, L1287–L1297 (1982) (cit. on p. 2).

[41]   B. J. van Wees, H. van Houten, C. W. J. Beenakker, J. G. Williamson, L. P. Kouwenhoven, D. van der Marel, and C. T. Foxon, "Quantized conductance of point contacts in a two-dimensional electron gas," Phys. Rev. Lett. **60**, 848–850 (1988) (cit. on p. 2).

[42]   D. A. Wharam, T. J. Thornton, R Newbury, M Pepper, H Ahmed, J. E. F. Frost, D. G. Hasko, D. C. Peacock, D. A. Ritchie, and G. A. C. Jones, "One-dimensional transport and the quantisation of the ballistic resistance," Journal of Physics C: Solid State Physics **21**, L209–L214 (1988) (cit. on p. 2).

[43]   T. J. Thornton, M. Pepper, H. Ahmed, D. Andrews, and G. J. Davies, "One-Dimensional Conduction in the 2D electron Gas of a GaAs-AlGaAs Heterojunction," Phys. Rev. Lett. **56**, 1198–1201 (1986) (cit. on p. 2).

[44]   M. Büttiker, "Quantized transmission of a saddle-point constriction," Phys. Rev. B **41**, 7906–7909 (1990) (cit. on p. 2).

[45]   H. van Houten and C. W. J. Beenakker, "Quantum point contacts," Physics Today **49**, 22 (1996) (cit. on p. 2).

[46]   C Rössler, S Baer, E de Wiljes, P.-L. Ardelt, T Ihn, K Ensslin, C Reichl, and W Wegscheider, "Transport properties of clean quantum point contacts," New Journal of Physics **13**, 113006 (2011) (cit. on p. 3).

[47]   A. T. Hatke, M. A. Zudov, L. N. Pfeiffer, and K. W. West, "Shubnikov–de Haas oscillations in GaAs quantum wells in tilted magnetic fields," Phys. Rev. B **85**, 241305 (2012) (cit. on p. 3).

[48] V. Umansky, M. Heiblum, Y. Levinson, J. Smet, J. Nübler, and M. Dolev, "MBE growth of ultra-low disorder 2DEG with mobility exceeding 35×10^6 cm^2/V s," Journal of Crystal Growth **311**, 1658 –1661 (2009) (cit. on p. 3).

[49] P. Roulleau, F. Portier, P. Roche, A. Cavanna, G. Faini, U. Gennser, and D. Mailly, "Direct Measurement of the Coherence Length of Edge States in the Integer Quantum Hall Regime," Phys. Rev. Lett. **100**, 126802 (2008) (cit. on p. 4).

[50] K. von Klitzing, "Metrology in 2019," Nature Physics **13**, 198 (2017) (cit. on p. 4).

[51] K. von Klitzing, "Quantum Hall Effect: Discovery and Application," Annual Review of Condensed Matter Physics **8**, 13–30 (2017) (cit. on p. 4).

[52] L. Vannucci, "Electron quantum optics at fractional filling factor: minimal excitation states and interferometry," PhD thesis (Mar. 2018) (cit. on pp. 5, 79, 142).

[53] D. J. Thouless, M. Kohmoto, M. P. Nightingale, and M. den Nijs, "Quantized Hall Conductance in a Two-Dimensional Periodic Potential," Phys. Rev. Lett. **49**, 405–408 (1982) (cit. on pp. 6, 8, 83).

[54] M. V. Berry, "Quantal phase factors accompanying adiabatic changes," Proceedings of the Royal Society of London. A. Mathematical and Physical Sciences **392**, 45–57 (1984) (cit. on p. 6).

[55] S. Pancharatnam, "Generalized theory of interference, and its applications," Proceedings of the Indian Academy of Sciences - Section A **44**, 247–262 (1956) (cit. on p. 6).

[56] M. Born and V. Fock, "Beweis des Adiabatensatzes," Zeitschrift für Physik **51**, 165–180 (1928) (cit. on p. 6).

[57] R. Resta, *Geometry and Topology in Electronic Structure Theory*, Lecture notes available at `http://www-dft.ts.infn.it/~resta/gtse` (cit. on pp. 7, 8).

[58] M. Nakahara, *Geometry, topology, and physics* (Institute of Physics Publishing, 2003) (cit. on pp. 8, 9).

[59] M. Kohmoto, "Topological invariant and the quantization of the Hall conductance," Annals of Physics **160**, 343 –354 (1985) (cit. on p. 8).

[60] F. Bloch, "Über die Quantenmechanik der Elektronen in Kristallgittern," Zeitschrift für Physik **52**, 555–600 (1929) (cit. on p. 8).

[61] N. Ashcroft and N. Mermin, *Solid state physics*, Science: Physics (Saunders College, 1976) (cit. on p. 8).

[62] E. Fradkin, *Field Theories of Condensed Matter Physics* (Cambridge University Press, 2013) (cit. on pp. 8, 9).

[63]   D. Tong, "Lectures on the Quantum Hall Effect," arXiv:1606.06687 (2016) (cit. on pp. 8, 11).

[64]   D. R. Hofstadter, "Energy levels and wave functions of Bloch electrons in rational and irrational magnetic fields," Phys. Rev. B **14**, 2239–2249 (1976) (cit. on p. 9).

[65]   M. Y. Azbel, "Energy Spectrum of a Conduction Electron in a Magnetic Field," Sov. Phys. JETP **19**, 634 (1964) (cit. on p. 9).

[66]   R Kubo, "The fluctuation-dissipation theorem," Reports on Progress in Physics **29**, 255–284 (1966) (cit. on p. 9).

[67]   F. D. M. Haldane, "Model for a Quantum Hall Effect without Landau Levels: Condensed-Matter Realization of the "Parity Anomaly"," Phys. Rev. Lett. **61**, 2015 (1988) (cit. on pp. 10, 86).

[68]   X.-L. Qi, Y.-S. Wu, and S.-C. Zhang, "Topological quantization of the spin Hall effect in two-dimensional paramagnetic semiconductors," Phys. Rev. B **74**, 085308 (2006) (cit. on p. 10).

[69]   L. Landau and E. Lifshitz, *Quantum Mechanics: Non-Relativistic Theory*, Course of Theoretical Physics (Pergamon Press, 1977) (cit. on p. 11).

[70]   *NIST DIGITAL LIBRARY OF MATHEMATICAL FUNCTIONS*, http://dlmf.nist.gov/, Release 1.0.23 of 2019-06-15, F. W. J. Olver, A. B. Olde Daalhuis, D. W. Lozier, B. I. Schneider, R. F. Boisvert, C. W. Clark, B. R. Miller and B. V. Saunders, eds. (cit. on pp. 11, 31, 113, 135, 144).

[71]   R. Landauer, "Spatial Variation of Currents and Fields Due to Localized Scatterers in Metallic Conduction," IBM Journal of Research and Development **1**, 223–231 (1957) (cit. on p. 13).

[72]   M. Büttiker, Y. Imry, R. Landauer, and S. Pinhas, "Generalized many-channel conductance formula with application to small rings," Phys. Rev. B **31**, 6207–6215 (1985) (cit. on p. 13).

[73]   D. C. Tsui, H. L. Stormer, and A. C. Gossard, "Two-Dimensional Magnetotransport in the Extreme Quantum Limit," Phys. Rev. Lett. **48**, 1559–1562 (1982) (cit. on p. 14).

[74]   R. B. Laughlin, "Anomalous Quantum Hall Effect: An Incompressible Quantum Fluid with Fractionally Charged Excitations," Phys. Rev. Lett. **50**, 1395–1398 (1983) (cit. on p. 14).

[75]   X. G. Wen and A. Zee, "Classification of Abelian quantum Hall states and matrix formulation of topological fluids," Phys. Rev. B **46**, 2290–2301 (1992) (cit. on p. 14).

[76]   C. Chamon, E. Fradkin, and A. López, "Fractional Statistics and Duality: Strong Tunneling Behavior of Edge States of Quantum Hall Liquids in the Jain Sequence," Phys. Rev. Lett. **98**, 176801 (2007) (cit. on p. 14).

[77] M. Banerjee, M. Heiblum, V. Umansky, D. E. Feldman, Y. Oreg, and A. Stern, "Observation of half-integer thermal Hall conductance," Nature **559**, 205–210 (2018) (cit. on p. 14).

[78] S. H. Simon, "Interpretation of thermal conductance of the $\nu = 5/2$ edge," Phys. Rev. B **97**, 121406 (2018) (cit. on p. 14).

[79] K. K. W. Ma and D. E. Feldman, "Partial equilibration of integer and fractional edge channels in the thermal quantum Hall effect," Phys. Rev. B **99**, 085309 (2019) (cit. on p. 14).

[80] D. Ferraro, J. Rech, T. Jonckheere, and T. Martin, "Single quasiparticle and electron emitter in the fractional quantum Hall regime," Phys. Rev. B **91**, 205409 (2015) (cit. on p. 14).

[81] J. Rech, D. Ferraro, T. Jonckheere, L. Vannucci, M. Sassetti, and T. Martin, "Minimal Excitations in the Fractional Quantum Hall Regime," Phys. Rev. Lett. **118**, 076801 (2017) (cit. on pp. 14, 79, 96, 104, 116, 124).

[82] L. Vannucci, F. Ronetti, J. Rech, D. Ferraro, T. Jonckheere, T. Martin, and M. Sassetti, "Minimal excitation states for heat transport in driven quantum Hall systems," Phys. Rev. B **95**, 245415 (2017) (cit. on pp. 14, 115, 124).

[83] D. Ferraro, T. Jonckheere, J. Rech, and T. Martin, "Electronic quantum optics beyond the integer quantum Hall effect," physica status solidi (b) **254**, 1600531 (2017) (cit. on p. 14).

[84] L. Vannucci, F. Ronetti, D. Ferraro, J. Rech, T. Jonckheere, T. Martin, and M. Sassetti, "Photoassisted shot noise spectroscopy at fractional filling factor," J. Phys. Conf. Ser. **969**, 012143 (2018) (cit. on p. 14).

[85] F. Ronetti, L. Vannucci, D. Ferraro, T. Jonckheere, J. Rech, T. Martin, and M. Sassetti, "Crystallization of levitons in the fractional quantum Hall regime," Phys. Rev. B **98**, 075401 (2018) (cit. on pp. 14, 96, 115, 124).

[86] D. Ferraro, F. Ronetti, L. Vannucci, M. Acciai, J. Rech, T. Jonckheere, T. Martin, and M. Sassetti, "Hong-Ou-Mandel characterization of multiply charged Levitons," The European Physical Journal Special Topics **227**, 1345–1359 (2018) (cit. on pp. 14, 142).

[87] F. Ronetti, L. Vannucci, D. Ferraro, T. Jonckheere, J. Rech, T. Martin, and M. Sassetti, "Hong-Ou-Mandel heat noise in the quantum Hall regime," Phys. Rev. B **99**, 205406 (2019) (cit. on pp. 14, 124).

[88] F. Ronetti, M. Acciai, D. Ferraro, J. Rech, T. Jonckheere, T. Martin, and M. Sassetti, "Symmetry Properties of Mixed and Heat Photo-Assisted Noise in the Quantum Hall Regime," Entropy **21**, 730 (2019) (cit. on p. 14).

[89] J. D. Fletcher et al., "Clock-Controlled Emission of Single-Electron Wave Packets in a Solid-State Circuit," Phys. Rev. Lett. **111**, 216807 (2013) (cit. on p. 14).

[90] N. Johnson et al., "LO-Phonon Emission Rate of Hot Electrons from an On-Demand Single-Electron Source in a GaAs/AlGaAs Heterostructure," Phys. Rev. Lett. **121**, 137703 (2018) (cit. on p. 14).

[91] T. Ota, S. Akiyama, M. Hashisaka, K. Muraki, and T. Fujisawa, "Spectroscopic study on hot-electron transport in a quantum Hall edge channel," Phys. Rev. B **99**, 085310 (2019) (cit. on p. 14).

[92] S. Hermelin, S. Takada, M. Yamamoto, S. Tarucha, A. D. Wieck, L. Saminadayar, C. Bäuerle, and T. Meunier, "Electrons surfing on a sound wave as a platform for quantum optics with flying electrons," Nature **477**, 435 (2011) (cit. on p. 15).

[93] R. P. G. McNeil, M. Kataoka, C. J. B. Ford, C. H. W. Barnes, D. Anderson, G. A. C. Jones, I. Farrer, and D. A. Ritchie, "On-demand single-electron transfer between distant quantum dots," Nature **477**, 439 (2011) (cit. on p. 15).

[94] A. Mahé, F. D. Parmentier, E. Bocquillon, J.-M. Berroir, D. C. Glattli, T. Kontos, B. Pla çais, G. Fève, A. Cavanna, and Y. Jin, "Current correlations of an on-demand single-electron emitter," Phys. Rev. B **82**, 201309 (2010) (cit. on p. 15).

[95] F. D. Parmentier, E. Bocquillon, J.-M. Berroir, D. C. Glattli, B. Pla çais, G. Fève, M. Albert, C. Flindt, and M. Büttiker, "Current noise spectrum of a single-particle emitter: Theory and experiment," Phys. Rev. B **85**, 165438 (2012) (cit. on pp. 16, 17).

[96] M. Albert, C. Flindt, and M. Büttiker, "Accuracy of the quantum capacitor as a single-electron source," Phys. Rev. B **82**, 041407 (2010) (cit. on p. 16).

[97] J. Keeling, A. V. Shytov, and L. S. Levitov, "Coherent Particle Transfer in an On-Demand Single-Electron Source," Phys. Rev. Lett. **101**, 196404 (2008) (cit. on p. 16).

[98] E. Bocquillon, V. Freulon, J.-M Berroir, P. Degiovanni, B. Plaçais, A. Cavanna, Y. Jin, and G. Fève, "Coherence and Indistinguishability of Single Electrons Emitted by Independent Sources," Science **339**, 1054 (2013) (cit. on pp. 17, 18).

[99] A. Marguerite et al., "Decoherence and relaxation of a single electron in a one-dimensional conductor," Phys. Rev. B **94**, 115311 (2016) (cit. on p. 17).

[100] R. Hanbury Brown and R. Q. Twiss, "A Test of a New Type of Stellar Interferometer on Sirius," Nature **178**, 1046 (1956) (cit. on p. 17).

[101] C. K. Hong, Z. Y. Ou, and L. Mandel, "Measurement of subpicosecond time intervals between two photons by interference," Phys. Rev. Lett. **59**, 2044–2046 (1987) (cit. on p. 17).

[102] C. Wahl, J. Rech, T. Jonckheere, and T. Martin, "Interactions and Charge Fractionalization in an Electronic Hong-Ou-Mandel Interferometer," Phys. Rev. Lett. **112**, 046802 (2014) (cit. on p. 18).

[103] R. J. Glauber, "Photon Correlations," Phys. Rev. Lett. **10**, 84–86 (1963) (cit. on p. 24).

[104] R. J. Glauber, "The Quantum Theory of Optical Coherence," Phys. Rev. **130**, 2529–2539 (1963) (cit. on p. 24).

[105] R. J. Glauber, "Coherent and Incoherent States of the Radiation Field," Phys. Rev. **131**, 2766–2788 (1963) (cit. on p. 24).

[106] M. Moskalets, "Two-electron state from the Floquet scattering matrix perspective," Phys. Rev. B **89**, 045402 (2014) (cit. on p. 24).

[107] E. Thibierge, D. Ferraro, B. Roussel, C. Cabart, A. Marguerite, G. Fève, and P. Degiovanni, "Two-electron coherence and its measurement in electron quantum optics," Phys. Rev. B **93**, 081302 (2016) (cit. on p. 24).

[108] M. Moskalets, "Single-electron second-order correlation function $G^{(2)}$ at nonzero temperatures," Phys. Rev. B **98**, 115421 (2018) (cit. on pp. 24, 96).

[109] C. Cabart, "Measurement and control of electronic coherences," PhD thesis (Sept. 2018) (cit. on p. 24).

[110] G. Haack, M. Moskalets, and M. Büttiker, "Glauber coherence of single-electron sources," Phys. Rev. B **87**, 201302 (2013) (cit. on p. 24).

[111] E. Wigner, "On the Quantum Correction For Thermodynamic Equilibrium," Phys. Rev. **40**, 749–759 (1932) (cit. on pp. 26, 129).

[112] M. Hillery, R. O'Connell, M. Scully, and E. Wigner, "Distribution functions in physics: Fundamentals," Physics Reports **106**, 121 –167 (1984) (cit. on p. 26).

[113] D. Ferraro, A. Feller, A. Ghibaudo, E. Thibierge, E. Bocquillon, G. Fève, C. Grenier, and P. Degiovanni, "Wigner function approach to single electron coherence in quantum Hall edge channels," Phys. Rev. B **88**, 205303 (2013) (cit. on pp. 27, 31, 33, 116, 133, 163, 164).

[114] C. Grenier, J. Dubois, T. Jullien, P. Roulleau, D. C. Glattli, and P. Degiovanni, "Fractionalization of minimal excitations in integer quantum Hall edge channels," Phys. Rev. B **88**, 085302 (2013) (cit. on pp. 30, 35, 36, 54, 68, 76, 104).

[115] M. Moskalets, "First-order correlation function of a stream of single-electron wave packets," Phys. Rev. B **91**, 195431 (2015) (cit. on p. 30).

[116] D. Glattli and P. Roulleau, "Hanbury-Brown Twiss noise correlation with time controlled quasi-particles in ballistic quantum conductors," Physica E: Low-dimensional Systems and Nanostructures **76**, 216 (2016) (cit. on pp. 30, 96).

[117] J. Dubois, T. Jullien, C. Grenier, P. Degiovanni, P. Roulleau, and D. C. Glattli, "Integer and fractional charge Lorentzian voltage pulses analyzed in the framework of photon-assisted shot noise," Phys. Rev. B **88**, 085301 (2013) (cit. on pp. 35, 78, 79, 95, 96, 104, 112, 114–116, 118, 121, 124).

[118] G. Giuliani and G. Vignale, *Quantum Theory of the Electron Liquid* (Cambridge University Press, 2005) (cit. on pp. 39, 40).

[119] T. Giamarchi, *Quantum Physics in One Dimension* (Oxford University Press, Oxford, 2003) (cit. on pp. 39, 40, 46, 92, 93).

[120] A. J. Schofield, "Non-Fermi liquids," Contemporary Physics **40**, 95–115 (1999) (cit. on p. 40).

[121] S.-i. Tomonaga, "Remarks on Bloch's Method of Sound Waves applied to Many-Fermion Problems," Progress of Theoretical Physics **5**, 544–569 (1950) (cit. on p. 40).

[122] J. M. Luttinger, "An Exactly Soluble Model of a Many-Fermion System," Journal of Mathematical Physics **4**, 1154–1162 (1963) (cit. on p. 40).

[123] J. von Delft and H. Schoeller, "Bosonization for beginners — refermionization for experts," Ann. Phys. **7**, 225 (1998) (cit. on pp. 40, 42–45, 93, 156).

[124] M. Bockrath, D. H. Cobden, J. Lu, A. G. Rinzler, R. E. Smalley, L. Balents, and P. L. McEuen, "Luttinger-liquid behaviour in carbon nanotubes," Nature **397**, 598–601 (1999) (cit. on p. 40).

[125] O. M. Auslaender, H. Steinberg, A. Yacoby, Y. Tserkovnyak, B. I. Halperin, K. W. Baldwin, L. N. Pfeiffer, and K. W. West, "Spin-Charge Separation and Localization in One Dimension," Science **308**, 88–92 (2005) (cit. on pp. 40, 91).

[126] O. M. Auslaender, A. Yacoby, R. de Picciotto, K. W. Baldwin, L. N. Pfeiffer, and K. W. West, "Tunneling Spectroscopy of the Elementary Excitations in a One-Dimensional Wire," Science **295**, 825 (2002) (cit. on pp. 40, 91).

[127] H. Steinberg, G. Barak, A. Yacoby, L. N. Pfeiffer, K. W. West, B. I. Halperin, and K. Le Hur, "Charge fractionalization in quantum wires," Nature Physics **4**, 117 (2007) (cit. on p. 40).

[128] P. Brasseur, N. H. Tu, Y. Sekine, K. Muraki, M. Hashisaka, T. Fujisawa, and N. Kumada, "Charge fractionalization in artificial Tomonaga-Luttinger liquids with controlled interaction strength," Phys. Rev. B **96**, 081101 (2017) (cit. on p. 40).

[129] R. Shankar, "Renormalization-group approach to interacting fermions," Rev. Mod. Phys. **66**, 129–192 (1994) (cit. on p. 40).

[130] J Voit, "One-dimensional Fermi liquids," Reports on Progress in Physics **58**, 977 (1995) (cit. on pp. 40, 45, 46, 92).

[131] J. Sólyom, "The Fermi gas model of one-dimensional conductors," Advances in Physics **28**, 201–303 (1979) (cit. on p. 40).

[132] C. Wu, B. A. Bernevig, and S.-C. Zhang, "Helical Liquid and the Edge of Quantum Spin Hall Systems," Phys. Rev. Lett. **96**, 106401 (2006) (cit. on pp. 43, 85).

[133] R. Heidenreich, R. Seiler, and D. A. Uhlenbrock, "The Luttinger model," Journal of Statistical Physics **22**, 27–57 (1980) (cit. on p. 43).

[134] K.-V. Pham, M. Gabay, and P. Lederer, "Fractional excitations in the Luttinger liquid," Phys. Rev. B **61**, 16397 (2000) (cit. on pp. 48, 49, 91).

[135] K.-I. Imura, K.-V. Pham, P. Lederer, and F. Piéchon, "Conductance of one-dimensional quantum wires," Phys. Rev. B **66**, 035313 (2002) (cit. on p. 48).

[136] K. L. Hur, B. I. Halperin, and A. Yacoby, "Charge fractionalization in nonchiral Luttinger systems," Annals of Physics **323**, 3037 –3058 (2008) (cit. on p. 48).

[137] V. V. Deshpande, M. Bockrath, L. I. Glazman, and A. Yacoby, "Electron liquids and solids in one dimension," Nature **464**, 209–216 (2010) (cit. on p. 48).

[138] E. Perfetto, G. Stefanucci, H. Kamata, and T. Fujisawa, "Time-resolved charge fractionalization in inhomogeneous Luttinger liquids," Phys. Rev. B **89**, 201413 (2014) (cit. on pp. 48, 91).

[139] I. Safi and H. J. Schulz, "Transport in an inhomogeneous interacting one-dimensional system," Phys. Rev. B **52**, R17040 (1995) (cit. on pp. 48, 91).

[140] D. L. Maslov and M. Stone, "Landauer conductance of Luttinger liquids with leads," Phys. Rev. B **52**, R5539–R5542 (1995) (cit. on p. 48).

[141] T. Karzig, G. Refael, L. I. Glazman, and F. von Oppen, "Energy Partitioning of Tunneling Currents into Luttinger Liquids," Phys. Rev. Lett. **107**, 176403 (2011) (cit. on pp. 50, 51).

[142] A. Calzona, M. Acciai, M. Carrega, F. Cavaliere, and M. Sassetti, "Time-resolved energy dynamics after single electron injection into an interacting helical liquid," Phys. Rev. B **94**, 035404 (2016) (cit. on p. 50).

[143] I. P. Levkivskyi and E. V. Sukhorukov, "Dephasing in the electronic Mach-Zehnder interferometer at filling factor $\nu = 2$," Phys. Rev. B **78**, 045322 (2008) (cit. on p. 51).

[144] X. G. Wen, "Chiral Luttinger liquid and the edge excitations in the fractional quantum Hall states," Phys. Rev. B **41**, 12838–12844 (1990) (cit. on p. 51).

[145] E. Bocquillon, "Electron quantum optics in quantum Hall edge channels," PhD thesis (Nov. 2012) (cit. on p. 51).

[146] A Braggio, D Ferraro, M Carrega, N Magnoli, and M Sassetti, "Environmental induced renormalization effects in quantum Hall edge states due to 1/f noise and dissipation," New Journal of Physics **14**, 093032 (2012) (cit. on p. 54).

[147] E. Berg, Y. Oreg, E.-A. Kim, and F. von Oppen, "Fractional Charges on an Integer Quantum Hall Edge," Phys. Rev. Lett. **102**, 236402 (2009) (cit. on p. 54).

[148] I. Neder, "Fractionalization Noise in Edge Channels of Integer Quantum Hall States," Phys. Rev. Lett. **108**, 186404 (2012) (cit. on p. 54).

[149] M. Milletarì and B. Rosenow, "Shot-Noise Signatures of Charge Fractionalization in the $\nu = 2$ Quantum Hall Edge," Phys. Rev. Lett. **111**, 136807 (2013) (cit. on pp. 54, 76).

[150] H. Inoue, A. Grivnin, N. Ofek, I. Neder, M. Heiblum, V. Umansky, and D. Mahalu, "Charge Fractionalization in the Integer Quantum Hall Effect," Phys. Rev. Lett. **112**, 166801 (2014) (cit. on pp. 56, 76).

[151] M. Hashisaka, N. Hiyama, T. Akiho, K. Muraki, and T. Fujisawa, "Waveform measurement of charge- and spin-density wavepackets in a chiral Tomonaga-Luttinger liquid," Nature Physics **13**, 559–562 (2017) (cit. on pp. 56, 58).

[152] M. Hashisaka and T. Fujisawa, "Tomonaga–Luttinger-liquid nature of edge excitations in integer quantum Hall edge channels," Reviews in Physics **3**, 32 –43 (2018) (cit. on p. 56).

[153] K. Itoh, R. Nakazawa, T. Ota, M. Hashisaka, K. Muraki, and T. Fujisawa, "Signatures of a Nonthermal Metastable State in Copropagating Quantum Hall Edge Channels," Phys. Rev. Lett. **120**, 197701 (2018) (cit. on p. 56).

[154] M. Acciai, A. Calzona, G. Dolcetto, T. L. Schmidt, and M. Sassetti, "Charge and energy fractionalization mechanism in one-dimensional channels," Phys. Rev. B **96**, 075144 (2017) (cit. on pp. 66, 94).

[155] A. O. Slobodeniuk, E. G. Idrisov, and E. V. Sukhorukov, "Relaxation of an electron wave packet at the quantum Hall edge at filling factor $\nu = 2$," Phys. Rev. B **93**, 035421 (2016) (cit. on p. 66).

[156] F. Ronetti, "Charge and heat transport in topological systems," PhD thesis (Dec. 2018) (cit. on pp. 79, 142).

[157] D. Ferraro, F. Ronetti, J. Rech, T. Jonckheere, M. Sassetti, and T. Martin, "Enhancing photon squeezing one leviton at a time," Phys. Rev. B **97**, 155135 (2018) (cit. on pp. 81, 95, 96, 112).

[158] B. Simon, "Holonomy, the Quantum Adiabatic Theorem, and Berry's Phase," Phys. Rev. Lett. **51**, 2167–2170 (1983) (cit. on p. 83).

[159] X.-G. Wen, "Topological orders and edge excitations in fractional quantum Hall states," Advances in Physics **44**, 405–473 (1995) (cit. on p. 83).

[160] C. L. Kane and E. J. Mele, "Quantum Spin Hall Effect in Graphene," Phys. Rev. Lett. **95**, 226801 (2005) (cit. on pp. 83, 85).

[161] C. L. Kane and E. J. Mele, "Z_2 Topological Order and the Quantum Spin Hall Effect," Phys. Rev. Lett. **95**, 146802 (2005) (cit. on p. 83).

[162] C. Liu, T. L. Hughes, X.-L. Qi, K. Wang, and S.-C. Zhang, "Quantum Spin Hall Effect in Inverted Type-II Semiconductors," Phys. Rev. Lett. **100**, 236601 (2008) (cit. on p. 83).

[163] I. Knez, R.-R. Du, and G. Sullivan, "Evidence for Helical Edge Modes in Inverted InAs/GaSb Quantum Wells," Phys. Rev. Lett. **107**, 136603 (2011) (cit. on p. 83).

[164] L. Du, I. Knez, G. Sullivan, and R.-R. Du, "Robust Helical Edge Transport in Gated InAs/GaSb Bilayers," Phys. Rev. Lett. **114**, 096802 (2015) (cit. on p. 83).

[165] A. P. Schnyder, S. Ryu, A. Furusaki, and A. W. W. Ludwig, "Classification of topological insulators and superconductors in three spatial dimensions," Phys. Rev. B **78**, 195125 (2008) (cit. on p. 83).

[166] A. Kitaev, "Periodic table for topological insulators and superconductors," AIP Conference Proceedings **1134**, 22–30 (2009) (cit. on p. 83).

[167] A. P. Schnyder, S. Ryu, A. Furusaki, and A. W. W. Ludwig, "Classification of Topological Insulators and Superconductors," AIP Conference Proceedings **1134**, 10–21 (2009) (cit. on p. 83).

[168] S. Ryu, A. P. Schnyder, A. Furusaki, and A. W. W. Ludwig, "Topological insulators and superconductors: tenfold way and dimensional hierarchy," New Journal of Physics **12**, 065010 (2010) (cit. on p. 83).

[169] S. Murakami, "Phase transition between the quantum spin Hall and insulator phases in 3D: emergence of a topological gapless phase," New Journal of Physics **9**, 356–356 (2007) (cit. on p. 85).

[170] X.-L. Qi and S.-C. Zhang, "The quantum spin Hall effect and topological insulators," Physics Today **63**, 33–38 (2010) (cit. on p. 86).

[171] J. I. Väyrynen, F. Geissler, and L. I. Glazman, "Magnetic moments in a helical edge can make weak correlations seem strong," Phys. Rev. B **93**, 241301 (2016) (cit. on p. 89).

[172] F. Dolcini, R. C. Iotti, A. Montorsi, and F. Rossi, "Photoexcitation of electron wave packets in quantum spin Hall edge states: Effects of chiral anomaly from a localized electric pulse," Phys. Rev. B **94**, 165412 (2016) (cit. on p. 92).

[173] F. Dolcini and F. Rossi, "Photoexcitation in two-dimensional topological insulators," The European Physical Journal Special Topics **227**, 1323 (2018) (cit. on p. 92).

[174] D. Ferraro, B. Roussel, C. Cabart, E. Thibierge, G. Fève, C. Grenier, and P. Degiovanni, "Real-Time Decoherence of Landau and Levitov Quasiparticles in Quantum Hall Edge Channels," Phys. Rev. Lett. **113**, 166403 (2014) (cit. on p. 96).

[175] M. Moskalets, "Fractionally Charged Zero-Energy Single-Particle Excitations in a Driven Fermi Sea," Phys. Rev. Lett. **117**, 046801 (2016) (cit. on pp. 96, 115).

[176] M. Moskalets and G. Haack, "Single-electron coherence: Finite temperature versus pure dephasing," Physica E: Low-dimensional Systems and Nanostructures **82**, 204 (2016) (cit. on p. 96).

[177] P. P. Hofer, D. Dasenbrook, and C. Flindt, "On-demand entanglement generation using dynamic single-electron sources," physica status solidi (b) **254**, 1600582 (2017) (cit. on p. 96).

[178] M. Moskalets and G. Haack, "Heat and charge transport measurements to access single-electron quantum characteristics," physica status solidi (b) **254**, 1600616 (2017) (cit. on p. 96).

[179] C. Cabart, B. Roussel, G. Fève, and P. Degiovanni, "Taming electronic decoherence in one-dimensional chiral ballistic quantum conductors," Phys. Rev. B **98**, 155302 (2018) (cit. on p. 96).

[180] N. Dashti, M. Misiorny, S. Kheradsoud, P. Samuelsson, and J. Splettstoesser, "Minimal excitation single-particle emitters: Comparison of charge-transport and energy-transport properties," Phys. Rev. B **100**, 035405 (2019) (cit. on p. 96).

[181] R. Bisognin et al., "Quantum tomography of electrical currents," Nature Communications **10**, 3379 (2019) (cit. on p. 96).

[182] P. Burset, J. Kotilahti, M. Moskalets, and C. Flindt, "Time-Domain Spectroscopy of Mesoscopic Conductors Using Voltage Pulses," Advanced Quantum Technologies **2**, 1900014 (2019) (cit. on p. 96).

[183] S. Das and S. Rao, "Spin-Polarized Scanning-Tunneling Probe for Helical Luttinger Liquids," Phys. Rev. Lett. **106**, 236403 (2011) (cit. on p. 100).

[184] A. Calzona, M. Carrega, G. Dolcetto, and M. Sassetti, "Transient dynamics of spin-polarized injection in helical Luttinger liquids," Physica E Low-Dimensional Systems and Nanostructures **74**, 630 (2015) (cit. on p. 100).

[185] L. Liu, A. Richardella, I. Garate, Y. Zhu, N. Samarth, and C.-T. Chen, "Spin-polarized tunneling study of spin-momentum locking in topological insulators," Phys. Rev. B **91**, 235437 (2015) (cit. on p. 100).

[186] S. M. Hus, X.-G. Zhang, G. D. Nguyen, W. Ko, A. P. Baddorf, Y. P. Chen, and A.-P. Li, "Detection of the Spin-Chemical Potential in Topological Insulators Using Spin-Polarized Four-Probe STM," Phys. Rev. Lett. **119**, 137202 (2017) (cit. on p. 100).

[187] B. Voigtländer, V. Cherepanov, S. Korte, A. Leis, D. Cuma, S. Just, and F. Lüpke, "Multi-tip scanning tunneling microscopy: Experimental techniques and data analysis," Review of Scientific Instruments **89**, 101101 (2018) (cit. on p. 100).

[188] W. Belzig and M. Vanevic, "Elementary Andreev processes in a driven superconductor–normal metal contact," Physica E: Low-dimensional Systems and Nanostructures **75**, 22 (2016) (cit. on p. 105).

[189] B. D. Josephson, "Coupled Superconductors," Rev. Mod. Phys. **36**, 216–220 (1964) (cit. on p. 107).

[190] J. R. Waldram, "The Josephson effects in weakly coupled superconductors," Rep. Prog. Phys. **39**, 751–827 (1976) (cit. on pp. 107, 114, 115).

[191] K. K. Likharev, "Superconducting weak links," Rev. Mod. Phys. **51**, 101–159 (1979) (cit. on p. 107).

[192] B. D. Josephson, "Possible new effects in superconductive tunnelling," Phys. Lett. **1**, 251 –253 (1962) (cit. on pp. 107, 108, 115).

[193] C. W. J. Beenakker and H. van Houten, "Josephson current through a superconducting quantum point contact shorter than the coherence length," Phys. Rev. Lett. 66, 3056–3059 (1991) (cit. on p. 107).

[194] C. Beenakker and H. van Houten, "The superconducting quantum point contact," in *Nanostructures and mesoscopic systems*, edited by W. P. Kirk and M. A. Reed (Academic Press, 1992), pp. 481 –497 (cit. on pp. 107, 109).

[195] E. Scheer, P. Joyez, D. Esteve, C. Urbina, and M. H. Devoret, "Conduction Channel Transmissions of Atomic-Size Aluminum Contacts," Phys. Rev. Lett. 78, 3535–3538 (1997) (cit. on p. 107).

[196] M. F. Goffman, R. Cron, A. Levy Yeyati, P. Joyez, M. H. Devoret, D. Esteve, and C. Urbina, "Supercurrent in Atomic Point Contacts and Andreev States," Phys. Rev. Lett. 85, 170–173 (2000) (cit. on p. 107).

[197] L. Bretheau, Ç. Girit, L. Tosi, M. Goffman, P. Joyez, H. Pothier, D. Esteve, and C. Urbina, "Superconducting quantum point contacts," Comptes Rendus Physique 13, 89 –100 (2012) (cit. on pp. 107, 109).

[198] S. S. Pershoguba and L. I. Glazman, "Thermopower and thermal conductance of a superconducting quantum point contact," Phys. Rev. B 99, 134514 (2019) (cit. on p. 107).

[199] J. Moreland and J. W. Ekin, "Electron tunneling experiments using Nb-Sn 'break' junctions," J. Appl. Phys. 58, 3888–3895 (1985) (cit. on p. 107).

[200] C. Muller, J. van Ruitenbeek, and L. de Jongh, "Experimental observation of the transition from weak link to tunnel junction," Physica C: Superconductivity 191, 485 –504 (1992) (cit. on p. 107).

[201] J. M. van Ruitenbeek, A. Alvarez, I. Piñeyro, C. Grahmann, P. Joyez, M. H. Devoret, D. Esteve, and C. Urbina, "Adjustable nanofabricated atomic size contacts," Rev. of Sci. Instrum. 67, 108–111 (1996) (cit. on p. 107).

[202] J. M. van Ruitenbeek, "Quantum Point Contacts Between Metals," in *Mesoscopic Electron Transport*, edited by L. L. Sohn, L. P. Kouwenhoven, and G. Schön (Springer Netherlands, Dordrecht, 1997), pp. 549–579 (cit. on p. 107).

[203] B. Ludoph, N. van der Post, E. N. Bratus, E. V. Bezuglyi, V. S. Shumeiko, G. Wendin, and J. M. van Ruitenbeek, "Multiple Andreev reflection in single-atom niobium junctions," Phys. Rev. B 61, 8561–8569 (2000) (cit. on p. 107).

[204] R. Cron, M. F. Goffman, D. Esteve, and C. Urbina, "Multiple-Charge-Quanta Shot Noise in Superconducting Atomic Contacts," Phys. Rev. Lett. 86, 4104–4107 (2001) (cit. on p. 107).

[205] E. Scheer, W. Belzig, Y. Naveh, M. H. Devoret, D. Esteve, and C. Urbina, "Proximity Effect and Multiple Andreev Reflections in Gold Atomic Contacts," Phys. Rev. Lett. **86**, 284–287 (2001) (cit. on p. 107).

[206] M. Chauvin, P. vom Stein, H. Pothier, P. Joyez, M. E. Huber, D. Esteve, and C. Urbina, "Superconducting Atomic Contacts under Microwave Irradiation," Phys. Rev. Lett. **97**, 067006 (2006) (cit. on pp. 107, 121).

[207] M. Chauvin, P. vom Stein, D. Esteve, C. Urbina, J. C. Cuevas, and A. L. Yeyati, "Crossover from Josephson to Multiple Andreev Reflection Currents in Atomic Contacts," Phys. Rev. Lett. **99**, 067008 (2007) (cit. on p. 107).

[208] H. Takayanagi, T. Akazaki, and J. Nitta, "Observation of Maximum Supercurrent Quantization in a Superconducting Quantum Point Contact," Phys. Rev. Lett. **75**, 3533–3536 (1995) (cit. on p. 107).

[209] H. Thierschmann, E. Mulazimoglu, N. Manca, S. Goswami, T. M. Klapwijk, and A. D. Caviglia, "Transport regimes of a split gate superconducting quantum point contact in the two-dimensional LaAlO3/SrTiO3 superfluid," Nat. Commun. **9**, 2276 (2018) (cit. on pp. 107, 121).

[210] J. C. Cuevas, A. Martín-Rodero, and A. L. Yeyati, "Hamiltonian approach to the transport properties of superconducting quantum point contacts," Phys. Rev. B **54**, 7366–7379 (1996) (cit. on pp. 107, 110, 111, 114).

[211] T. Klapwijk, G. Blonder, and M. Tinkham, "Explanation of subharmonic energy gap structure in superconducting contacts," Physica B+C **109-110**, 1657 –1664 (1982) (cit. on p. 107).

[212] G. E. Blonder, M. Tinkham, and T. M. Klapwijk, "Transition from metallic to tunneling regimes in superconducting microconstrictions: Excess current, charge imbalance, and supercurrent conversion," Phys. Rev. B **25**, 4515–4532 (1982) (cit. on p. 107).

[213] S. Shapiro, "Josephson Currents in Superconducting Tunneling: The Effect of Microwaves and Other Observations," Phys. Rev. Lett. **11**, 80–82 (1963) (cit. on pp. 108, 109, 114).

[214] J. C. Cuevas, J. Heurich, A. Martín-Rodero, A. Levy Yeyati, and G. Schön, "Subharmonic Shapiro Steps and Assisted Tunneling in Superconducting Point Contacts," Phys. Rev. Lett. **88**, 157001 (2002) (cit. on p. 108).

[215] G. Stefanucci, E. Perfetto, and M. Cini, "Time-dependent quantum transport with superconducting leads: A discrete-basis Kohn-Sham formulation and propagation scheme," Phys. Rev. B **81**, 115446 (2010) (cit. on p. 108).

[216] F. S. Bergeret, P. Virtanen, T. T. Heikkilä, and J. C. Cuevas, "Theory of Microwave-Assisted Supercurrent in Quantum Point Contacts," Phys. Rev. Lett. **105**, 117001 (2010) (cit. on p. 108).

[217] F. S. Bergeret, P. Virtanen, A. Ozaeta, T. T. Heikkilä, and J. C. Cuevas, "Supercurrent and Andreev bound state dynamics in superconducting quantum point contacts under microwave irradiation," Phys. Rev. B **84**, 054504 (2011) (cit. on p. 108).

[218] Y.-H. Li, J. Song, J. Liu, H. Jiang, Q.-F. Sun, and X. C. Xie, "Doubled Shapiro steps in a topological Josephson junction," Phys. Rev. B **97**, 045423 (2018) (cit. on p. 108).

[219] V. L. Ginzburg and L. D. Landau, "On the Theory of superconductivity," Zh. Eksp. Teor. Fiz. **20**, 1064–1082 (1950) (cit. on p. 108).

[220] L. N. Cooper, "Bound Electron Pairs in a Degenerate Fermi Gas," Phys. Rev. **104**, 1189–1190 (1956) (cit. on p. 108).

[221] A. Martín-Rodero, F. J. García-Vidal, and A. Levy Yeyati, "Microscopic theory of Josephson mesoscopic constrictions," Phys. Rev. Lett. **72**, 554–557 (1994) (cit. on p. 110).

[222] A. Levy Yeyati, A. Martín-Rodero, and F. J. García-Vidal, "Self-consistent theory of superconducting mesoscopic weak links," Phys. Rev. B **51**, 3743–3753 (1995) (cit. on p. 110).

[223] J. Bardeen, L. N. Cooper, and J. R. Schrieffer, "Microscopic Theory of Superconductivity," Phys. Rev. **106**, 162–164 (1957) (cit. on p. 110).

[224] D Rogovin and D. Scalapino, "Fluctuation phenomena in tunnel junctions," Annals of Physics **86**, 1 –90 (1974) (cit. on pp. 110, 115).

[225] A Barone and G Paterno, *Physics and Applications of the Josephson Effect* (Wiley, New York, 1982) (cit. on pp. 110, 115).

[226] L. V. Keldysh, "Diagram Technique for Nonequilibrium Processes," Zh. Eksp. Teor. Fiz. **47**, 1515–1527 (1964) (cit. on p. 110).

[227] J. Rammer and H. Smith, "Quantum field-theoretical methods in transport theory of metals," Rev. Mod. Phys. **58**, 323–359 (1986) (cit. on p. 110).

[228] A. Kamenev and A. Levchenko, "Keldysh technique and non-linear σ-model: basic principles and applications," Adv. Phys. **58**, 197–319 (2009) (cit. on p. 110).

[229] Y. Nambu, "Quasi-Particles and Gauge Invariance in the Theory of Superconductivity," Phys. Rev. **117**, 648–663 (1960) (cit. on p. 110).

[230] J. C. Cuevas, A. Martín-Rodero, and A. L. Yeyati, "Shot Noise and Coherent Multiple Charge Transfer in Superconducting Quantum Point Contacts," Phys. Rev. Lett. **82**, 4086–4089 (1999) (cit. on p. 111).

[231] I. Gradshteyn and I. Ryzhik, *Table of Integrals, Series, and Products* (Academic Press, 2014) (cit. on p. 113).

[232] D. N. Langenberg, "Physical interpretation of the $\cos\varphi$ term and implications for detectors," Rev. Phys. Appl. (Paris) **9**, 35–40 (1974) (cit. on p. 115).

[233] M. Moskalets, "High-temperature fusion of a multielectron leviton," Phys. Rev. B **97**, 155411 (2018) (cit. on p. 115).

[234] D. C. Glattli and P. S. Roulleau, "Levitons for electron quantum optics," Phys. Status Solidi (b) **254**, 1600650 (2017) (cit. on p. 115).

[235] F. Dolcini and F. Rossi, "Photoexcitation in two-dimensional topological insulators," The European Physical Journal Special Topics **227**, 1323 (2018) (cit. on p. 115).

[236] P. K. Tien and J. P. Gordon, "Multiphoton Process Observed in the Interaction of Microwave Fields with the Tunneling between Superconductor Films," Phys. Rev. **129**, 647–651 (1963) (cit. on p. 116).

[237] M. Kapfer, P. Roulleau, M. Santin, I. Farrer, D. A. Ritchie, and D. C. Glattli, "A Josephson relation for fractionally charged anyons," Science **363**, 846–849 (2019) (cit. on p. 124).

[238] I. Gurman, R. Sabo, M. Heiblum, V. Umansky, and D. Mahalu, "Extracting net current from an upstream neutral mode in the fractional quantum Hall regime," Nature Communications **3**, 1289 (2012) (cit. on p. 124).

[239] A. Y. Kitaev, "Unpaired Majorana fermions in quantum wires," Physics-Uspekhi **44**, 131–136 (2001) (cit. on p. 124).

[240] W. B. Case, "Wigner functions and Weyl transforms for pedestrians," American Journal of Physics **76**, 937–946 (2008) (cit. on p. 129).

[241] H.-W. Lee, "Theory and application of the quantum phase-space distribution functions," Physics Reports **259**, 147 –211 (1995) (cit. on p. 129).

[242] J. Weinbub and D. K. Ferry, "Recent advances in Wigner function approaches," Applied Physics Reviews **5**, 041104 (2018) (cit. on p. 129).

[243] S. Haroche and J.-M. Raimond, *Exploring the Quantum: Atoms, Cavities, and Photons* (Oxford University Press, Oxford, 2006) (cit. on p. 132).

[244] H. Groenewold, "On the principles of elementary quantum mechanics," Physica **12**, 405 –460 (1946) (cit. on p. 133).

[245] J. E. Moyal, "Quantum mechanics as a statistical theory," Mathematical Proceedings of the Cambridge Philosophical Society **45**, 99–124 (1949) (cit. on p. 133).

[246] G. A. Baker, "Formulation of Quantum Mechanics Based on the Quasi-Probability Distribution Induced on Phase Space," Phys. Rev. **109**, 2198–2206 (1958) (cit. on p. 133).

[247] D. B. Fairlie, "The formulation of quantum mechanics in terms of phase space functions," Mathematical Proceedings of the Cambridge Philosophical Society **60**, 581–586 (1964) (cit. on p. 133).

[248] T. Curtright, D. Fairlie, and C. Zachos, "Features of time-independent Wigner functions," Phys. Rev. D **58**, 025002 (1998) (cit. on p. 133).

[249] W. N. Bailey, "On the Product of two Legendre Polynomials with Different Arguments," Proceedings of the London Mathematical Society **s2-41**, 215–220 (1936) (cit. on p. 134).

[250] Y. M. Blanter and M. Büttiker, "Shot noise in mesoscopic conductors," Phys. Rep. **336**, 1 (2000) (cit. on p. 138).

[251] T. Martin, "Noise in mesoscopic physics," in *Nanophysics: coherence and transport*, Vol. 81, edited by H. Bouchiat, Y. Gefen, S. Guéron, G. Montambaux, and J. Dalibard, Les Houches (Elsevier, 2005), pp. 283 –359 (cit. on p. 138).

[252] G. B. Lesovik and I. A. Sadovskyy, "Scattering matrix approach to the description of quantum electron transport," Physics-Uspekhi **54**, 1007–1059 (2011) (cit. on p. 138).